Global mantle tomography using Backus–Gilbert inversion of normal-mode and finite-frequency S-wave data

Frédéric Dubois

École et observatoire
des **sciences de la Terre**
de l'Université de Strasbourg
et du CNRS

Laboratoire
Institut de **physique** du **globe**
de Strasbourg | IPGS | UMR 7516
de l'Université de Strasbourg
et du CNRS

Université de Strasbourg

École doctorale nº 413 : Sciences de la Terre et Environnement

Institut de Physique du Globe de Strasbourg

THÈSE

présentée et soutenue publiquement par

Frédéric DUBOIS

le 24 janvier 2020

pour l'obtention du grade de : **Docteur de l'Université de Strasbourg**
discipline et spécialité : **Sciences de la Terre et de l'univers - Géophysique**

Global mantle tomography using Backus–Gilbert inversion of normal-mode and finite-frequency S-wave data

Thèse dirigée par :

Luis	RIVERA	Professeur	Université de Strasbourg
Christophe	ZAROLI	Maître de conférence	Université de Strasbourg
Sophie	LAMBOTTE	Physicienne adjointe	Université de Strasbourg

---

Rapporteurs :

Lapo	BOSCHI	Professeur	Université de Padoue
Éléonore	STUTZMANN	Physicenne	IPG de Paris

Autres membres du jury :

Alessia	MAGGI	Professeur	Université de Strasbourg
Stéphanie	DURAND	Chargée de recherche	ENS de Lyon
Paula	KOELEMEIJER	Maître de conférence	Université de Londres

Remerciements

Je souhaite tout d'abord remercier mes directeurs de thèse Christophe Zaroli, Sophie Lambotte et Luis Rivera pour leurs temps et toute l'aide qu'ils m'ont fournis durant ces trois années de thèse. Plus largement, je remercie toute l'équipe de l'EOST pour ces six années de l'école d'ingénieur à la thèse. Merci également aux étudiants des promotions 2020/2021/2022 pour toute leur bonne humeur le lundi après-midi pour les TD d'infos. Merci à Jean-Marc Brendle pour son aide tout au long de la thèse et encore après.

Plus particulièrement, je voudrais remercier Christophe Zaroli qui a initié cette thèse il y a maintenant cinq ans avec Sophie Lambotte. Tu as toujours eu ton bureau ouvert pour moi et su répondre à mes questions. De tes cours de maths de première année aux dernières minutes avant la soutenance, tu as toujours su m'encourager avec un optimisme à toutes épreuves que j'espère avoir hérité durant ces dernières années. Merci à Sophie Lambotte pour toute son aide, son soutien et sa confiance tout au long de la thèse et mon master. Je n'aurais jamais atteint la fin de thèse sans toi, aussi bien face aux problèmes scientifiques qu'aux problèmes administratifs. Christophe et Sophie vous avez été le véritable équilibre dans ma thèse et je ne vous remercierai jamais assez pour ça. Merci à Luis d'avoir accepté d'être mon directeur de thèse officiel. J'ai toujours adoré nos discussions qui étaient parfois loin de la sismologie et tes cours laisseront un souvenir vivace dans ma mémoire d'étudiant. Au-delà de la science, tu as toujours été d'une incroyable gentillesse et une personne soucieuse de la santé aussi bien physique et morale des personnes avec lesquelles tu travailles, et plus particulièrement tes doctorants. J'aimerais également remercier Jean-Marc Brendle que je considère comme un quatrième encadrant de thèse. J'ai appris énormément de chose avec toi et ton calme légendaire face aux plus terribles incidents informatiques de l'IPGS restera dans ma mémoire. Sans toi j'aurais certainement dû faire mes calculs sur ma TI-84 et rédiger ma thèse sur une machine à écrire.

Merci également à tous mes amis qui ont vécu cette thèse avec moi Damian, Baptiste, Luke, Chloé, Bruno, Michi, Jeanne, Paul Bernard, Paul Calou, Marta, Agnès, Cooper, Lucille, Max, Benoît, Thomas, Myriam, Francis, Marie-Eva, Antoine, Coralie, Romain, Yacouba et tous les autres. Merci à toute ma famille pour m'avoir soutenu et accompagné tout au long de cette thèse. Merci à Anne pour son soutien durant ces années de thèse. Je n'aurais ni commencé ni fini la thèse sans toi. Merci pour toutes les relectures et les répétitions que tu as subies sans t'endormir, la plupart du temps.

Contents

Abstract

Knowledge about the Earth's deep structures comes mainly from seismic tomography. Off course, other sources of information are available to better understand the deep Earth's interior such as magnetism, geodesy or geochemistry. For several years, seismic tomography steadily improved, by both new developments in theory and new data. In this study, we will present the first unbiased tomographic images of the mantle obtained through a rejuvenated Backus–Gilbert joint inversion of two different data sets: finite-frequency shear-wave time-residuals and normal modes data. The Backus–Gilbert inversion scheme allows to interpret quantitatively the unbiased multi-resolution images.

To better constrain the fine structures of the mantle a good body-wave coverage need to be set across the mantle. To this end, we build a new database of time residuals by measuring different kind of shear waves. It includes S, ScS, SS, ScS_2 waves and even interferences between S and ScS waves at large epicentral distances ($> 75°$). This new finite-frequency shear-wave data set, containing more than 630 000 time-residuals, is measured over five different period bands: 10 s, 15 s, 22.5 s, 34 s and 51 s. In this finite-frequency frame, the crustal influence on shear time-residuals is studied. We show that the crust has a major dispersive effect on teleseismic body-wave time-residuals measured by cros-correlation. Although ray crustal corrections remain important, we report the need to correct for finite-frequency crustal effects. To depict these effects, two different 3-D crustal models have been explored: CRUST1.0 and CRUST2.0. It appears that crustal finite-frequency effects may lead to a bias in measurements. On average, it may reach 0.9–1.6 s for CRUST2.0 and 0.5–1.6 s for CRUST1.0, for filtering central period ranging from 10–51 s, respectively. This biais can ultimately have a deep impact over the tomographic images, hence needs to be properly accounted for.

Once body-wave data are recovered and corrected for crustal contributions, normal modes data are integrated to the database. Normal mode selection is carried out in order to offer the best sensitivity compromise between normal modes and body waves. In this view, Stoneley normal modes have been added to our selection to improve constraints on the lowermost mantle. Normal mode data are retrieved from the literature (Deuss et al., 2013; Koelemeijer et al., 2013). Then, we jointly invert in a Backus–Gilbert scheme, shear waves data measured at 22.5 s with normal modes. To better exploit information of these two datasets, we use an irregular parametrization to better mimic the geographic ray density variation of shear wave data. The Backus–Gilbert inversion allows to obtain unbiased model estimates and the associated appraisal (resolution and uncertainties). For the first time, a joint Backus–Gilbert tomography is delivered to the community with its associated appraisal. In the last part we show how we can quantitatively interpret a complex geodynamical structure inside the mantle. The Samoa plume is taken as an example to illustrate the walk in the appraisal workflow.

Résumé

La tomographie sismique est fondamentale dans l'apport des connaissances liées aux structures profondes de la Terre. Bien que d'autres domaines des géosciences soient également des sources importantes d'information tels que le géomagnétisme, la géodésie ou la géochimie. Depuis plusieurs années, la technique de tomographie sismique ne cesse de s'améliorer et des images toujours plus précises de l'intérieur de la Terre sont produites. L'amélioration de ces images est principalement due aux développements théoriques mais également à l'acquisition de nouvelles données permettant d'imager des zones jusqu'ici peu contraintes. Dans cette étude, nous présentons le premier modèle tomographique du manteau terrestre inversé conjointement avec des ondes de volume et des modes propres dans un schéma d'inversion de type Backus–Gilbert. Ce schéma d'inversion permet de produire des images quantitatives et non biaisées du manteau terrestre.

La couverture des ondes de volume dans le manteau profond est dépendante de la répartition globale entre les stations et les séismes. Pour améliorer cette couverture en profondeur nous avons constitué une nouvelle base de données en temps de trajet d'ondes S. Celle-ci contient des mesures d'ondes S, SS, ScS, ScS_2 et même des interférences d'ondes S et ScS à grande distance épicentrale ($> 75°$). Cette nouvelle base de données contient plus de 630 000 mesures de temps de trajet effectuées sur 5 gammes de période : 10 s, 15 s, 22.5 s, 34 s et 51 s. Dans le cadre de la théorie des fréquences finies, nous nous sommes intéressés à l'influence de la croûte sur la mesure de temps de trajet à différentes périodes. Nous montrons que la croûte a un effet dispersif important sur la mesure des temps de trajet des ondes télésismiques mesurés par inter-corrélation. Bien que les corrections de croûte basées sur la théorie des rais soient toujours nécessaires, nous soulignons l'importance de corriger les temps de trajet pour les effets fréquence-finie induits par la croûte. Pour illustrer ce phénomène, nous avons comparé deux modèles de croûte : CRUST1.0 et CRUST2.0. Il apparaît que ces effets à fréquence-finie peuvent engendrer un biais dans les mesures variant entre 0.9-1.6 s pour CRUST2.0 et 0.5-1.6 s pour CRUST1.0 pour une gamme de période entre 10-51 s. Au final ce biais peut impacter la qualité de nos images tomographiques d'où l'importance de corriger ces effets de croûte à fréquences finies.

Une fois la base de données constituée et corrigée de la croûte, les données des modes propres ont été sélectionnées. La sélection des ces modes a pour but d'offrir la meilleure combinaison possible en sensibilité avec celle des ondes de volume. Nous avons donc ajouté des modes particulièrement sensibles au manteau profond tels que les modes de Stoneley. Ces données de modes propres proviennent de la littérature (Deuss et al., 2013; Koelemeijer et al., 2013). Par la suite, nous inversons conjointement les ondes S mesurées à 22.5 s avec les modes propres dans une inversion de type Backus–Gilbert. Pour extraire le plus d'information possible des ondes de volume, nous utilisons une paramétrisation irrégulière permettant de s'adapter aux variations géographiques de la densité de données. L'inversion Backus–Gilbert permet d'obtenir des estimations du modèle de Terre non biaisées avec des outils permettant d'évaluer le modèle (résolution et incertitudes). L'utilisation de ces outils d'évaluation du modèle tomographique est présentée à travers un exemple concret. Pour cela nous nous intéressons au plume mantellique se trouvant sous Samoa, nous montrons les différentes étapes à suivre afin d'interpréter (ou non) cette structure.

Chapitre I

Résumé étendu

Chapitre I

Résumé étendu

I.1 Présentation de la thèse et des méthodes employées

L'objectif de cette thèse est de produire une image tomographique (sismique) quantitative multi-résolution du manteau terrestre (entre 410 et 2889 km de profondeur). Bien que différents modèles du manteau existent aucun d'entre eux ne permet de fournir une image *quantitative* des anomalies sismiques détectées. Pour cela nous utilisons une inversion de type Backus–Gilbert récemment remise au goût du jour en tomographie sismique (Zaroli, 2016). Ces images sont accompagnées d'outils permettant d'interroger le modèle sur les anomalies présentées. Ces outils se composent de la **résolution** en chaque point du modèle ainsi que des **incertitudes** associées, deux éléments fondamentaux dans les problèmes d'imagerie.

Nous utiliserons ici deux jeux de données sismiques de différente nature permettant d'imager le manteau terrestre : les *ondes de volumes* qui serviront à la résolution fine de notre modèle et les *modes propres* qui contraindront les grandes longueurs d'ondes de l'image tomographique. Ces deux types d'ondes sont complémentaires et permettent d'avoir une vision multi-résolution du manteau terrestre.

I.2 Les données sismologiques : ondes de volume et modes propres

I.2.1 Intégration des données d'ondes de volume

Une base de données en temps de trajet d'ondes S avait été constituée lors de la thèse de C. Zaroli, cependant la couverture de ces données se dégrade rapidement pour des profondeurs supérieures à 1500 km. Nous avons donc effectué de nouvelles mesures, afin d'en améliorer la couverture, et ainsi d'imager la partie profonde du manteau.

La couverture des ondes de volume dépend de la géométrie stations-séismes. Comme la répartition géographique de la sismicité mondiale ne change que très peu au cours du temps, il faut donc travailler sur la répartition des stations pour pouvoir illuminer de nouvelles zones. De nombreuses stations ont été installées depuis 2008 (date où s'arrête l'ancienne base de données) ce qui nous offre la possibilité d'améliorer la couverture spatiale. De plus, des données provenant de réseaux temporaires parfois localisés dans régions isolées (Antarctique) ont également été traitées. Ceci afin d'améliorer localement la couverture dans certaines régions. L'ensemble des stations et des séismes utilisés dans cette base de données sont présentés sur la figure I.1.

Nous avons retraité l'intégralité des tremblements de terre sur la période 1976-2008 et effectué de nouvelles mesures sur la période 2008-2017. Différentes phases sismiques ont été

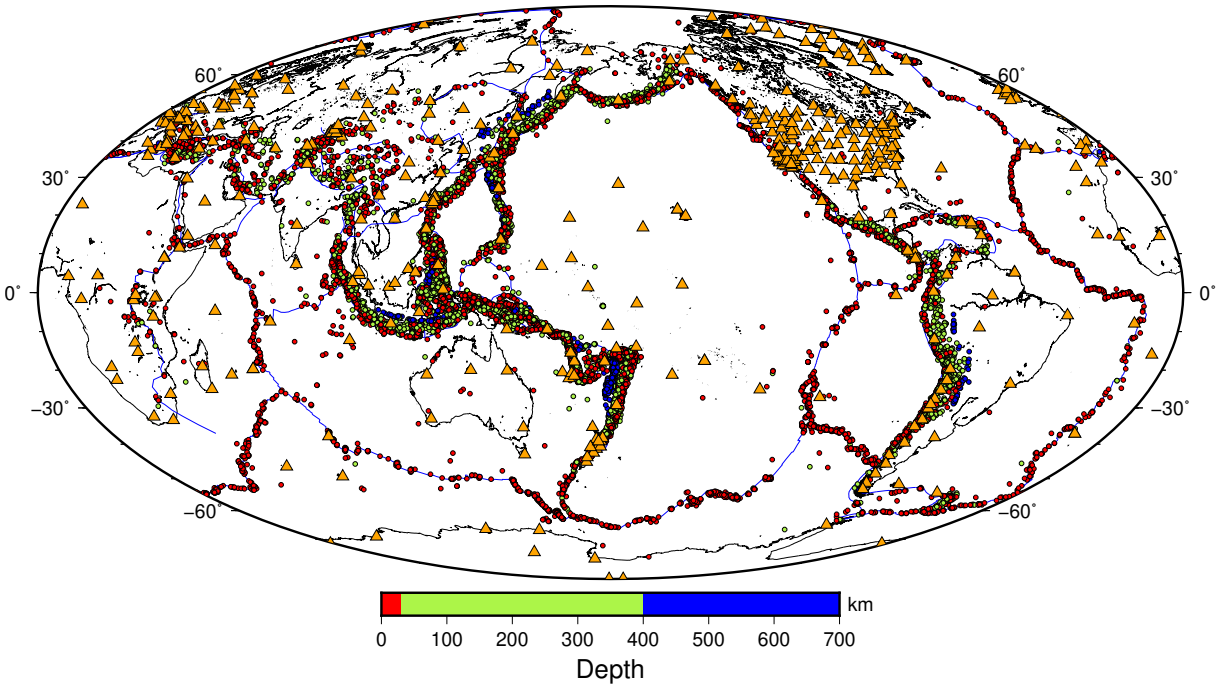

FIGURE I.1 – Répartition géographique des stations et des séismes pour notre nouvelle base de données d'ondes S : la position des stations est indiquée par les triangles oranges, ainsi que les séismes sélectionnés avec une magnitude comprise entre $5.5 < M_w < 6.5$ (à partir du catalogue GCMT). La couleur de chaque cercle indique la profondeur du séisme. Les transitions de couleurs se situent à 30 et 400 km de profondeur. Les limites des plaques tectoniques sont indiquées par un contour bleu.

mesurées parmi lesquelles nous avons les S, ScS, SS ainsi que deux nouvelles phases absentes de l'ancienne base de données. Parmi celles-ci, nous avons les ScS_2 qui sont des ondes S se réfléchissant deux fois à la limite manteau-noyau ou encore les interférences d'ondes S+ScS se produisant à grandes distances épicentrales ($\geq 75°$) (Figure I.2). Ces interférences entre S et ScS sont particulièrement importante lorsque l'on étudie le manteau terrestre profond.

Les temps de trajet des ondes de volume sont mesurés par inter-corrélation nécessitant la définition d'une fenêtre temporelle sur laquelle les deux formes d'ondes (synthétique et observée) vont être comparées. La définition de cette fenêtre est adaptée à la phase considérée (Figure I.3), elle sera notamment plus grande dans le cas d'interférence entre plusieurs phases. Pour automatiser la définition de cette fenêtre d'inter-corrélation un logiciel de mesure automatique en langage python (ACTA.py : automatic cross-correlation traveltimes and amplitudes) a été développé en collaboration avec le LMU de Munich, à partir des travaux réalisés par Zaroli (2010). Ce code permet de mesurer automatiquement et en parallèle une grande quantité de résidus temporels à partir d'inter-corrélation entre sismogrammes observés et prédits.

Pour pouvoir au mieux extraire l'information sur les délais à fréquences finies, il faut pour cela associer chaque délai à une zone de sensibilité (noyaux de sensibilité). Cette zone de sensibilité définit une région dans laquelle toute anomalie présente aura un impact sur le délai mesuré à la station. Deux nouveaux noyaux de sensibilité ont dû être développés ici, celui pour les ondes ScS_2 et celui pour les interférences S+ScS (Figure I.4).

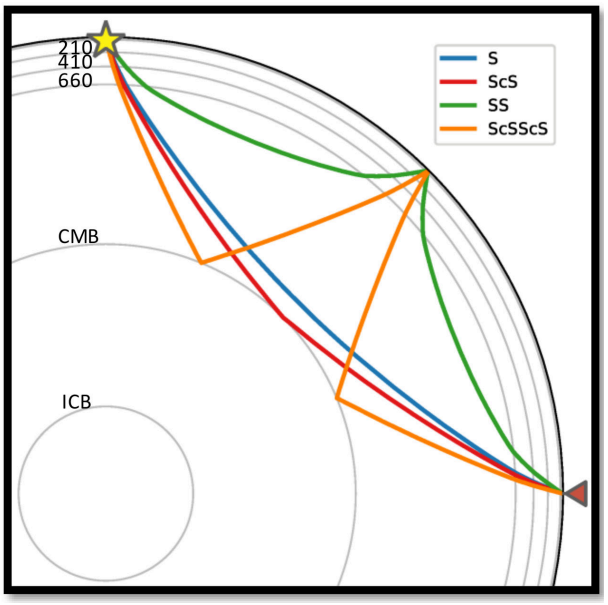

FIGURE I.2 – Exemple de trajectoires des ondes mesurées dans cette étude. Ces trajectoires sont calculées pour un séisme localisé à 50 km (étoile jaune) et une distance épicentrale de $90°$.

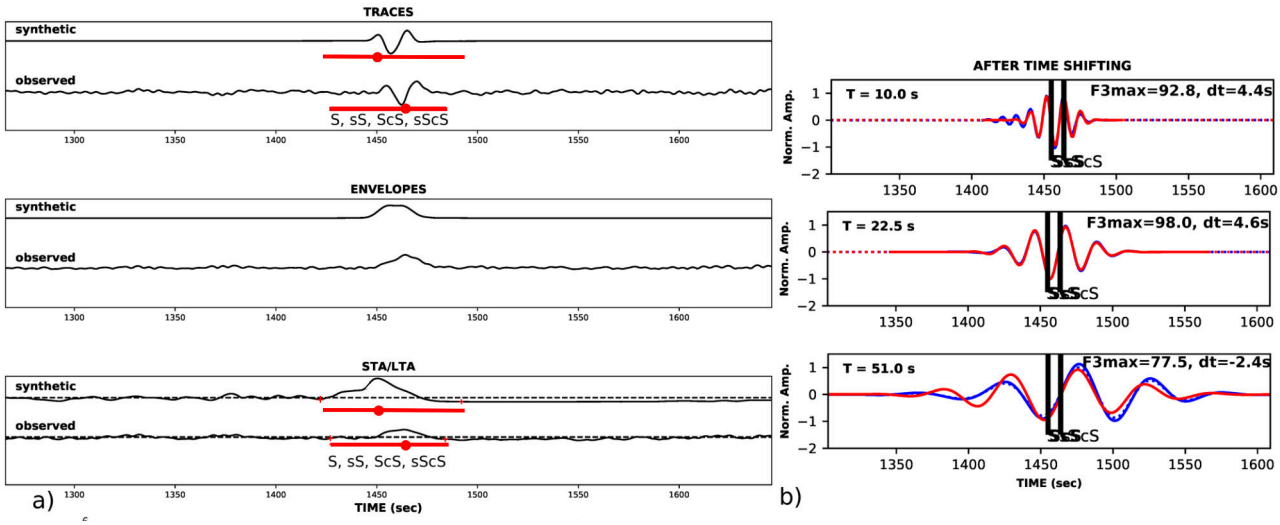

FIGURE I.3 – Exemple de mesure par inter-corrélation d'interférences S+ScS sur la composante transverse à une distance de $92.7°$. À cette distance les phases S, sS, ScS et sScS interfèrent. a) (de haut en bas) Traces synthétiques et observées filtrées entre 7 et 81 s, enveloppes, la forme d'onde STA/LTA. Les fenêtres d'inter-corrélation sont représentées par des barres rouges horizontales avec toutes les phases interférant au-dessous. b) Formes d'ondes synthétiques (rouges) et observées (bleues) après le calage en temps et filtrées entre 10 s, 22.5 s and 51 s (de haut en bas).

I.2.2 Comparaison de codes de calcul de sismogrammes synthétiques

La méthode de mesure utilisée dans cette étude repose sur l'idée que la Terre réelle n'est pas trop éloignée, en terme d'hétérogénéités, d'une Terre 1-D de référence. En se basant sur cette idée on compare les sismogrammes observés (réels) avec des sismogrammes synthétiques

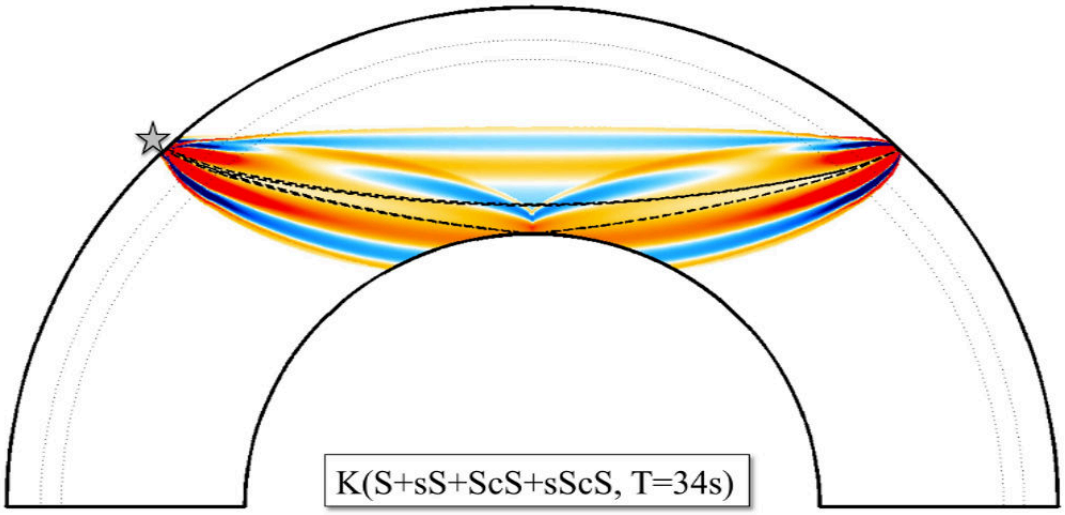

FIGURE I.4 – Noyau de sensibilité pour une interférence d'onde S+sS+ScS+sScS à T=34 s. Le séisme se situe à 0 km à une distance épicentrale de $90°$. Les deux lignes en pointillées représentent les discontinuités sismiques à 410 et 660 km de profondeur. Les deux lignes en tirets gras représentent les trajectoires géométriques des rais S et ScS. Courtesy from C. Zaroli. Merci à Paula Koelemeijer pour avoir donné un nom à ce kernel : the "mustache kernel".

créés à partir du modèle de Terre 1-D. Différents logiciels existent pour générer ces synthétiques, cependant tous n'ont pas les mêmes caractéristiques et ne génèrent pas les mêmes sismogrammes pour un même modèle de Terre.

Nous avons testé quelques logiciels parmi les plus utilisés permettant de créer les sismogrammes synthétiques (SPECFEM, AxiSEM, Yspec). Cependant deux de ces codes (AxiSEM, Yspec) ne satisfont pas nos exigences en terme de prise en compte de la croûte. SPECFEM n'a pas été retenu à cause du temps de calcul trop important. Nous avons donc opté pour un code un peu moins utilisé pour générer nos synthétiques. Ce code repose sur l'approximation WKBJ permettant de résoudre les équations différentielles linéaires du second ordre. Nous utilisons l'implémentation de Chapman (1978) de cette approximation permettant de créer de manière très économique les sismogrammes synthétiques. Par ailleurs, au contraire de Yspec, WKBJ peut utiliser un modèle de croûte adapté sous chaque station alors que Yspec est limité à un seul modèle 1-D. Cette implémentation n'étant pas simple d'utilisation, nous avons créé un enrobage Python permettant à la fois d'interagir avec WKBJ (implémentation de Chapman (1978)) ainsi que d'effectuer les opérations de post-traitement sur les synthétiques (convolution avec la source, correction d'atténuation).

I.2.3 Intégration des données de modes propres

Bien que la couverture en ondes de volume du manteau se soit améliorée, il subsiste des zones peu couvertes, notamment dans le manteau le plus profond. Pour remédier à ce problème nous avons ajouté des données de modes propres. Les modes propres ont une sensibilité intégrée à l'ensemble de la Terre mais uniquement sensibles aux grandes longueurs d'ondes. En plus des modes régulièrement utilisés pour les tomographies du manteau, nous avons ajouté des modes

de Stoneley particulièrement sensibles aux hétérogénéités du manteau inférieur. De plus, le couplage entre certains modes est pris en compte dans notre inversion. Ceci permet d'avoir accès à la fois aux structures de degrés paires et impaires du modèle de Terre.

I.3 Étude des corrections crustales à fréquences finies

Lors des mesures de délais obtenus par inter-corrélation, certaines fractions du délai ne sont pas dues aux anomalies se situant dans le manteau. Ces fractions non désirées font l'objet de corrections et sont d'origines variées : l'ellipticité de la Terre, la topographie, les hétérogénéités de la croûte terrestre.

Un travail important a été mené sur l'étude des corrections crustales en tomographie globale (Dubois et al., 2019). Dans cet article nous montrons l'effet de la croûte sur la mesure de temps de trajet par inter-corrélation pour différentes périodes de mesures. Dans ce cadre, deux modèles de croûte ont été testés : CRUST1.0 (Laske et al., 2013) et CRUST2.0 (Bassin et al., 2000). À partir de ces deux modèles nous avons évalué de manière quantitative l'impact de la croûte sur les temps de trajet des ondes S. La correction crustale peut être divisée en deux parties : une partie de la correction correspond au décalage temporel de l'arrivée de la forme d'onde en temps, cette correction peut être calculée à partir de la théorie des rais. La seconde partie de cette correction correspond à la perturbation de la forme d'onde et dépend de la période à laquelle la mesure est faite.

Les effets à fréquences finies de la croûte se traduisent par un effet dispersif lors de la mesure du délai temporel par cross-corrélation. Cet effet dispersif provient de l'interférence de l'onde principale S avec les réverbérations crustales générées par cette onde S lors de son passage dans la croûte. Selon la période à laquelle l'onde est mesurée, des délais significatifs peuvent apparaître entre des mesures à 10 s et des mesures à 51 s uniquement à cause de l'effet de la croûte. La comparaison des deux modèles de croûtes testés (CRUST2.0 et CRUST1.0), montre que CRUST2.0 est un modèle plus homogène en terme de propriétés élastiques que CRUST1.0. Cependant, CRUST1.0 permet de mieux prédire globalement la réponse de la croûte lorsqu'une onde S la traverse, même si à certaines stations CRUST2.0 est plus proche de la "vraie" croûte. Par ailleurs, nous avons également montré que dans certains contextes géologiques la réponse à fréquences finies est nulle (cratons, jeunes chaînes de montagnes) alors que dans d'autres la différence entre hautes fréquences et basses fréquences est très importante (bassins sédimentaires ainsi que certaines régions telles que le bassin de Mexico et l'Est de la Méditerranée). Ces effets à fréquences finies sont particulièrement visibles dans les zones où l'épaisseur sédimentaire est importante (Figure I.5). Bien que la correction crustale théorie des rais demeure importante, les effets à fréquences finies de la croûte peuvent biaiser les délais et induire en moyenne 0.9–1.6 s pour CRUST2.0 et 0.5–1.6 s pour CRUST1.0 sur des périodes de mesures allant de 10 à 51 s.

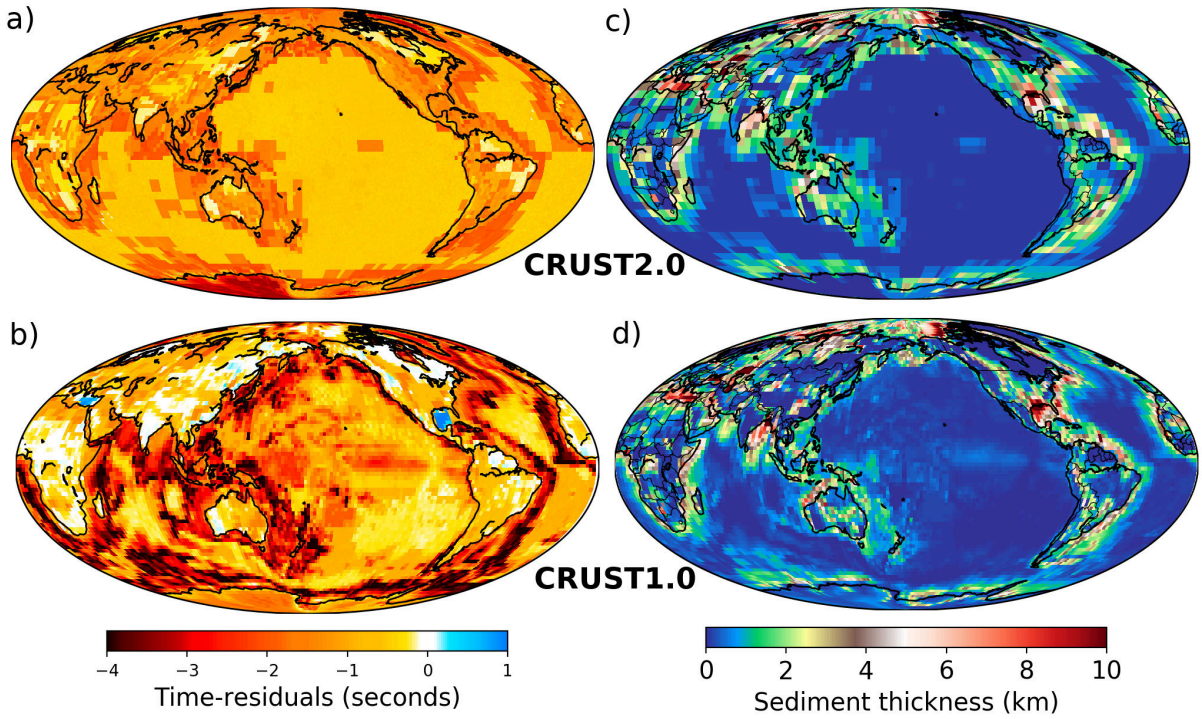

FIGURE I.5 – (a,b) Moyenne des résidus temporels d'ondes S mesurées par inter-corrélation entre deux synthétiques filtrés à 22.5 s, l'un contenant des phases crustales et l'autre sans (a) Modèle CRUST2.0 ($dt_{\text{synth}}^{\text{crust2, FF}}(22.5s)$) sur une grille $2° \times 2°$, (b) Modèle CRUST1.0 ($dt_{\text{synth}}^{\text{crust1, FF}}(22.5s)$) sur une grille $1° \times 1°$. (c, d) Les épaisseurs sédimentaires pour CRUST2.0 et CRUST1.0 (en incluant la couche de glace si celle-ci existe).

I.4 Inversion conjointe

Une fois notre base de données en onde de volume complétée et corrigée de la croûte, nous nous sommes intéressés à la partie inversion. Cette partie consiste à inverser conjointement deux types de données : ondes de volume et modes propres, en utilisant une méthode d'inversion de type Backus–Gilbert (B–G). La plupart des inversion actuelles sont des dérivées d'une autre méthode que l'on appelle généralement 'régularisée au sens des moindres carrés' (DLS, damped least squares).

I.4.1 Les inversions DLS

Dans un premier temps, nous avons inversé séparément les ondes de volume et les modes propres. Ces premières inversions utilisent le formalisme DLS qui consiste à minimiser la différence entre données prédites et données observées tout en gardant une norme du modèle relativement faible. Ceci a permis d'apprécier les tailles et les amplitudes des anomalies récupérées à la fin de l'inversion. Grâce à l'utilisation du χ^2 (e.g., Nolet et al., 2008), qui estime le fit entre données observées et prédites, nous avons pu évaluer si l'estimation globale des erreurs sur les données était correcte.

Bien que des efforts aient été faits dans l'amélioration des estimations d'erreurs sur les données, une sous-estimation des ces erreurs a été observés via le χ^2. Nous avons notamment observé plus de 400% d'erreur sur l'estimation des incertitudes sur les données de modes propres. Ceci nous a conduit a augmenter artificiellement les erreurs sur les données des ondes de volume et des modes propres.

I.4.2 L'inversion Backus-Gilbert (BG)

I.4.2.1 Concept de l'inversion Backus–Gilbert

Nous avons ensuite procédé à l'inversion conjointe des ondes de volume et des modes propres. Nous avons pour cela utilisé le processus d'inversion Backus-Gilbert (Zaroli, 2016). Ce schéma d'inversion permet de produire des images tomographiques non biaisées (e.g., Backus and Gilbert, 1967). L'inversion Backus–Gilbert fournit à la fois le modèle inversé, mais également tous les outils nécessaires pour interpréter quantitativement les images. Ces outils sont composés de deux éléments : la résolution et les incertitudes. À partir de la résolution il est possible de savoir si l'on peut physiquement détecter une anomalie. Et à partir des incertitudes nous pouvons savoir si nous voyons réellement cette anomalie. Être capable de voir et voir une anomalie sont deux questions très différentes dans les problématiques d'imagerie.

L'inversion Backus–Gilbert repose sur un principe simple : la moyenne pondérée. Dans n'importe quelle inversion il est difficile d'avoir une estimation précise de la valeur d'un seul point. Dans la grande majorité des cas, la valeur de ce paramètre correspond à une moyenne sur un volume autour de ce point (Nolet et al., 2008). La particularité de l'inversion B–G est de pouvoir fournir une moyenne pondérée non biaisée des points désirés. Le terme *biaisé* a ici une signification bien particulière. En effet, les inversion type DLS fournissent également

des moyennes mais potentiellement biaisées à certaines positions dans le modèle. Le terme biaisé signifie ici que la somme des poids dans la moyenne pondérée n'est pas égale à 1. Ceci implique des amplifications ou des réductions locales et artificielles des amplitudes du modèle tomographique. Un des avantages de l'inversion Backus–Gilbert est d'imposer qu'autour de chaque paramètre la moyenne soit égale à 1.

Durant les dernières décennies plusieurs articles rapportaient que l'inversion B–G ne pouvait pas être utilisée à cause du coût de calcul trop important ainsi que des problèmes de stabilité en présence de bruit étaient signalés (e.g., Trampert, 1998; Aster et al., 2012). Cependant, Zaroli (2016) a montré qu'il est possible d'appliquer une version dérivée de l'inversion B–G nommée SOLA (Subtractive Optimally Localized Averages) applicable à des problèmes de tomographie sismique. Cette version fut pour la première fois appliquée par Pijpers and Thompson (1992, 1994) sur des problématiques d'héliosismologie. Cette méthode garde tous les avantages de l'inversion B–G tout en étant plus efficace numériquement.

I.4.2.2 Application de SOLA à l'inversion jointe : ondes de volume et modes propres

Le premier modèle SOLA joint avec des ondes de volume et des modes propres a ainsi été produit. Nous avons donc nommé le modèle tomographique résultant : *SOLA-NOMBOW* (pour normal modes and body waves). Ce modèle présente les anomalies 3-D isotropiques en vitesse d'onde S entre 410 et 2889 km. Ce modèle contient les données d'onde S mesurées à 22.5 s, ainsi que les coefficients de structure des modes propres sélectionnés. En plus du modèle, les informations sur la résolution et les incertitudes sont disponibles pour tous les points pertinents du modèle. Ces deux éléments permettent d'effectuer des interprétations quantitatives des anomalies observées dans le modèle tomographique. Dans une dernière partie, nous présentons comment à partir des incertitudes, et de la résolution sur le modèle, nous pouvons interpréter quantitativement les anomalies sismique. Pour l'exemple, nous choisissons d'étudier la continuité verticale du plume mantellique sous Samoa. La figure I.6 présente les inversions DLS et SOLA côte à côte pour différentes profondeurs. Selon les profondeurs affichées les différences sont plus ou moins grandes. On voit notamment qu'à 1810 km de profondeur, là où la couverture des ondes de volume diminue, on voit une nette différence entre les schémas d'inversion DLS et SOLA.

Pour mieux exploiter notre travail sur les corrections de croûte à fréquences finies (chapitre 4) il faudra dans le futur pouvoir travailler sur des inversions sans paramétrisation. En effet, la projection de nos noyaux de sensibilité sur la grille dégradent fortement leurs qualités (voir fin du chapitre 3). Cependant, la partie donnée de cette thèse a permis de mieux comprendre les sources d'erreurs attribuées aux données de temps de trajet des ondes de volume, notamment la contribution provenant du modèle de croûte. Comme résultat final, nous présentons le premier modèle global joint Backus–Gilbert du manteau terrestre. En plus de ce modèle tous les outils permettant d'estimer la robustesse des anomalies sont fournis (**résolution** et **incertitude**). Dans ce cadre, nous illustrons à la fin du chapitre 5 comment estimer quantitativement les anomalies détectées par la tomographie sismique. La problématique de la continuité verticale du plume sous Samoa est pris pour exemple.

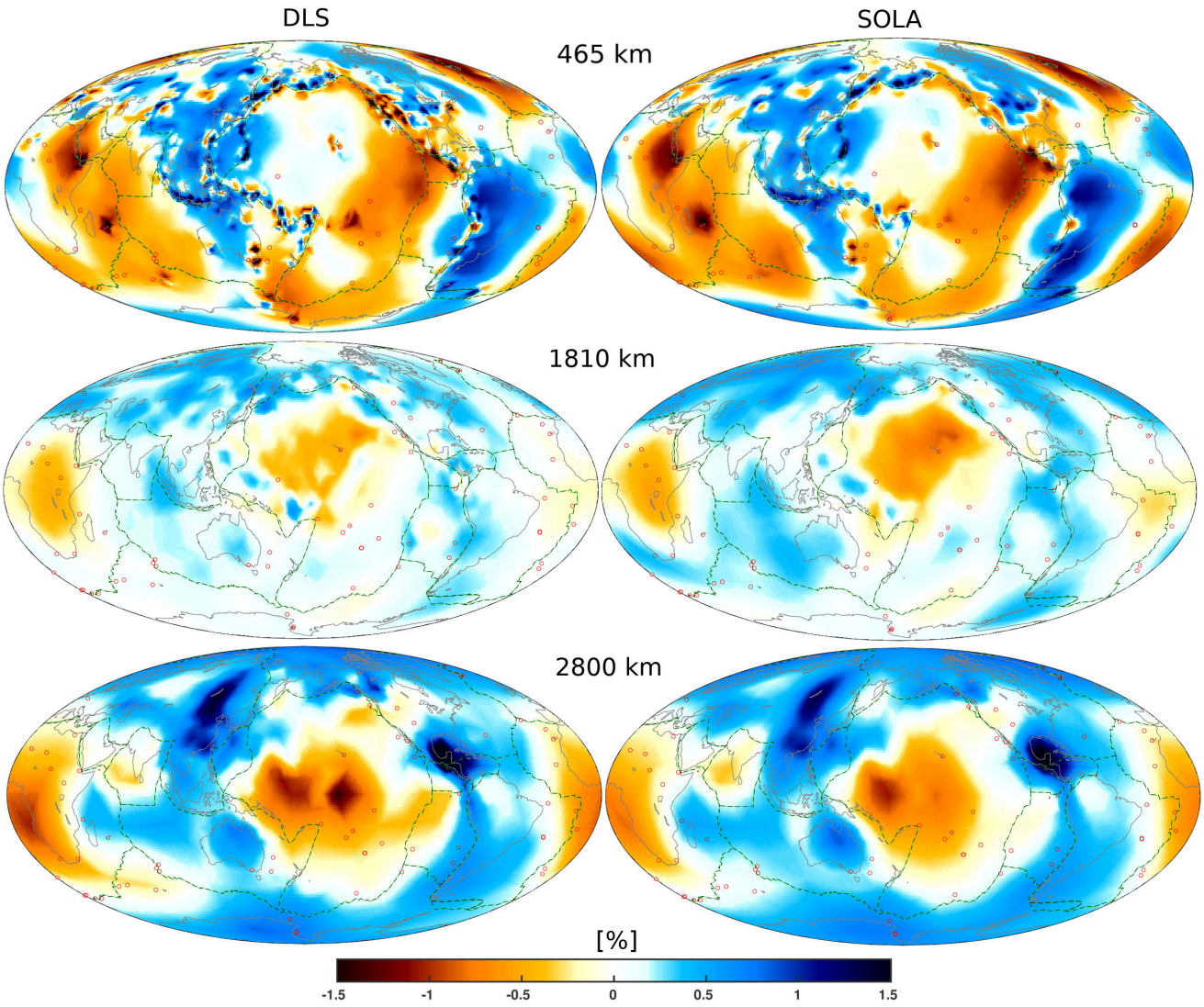

FIGURE I.6 – Comparaisons d'images tomographiques réalisées avec une inversion DLS (colonne de gauche), et une inversion SOLA (colonne de droite). Chaque ligne correspond à une profondeur différente : 465 km, 1810 km et 2800 km. Les lignes vertes et noires en pointillées représentent les limites de plaques tectoniques, les cercles rouges correspondent aux positions des points chauds. Les perturbations de vitesse sont données par rapport au modèle 1-D de référence IASP91 (Kennett and Engdahl, 1991).

Chapter II

Introduction

Chapter II

Introduction

II.1 General introduction

II.1.1 Structure of the Earth

In the early twentieth century, seismology emerges as a valuable tool to learn more about the Earth's interior. It begins with the discovery of the main concentric layers of the Earth.

II.1.1.1 Bulk structure

Main knowledge on the deep structure of the Earth is brought by seismology. One of the field in seismology called *tomography* aims at providing images of the Earth's interior. First, the Earth is laterally homogeneous but varies abruptly vertically. The main "layers" are composed of the *crust*, the *mantle* and the *core*, then this description can be refined (Figure II.1).

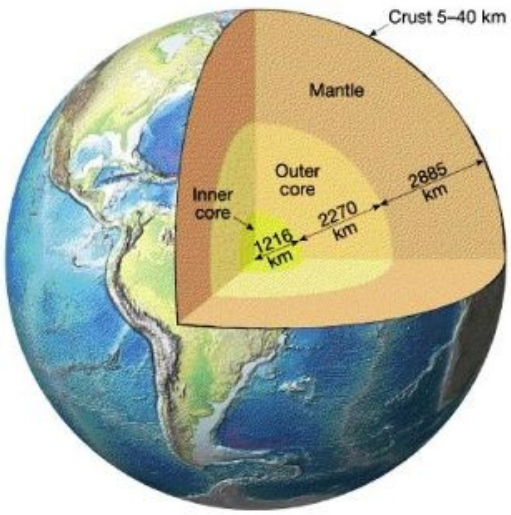

Figure II.1 – A simplistic model of the Earth described by four layers: the crust, the mantle, the outer core and the inner core. Layer thicknesses are rough estimations but give the order of thickness for each "layer". Source: Encyclopedia (2016).

Each of these entities can be broke down into smaller layers. The core can be divided into two parts: the liquid outer core that is the host of the global geodynamo[1], and the solid inner core. One of the most well-known seismological model of the Earth is PREM (Preliminary

1. The geodynamo creates a magnetic field which encompasses the whole Earth. This field is protecting the Earth against solar wind and energetic particles coming from deep space.

Reference Earth Model), published by Dziewonski and Anderson (1981). This model is a 1-D representation of the Earth and contains the radially averaged properties of the Earth (Figure II.2). It includes elastic parameters, attenuations, gravity values and densities. Other models have then followed such as IASP91 (Kennett and Engdahl, 1991) or AK135 (Kennett et al., 1995).

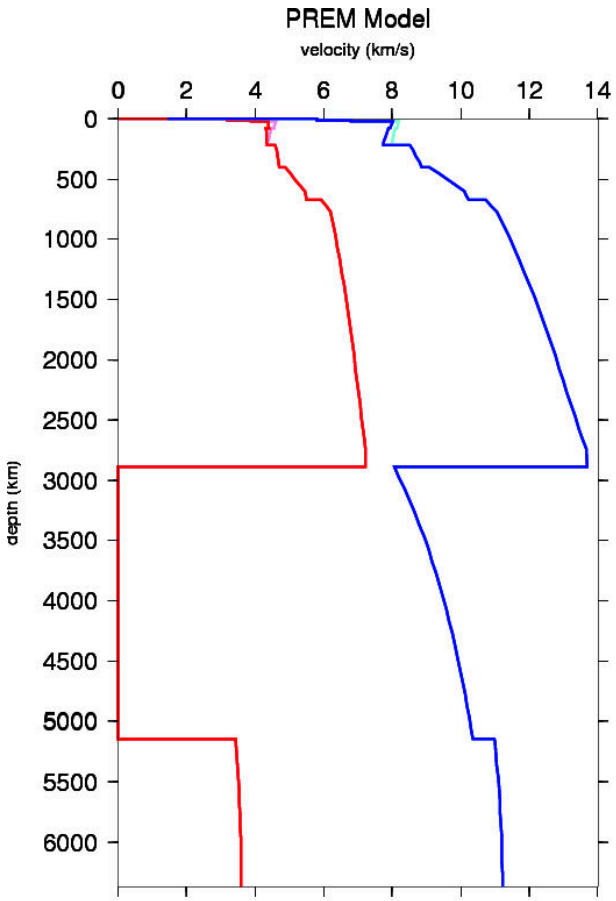

Figure II.2 – PREM model for P and S-wave velocity. PREM model is anelastic and anisotropic that is why four curves are indicated. Blue and red curves represent the P and S-wave velocity for vertical travelling waves. Light blue and pink curves represent the P and S-wave velocity for horizontal travelling waves. Model is from Dziewonski and Anderson (1981), this figure is modified from IRIS website.

The crust is the most superficial layer of the Earth. It extends from 0 to 7 km for an oceanic crust, and 35 km for continental crust, and is delimited by the Moho discontinuity (1909). From this discontinuity, the mantle extends down to 2889 km at the CMB (Core Mantle Boundary), also called the Gutenberg discontinuity (1912). Deeper, in the liquid outer core, vigorous convection motions of hot metal take place. In turns these motions maintain the global magnetic field of the Earth. The Gutenberg discontinuity is as important as the limit between the atmosphere and the lithosphere. It marks the transition between solid silicates of mantle with liquid iron from the core. It is not only an elastic discontinuity but also a chemical one. Below the outer core comes the inner core which is still made of iron but under solid state. Discontinuity between inner and outer core is called the Lehmann discontinuity (1936).

By far the mantle is the largest part of the Earth, it represents 80 % of the total volume. With a thickness of 2880 km (almost half of the Earth's radius), it constitutes a fundamental stake in the understanding of the Earth's structure and its dynamics.

II.1.1.2 Mantle structure

Mantle extends from 0 km (up to 75 km)[2] down to 2889 km depth. It is the largest solid part of the Earth with large temperature and pressure ranges, these large variations induce very different mechanical behaviors between upper and lower mantle rocks. Viscosity strongly controls the dynamics of the mantle and may vary significantly between the upper and lower mantle up to a factor 10 or 100. The mantle has a fundamental role in Earth's convection, mainly as a heat exchanger from core to surface, where the tectonic expresses (e.g. Morgan, 1968). Several zones of the mantle are of particular interests in the geoscience community. Among them two specific transition zones draw great interdisciplinary interest for many years: the first transition zone located between 410 and 660 km (named the transition zone), the second one is located at the bottom of the Earth's mantle (between roughly 2600 and 2900 km) and is named the D" layer.

II.1.1.3 The transition zone

This zone is defined between two depths: 410 km and 660 km clearly visible by velocity jumps with seismological studies (e.g., based on receiver functions, see for example: Gurrola et al. (1994); Helffrich et al. (2003)). These limits show depth variations according to the geodynamical context. Olivine phase changes are thought to be the origin of the two velocity jumps observed at 410 and 660 km (see figure II.2).

The most abundant rock inside the mantle, is called peridotite. This rock is composed of olivine (40-60%) and other constituents such as iron silicates (pyroxene) and garnet. Olivine ($(Mg,Fe)_2SiO_4$) is thus the main component of the mantle and can be view under different configurations inside the mantle. From lab experiments, we know the olivine undergoes a phase transition at 410 km to turn out from α phase to β phase (said "wadsleyite" keeping the orthorhombic configuration). At 520 km, β phase turns into γ phase named "ringwoodite" or "spinel" (same formula but with cubic configuration). At 660 km, pressure is still increasing and ringwoodite splits into two high-pressure phases called "perovskyte" ($(Mg,Fe,Al)SiO_3$) and "magnesiowüstite" ((Mg,Fe)O) (Merkel, 2001).

All phase transitions are characterized by a Clapeyron slope, defined as:

$$\frac{dT}{dP} = \frac{\Delta V}{\Delta S} \tag{II.1}$$

with T the temperature, P the pressure, ΔV is volume change and ΔS is entropy change. The sign of the Clapeyon slope brings information on the nature of the phase transition. For instance, the sign of the Clapeyron slope for α-β transition is positive which indicates an exothermic phase transition. The γ-perovskite transition contrasts with a negative Clapeyron slope meaning a endothermic phase transition. These phase transitions induce velocity discontinuities, and topography variations can be tracked thanks to specific seismic phases.

2. Mantle outcrops at 0 km at ridges but can start at 75 km depth under mountains.

Therefore knowledge on the Clapeyron slope of phase transitions help to appreciate the origin of the topographic variations. Over and above petrological considerations, the transition zone is thought to be not only a petrological limit but also a physical transition inside the mantle. It could be the limit between a high viscous lower mantle and a much less viscous upper mantle. We will show in the following what are the arguments for the viscosity jump at this depth. This transition zone can be seen as an exchanger between the upper and the lower mantle in terms of materials but also heat.

II.1.1.4 The D" layer

This D" layer (pronounced "D double prime") is located at the very base of the Earth's mantle. This zone, close to the CMB, is fundamental if we want to figure out the exchanges between the core and the mantle. This second transition zone is not as well known as the previous one. Last estimations give a thickness of about 250 km ($\pm$ 50 km) (e.g., Lay and Garnero, 2004; Peltier, 2007; Stanford, 2019) which extends the D" layer from 2689 km to 2889 km depth. This layer marks the transition between solid silicate mantle and liquid iron core. It is therefore a chemical, physical, mineralogical and thermal boundary.

The D" layer was discovered thanks to precursors of specific seismic phases (e.g., Olivieri and Pino, 1998). This layer is also characterized by strong lateral seismic heterogeneities. Large fast seismic anomalies in the lower mantle are often referenced as "slab graveyard" (e.g. Spasojevic et al., 2010; McGowan et al., 2015), and are associated to old subducted slabs coming from the surface and stagnating on/in the D" layer (see Stein and Wysession (2009); Tackley (2011) for more details). The slow anomalies are viewed as areas with elevated temperature where mantellic plumes are rooted. Chemical exchanges are though to occur in these areas between iron elements and silicate minerals (e.g. Goarant et al., 1992). Another important phase transition occurs in this layer: the "perovskyte" ((Mg,Fe,Al)SiO_3) are turning into "post-perovskyte" ($MgSiO_3$), which is more compact than perovskyte (e.g., Murakami et al., 2004; Oganov and Ono, 2004). This phase transition has a positive Clapeyron slope and so, is highly exothermic (Ferroir and Dequincey, 2008). The adiabatic gradient indicates that post-perovskyte is more likely to be present in cold regions (with slabs) and less present in hot regions (with plumes) (Figure II.3).

II.1.1.5 Current challenges in tomography

Seismic tomography aims at better understanding the 3-D structure of the Earth. Foremost, the Earth is a sphere radially heterogeneous and laterally homogeneous (different layers, see bulk structure part). However, in some regions of the globe, this approximation is far from truth since seismological studies have reported deviations from the Earth 1-D model for 40 years: fast anomalies related to subduction processes; and slow anomalies related to upwelling materials called plume. Better imaging slabs and plumes are still important challenges in modern global seismic tomography.

Plumes: thermal or thermo-chemical?

Slow seismic anomalies imaged in the mantle are depicted as plumes conveying upwelling hot materials from the deep mantle to the surface. Some of these plumes seem to be related

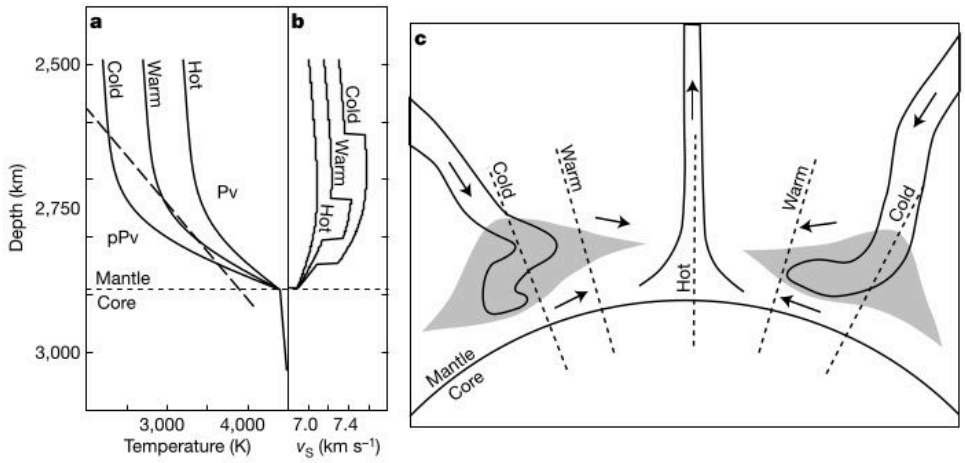

Figure II.3 – Schematic representation of three possible mantle geotherms. (a) different mantle geotherms with stability domains of perovskyte and post-perovskyte. (b) shear-wave velocity for the three different geotherms. (c) geodynamical contexts where the three geotherms can be found in the lowermost mantle. One can notice the possible double-crossing for perovskyte (Pv) and post-perovskyte (pPv) in the lower mantle for a cold geotherm (Hernlund et al., 2005).

downward to two large low seismic velocity provinces (LLSVPs, (e.g., Garnero and McNamara, 2008)) at the CMB and upward at some hot spot locations (e.g., Ritsema et al., 2011). Seismic studies highlight these two LLSVPs and several smaller but more intense anomalies called ULVZ for "ultra-low velocity zones". The two well-known LLSVPs are located under Africa and Pacific surrounded by fast materials. LLSVPs are thought to be warmer than the average temperature at the CMB and to be the anchors of plumes in the mantle. Hypothesis on the potential link between plumes and hot spots emerged in the eighties and show mantellic plumes as vertical features starting from LLSVPs at CMB and reaching the surface. Due to this large depth extension but small thickness, plumes in the deep mantle are ones of the most difficult objects to seismically image inside the Earth. As a consequence, various LLSVP types can be conceived to explain plume tomographically imaged.

Nowaday one of the most fiercest debate over mantle dynamics is about the nature of LLSVPs and thus what is their precise structure (Figure II.4). A first option is to consider plumes as generated by thermal heterogeneities, i.e., thermal plumes. A second option would involve chemical heterogeneities to explain low seismic anomalies in the lower mantle, i.e., thermochemical plumes. Moreover, plumes imaged in seismic tomography exhibit different behaviors. For instance, instead of being deeply anchored at the CMB, some plumes seem to appear in the mid-mantle. French and Romanowicz (2015) sort plumes according to their depth extensions, they call "primary" plumes those with a likely connection between the CMB and the surface. Other less-resolved plumes are categorized as "secondary" plumes (see French and Romanowicz (2015) for detailed plume classification).

Plumes surface expression (hot spots) such as Yellowstone (e.g. Camp, 2019) are still under vigorous debates. If plumes are characterized by thermal and chemical anomalies, then, an unusual chemical composition could be detected by analyzing magmas erupted at hot spot locations(Tackley, 2000). Hot spots and surface flood basalt areas named "traps" are thus used to constraints the plume positions and eventually the LLSVPs composition. Numerous studies show the correlation between large igneous provinces (LIP) and edges of LLSVPs (e.g.,

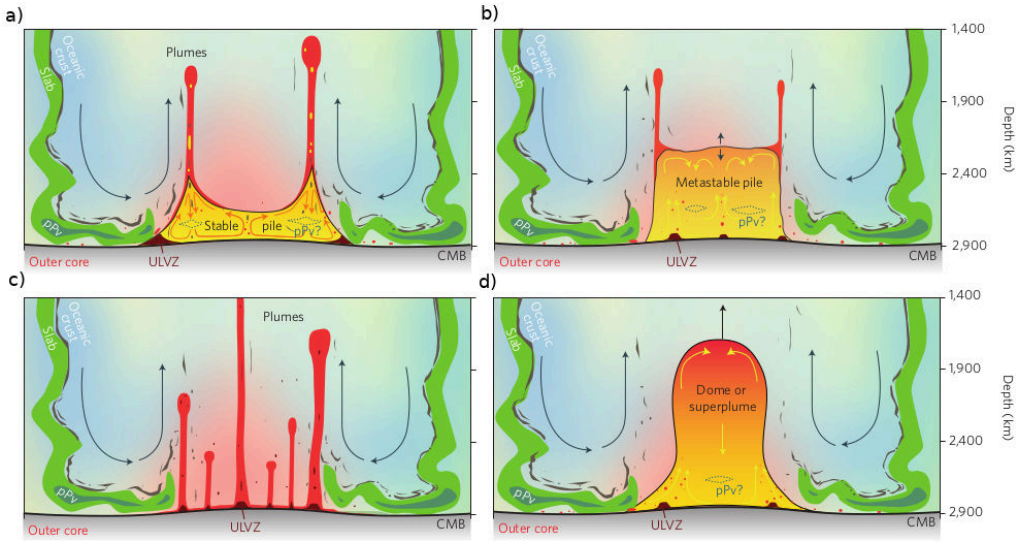

Figure II.4 – Different scenarios for plume geometries with thermo-chemical LLSVPs. In all cases, subducted materials with potential post-perovskyte (pPv) surround LLSVPs. a) Stable thermochemical plume. b) Metastable thermochemical pile. c) Plume clusters. d) Thermochemical superplume (Garnero et al., 2016).

Torsvik et al., 2006). Long-term stability of LLSVPs is a crucial question to decipher mantle convection mechanisms. High viscosity and density might be necessary to have a temporal stability for LLSVPs, however the geographical stability would depend on tectonic plate motions (Heyn et al., 2018).

Large-scale anomalies located at the CMB are strongly limited to low spherical harmonic degrees with a degree 2 dominant (e.g. Dziewonski et al., 2010). Figure II.5 shows the strong correlation between the S-wave anomalies at the CMB and the Earth's geoid. By comparing geoid and tomographic images we could deduce that LLSVPs are thus composed of materials with higher density than the surrounding mantle (Ishii and Tromp, 1999; Moulik and Ekström, 2016). Dziewonski et al. (2010) report that the antipodal axis crossing the two LLSVPs is mixed with the axis of the lowest moment of inertia given by the geoid, which is an indication of mass excess along the axis. Consequently, LLSVPs may have a significant impact on the geoid and rotation axis of the Earth. Nevertheless, Koelemeijer et al. (2017) states that LLSVPs might be lighter than the surrounding mantle from normal mode tomographic studies. Thus, the question of stability with ligth LLSVPs should be assessed.

Slabs: Sink or stall?

Slabs seismically imaged within the mantle are the result of oceanic plate subductions under another oceanic or continental tectonic plate. Slabs show a wide variety of behaviors inside the mantle (Figure II.6). Some of them dive directly into the lower mantle, whereas others pond at specific depths before falling again. Some correlation between slab stagnancy and slab age seems to appear. Young slabs are thus more likely to dive directly into the lower mantle whereas old slabs tend to stagnate at 660 km (e.g., Agrusta et al., 2017). Several studies show that many slabs stall at 660 km as a result of a viscosity jump between the upper and lower-mantle and the endothermic phase transition at 660 km (e.g., Goes et al., 2017). Fukao and Obayashi (2013) even report stagnant materials below 660 km, but no general

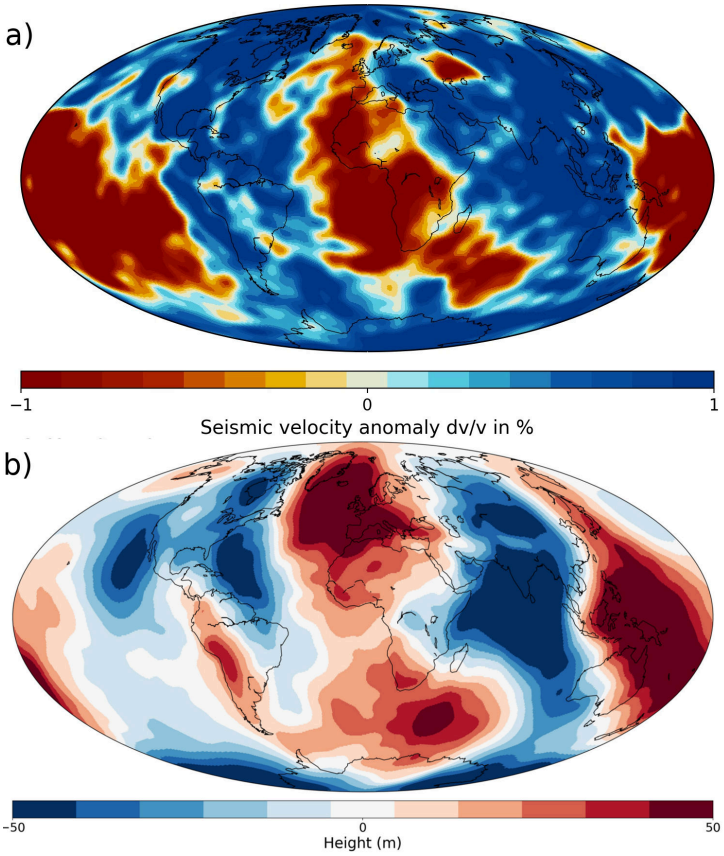

Figure II.5 – a) S40RTS shear-wave velocity model (Ritsema et al., 2011) at 2900 km of depth. b) Geoid model EGS08 (Pavlis et al., 2012). This plot is created with the help of Submachine (Hosseini et al., 2018). These two maps are built using spherical harmonics expansion up to the degree 40.

consensus seems to emerge among the geoscience community. Questions about interactions between slabs and the 660 transition depth are fundamental for those who are interested in the efficiency of the mantle mixing and thus in plate reconstruction.

It is interesting to note that the stagnation at the 660 km does not last more than 60 Myr according to current observations mainly due to slab buoyancy changes. Considering the velocity of plates, this implies that stagnant portions of slabs are resting between 500 km and 2000 km at most. Another tomographic charactersitic of slabs in the lower mantle is their thickening. One could think it is only due to a worse resolution of tomographic models in the lower mantle but it seems that even in well-covered region this effect can be observed (e.g., Hafkenscheid et al., 2006). This thickening of the slab which starts at the 660 km could be imputed to the buckling of the slab while stagnating (e.g., Lee and King, 2011).

Another important research subject about slabs is the water transport into the mantle. Water contained in the mantle would change the physical properties of mantellic rocks and can locally change the state of the matter. For instance, it is well-known that water contained in the slab during the subduction will migrate through the overriding continental plate and induce partial melting. This partial melting is the source of volcanic arcs that appear in front of subduction trenches. Geophysical studies have already made evidences of hydration-dehydration cycles during the subduction process (e.g., Worzewski et al., 2011). For water content analyses, seismic is not as useful as electromagnetic studies, especially to detect the

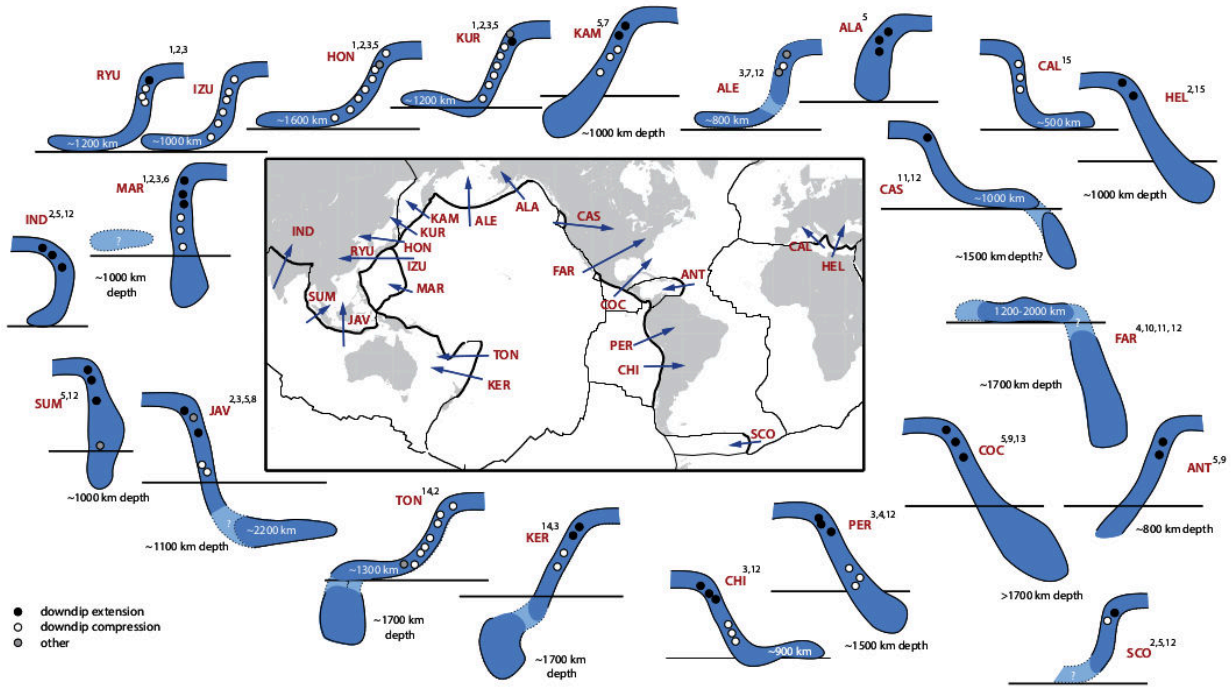

Figure II.6 – Diversity of slab-transition zones. Morphologies of slab-transition zone as imaged by tomographic studies. Horizontal black lines indicate the 660 km discontinuity. For flattened slabs, an indication of the length of the flattened part is written in white over the slabs. Earthquake locations are indicated on slabs by circles, inner color depends on the focal mechanism (black for extension and white for compression) (Goes et al., 2017).

quantity of water injected in the slab. Magnetotelluric method is a good technique to estimate the fluid fraction in the slab since induced electromagnetic currents are very sensitive to fluids in rocks. However, analyses of water content is complicated by temperature variations between subduction zones. Temperature has a strong impact on electrical conductivity which can bias interpretation only based on water effect. If subduction zone is too hot, water in the slab will not enter in the deep mantle but will be evacuated at shallow depths[3]. In cold subduction, α-phase olivine is transformed into β-phase and mineral bound water may go deep in the mantle.

Various slabs are located in the deep mantle (see figure II.6), among them, the Farallon subduction beneath North America and Tethys slab beneath Eurasia. Deeper in the mantle, fast anomalies are mainly located below Asia and America. If these fast anomalies are associated to slabs, the graveyard hypothesis would support the high mass anomaly.

To summarize, young slabs are expected to penetrate in the lower mantle whereas old slabs are supposed to flatten at 660 km. Stagnancy of slabs needs three elements: a jump in viscosity between upper and lower mantle, a negative phase buoyancy (exothermic) and a trench mobility. This is only a general idea of subduction-transition zone behaviors, and can be quite far from reality in some cases. For example, Java slab is tomographically detected

3. Cascadia subduction is one of the hottest subduction zone in the world, and no water can be brought in the mantle in this case.

well below 660 km or the peculiar behavior of the Indian slab shows much more complexity than a simple correlation between age and stagnancy.

II.1.2 Insights from other geoscience fields

Geophysical images of the Earth's mantle are only snapshots of the current Earth's structure. Seismology needs information from other fields such as geochemistry, geodynamics or geomagnetism to constrain not only the locations but also the temporal stability of Earth's structure. Let see how others fields in geoscience can bring valuable information to seismic tomographic images.

II.1.2.1 Upper mantle and slab dynamics

Seismic tomographic images show stagnant slabs at 660 km but others fall in the lower mantle without any resistance. What makes these slab behaviors so different? A raw sum up of all forces applied to slabs can help us to understand their dynamics (Figure II.7).

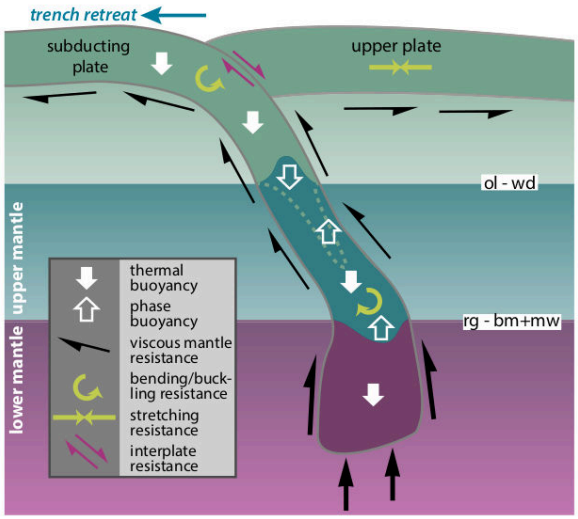

Figure II.7 – Main forces applied during a subduction (Goes et al., 2017).

The most natural way of subduction, called "lazy" mode, is when the slab sink freely in the mantle. It is dominated by the slab buoyancy (white arrow, figure II.7). In this lazy subduction mode, the trench retreat enables to considerably limit the energy cost in slab bending (Kincaid and Olson, 1987). Although the slab pull is from far the largest force, opposite forces are applied to the slab such as the mantle drag (black half arrows, figure II.7) due to the visquous mantle and the internal bending of the slab (yellow circled arrows, figure II.7) (Capitanio et al., 2007). Hereafter, some general ideas about slab correlations:

- There is a correlation between the slab velocity and the slab density (denser slabs are falling faster) (Capitanio et al., 2007).
- There is no global correlation between slab age and the trench motion, however the trench seems to retreat faster with old slabs.

- There is no correlation between slab age and the dip at the trench (e.g. Lallemand et al., 2005).
- There is a broad correlation between slab stagnancy at 660 km and thermal structure of the slab (derived from slab age and its velocity). But notable exceptions can be picked out (see Goes et al. (2017)).

II.1.2.2 Deep mantle

At the base of the mantle, rocks have to undergo harsh conditions such as temperatures over 3000 K and pressures at 135 GPa. Besides, below the CMB the pressure is not so far from 135 GPa, but the temperature can reach 4000 K which implies a strong temperature gradient across the CMB.

Heat transfer

Having a good estimation of the heat transfer is fundamental to understand the whole dynamics of the Earth and its evolution. Heat flow measurements can be carried out in boreholes considering the thermal conductivity of the rock. We consider a heat flow of $90\,\mathrm{mW/m^2}$ at the Earth's surface, which gives a total global heat flow of 45 ± 3 TW (Lay et al., 2008). Heat flow contains thermal energy from core conveyed through the mantle, mantle cooling and radiogenic heating from crust and mantle elements. The radiogenic contribution is mainly produced by three elements: ^{40}K, ^{232}Th, ^{235,238}U (e.g., O'nions and Oxburgh, 1983). Heat is transported by two different processes inside the Earth. The first one, and the most inefficient, is the *conductive transfer* which is active at shallow depths. The second appears when too much heat have to be evacuated and conductive transport is no more sufficient. In this case, macroscopic displacement of rocks can be observed, and we enter in the regime of *convective transfer*. Similarly, convection cells appear in the mantle to evacuate heat from core to surface and mantellic plumes are the most obvious evidences of this large-scale convection. These plumes may convey a significant part of the heat through the mantle feeding hot spots and traps. The quantification of heat transfer is fundamental to understand the role of plumes in global convection. Different techniques are applied to estimate these quantities. Surface observations of dynamic topography can give estimates of the thermal buoyancy flux and thus the heat transfer. Other methods, such as seismic tomography, can help to solve this problem by converting velocity anomalies into thermal buoyancy flux with Stokes flow models (e.g., Nolet et al., 2006). Estimations of heat flux through plumes are quite variable, we can report variations from 3 to 30 TW according to different studies (e.g., Anderson, 2002; Zhong, 2006; Nolet et al., 2006; Lay et al., 2008), which may be large considering a total amount of 43 TW. Plume role in mantle convection is then far to be understood and works should be done to better highlight their implications in global convection.

For instance, if Earth would be hotter of 200°C, we may not see slab stalling at the 660 km. Therefore, the main parameter controlling the slab stalling is the viscosity contrast between the mantle and the slab. Since temperature has a intense effect on viscosity (Arrhenius law), strong uncertainties on temperature over the mantle will induce risky forecasts for global mantle circulation model. An example of a possible viscosity profile is presented in figure II.8. We clearly see the viscosity jump at 660 km which could induce strong perturbations for slabs diving (fall or stall) and plume rising (plume splitting and deflected) (e.g., Nolet et al., 2006).

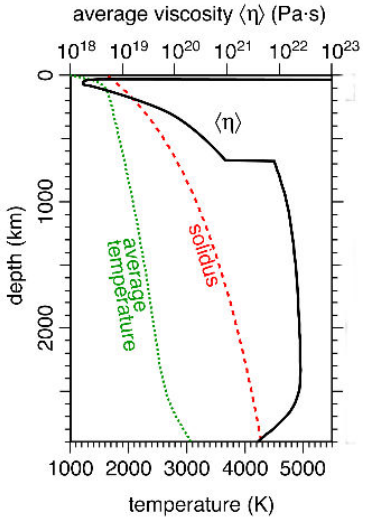

Figure II.8 – One possible viscosity profile along the depth (η, black line). A clear jump is observed between the upper and lower mantle at 660 km (Les Houches 2017, S.Goes).

However, recent studies report that viscosity changes could occur deeper at 1,000 km (e.g., Rudolph et al., 2015; Durand et al., 2017). This could have large impacts on the global model circulation of the mantle.

Geochemistry

We could think that mantle elements are globally mixed over the successive convection cycles: deep material emerging at mid-ocean ridges and then diving back to mantle at subduction areas. However, mid-ocean ridge basalts (MORB) and ocean island basalt (OIB) do not have identical isotopic ratios. The strongest evidence comes from the $^4He/^3He$ ratio. Helium behaves like an extreme incompatible element while mantle melting, besides it is not lithophile which makes him a perfect tracer of primordial reservoir. Two different isotopes of helium exist inside the Earth: ^3He which is primordial and stable, and ^4He which is mainly produced by the radioactive decay of Th and U. Helium isotope ratio measured in MORB have a narrow range of value between 80,000-100,000 (e.g., Graham et al., 2016). Whereas isotopic ratio measured on OIB basalt have a larger range of variation and a minimal value of 14,200 (e.g., Williams et al., 2019) meaning weakly processed materials and so may be sampled from a primordial reservoir. These differences prove than mid-ocean ridges and ocean islands sample differently the mantle. It is generally accepted that MORB comes from the decompression of the rocks from the upper mantle whereas OIB potentially sample very deep reservoirs feeding plumes. The geographical distribution of the these deep reservoirs would offer strong constraints on the mantle convection dynamics (e.g., Tackley, 2000).

Several lines suggest that these deep reservoirs of primordial material could be associated to LLSVPs in the deep mantle. However, LLSVPs might be chemically distinct from the surrounding mantle, and thus be the reason of isotopic differences between OIB and MORB. In this case, this would support the long-term stability of these LLSVPs with small chunks entrained back to the surface at hot spot locations. Alternatively, these large slow anomalies could be the result of an accumulation of slabs coming from the upper mantle (e.g., Burke et al., 2008). In this case lead isotope ratio could help to discriminate oceanic crust, though

recent studies show no direct correlation between LLSVP locations and characteristic oceanic crust lead ratio from OIB ($^{208}Pb/^{206}Pb$)(Williams et al., 2019).

Mantellic plumes are still challenging objects to be tomographically imaged inside the Earth's mantle. Plumes have potential strong implications in the heat dissipation of the Earth by bringing up to the surface hot materials and thus actively participate to the mantle convection. Some of these plumes seem to be characterized in surface by hot spots - i.e., volcanic archipelagos or traps. Lavas emitted from hot spots have different geochemical signature than lavas emitted at mid-ocean ridges. This implies a potential deep origin of the the melted materials produced at hot spot locations which supports a link between the deep mantle and the surface. To better visualize this link between surface and deep mantle, we propose to produce a tomographic image of the mantle by using a rejuvenated inversion scheme called Backus–Gilbert.

II.2 Purposes, plan and challenges

In this study, we aim at producing quantitative and unbiased tomographic images of the whole mantle from 400 km down to 2889 km. In this context, we use finite-frequency body-wave as well as normal mode data both sensitive to shear-wave perturbations in the mantle. A recent version of the Backus–Gilbert inversion is used to jointly invert these two data allowing to produce quantitative images. Quantitative interpretations can then be used as input parameters in geodynamical simulations or as support data for other geoscience fields.

Backus–Gilbert inversion

For this purpose, we make use of a recently rejuvenated inversion method called Backus-Gilbert (B–G) inversion. This inversion scheme allows to produce quantitative unbiased tomographic images for linear inverse problems (e.g., Backus and Gilbert, 1967, 1968). The Backus-Gilbert inversion provides not only a model but the full appraisal associated to this model. This appraisal is composed of uncertainties and unbiased resolutions for any arbitrary locations inside the model. From the resolution, we will have the answer to: Can we physically detect this specific seismic anomaly?. And from the uncertainties: Do we actually see this seismic anomaly. To be able and to actually see an anomaly are two fundamentally different problematics. For instance, one could be able to detect a very large anomaly but would not see it due to noise contamination.

Backus-Gilbert inversion relies on a very simple concept: a weighted average. For a single model point, we never recover an accurate estimate at this point but an average over a volume

including the targeted point (Nolet et al., 2008). The strength of the Backus-Gilbert inversion is to produce *unbiased* weighted averages over the desired points of the model. The term *unbiased* is here essential, since other methods such as the damped least-squares method provides averages of the model but potentially locally biased. The term biased refers to a very peculiar behavior of averaging. It means that the sum of all coefficients used in the average is not equal to 1. This last remark ultimately induced an artificial increase or decrease of the model amplitude. Over the past decades, numerous studies reported that B–G inversions required a too high computational cost, and can be unstable in presence of data noise (e.g., Trampert, 1998; Aster et al., 2012). However, Zaroli (2016) shows that is is possible to apply a derived version of the Backus-Gilbert inversion named SOLA (Subtractive Optimally Localized Averages) to seismic tomographic problems. SOLA inversion was first developed by Pijpers and Thompson (1992, 1994) for helioseismology problematics. It is more computationally efficient and versatile in the construction of the averaging volume at each parameter than the original B–G scheme (Zaroli, 2016). The original version of the B–G inversion is *parameter-free*, meaning that the retrieved model is a filtered image of the true Earth. An application of the *parameter-free* version of the B–G inversion is illustrated for a regional tomography in Zaroli (2019).

Although other tomographic methods such as full waveform inversion (FWI) have been urged these last years. FWI remains a non linear process, compared to linear time-residual inversions, and is computationnaly demanding. Besides, information about the resolution is still difficult to obtain and need an additonnal computationnal cost. As most inversion schemes, FWI uses prior models in order to remove the non-uniqueness of the problem. In B-G inversion, no prior is asked, and the non-uniqueness is removed by averaging rather than regularizing. Only information contained in the data are used in the inversion. As a matter of fact, prior model can be seen as virtual data with the obligation to have uncertainties on prior values. The difficulty to define a proper a priori model is pervasive. One has to ask himself if prior information injected into the inversion is not contaminated by the prior ideas that we have on earth. If objective information are available on Earth, Bayesian inversions appear as good alternative to others regularized inversion schemes. As a consequence, for linear or linearized problems, Backus-Gilbert methods or Bayesian methods should be used. For non-linear inversion, it is common to use sampling methods sucha MCMC or neighbourhood algorithm. These sampling methods allow to have an estimation of the uncertainties on parameter values but clear resolution estimates are still debated.

Seismological data

For this inversion we use seismological data composed of finite-frequency shear-wave time-residuals and structure coefficients from normal modes. Finite-frequency shear-wave data are relative seismic time-arrivals measured at different periods between an observed and a synthetic seismogram. With synthetic seismograms generated in a 1-D reference Earth model, IASP91 (Kennett and Engdahl, 1991). Finite-frequency measurements sample a limited volume of the Earth encompassing the specific ray path. Each period is associated to a different volume around the ray path varying according to the measurement period. This allows to extract multiple independent information by measuring at different periods one travel-time. Then, analyzes of the structural dispersion contained in body-wave dispersion curve is possible.

Normal mode data are related to recordings of standing waves detectable when large earthquakes occurred. Normal modes have an integrated sensitivity to the whole Earth unlike the limited sensitivity volume of finite-frequency body waves. Since each mode has its own depth sensitivity, it is then possible to select a limited number of modes in order to fill the gaps in the body-wave data coverage. To better constrain the deep mantle structures, we also use Stoneley normal modes (Stoneley, 1924; Koelemeijer et al., 2013).

Chapter 3 gives details on these two kind of data, with a particular focus on finite-frequency body-wave data measurements and the new database built during this work.

Finite-frequency crustal corrections

To fully exploit the information contained in finite-frequency body-wave data on mantle structure, proper body-wave data corrections need to be set. Kolstrup and Maupin (2015) show that crust could have a finite-frequency impact on P-wave time-residuals measured for periods above 1 s in the Scandinavian region. We study, in a more systematically way, the crustal influence on S-wave time-residuals measured for different periods and over various geological settings. This study brings forth interesting questions about crustal corrections for long-period body-wave. First, it recognizes the importance to apply the correct crustal correction for every seismic phases and specifically when one measures interfering phases. Though, the scale of crustal heterogeneities is well below our resolving length. Second, crustal reverberations have an impact over time-residuals measured by cross-correlation. We showed that the crustal influence is varying as a function of the filtering period used for cross-correlation.

Chapter 4 introduces finite-frequency crustal corrections for long-period shear-waves in details. Emphasis is on the finite-frequency part of the crustal correction and the crustal model uncertainties.

Joint discrete Backus–Gilbert tomography

In a context of global tomography, the combination of different kind of data is more and more important. Most of the current tomographic models use body-waves, surface wave and also normal modes in order to constraint different depths and heterogeneity wavelengths (e.g., Ritsema et al., 2011; Zaroli et al., 2015; Koelemeijer et al., 2016; Durand et al., 2017). So far B–G inversions were only applied to either body waves (Zaroli, 2016) or surface waves (Ouattara, 2019). Therefore, concrete examples of B–G inversion to large joint tomographic problems have to be shown.

Though global *parameter-free* B–G inversion seems enticing, a significant barrier appear for large data sets. *Parameter-free* B–G is more demanding in computational time for large data set than the *discrete* B–G inversion. Thereby, we first decide to stay in the *discrete* version of B–G inversion. This allows to work with a large data set, $N = 130\,000$ and moderate number of model parameters $M = 38\,125$. Although kernel degradation occurred by projecting them over a mesh for discrete B–G, the *discrete* version keeps all the unbiased features of the B–G philosophy. Besides, even for the *discrete* form, model appraisal is available at the end of the inversion. Though we are not able in this thesis to fully exploit efforts put in finite-

frequency crustal corrections, benefits will come later. This new body-wave database corrected for crustal finite-frequency effects could be used in the future for *parameter-free* B–G inversion in regional/global contexts.

Even with the *discrete* version of B–G inversion, the size of the problem and the joint nature of the inversion make the problem challenging in terms of methodology and computational resources. For the first time, we deliver a *discrete* joint finite-frequency shear-wave and normal-mode Backus-Gilbert tomographic image of the whole mantle, from 410 km down to 2889 km. To highlight the unbiased and quantitative nature of this inversion, we present an example of appraisal of a geodynamic complex object of the mantle. The Samoa plume located in the south-west Pacific is analyzed with the B–G inversion and quantitative interpretations are given on its vertical continuity from 660 km down to 2889 km.

Chapter 5 presents how the joint inversion is carried out in the B–G context. An appraisal example of the Samoa plume is illustrated at the end of this chapter.

In short

- *Joint inversion of finite-frequency shear waves with normal modes to image the whole mantle.*
- *Discrete Backus–Gilbert inversion to produce quantitative and unbiased tomographic images.*
- *Quantitative interpretations can be used with geodynamics and geochemistry to better understand the multi-scale convection of the Earth.*

Chapter III

Seismological data: overview and analysis

Chapter III

Seismological data: overview and analysis

III.1 Seismological data

In this chapter, we are going to present seismological data used in this study: body waves and normal modes. Body-waves are propagating waves generating by an earthquake and recorded at a station, whereas, normal modes are standing waves exciting the whole Earth and particularly detectable after large earthquakes.

III.1.1 Body-wave data

Seismic body-waves are elastic waves propagating in solid and fluid media. Most of the time, seismic waves are generated by earthquakes and are propagating all around the globe. These waves can be recorded at Earth's surface with a seismic sensor and carry valuable information on internal Earth's heterogeneities. Diverse kind of information can be extracted from body-wave data such as: travel-time, amplitude, frequency content, waveform. These last years a growing interest on full waveform measurements emerged. It consists in measuring the whole seismograms and exploit all possible information related to the waveform (amplitude, phase) which is called "full waveform inversion" (FWI). Since FWI is a strongly non-linear process, resolution of these problems are harder and needs large computational resources to provide a global tomography of the Earth. In this study, we choose to measure relative time arrivals of specific seismic waves only. We compare the observed seismogram with a synthetic seismogram generated in a 1-D reference Earth model called IASP91 (Kennett and Engdahl, 1991).

Different methods exist to measure travel-times. The chosen measurement technique must be in agreement with the theory used in the inversion. For instance, if data are first onset picking we should invert with the ray theory. For cross-correlation measurements we should always considered first finite-frequency sensitivity kernels (e.g. Mercerat et al., 2013). In this study, we are working in the finite-frequency framework and we measure relative travel-time by comparing synthetics with observed seismograms via the cross-correlation technique.

III.1.1.1 Polarization of seismic waves

First we consider an isotropic media for the basic description of seismic waves. Unlike acoustic waves, seismic elastic waves have various directions of vibration, two vibration modes are well-known: the compressional wave (P-wave) has a coincident direction of particle motion

and propagation[1], and shear wave (S-wave) with perpendicular directions of particle motions and propagation. The shear wave can in turn be split in two polarizations: one horizontal (SH) and one vertical (SV) (Figure III.1). We only consider in this work shear waves (SH) to constitute our new body wave dataset. First, because shear waves are much more sensitive to temperature heterogeneities than compressional waves (e.g. Trampert et al., 2001). Second, core reflected S waves have larger amplitudes than core reflected P waves which make them easier to measure on a seismogram (Stein and Wysession, 2009).

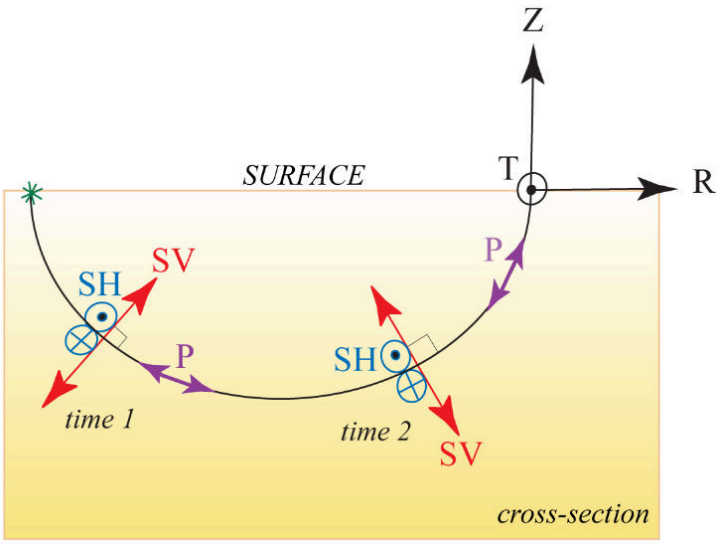

Figure III.1 – P and S wave particle motion modes. Two polarizations are observed for shear waves: SH (horizontal particle motion) and SV (vertical particle motion). They are represented in the earthquake-oriented RTZ frame with R the radial component (SV-wave), T the transverse component (SH-wave) and Z (P-wave). Green star symbolizes the earthquake and the RTZ frame is located at station location. Source: IRIS website.

The choice of measuring SH waves comes from the non coupling of SH waves with SV or P waves for isotropic medium. For isotropic medium, vertically polarized shear waves (SV) are coupled with P-wave unlike horizontally polarized shear-waves (SH). Thus, SH waves are only recorded on the transverse component and the SV waves on the radial and vertical components. For anisotropic medium, a coupling between SH and SV can appear and induce SH energy over R component and SV energy on T component. In this study, we suppose an isotropic medium and thus the coupling between different polarizations is neglecting, we consider an isotropic Earth and measure shear waves with horizontal polarizations (SH) only.

III.1.1.2 Finite-frequency theory

The simplest way to conceive a body wave propagating through a medium is using the ray theory. In ray theory (infinite frequency approximation), seismic wave paths can be visualized as a ray starting from an earthquake location and reaching a station. In this case, anomalies detected by body-waves are only sensitive to elastic anomalies along this geometrical ray path (Nolet et al., 2008). However, in finite-frequency theory, the sensitivity related to a body-wave traveltime is no longer infinitely reduced to a thin ray, but related to a volume

1. Equivalent to an acoustic wave in a fluid.

around the geometrical ray[2]. These finite-frequency sensitivity volumes are called *Fréchet kernels* or sensitivity kernels. There are different kind of kernels: some of them are used to interpret traveltime anomalies (Dahlen et al., 2000; Hung et al., 2000), other are used to invert amplitude anomalies (Dahlen and Baig, 2002). Here, we are making use of travel-time Fréchet kernels ($K(\boldsymbol{r})$) associating the model parameters $m(\boldsymbol{r})$ (velocity perturbation) to data dt (time-residuals)

$$dt = \int_{\oplus} K(\boldsymbol{r})\, m(\boldsymbol{r})\, dV \tag{III.1}$$

with $\oplus$ the volume of the Earth. A visual representation of these sensitivity kernels lead to be named "banana-doughnut kernel" in Marquering et al. (1999) (Figure III.2).

Marquering et al. (1999) highlight the banana-doughnut paradox, as we can see in figure III.2 the S-wave kernel has zero sensitivity along the geometrical ray path (dashed line). This is a disturbing feature since ray-theory implies a sensitivity only limited to the ray path. The "hole" in sensitivity appears nearly all along the ray for the S and the ScS-wave. For the SS wave, this attribute disappears punctually due to caustics (Zhao et al., 2000; Zaroli et al., 2010) (Figure III.2). To build these finite-frequency kernels, we follow Dahlen et al. (2000) and rely on the code from Zaroli et al. (2010) updated for new seismic phases and interferences. For a single phase one can write the travel-time finite-frequency sensitivity kernel for a body-wave to a velocity perturbation located at a position $\boldsymbol{r}_x$ as

$$K(\boldsymbol{r}_x) = -\frac{1}{2\pi c(\boldsymbol{r}_x)} \frac{R_{rs}}{c_r\, R_{rx}\, R_{sx}} \frac{\int_0^\infty \omega^3\, |\dot{m}(\omega)|^2\, \sin[\omega \Delta\, T(\boldsymbol{r}_x) - \Delta\, \Phi(\boldsymbol{r}_x)] d\omega}{\int_0^\infty \omega^2\, |\dot{m}(\omega)|^2 d\omega} \quad . \tag{III.2}$$

The kernel depends on $\Delta\Phi$ which is the phase shift due to passage through caustics (for SS wave) or super critical reflection, [R_{rs}, R_{xr}, R_{xs}] are the geometrical spreading factors, $|\dot{m}(\omega)|^2$ is the source power spectrum considered as Gaussian, ΔT is the detour time of the scattered wave, c_r and $c(\boldsymbol{r}_x)$ are the velocities at receiver and scatterer position, respectively. Further details can be found in Dahlen et al. (2000) and Zaroli et al. (2010). As an additional remark, the minus sign in the equation III.2 can be easily explained. Indeed, a fast velocity anomaly will induce a negative time-residual, the wave will arrive before the predicted travel-time.

Analytical expressions make kernel computations relatively cheap (on average 1 s for a S-wave (ScS) and 1.5 s for a SS-wave (ScS_2). These kernels are generated under the paraxial approximation allowing to compute kernels very economically. Paraxial approximation, also called "forward-scattering approximation", consists in taking only scatterer waves which have paths not too far from the ray-theoretical path. We also assume that S wave only scatters into S wave, in other words no conversion into P-wave are generated. In the paraxial approximation, ones needs only a kinematic and a dynamic tracing along a source-receiver path (Dahlen et al., 2000) instead of summation of coupled surface waves which is much more expensive (Marquering et al., 1999). This computational advantage is also due to the Gaussian shape of the source power spectrum ($|\dot{m}(\omega)|^2$) used in the analytical expression. If estimated source time function are used to compute kernels (e.g. Hosseini and Sigloch, 2015) then one needs to compute kernels numerically, which is slower and less accurate.

2. A good explanation of the ray versus finite-frequency debate can be found here: `https://www.geoazur.fr/GLOBALSEIS/nolet/BDdiscussion.html`

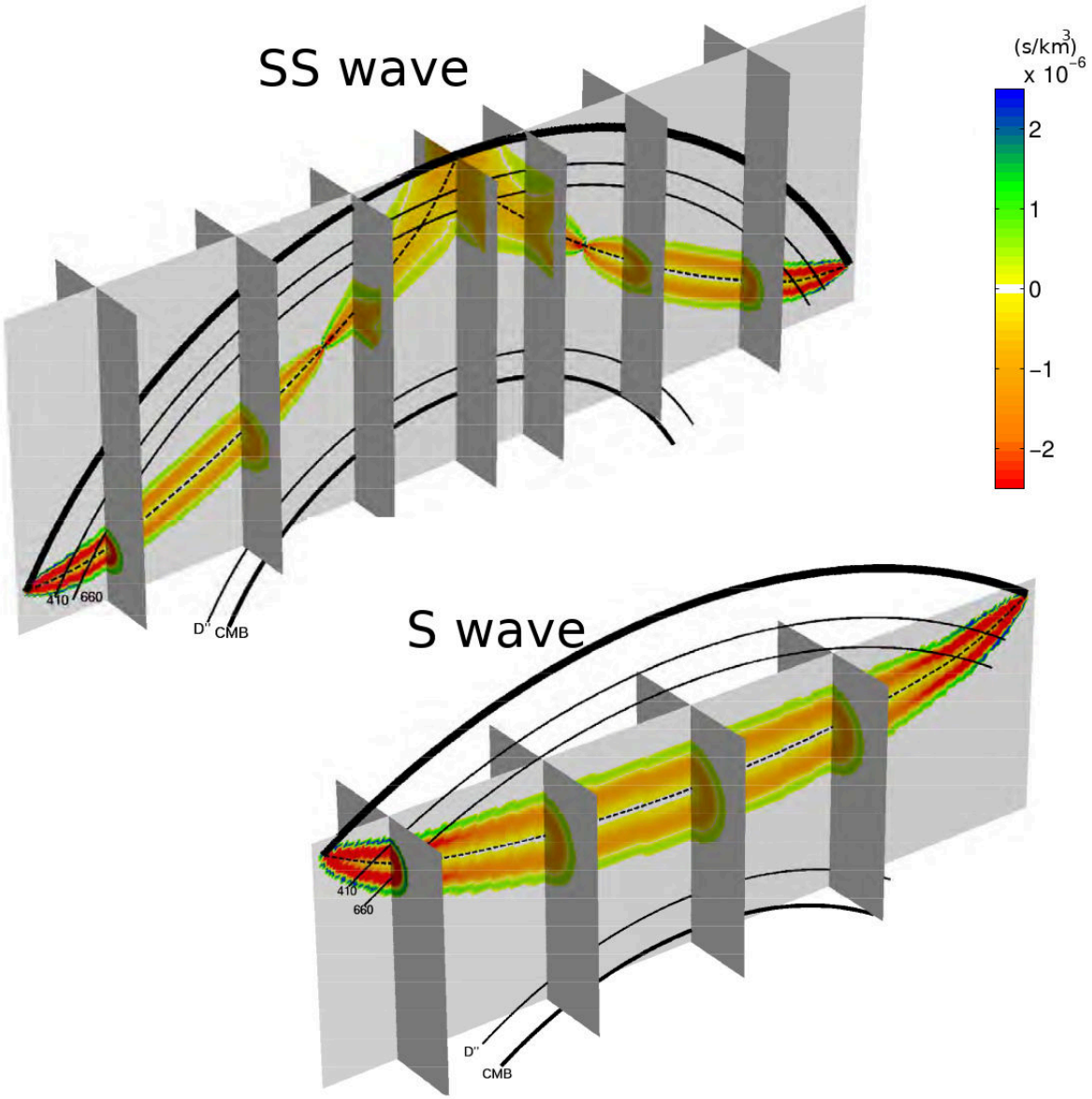

Figure III.2 – 3-D views of a SS and S-wave traveltime finite-frequency (Fréchet) kernels at T=20 s. Source is located at 0 km of depth and the epicentral distance is $64.5°$ for the S-wave and $120.6°$ for the SS-wave. The negative part (red) is the first Fresnel zone and the positive part (green) is the second Fresnel zone. Extracted from Zaroli (2010).

Since we consider only shear waves (SH) in an isotropic medium, we can rewrite the SH-wave sensitivity kernels as

$$dt = \int_{\oplus} K_\beta(\boldsymbol{r})\, \delta\beta(\boldsymbol{r})\, dV \tag{III.3}$$

with $K_\beta(\boldsymbol{r})$ the sensitivity kernels for S-wave heterogeneities and $\delta\beta(\boldsymbol{r})$ model parameters for S-wave anomalies (with $\delta\beta = dln(\beta)$). We can neglect every contribution from P-wave velocity and density anomalies to the the shear-wave time-residuals.

III.1.2 Normal modes data

The Earth like all finite mechanical systems shows an infinite discrete number of free oscillations (or normal modes). These resonant frequencies can be assimilated to specific sounds emitted by a bell while ringing. In terms of wave propagation, normal modes are stationary waves, the result of interferences between two propagating waves with opposite directions of propagation.

Normal modes measurements are characterized by a frequency (f), an amplitude (A), a phase (ϕ) and a quality factor (Q, attenuation feature). The frequency and the quality factor are only dependent on the structure of the Earth. The amplitude and the phase depend on the earthquake's attributes such as its depth, magnitude and focal mechanism.

Seismic normal modes can be classified into two groups: the spheroidal modes (S) and the toroidal modes (T) (Figure III.3). Toroidal normal mode are characterized by tangential motions meaning there is no variation of the volume of the Earth (and so no gravity changes). Spheroidal normal modes are described by radial and tangential motions, inducing gravity changes. Here, we exclusively consider spheroidal normal mode with strong sensitivity to Earth mantle structure. The number of seismic normal modes are infinite and are commonly limited to periods less than 1 hr. Each mode is characterized by two quantum numbers n, l: with n the overtone number ($n \geq 0$) and l the harmonic degree ($l \geq 0$) noted as ${}_nS_l$ for spheroidal mode.

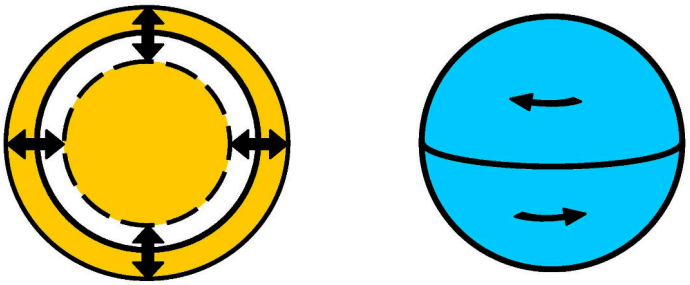

Figure III.3 – Examples of normal modes motions for (left) the radial normal mode ${}_0S_0$ with a period of 20.5 minutes called "breathing" mode, (right) the toroidal normal mode ${}_0T_2$ with a period of 44,2 minutes (Van Camp, 2006).

In this work, for simplicity, we shall only treat spheroidal modes, denoted as:

$$\underline{k} = \{{}_nS_l\} \tag{III.4}$$

In a spherical, homogeneous, isotropic and non-rotating Earth, normal modes are *degenerated*, only two parameters are necessary to describe them. In this case, the displacement **s**, recorded at a location $\mathbf{r} = (r, \theta, \phi)$ generated by an earthquake located at $\mathbf{r}_0$ and associated to a seismic moment tensor **M** can be expressed as (Gilbert and Dziewonski, 1975):

$$\mathbf{s}(\mathbf{r}, t) = \mathrm{Re}\left[\sum_{\underline{k}} \boldsymbol{\sigma}_{\underline{k}}^{T}(\mathbf{r})\, \mathbf{a}_{\underline{k}}(\mathbf{r}_0)\, \exp(i\underline{\omega}_k t)\right] \tag{III.5}$$

with $\boldsymbol{\sigma}$ holding for the receiver function, it contains information about the seismometer location, and eigenfunctions of normal mode $\underline{k}$ at **r**. The source term **a** contains information about the earthquake source (seismic moment tensor, M). Besides, we assume that the eigenfunctions in the source term are normalized following Gilbert and Dziewonski (1975). $\underline{\omega_k}$ represents the degenerated frequency of the normal mode $\underline{k}$.

For elliptic, rotating, anisotropic or heterogeneous Earth, normal modes splitting occurs in frequency. Thus, to identify each specific singlet in the splitting of a multiplet (n, l), we need to define another parameter called the azimuthal index m (with $-l \leq m \leq l$). In that case, we can rewrite equation III.5 by adding a splitting term $(\exp(i\mathbf{H}^{\underline{k}}t))$

$$\mathbf{s}(\mathbf{r}, t) = \mathrm{Re}\Big[\sum_{\underline{k}} \boldsymbol{\sigma}_{\underline{k}}^{T}(\mathbf{r}) \, \exp(i\mathbf{H}^{\underline{k}}t) \, \mathbf{a}_{\underline{k}}(\mathbf{r}_0) \, \exp(i\underline{\omega_k}t) \Big] \qquad \text{(III.6)}$$

The splitting (complex) matrix $\exp(i\mathbf{H}^{\underline{k}}t)$ contains all the splitting induced by ellipticity, rotation and all 3-D heterogeneities influencing the $\underline{k}$ normal mode. So far, all multiplets are considered independent between each other (the splitting matrix is block diagonal). This matrix can be written as

$$H_{mm'}^{\underline{k}} = \omega_{\underline{k}}(1 + a + bm + cm^2)\delta_{mm'} + \sum_{\substack{s=0 \\ s\,even}}^{2l} \sum_{t=-s}^{s} \gamma_{st}^{mm'} \, {}_{\underline{k}}c_s^t \qquad \text{(III.7)}$$

with $t = m - m'$. The first term of this equation corresponds to the splitting induced by ellipticity and rotation (a, b, c coefficients), whereas the second term brings information on the splitting induced by the 3-D heterogeneities. The splitting matrix is linearly linked to the structure coefficients ${}_{\underline{k}}c_s^t$ containing all the information about the 3-D heterogeneities of the Earth probed by the normal mode $\underline{k}$. However, the displacement recorded at a station **s** is strongly non linearly linked to the structure coefficients ${}_{\underline{k}}c_s^t$ (see the exponential in equation III.6).

As a consequence, imagery problems using normal modes can be solved in two steps: first, a non linear inversion to obtain the structure coefficients $({}_{\underline{k}}c_s^t)$ (Ritzwoller et al., 1986, 1988). This nonlinear inversion consists in inverting seismograms spectrum $(\mathbf{s}(\omega))$ at different stations to obtain the structure coefficients $({}_{\underline{k}}c_s^t)$ with s, t the degree and the order of the spherical decomposition. From the structure coefficients, a second linear inversion extract the elastic parameters perturbations.

After this first inversion, structure coefficients can be linearly related to the 3-D relative perturbations to a radial reference model in shear velocity, compressional velocity, density and to the internal topography variations (Woodhouse and Dahlen, 1978; Ritzwoller et al., 1988)

$${}_{\underline{k}}c_s^t = \int_0^a \Big[\delta\alpha_s^t(r) \, {}_{\underline{k}}K_s(r) + \delta\beta_s^t(r) \, {}_{\underline{k}}M_s(r) + \delta\rho_s^t(r) \, {}_{\underline{k}}R_s(r) \Big] r^2 \, dr - \sum_i r_i^2 \, h_{si}^t \, {}_{\underline{k}}B_{si} \qquad \text{(III.8)}$$

with $\delta\alpha_s^t(r)$, $\delta\beta_s^t(r)$, $\delta\rho_s^t(r)$ and h_{si}^t the spherical harmonic coefficients of P and S-wave velocities, density and topography perturbations to a 1-D reference Earth model (PREM). ${}_{\underline{k}}K_s(r)$, ${}_{\underline{k}}M_s(r)$, ${}_{\underline{k}}R_s(r)$ and B_{si} are the sensitivity kernels for P-wave, S-wave, density and topographic perturbations for the normal mode $\underline{k}$ (Woodhouse and Dahlen, 1978), r the variable of integration over the radius and a the radius of the Earth. Every spherical coefficient

(X hold for α, β, ρ and h) can then be write as

$$\delta X(r,\theta,\phi) = \sum_{s,t} \delta X_s^t(r)\, Y_s^t(\theta,\phi) \tag{III.9}$$

with Y_s^t denoting the surface spherical harmonic of degree s and order t (Edmonds, 1960). In this study, we consider topography disturbances small compared to elastic parameters perturbations ($\int_0^a \delta\beta_s^t(r)\, {}_{\underline{k}}M_s(r) \gg \sum_i r_i^2\, h_{si}^t\, {}_{\underline{k}}B_{si}$). Besides, since we are only interested in S-wave velocity variations ($\delta\beta_s^t(r)$), we scale P-wave velocity and density anomalies into S-wave velocity anomalies. We assume that elastic parameters and density changes in the same way along depth (hypothesis relying on the thermal origin of seismic anomalies). Though, this can be far from truth for the lowermost part of the mantle (potential heterogeneities induced by chemical reactions). Thus, to reduce the number of parameters in the tomographic normal mode inversion, we define an apparent sensitivity kernel such as

$${}_{\underline{k}}M_s^*(r) = {}_{\underline{k}}M_s(r) + \nu_\alpha\, {}_{\underline{k}}K_s(r) + \nu_\rho\, {}_{\underline{k}}R_s(r) \tag{III.10}$$

with

$$\nu_\alpha = \frac{\delta \ln(\alpha)}{\delta \ln(\beta)} \approx 0.55 \tag{III.11}$$

$$\nu_\rho = \frac{\delta \ln(\rho)}{\delta \ln(\beta)} \approx 0.2 \tag{III.12}$$

These values come from thermo-geodynamic hypothesis and lab experiments (Ritzwoller et al., 1988; Anderson et al., 1968). However, these values are not universally accepted especially in the lower-mantle conditions where chemical interactions can occur. Examples of sensitivity kernels and apparent sensitivity kernels (${}_{\underline{k}}M_s^*(r)$) are given in figure III.4.

However, in equation III.7, one can note that only even degrees of the Earth's structure can be recovered with normal modes (sum over s in equation III.7) under the "self-coupling" approximation. In this case, multiplets are considered as isolated, with no interactions with other modes. To have access to even and odd degrees of the Earth's structure we need to consider cross-coupling between normal modes, coupling is particularly strong for modes with similar features (frequency, attenuation, depth sensitivity). In case of cross-coupling, the block diagonal splitting matrix $H_{mm'}^{\underline{k}}$ becomes more complex. Off diagonal blocks appear and represent the cross-coupling whereas diagonal blocks correspond to the self-coupling. Lateral heterogeneity of degree s causes same-type mode coupling (spheroidal-spheroidal or toroidal-toroidal) under the following conditions (e.g., Laske et al., 2007)

- $m + t - m' = 0$
- $l' + l + s$ is even
- $|l - l'| \leq s \leq l + l'$.

Under these conditions we can find cross-coupling modes that are sensitive to odd-degree structures such as ${}_0S_{14} - {}_2S_9$ sensitive to degrees 5 and 7.

Finally, from previous equations the tomographic problem to solve with normal mode data (structure coefficients) is the following

$$ {}_{\underline{k}}c_s^t = \int_0^a \left[\delta\beta_s^t(r)\, {}_{\underline{k}}M_s^*(r) \right] r^2\, dr \tag{III.13} $$

In this study, we choose to use normal mode data (${}_{\underline{k}}c_s^t$) from two previous studies: Deuss et al. (2013) and Koelemeijer et al. (2013). A strict selection of normal mode in Deuss et al. (2013) is taken and complemented by Stoneley normal modes data from Koelemeijer et al. (2013).

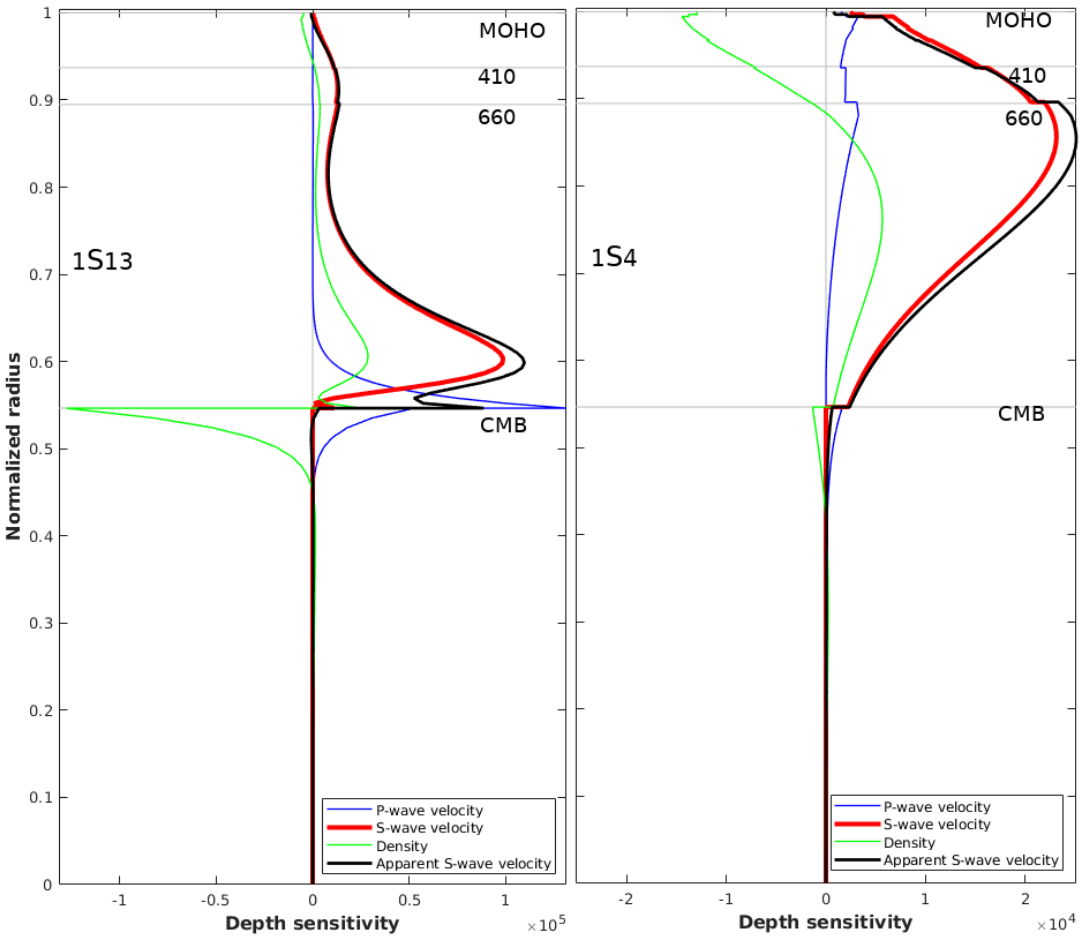

Figure III.4 – Sensitivity kernels for two normal modes used in this study. (left) ${}_1S_{13}$, (right) ${}_1S_4$. Grey horizontal lines symbolize the main discontinuities inside the Earth. Colors represent the sensitivity to P-wave velocity, S-wave velocity and density, the apparent S-wave velocity is in black.

III.2 Measurements of body waves

Our first step in the body-wave tomography is to set up a time-residual database. This new data set is aiming at improving the ray coverage, specifically in the lower mantle.

III.2.1 Measured seismic phases

We select waveforms generated by moderate earthquakes with $M_w \in [5.5, 6.5]$ all over the globe from 1976 to 2017 (Figure III.5), having a half time duration below 6 s. These requirements keep powerful earthquakes but with a source mechanism not too complicated. Stations-earthquakes distribution maps are displayed in figure III.5, we can see the improvements in the station coverage between this study (1976-2017, figure III.5b) and the one from Zaroli (2010) (1976-2008, figure III.5a).

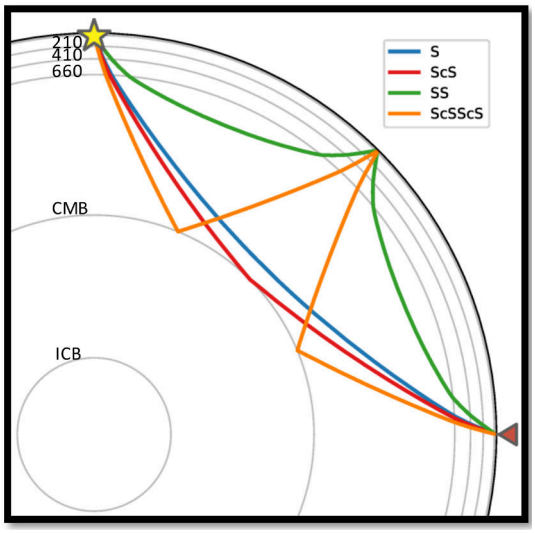

Figure III.6 – Examples of ray paths for all seismic waves measured in this study. These paths are computed for an earthquake located at 50 km depth (yellow star) and 90° away from the seismic station (reversed triangle).

The new body-wave database is composed of shear waves polarized in the horizontal direction (SH). We measure S, ScS, SS, ScS_2 waves as well as interferences between S and ScS waves (Figure III.6). S and SS waves are particularly efficient to bring information on the upper mantle. Core reflected phases such as ScS and ScS_2 will help to constrain lower mantle heterogeneities. To improve the body-wave data illumination in the lower mantle, we proceed to measurements of S+ScS at large epicentral distance from $75°$ to $95°$. For an uneven station-earthquake distribution, interference measurements allows to extend the coverage to areas where ScS waves cannot be useful. For future studies, diffracted S wave (Sdiff) should be considered to improve the data coverage in the lowermost mantle (e.g., Hosseini and Sigloch, 2015).

III.2.2 Cross-correlation measurements

III.2.2.1 Method

The measurement method relies on the cross-correlation between a synthetic and an observed seismogram (see appendix C for a basic description of the cross-correlation process). Both seismograms are first broadband filtered between 7 and 81 s to remove high frequency noise and low-frequency signals. Then, cross-correlation windows (red horizontal bars, figure III.7) are computed from ACTA software[3] heavily relying on codes developped by Zaroli et al. (2010). At the end, cross-correlation are performed over these windows (see the cross-correlation function figure III.7d). If the maximum of the cross-correlation function is above 80%, measurements at different periods will be carried out. To this aim, a Gaussian filter is applied at 10 s, 15 s, 22.5 s, 34 s and 51 s. In every case, a cross-correlation coefficient above 80% is required to accept the measurement. To avoid some drawbacks of cross-correlation

3. Automatic Cross-correlation Travel-time and Amplitude

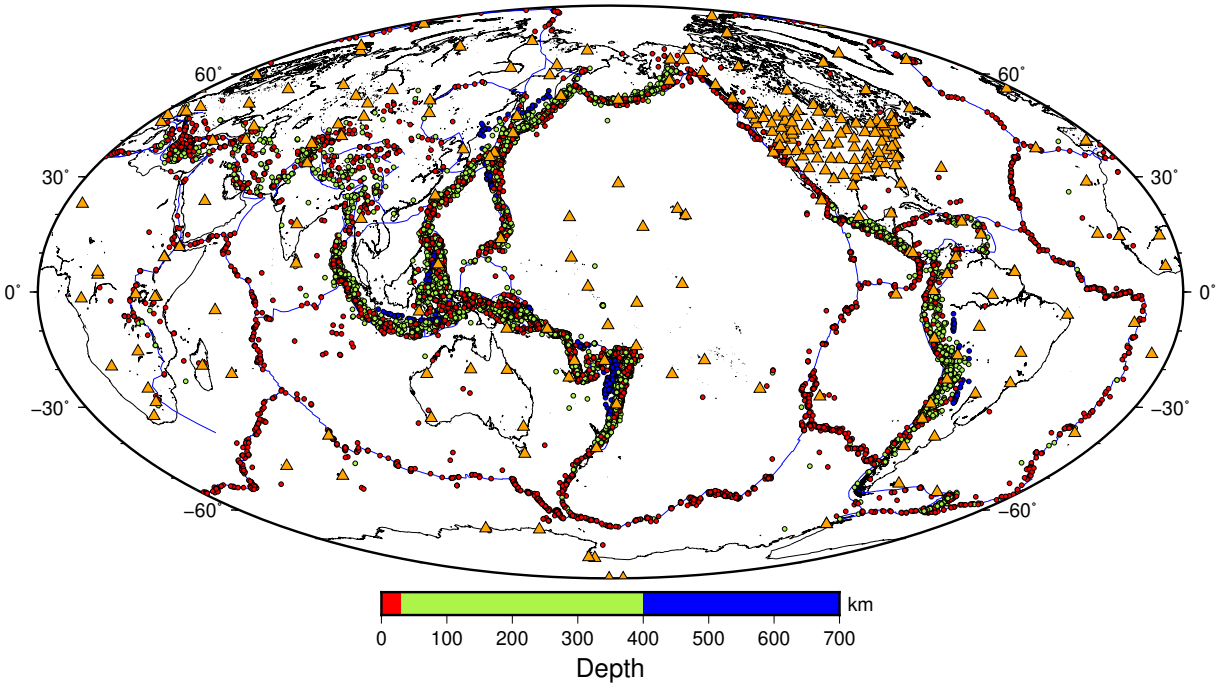

(a) Source-receiver distribution for the shear-wave dataset between 1976-2008 (Zaroli, 2010).

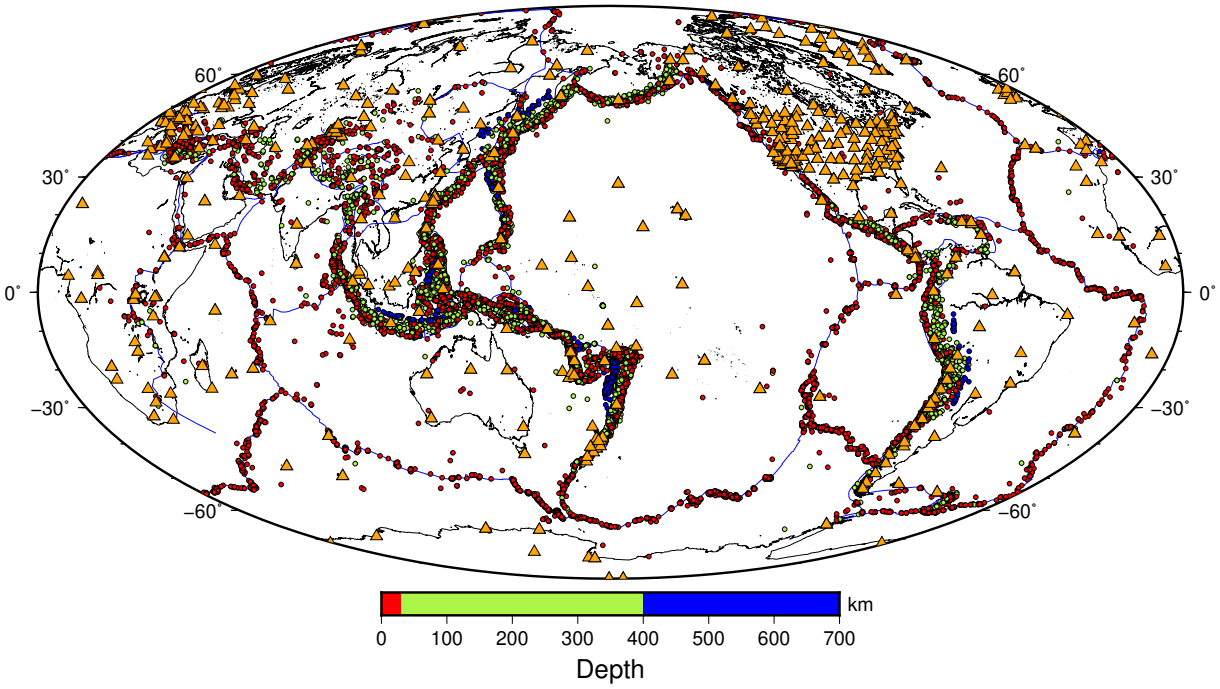

(b) Source-receiver distribution for the shear-wave dataset between 1976-2017 (used in this study).

Figure III.5 – Locations of broad-band stations (orange triangles), and selected earthquakes with $5.5 < M_w < 6.5$ from the GCMT catalog (circles filled with depth-dependent colors). Color transitions are at 30 km and 400 km of depth. Tectonic plates are delimited by blue contour.

measurements at high frequency such as cycle-skipping, we make use of the method applied by Zaroli et al. (2010). This method involves the use of a composite function (called F3) depending on the time-shift. This function takes into account the misfit between the recorded and the synthetic waveforms, and the amplitude difference (Ritsema and van Heijst, 2002). These two elements allow to discriminate the cycle-skipping cases especially for high frequency measurements. The F3 function gives similar results to the cross-correlation function when the measurement is good.

III.2.2.2 Example of interference measurement

Figure III.7 shows an example of time-residual measurement of interferences between S, sS, ScS and sScS waves. At this epicentral distance and depth (12 km), all these phases reach nearly simultaneously the seismometer (Figure III.7a). After the broadband filtering, the cross-correlation gives a time-residual of 4.5 s with a maximum of 93% for the correlation. Since the maximum of the cross-correlation function is above 80%, we can go on with finite-frequency measurements. As we can see in figure III.7b, at 22.5 s, the fit between synthetic and observed seismogram is really good. For measurements at 10 s and 22.5 s, fits are good with a maximum of the cross-correlation of 92.8% and 98.0%, respectively. At 51 s, the fit between synthetic and observed seismogram is much lower with a F3 at 77.5% which is rejected in this case. Figure III.7c shows the dispersive curves for different attenuation corrections. We note the missing measurement at 51 s due to the bad fit between synthetic and observed seismograms. Off course, this is a good example of interference measurements. However, in other cases data quality can be quite poor and adapted parameters for window selection need to be set. In particular, interference measurements exhibit a wide variety of waveforms, inducing a potential poor fit between the synthetic and the observed waveform. This problem implies different elements: an accurate synthetic seismogram and a well-adapted cross-correlation window.

Every measurement need to be associated to a sensitivity volume. Since we measure various type of waves such as S, ScS, ScS_2 as well as interfering phases: S+sS, ScS+sScS and S+sS+ScS+sScS, proper sensitivity volume has to be associated to each specific phases or group of phases. All interfering phases are not equivalent in terms of complexity and sensitivity. For instance, measurements of S+sS which are very common due to the large number of shallow earthquakes, exhibit simple sensitivity kernel features (see kernel Figure.III.2). Though, S-wave depth phases are modeled in synthetic seismograms, it is our experience that interfering kernels such as S+sS do not significantly change the model compared to pure S-wave kernels. Since the interfering kernels are more expensive to compute than single kernel, we decide to not include depth phase in the kernel computation[4].

As a consequence, the interfering measurements involving main and depth phases expressed as

$$dt_{S+sS} = \int \mathsf{K}_{S+sS}(\boldsymbol{r})\, m(\boldsymbol{r})\, dV \tag{III.14}$$

are approximated with

$$dt_{S+sS} \approx \int \mathsf{K}_{S}(\boldsymbol{r})\, m(\boldsymbol{r})\, dV \quad . \tag{III.15}$$

4. Besides, numerical modelings show that time-residuals computed in a Gaussian model with proper kernels (K_{S+sS}) are nearly indistinguishable from the S-wave kernel (K_S).

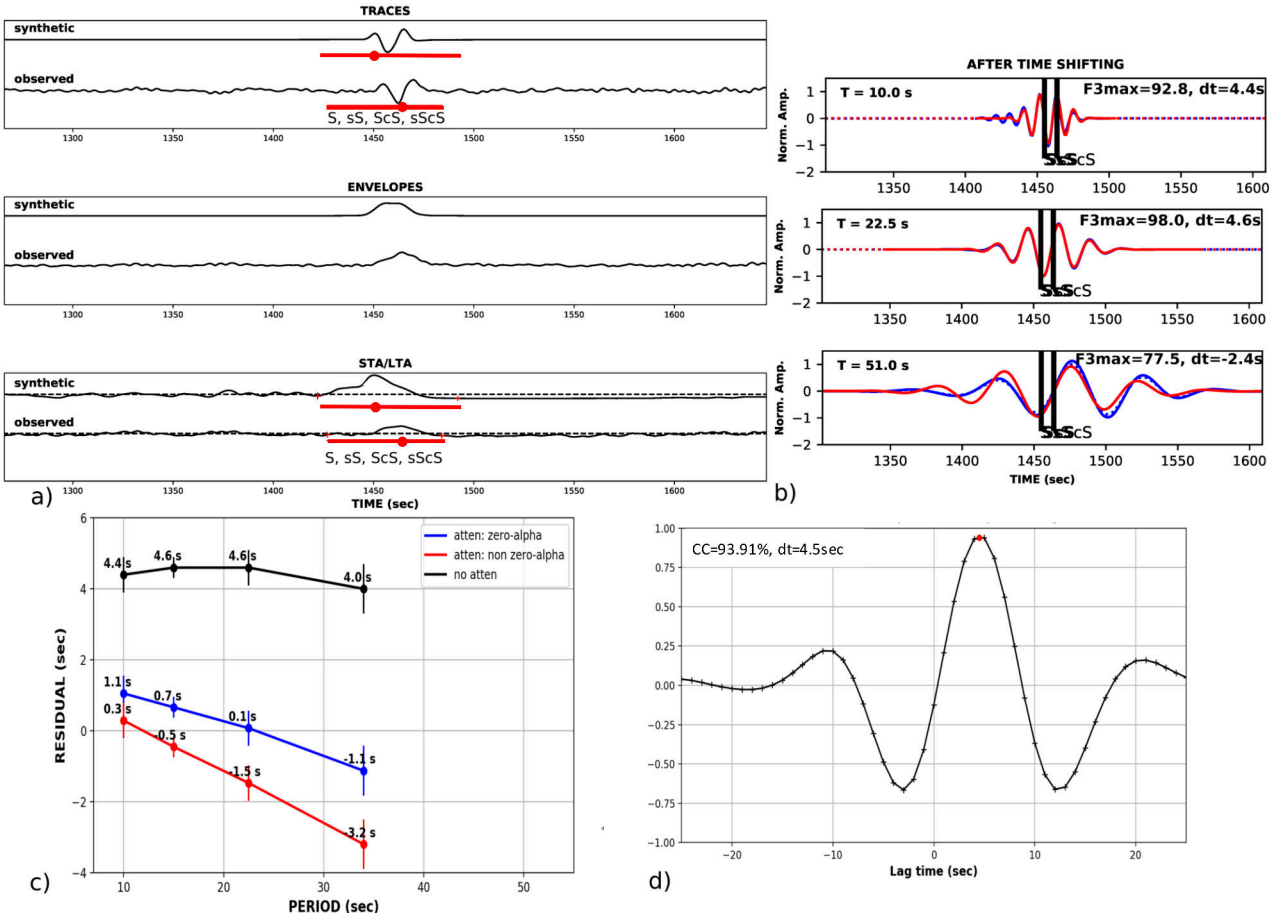

Figure III.7 – S+ScS interference measurement on the transverse component where the S, sS, ScS and sScS waves interfere at a distance of 92.7°. (From top to bottom) a) Synthetic and observed: traces filtered between 7-81 s, envelopes, STA/LTA waveforms. Cross-correlation windows are plotted as red horizontal bars with all interfering phases written below. b) Superimposed synthetic (red) and observed (blue) waveforms after time shifting filtered at 10 s, 22.5 s and 51 s (from top to bottom). c) Dispersion curves with measurements at 10, 15, 22.5 and 34 s: curves represent different attenuation corrections: (black) no attenuation correction, (red, blue) attenuation correction. d) Cross-correlation function computed from broad-band filtered seismograms [7-81 s].

This simplification is applied to all other phases:

- $K_{S+sS} \approx K_S$
- $K_{SS+sSS} \approx K_{SS}$
- $K_{ScS+sScS} \approx K_{ScS}$
- $K_{ScS_2+sScS_2} \approx K_{ScS_2}$

For unusual interference kernels, such as interferences between S and ScS, the problem is more complex. In this case, we have to properly model the interference kernel K_{S+ScS} since the sensitivity kernel is quite different from a simple S or ScS kernel. As we intend to properly

model sensitivity volume of interference measurements, we generate an interference kernel with S, sS, ScS and sScS (see Figure III.8)[5]. This interference kernel with four seismic phases is computed at a period of 34 s, and we see lots of details in the sensitivity variation compared to the S-wave kernel (see Figure III.2). In the parameter-free Backus-Gilbert inversion we could be able to exploit all sensitivity variations from this kernel (Zaroli, 2019). However in this study, the interference kernel S+ScS is going to be projected over a coarse mesh which will degrade the sensitivity kernels.

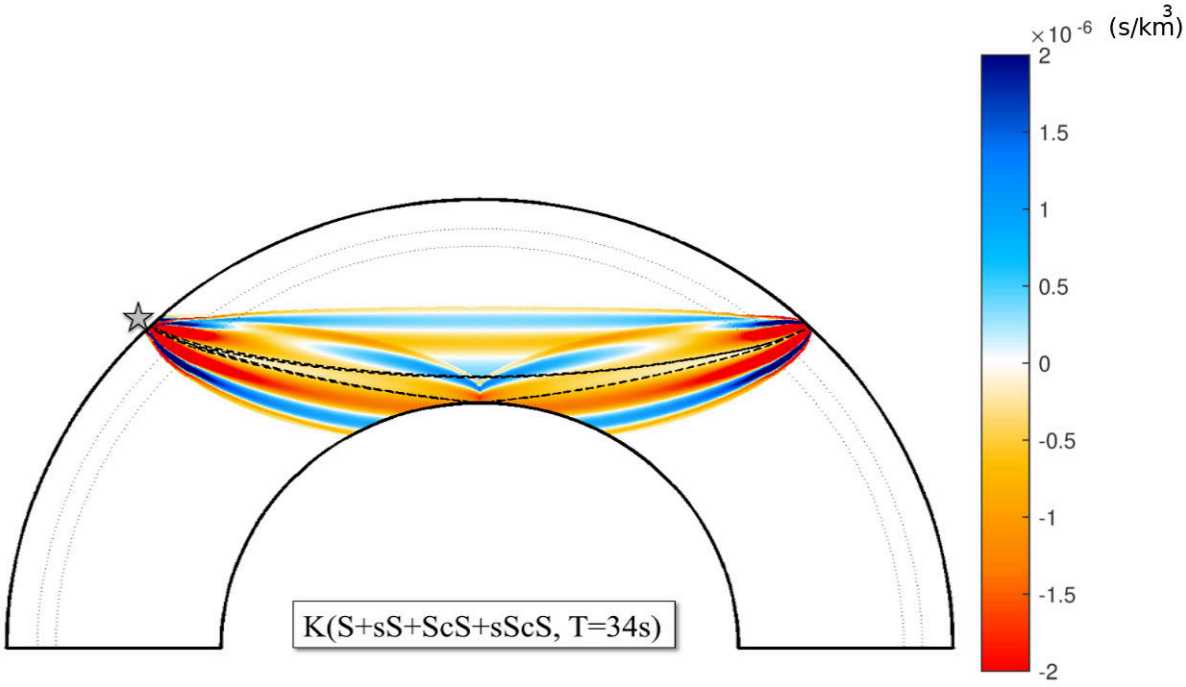

Figure III.8 – Finite-frequency travel-time Fréchet kernel at T=34 s for interferences between S+sS+ScS+sScS waves for an epicentral distance of $90°$ and a source located at 0 km. Dashed lines represent the ray geometrical paths of the S and ScS-waves. Dotted lines represent the 410 and 660 km discontinuities respectively. Courtesy from C. Zaroli

Synthetic seismograms: WKBJ.py

Synthetic seismograms used in this thesis are generated with an implementation of the WKBJ algorithm (Chapman, 1978). This fortran code is embedded in a python module allowing to easily choose which phase the user wants to add in the seismogram. This module is integrated to the ACTA.py cross-correlation measurement code, which enables to generate synthetic seismograms on-the-fly and thus saving a considerable amount of memory by not storing synthetic seismograms.

III.2.3 Error estimation on cross-correlation measurement

For tomographic studies using seismometer arrays, it is possible to estimate measurement uncertainties with statistic technique such as with summary rays (e.g. Nolet et al., 2008).

5. The “mustache" kernel, Paula Koelemeijer November 2016

Which supposes to have a large number of rays with the same path and so sensitive to the same anomalies. It is then possible to estimate a mean uncertainty on all measurements made inside this array. Though an uncertainty estimates can be obtained systematic errors cannot be included in this estimation. However, for isolated stations the problem is worst. Estimate of measurement uncertainty is generally done from a single cross-correlation function between the observed and the synthetic waveform (no statistics on measurements can be done).

In this study, we rely on Chevrot (2002) to approximate the error related to the cross-correlation process. Following Zaroli et al. (2010) the uncertainty estimate on each measurements is computed as

$$\sigma = \{\tau \mid \gamma_{d,s}(\tau_m) = \gamma_{s,s}(\tau)\} \tag{III.16}$$

with σ the measurement error, τ the time-shift, $\gamma_{d,s}$ the cross-correlation function between the observed (d) and the synthetic (s) seismogram, $\gamma_{s,s}$ the autocorrelation of the synthetic seismogram and τ_m the time-shift for which the maximum of the cross-correlation function is reached. To compute more precisely the time-residual the cross-correlation function is re-interpolated with a time step of 0.1 s. Therefore, we set a minimal error at 0.1 s.

This method has several advantages. The frequency content of the phase is taken into account by the width of the autocorrelation function. Thus, for a same correlation coefficient, low frequency measurements are going to have a larger measurement error than high frequency measurements. If observed waveform is distorted owing to noise contamination, the wave shape will be disturbed and the maximum of the cross-correlation function will be lower. But, this method does not protect from phase misidentification or cycle-skipping effect. Since estimations of measurement uncertainties are not perfect, we check the error distribution as a function of the SNR and the maximum of the cross-correlation coefficient for all periods (Figure III.9). Analysis of these distributions show a threshold effect at 0.1 s, visible at all measurement periods. This is produced by the lower limit we set for the measurement error. To not be biased by this threshold effect, we set a cut-off value for data error according to the measurement period, i.e. 0.1 s for T=10 s, 0.3 s for T=15 s, 0.5 s for T=22.5 s, 0.7 s for T=34 s and 1 s for T=51 s (see figure III.9).

We see a logical increase of data measurement errors with a decrease of the cross-correlation coefficient at all periods. This means that observed seismograms which do not look like the synthetic will give a more inaccurate measurement. The correlation between the data error and the SNR is more convoluted. Very large errors are mostly associated to low SNR, but tiny errors can be associated to either high or low SNR. The last subplot in figure III.9 (last row, right column) summarizes error distributions for all five periods by removing errors equal to 0.1 s. For large values of SNR, data error estimates are nearly independent of the SNR. For low values of SNR, it seems that data error slightly decreases with an increase of the SNR. This threshold effect appears for very low SNR (< 4). As soon as the SNR level is good enough, no variations in the data error estimates can be correlated to the SNR level.

For high frequency acoustic studies it is often considered that data error is proportional to $\frac{1}{\sqrt{SNR}}$ in which we assume a time-residual dt very small compared to the period T (e.g. Jameson, 2006; Tamim and Ghani, 2010; Carrier and Got, 2014). This is not the case for our study, as we could reach time-residuals between 0 to 20 s which can not be neglected

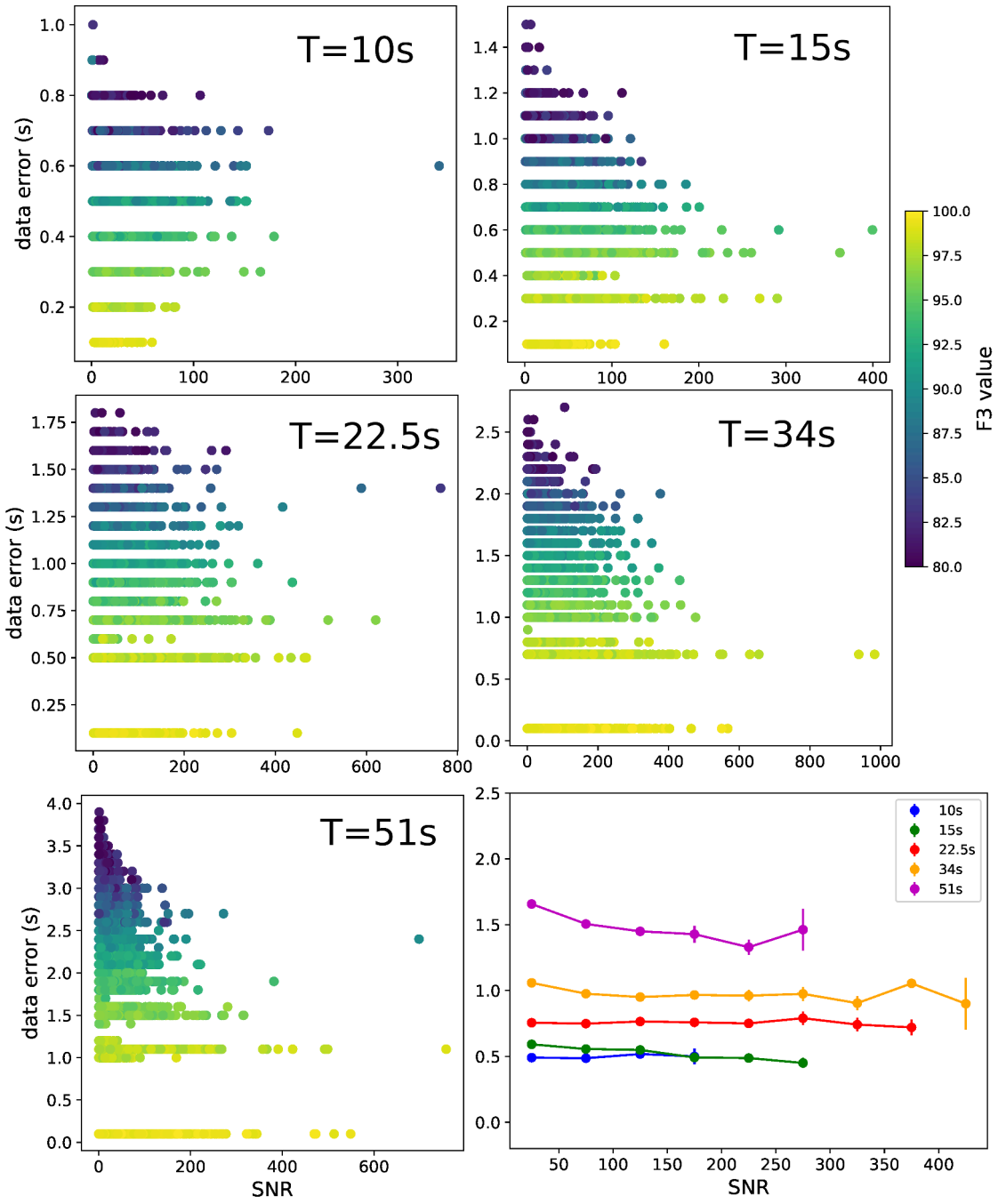

Figure III.9 – Distribution of time-residual errors as a function of the SNR (signal-to-noise ratio, with a minimal value for the SNR of 2). Distributions are displayed for each period: 10, 15, 22.5, 34 and 51 s with color code indicating the quality of the F3 coefficient (proxy for cross-correlation coefficient). Last inset in the bottom right is a weigthed average of data errors as a function of SNR for all periods.

compared to measurement periods (10, 15, 22.5, 34, 51) s. Finally, as inferred from equation V.1, data errors increase with the measurement period (last subplot of figure III.9).

III.3 Analysis of the body-wave database

At the end of the measurement part, about 18% of the full data set is kept. We will now assess the improvements brought by the new measurements. In this part, we show the body-wave data coverage specifically in the lower mantle and will analyze the specific contribution of the ScS-wave type.

III.3.1 Assessment of dataset robustness

Figure III.10 summarizes the measured travel-times (black dots) with associated theoretical travel-times (colored curves) for each phase as a function of the epicentral distance. Thanks to the adaptive measurement process, interference measurements for S and ScS waves are made for epicentral distances between $75°$ and $95°$ (blue and red curves merging at $75°$, Figure.III.10). Above $95°$, no more measurements are done because the diffracted S-waves are emerging. There is no measurement of ScS waves between $30°$ and $45°$ because of interferences with SS. Moreover, SS waves undergo triplication at these distances which is an additional difficulty when one is looking for phase interferences. We can notice a gap in measurements for ScS_2 between $115°$ and $135°$, this is due to interferences between ScS_2 with SSS, SKKS or SKS. Since these phases are not modeled in the synthetics, the fit between synthetic and observed seismograms is weak and measurements are not accepted. Since finite-frequency kernels are based on the paraxial approximation (Tian et al., 2007a), we will not invert time-residuals for measurements (SS and ScS_2) at epicentral distances above $130°$.

To assess the reliability of this new body-wave dataset we can check for specific finite-frequency effects. For instance, the wavefront healing is a well-known effect occurring when finite-frequency measurements are performed (Hung et al., 2001). This effect tends to remove the positive time-residual (due to slow seismic anomaly) for low-period waves. We can highlight this phenomenon by comparing, for a same ray path, time-residuals measured at high and low frequencies. Figure III.11 displays time-residuals measured at 15 s and 34 s: time-residuals at 34 s are, on average, smaller than time-residuals at 15 s. This is a clear impact of the wavefront healing phenomenon. Positive delays tend to vanish for large travel paths and for low frequency measurements. A similar effect can be found for negative time-residuals but it is not perfectly symmetrical to the wavefront healing (Wielandt, 1987) (supplementary figures on time-residual distributions can be found in appendix C).

III.3.2 Data coverage

Figure III.12 shows the ray density at the CMB in different configurations. Figure III.12a) contains ScS waves between 1976-2008 (data set from Zaroli et al. (2010) for the same earthquake magnitude range) which is coarse and weak, specifically under the Pacific and Africa where mantellic plumes are supposed to be observed. Earthquake locations do not fluctuate a lot over time, they preferentially occur along ridges and subduction zones. An improved data coverage implies new receiver locations, such as in isolated islands. In this study, the coverage improvement comes from two factors: supplementary data (extension

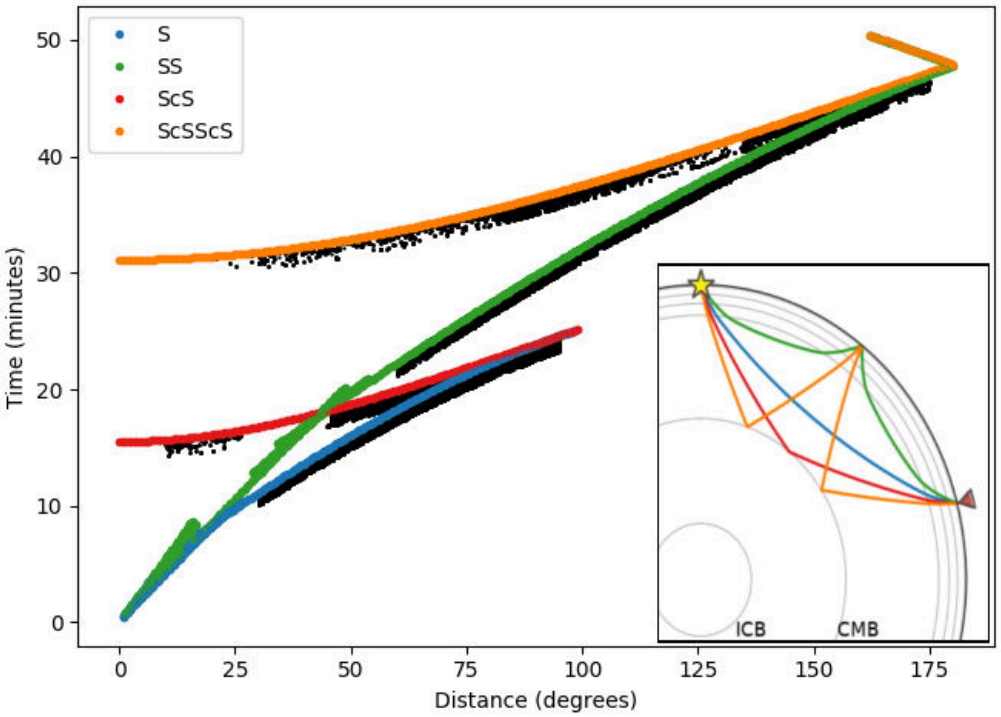

Figure III.10 – Theoretical travel-times versus epicentral distances for S (blue), ScS (red), SS (green) and ScS_2 (orange) wave. Observed travel-times (black dots) are deduced from time-residuals measured on broad-band filtered seismograms. Lower-right insert depicts the ray paths for S, ScS, SS and ScS_2 for an earthquake at 10 km depth and an epicentral distance of $75°$.

from 2008 to 2017) with new couples of earthquakes-stations, measurements of new seismic phases such as ScS_2 and interferences S+ScS. Improvements in ray coverage brought by these two elements are showed in figures III.12(b,c). The coverage difference between South and North hemisphere seems amplified when density ray plots from polar projection (Figure III.13). Poor data illumination is especially visible under Africa.

III.3.3 ScS wave type contribution

The most significant factor impacting data coverage is the measurements of interferences between S and ScS, and ScS_2 waves. We are going to show in more details what is the relative contribution of these two ScS wave type to lowermost mantle coverage.

III.3.3.1 ScS wave type coverage

We see in figure III.14 three different coverage maps at the CMB. The top one depicts ScS wave coverage where we see the usual good cover around the Pacific, and relatively poor in the Pacific ocean as well as Africa. The middle figure shows the coverage for interferences between S and ScS waves. Thanks to the epicentral distances where interferences appear, it allows to illuminate parts of center and south Pacific as well as Atlantic. At some locations, coverage seems like straight lines which is only the ghost of the seismicity pattern located at the bouncing points. For the last plot in figure.III.14, ScS_2 significantly improves the

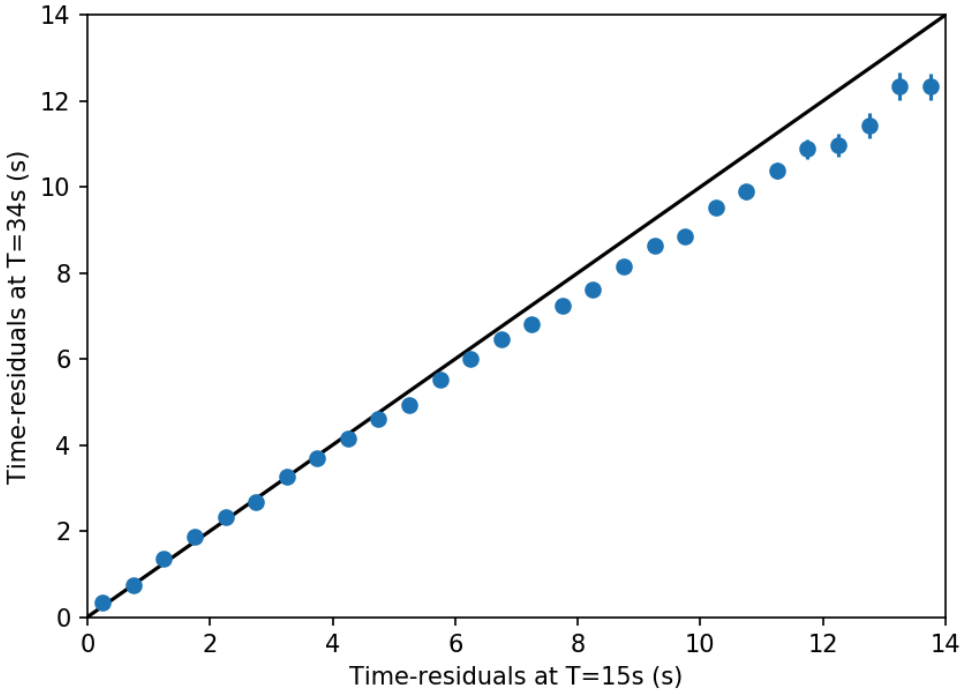

Figure III.11 – Wavefront-healing effect highlighted by differences between time-residuals measured at 15 s and 34 s. Measurements are made for the same station and earthquake. Dots are time-residuals averaged over windows of 0.25 s. Error bars are computed from a bootstrap process. Straight black line is the $y = x$ equation.

illumination in the mid and eastern part of the Pacific ocean. Obviously, for a same number of measurements, ScS_2 waves have twice more bouncing points than other ScS wave type. Although ScS, S+ScS and ScS_2 may sample common locations we should keep in mind that these plots only show the the number of hitting points at the CMB and not the direction of rays. Indeed, homogeneous coverage is not enough, it should be isotropic too.

III.3.3.2 Pseudo-tomography of ScS wave type

To associate time-residuals to ScS paths, we compute at the CMB the average over $5°$ by $5°$ cells of all time-residuals with common bouncing point locations. Figure III.15 shows the improvement brought by S+ScS interferences to the original coverage in ScS waves. Although strongly controlled by earthquake-station geometry, a clear improvement in data coverage is brought by S+ScS measurements. Central Pacific is one of the most improved zone compared to coverage without S+ScS (Figure.III.15a). Interference measurements highlight the positive time-residuals in the central part of the Pacific. The high velocity ring observed around the Pacific is also confirmed by these interferences.

One has to keep in mind that this representation can be misleading. Indeed, the time-residual is plotted at the reflection point but, in reality, time-residual has been acquired all along the ray path. Even if seismic anomalies can be plotted on the CMB, this delay can come from much shallower regions. For this reason we will not present comparative averaged time-residuals maps for ScS_2 since the same time-residual is plot at two different locations at the CMB. As a consequence, figure III.15b) does not represent the final coverage at the CMB since no ScS_2 are displayed.

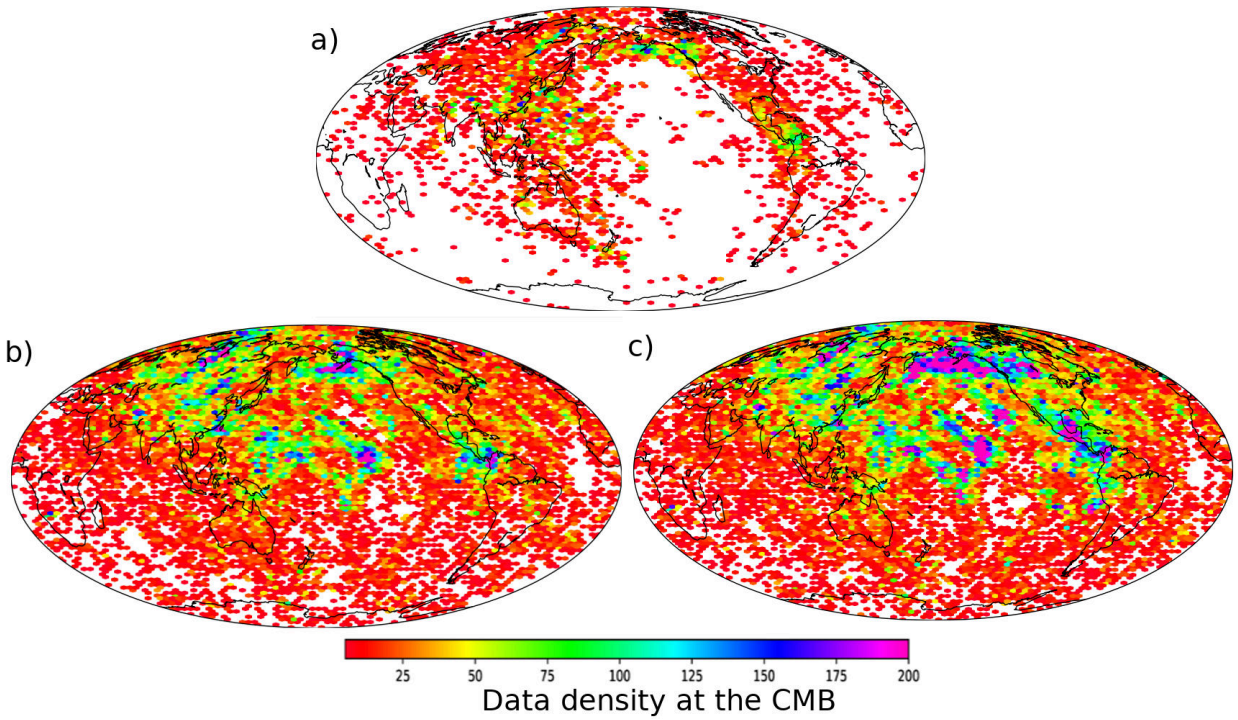

Figure III.12 – Ray density over the CMB. White regions depict poor data coverage. a) distribution of rays for Zaroli et al. (2010) data set between 1976 to 2008 with only ScS waves. Data coverage for figures b), c) are for data between 1976 to 2017 with ScS, ScS_2 and interferences S+ScS: b) coverage with permanent stations, c) coverage with permanent and temporary stations.

III.3.4 Toward the tomography

Once seismological data (d) and sensitivity kernels (K, section III.1.1.2) are computed we can address the inverse problem. In order to compute the solution, we define an irregular parametrization composed of Delaunay triangles with node density which mimics the data density (see appendix B for the parametrization used). It is thus necessary to project the sensitivity kernels on a mesh which is usually much coarser than the kernel grid. For all waves measured in this study, we give examples of the projected kernels. Since the parametrization is irregular projected kernels can be, in some cases, worst or better than those presented in the following. Figures 9-13 present S, ScS, S+ScS, SS and ScS_2 projected kernels on the mesh used for the inversion, respectively. We note a tremendous lost of details between the sensitivity kernel for interferences before projection (Figure III.8) and after the kernel projection (Figure III.18). These images should definitely convince tomographers to work toward free-parameter inversions. An option already exists with the free-parameter B–G inversion (Zaroli, 2019) but needs to be supported by large computational resources to invert large-scale model such as for global tomography. However, we are getting closer and closer to achieve global free-parameter B–G inversion. To get ready, we need finite-frequency data which are fully compatible with sensitivity kernels, and only sensitive to mantle finite-frequency effects. In this context, we introduce in the next chapter finite-frequency crustal corrections for long-period body wave data. We will show what are the origins of these finite-frequency effects and how to correct for them. Thus, finite-frequency time-residual data will be in agreement with their associated non-projected sensitivity kernels for future studies.

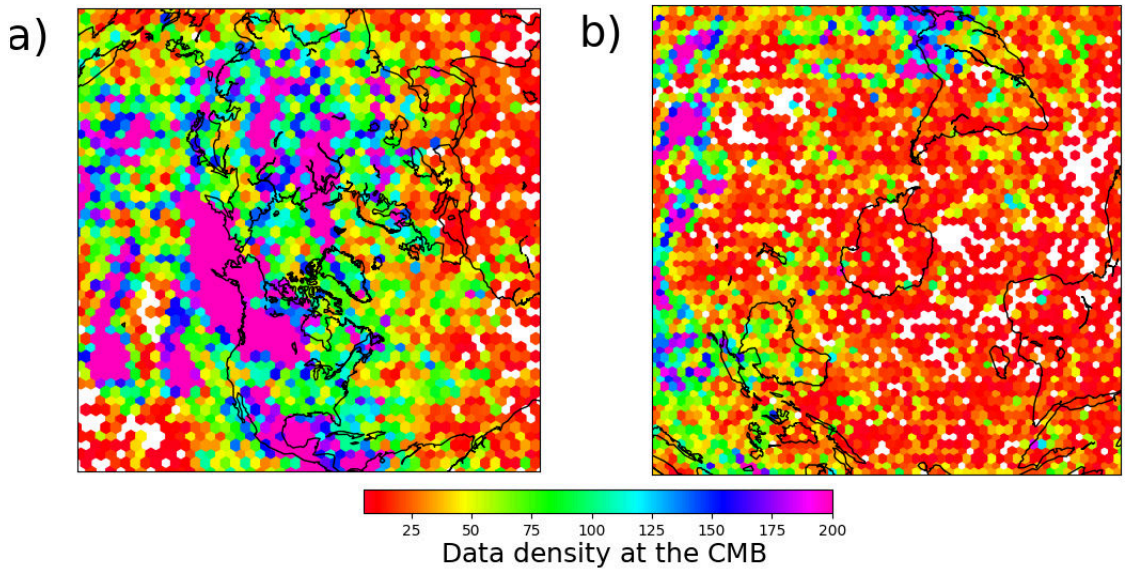

Figure III.13 – Polar projection of ray coverage over the CMB for permanent and temporary stations (same data as Figure III.12c) - a) for the North hemisphere, b) for the South hemisphere.

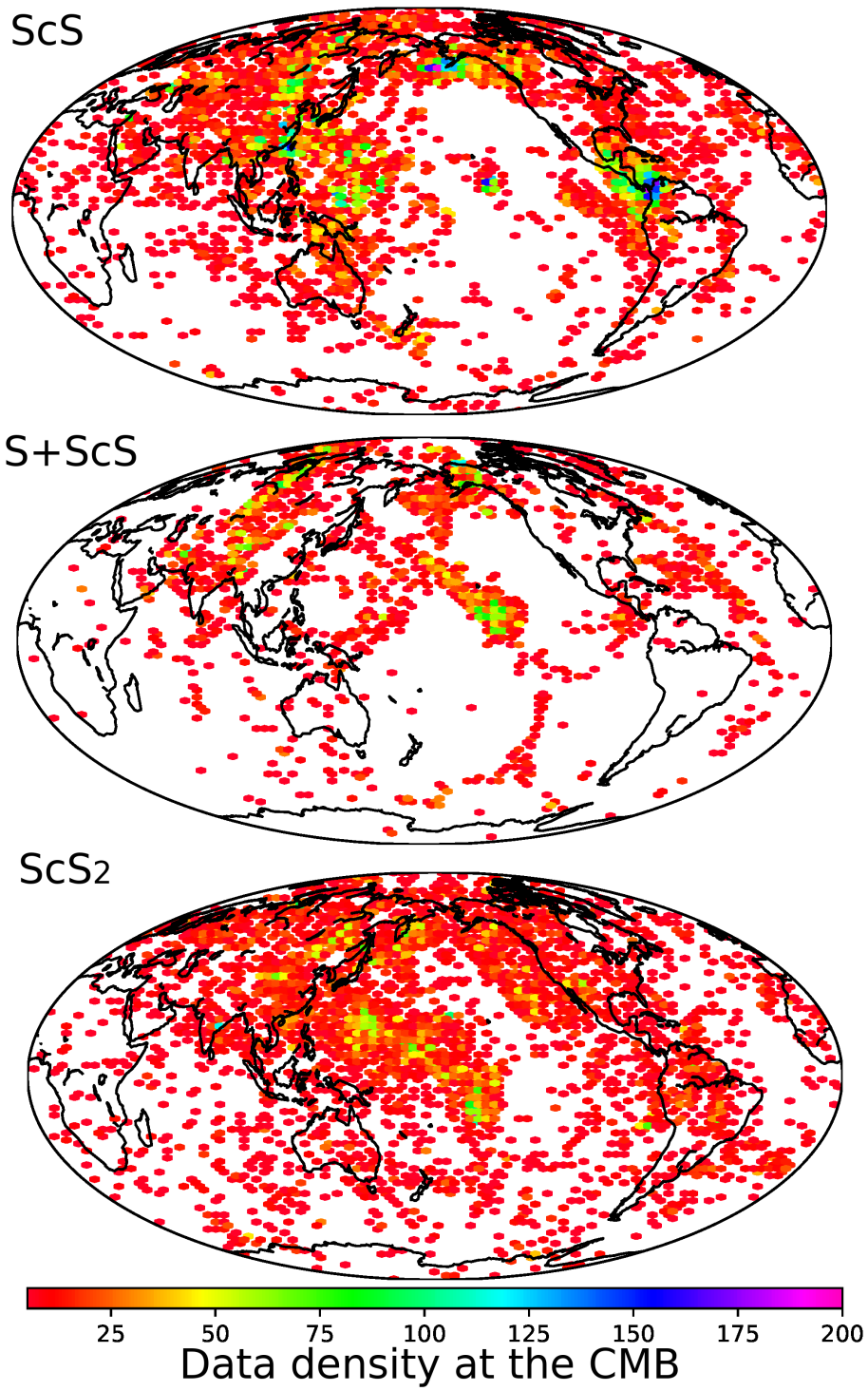

Figure III.14 – Data coverage at the CMB for (Top) ScS wave, (Middle) interference between S and ScS waves, (Bottom) ScS_2 wave.

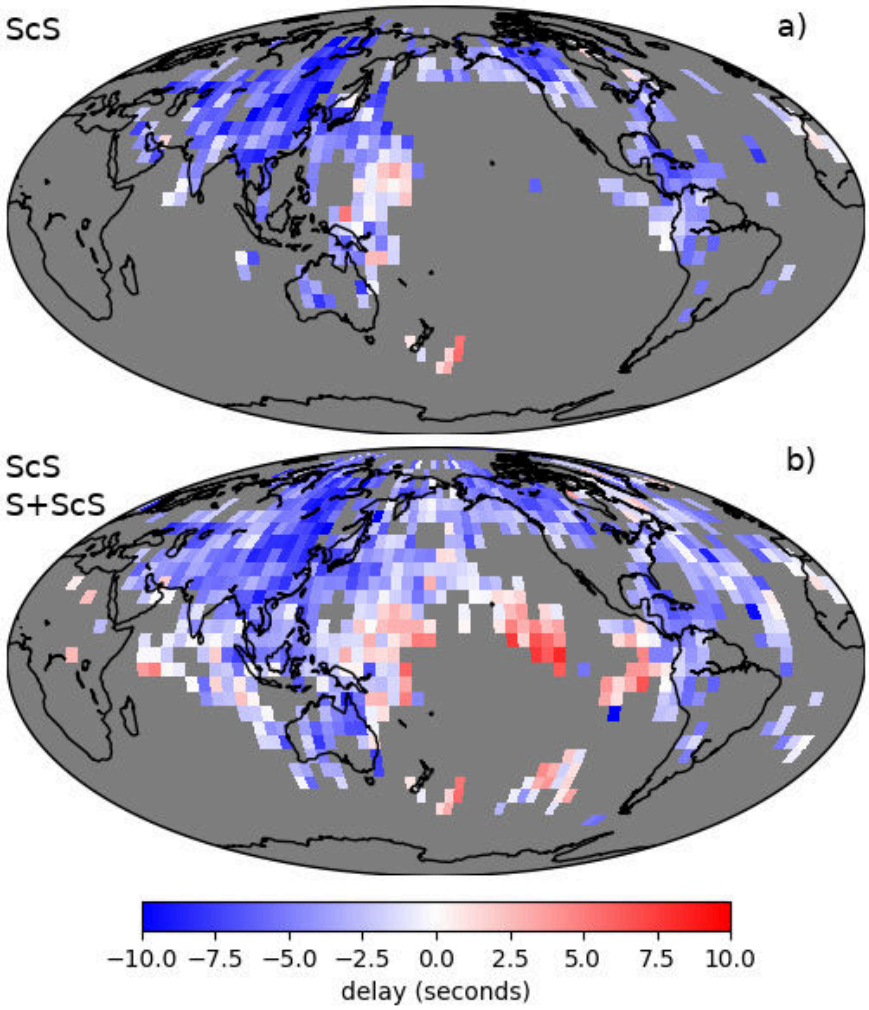

Figure III.15 – Mean time-residuals averaged over a $5°$ by $5°$ mesh with a mask for cells with less than 3 rays: a) only with ScS waves b) ScS waves with S+ScS interferences.

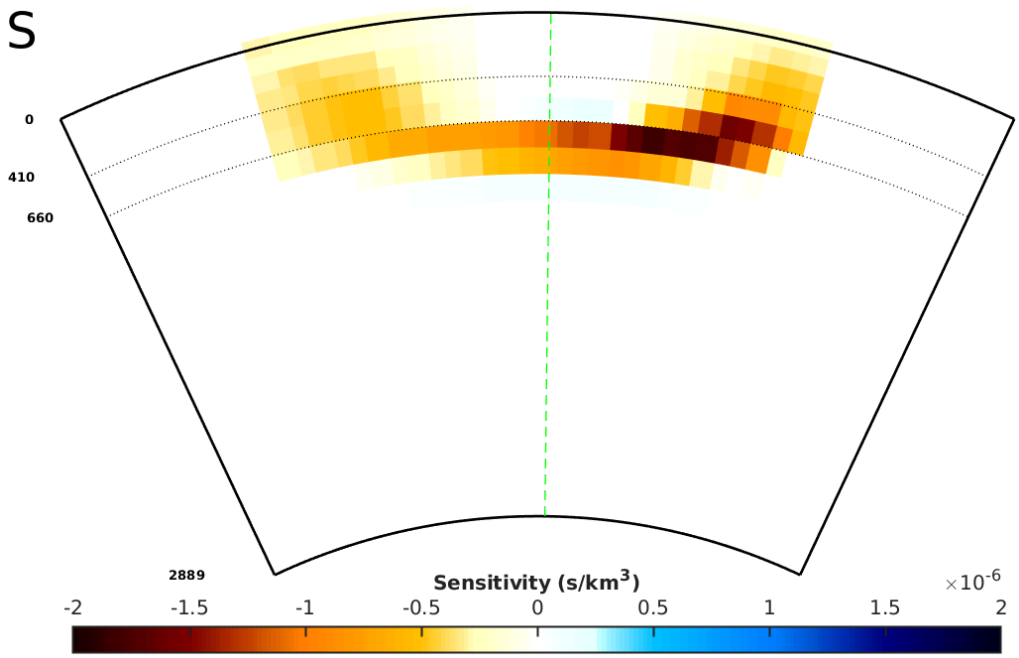

Figure III.16 – S-wave sensitivity kernel projected on the mesh computed for an epicentral distance of 32°, a depth of 208 km and a period of T=22.5 s. Dotted lines are the 410 and 660 discontinuities. Green line indicates the mid distance.

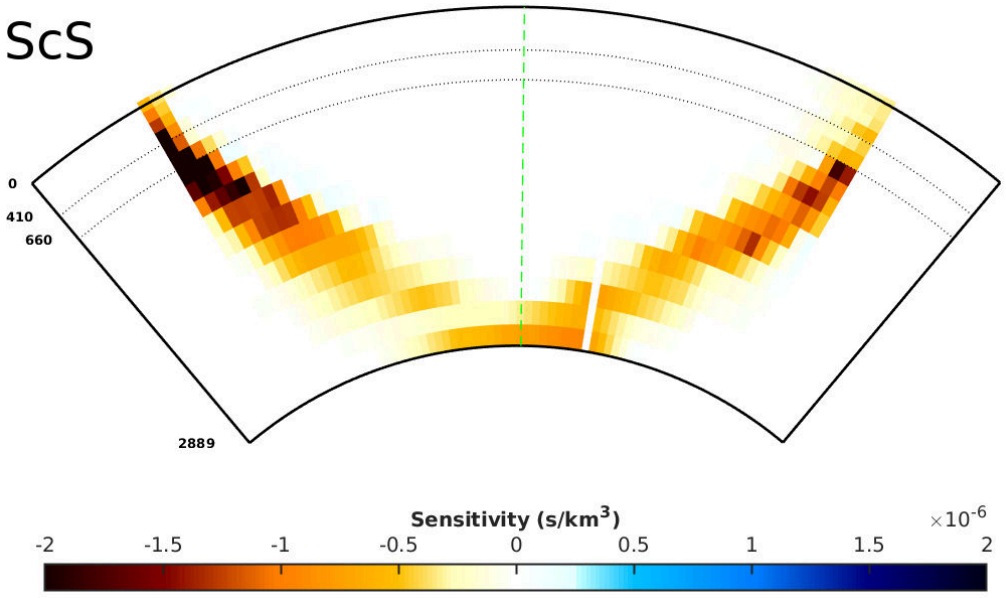

Figure III.17 – ScS-wave sensitivity kernel projected on the mesh computed for an epicentral distance of 64°, a depth of 12 km and a period of T=22.5 s. Dotted lines are the 410 and 660 discontinuities.

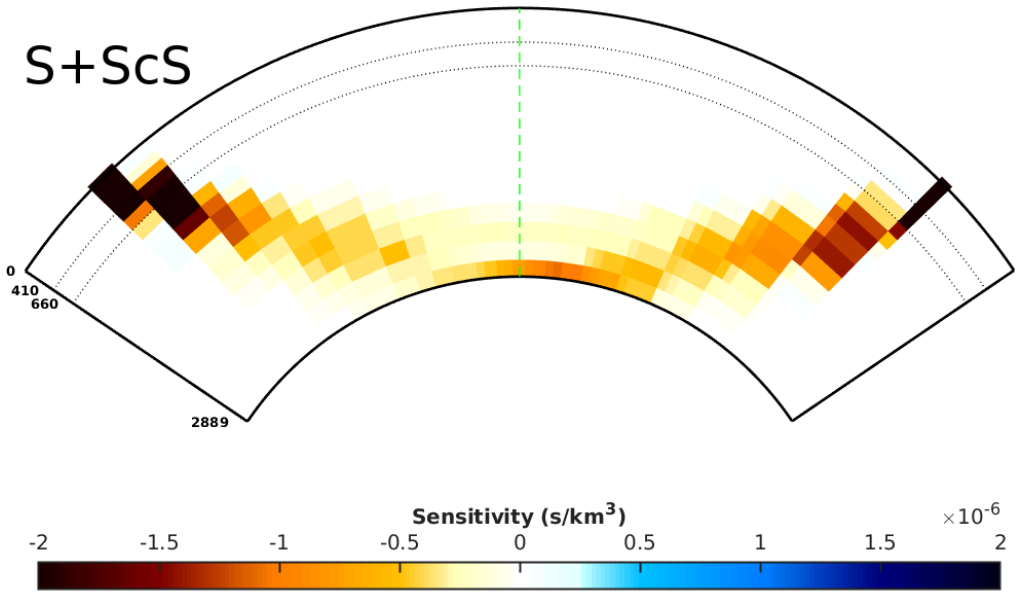

Figure III.18 – S+ScS interference sensitivity kernel projected on the mesh computed for an epicentral distance of 92°, a depth of 12 km and a period of T=22.5 s. Dotted lines are the 410 and 660 discontinuities.

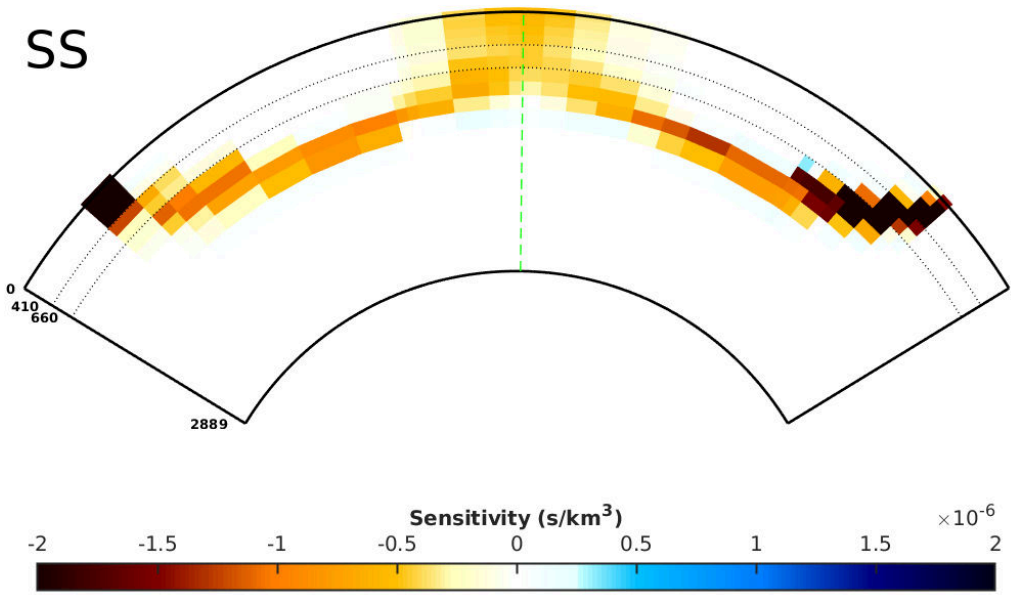

Figure III.19 – SS-wave sensitivity kernel projected on the mesh computed for an epicentral distance of 120°, a depth of 15 km and a period of T=22.5 s. Dotted lines are the 410 and 660 discontinuities.

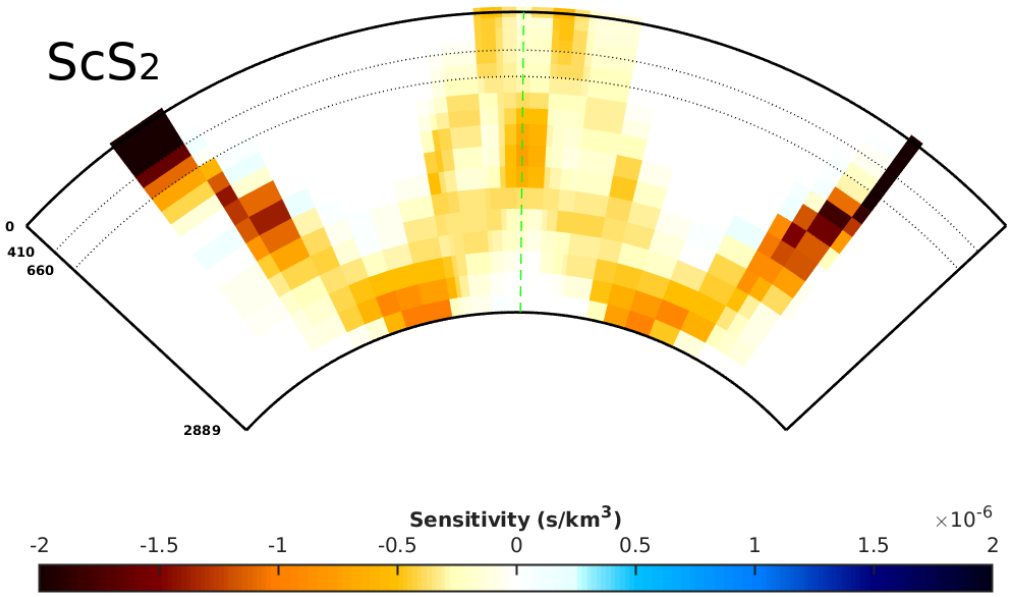

Figure III.20 – ScS_2-wave sensitivity kernel projected on the mesh computed for an epicentral distance of 74°, a depth of 15 km and a period of T=22.5 s. Dotted lines are the 410 and 660 discontinuities.

In short

- *Body-data are composed of time-residuals measured by cross-correlation at different periods, normal modes data are structure coefficients derived from the literature.*
- *Body-wave data coverage is mainly improved by the measurements of* ScS_2 *waves and interferences between S and ScS waves.*
- *Though precise sensitivity kernels are computed for the different seismic phases these ones have to be projected on a mesh and thus are degraded in details.*

Chapter IV

Global finite-frequency S-waves delay times: how much crust matters

Chapter IV

Global finite-frequency S-waves delay times: how much crust matters

Foreword

Common body-wave data corrections need to be applied to our new shear-wave time-reisuals databse. These corrections are essential to produce unbiased tomographic images. Some of those corrections are regularly applied in the community, such as the ellipticity or topography corrections. In this part we study in more details the crustal corrections applied to finite-frequency shear-waves time-residuals in global tomography. The finite-frequency signal coming from the mantle can be contaminated by finite-frequnecy signals coming from the crust. We study the deep influence of these crustal effects all over the globe and thus for various geological settings. The following chapter constitutes an article published in GJI in may 2019 (Dubois et al., 2019).

Abstract

We investigate the influence of crust on time residual measurements made by cross-correlation in the 10–51 s filtering period range on a global scale, considering two crustal models: CRUST2.0 and CRUST1.0. This study highlights, in a quantitative way, crust-related time corrections. One part of this correction is directly linked to the body wave travel time through the crust as predicted by the ray theory, whereas a second part is related to interferences with multiple crustal reflections. crustal seismic phases. This second component, called finite-frequency crustal correction, is frequency-dependent unlike the ray-theory based correction. We show that if this frequency-dependent crust-related correction is not taken into account in cross-correlation measurements, it may lead to a dispersive effect in S-wave delay-times that could ultimately bias tomographic models. On average, this finite-frequency correction increases with the filtering period. Comparisons between the two crustal models highlight the significant dispersive effect of the crust, which has complex patterns depending on geological contexts, with an important role of the sediment thickness. Although ray crustal corrections remain important, finite-frequency crustal effects may lead to a bias in measurements if not properly taken into account; on average they may reach 0.9–1.6 s for CRUST2.0 and 0.5–1.6 s for CRUST1.0, for period ranging from 10–51 s, respectively.

IV.1 Introduction to crustal correction for teleseismic S-wave

Body-wave seismic tomography allows to detect seismic heterogeneities into the Earth's interior induced by potential thermal and/or chemical anomalies. For several years, body-wave measurement methods in seismology have evolved from first-onset picking to time residual estimation by cross-correlation techniques. Cross-correlation operator estimates the similiarity between two different waveforms, such as between a synthetic seismogram and an observed one at different time-lags. Now the cross-correlation is widely used to estimate the time-shift between two waveforms in ray-theory (RT) (e.g., Ritsema et al., 2011) as well as in finite-frequency (FF) tomography (e.g., Sigloch and Nolet, 2006; Nolet et al., 2008; Hosseini and Sigloch, 2015; Zaroli et al., 2015; Kolstrup and Maupin, 2015), in particular for its robustness. The improvement brought by cross-correlation in travel-time measurements allows to investigate Earth's structure more accurately (e.g., Woodward and Masters, 1991a,b; Masters et al., 1996; Montelli et al., 2004; Hung et al., 2004; Montelli et al., 2006; Yang et al., 2006; Zaroli et al., 2015) and to refine hypocenter location for earthquakes (e.g., Shearer, 1997; Schaff et al., 2001). Cross-correlation measurements give much better results than picking, especially for S-waves which are often faded by P-waves coda (e.g., Schaff and Waldhauser, 2005).

In global mantle tomography we aim at imaging elastic heterogeneities in the mantle. Therefore, we would like to get rid of crustal signals since the crust is probably the most heterogeneous region of the Earth. Besides all seismic waves have to travel through the crust at least once before being recorded at a seismic station. Consequently the crust may have a significant influence on all travel-time measurements (Bolton and Masters, 2001; Nolet et al., 2008). The crustal structure may be known from local studies such as surface wave tomographies or seismic surveys. It is therefore possible to apply crustal corrections to travel time measurements (Nolet et al., 2008). Another way to overcome the problem of crustal influence is to work with differential traveltimes measurements Pdiff-PKP (e.g., Kárason and van der Hilst, 2001). They may be used to reduce the sensitivity around the source and receiver locations. When a seismic phase crosses the crust, reflections and conversions occur at the interfaces of the different crustal layers. These reflected/converted phases will reach the seismometer just after the main phase and may arrive close enough to be included in the time window used for the cross-correlation. Hence, all seismic waves experience waveform distortions produced by crustal reverberations. These interferences between crustal phases and the target seismic phase depend on the crustal structure and the dominant period used to filter seismograms (e.g., Ritsema et al., 2009). To our knowledge, a few previous studies have investigated these crustal effects on "broad-band" filtered seismic waveforms (usually the 2–50 s period range for S-waves) (e.g., Fukao et al., 2003; Obayashi et al., 2004; Yang and Shen, 2006; Ritsema et al., 2009; Kolstrup and Maupin, 2015; Obayashi et al., 2017). Moreover, some of them investigated crustal reverberations in specific geological contexts, like oceanic domain (Yang and Shen, 2006; Obayashi et al., 2017), or South Scandinavia (Kolstrup and Maupin, 2015), what may limit the assessment of crustal reverberations, and their effect on seismic data for other geological settings.

In the context of multiple-frequency seismic tomography, time residuals measured at different periods correspond to different sampling of the Earth's interior and they are expected to better constrain multi-scale seismic heterogeneities. We aim at investigating narrow-band filtered seismic waveforms to assess the crustal contribution at different frequencies. Our goal

is to show how much crust matters in cross-correlation S-wave time residuals on a global scale, including different geological settings.

The full shape of a seismic phase matters when measuring by cross-correlation (Dahlen et al., 2000). Therefore, it is essential to properly model crustal phases (CP) in seismograms in order to have an adequate frequency-dependent crustal time residual corrections (e.g., Ritsema et al., 2009; Zaroli et al., 2010; Kolstrup and Maupin, 2015). Otherwise one could interpret finite-frequency crustal signals as mantle-structure related anomalies . Off course, the ray-theory based correction must still be applied, but an additionnal correction is needed to take into account the variable sensitivity of finite-frequency body waves to the crust. Crustal reverberations are of first importance at low frequencies (Obayashi et al., 2004), and their influence increase with period. However, even when measuring travel-times by cross-correlation for RT tomography purposes, one has to take into account these crustal effects as well. Indeed, crustal phases can distort the waveform and thus ultimately impact the measured time residuals.

Since we are going to quantitatively evaluate the impact of crustal effects on teleseismic time residuals, one needs a crustal model. In an ideal world, we could find a good description of the geology and geotechnical features of the soil below all stations. But this cannot be systematically done due to economic or technical reasons. Off course, if an accurate crustal model under each station is available, one should used it to simulate crustal influence in synthetics. But in our global context we have to choose a 'not-too-bad' crustal model to simulate the effect of the crust. We investigate two global crustal models to infer crustal contribution on time residual measurements: CRUST2.0 (Bassin et al., 2000) and CRUST1.0 (Laske et al., 2013). Comparison of these two models may prove to be interesting since they show large structural differences (not only in terms of resolution) and they are among the most used crustal models in global tomography. However, these two models are only approximations of the 'true' Earth's crust. Different crustal models will induce differences on time residual measurements. These differences could be an indication of crustal model uncertainties to be taken into account in global tomographic inversions.

The purpose of this study is therefore to quantitatively estimate the dispersive effect of crust at global scale for these two selected crustal models. We present in a first part how synthetic seismograms are created and which seismic phases are measured. Then we introduce a two-components crustal correction which consist in a ray-theory and a finite-frequency part. We will analyse different factors influencing this "finite-frequency" correction such as sediment thickness. Finally, we show that the finite-frequency part of the correction cannot be neglected compared to the ray-theory part. Except for Obayashi et al. (2004, 2017), previous studies, aiming at correcting those crustal finite-frequency effects, have used a synthetic pre-computed correction and applied it after the measurement process (e.g., Hosseini and Sigloch, 2015). We quantitatively show that a better way to deal with crustal FF effects is to include crustal multiples directly in synthetics before the measurement process. We also show that this can be done with ray-theory based softwares at very low computationnal cost.

IV.2 Synthetic and observed data

The dispersive effect of the crust is explored, first by synthetic experiments at global scale to show the influence of crustal phases on time residuals in different crustal configurations. It allows to understand in a consistent way the crustal phase effects. Then, from a more tomographic point of view, we consider these synthetic examples at real station locations and compare them with observed data. We show in this section how synthetic seismograms are computed and how specific crustal seismic phases are selected. For this purpose, we consider shear waves with specific paths such as S, SS, ScS (shear waves reflected at the core-mantle boundary), ScS_2 (twice core reflected shear waves) and interferences between S and ScS at large epicentral distances.

IV.2.1 Synthetic data

Green's functions are computed with the Chapman's WKBJ code (Chapman, 1978). As inputs, we use the global centroid moment tensor information (Ekström et al., 2012; Dziewonski et al., 1981) and IASP91 (Kennett and Engdahl, 1991) as a 1D reference velocity model. Attenuation corrections have been added by using the Q-model of PREM distributed with the raydyntrace code (Tian et al., 2007a). Two different crustal models are considered: CRUST2.0 (Bassin et al., 2000) and CRUST1.0 (Laske et al., 2013). CRUST2.0 is a 7-layers model (ice, water, 2 layers of sediments and 3 layers of crystalline crust) whereas CRUST1.0 is a 8-layers model (same as CRUST2.0 but with an additional sediment layer). CRUST1.0 and CRUST2.0 are specified on a $1^\circ \times 1^\circ$ and $2^\circ \times 2^\circ$ grid, respectively.

To model FF effects from the crust, we generate crustal reverberations induced by impedance contrasts between crustal layers. We use the WKBJ algorithm which allows us to define every phases individually for a given earthquake-station pair and a crustal model. We only include crustal reverberations below the receiver in the synthetic waveform. We are able to model all crustal phases as in the case of reflectivity methods (Keith and Crampin, 1977). However some crustal phases do not influence time residuals measured by cross correlation because of small amplitude or arrival outside the time window selected for the cross-correlation. To save computational time, we select only crustal phases which have a significant impact on time residuals. For this selection, we cross-correlate two synthetics: one with the direct S wave, and the other containing the same S wave and all the associated crustal phases. Then we incrementally remove each crustal phase that do not change the time residual measured by cross-correlation by more than 0.1s. This test is done over several crustal structures independently for CRUST1.0 and CRUST2.0. Finally, we end up with a limited set of crustal phases to be systematically included into the synthetics; this set slightly differs for CRUST1.0 and CRUST2.0. This procedure ensures that all important phases are modeled, regardless of the crustal structure, while keeping a reasonable computational time. By doing that, we include in our synthetics the finite-frequency (FF) effects of the crust (which are not due to intrinsic attenuation).

It is important to notice that a cross-correlation time residual measurement is not only dependent on the Green function but also on the estimated source parameters, such as depth and source time functions (e.g., Hosseini and Sigloch, 2015). As we can note in Figure IV.1,

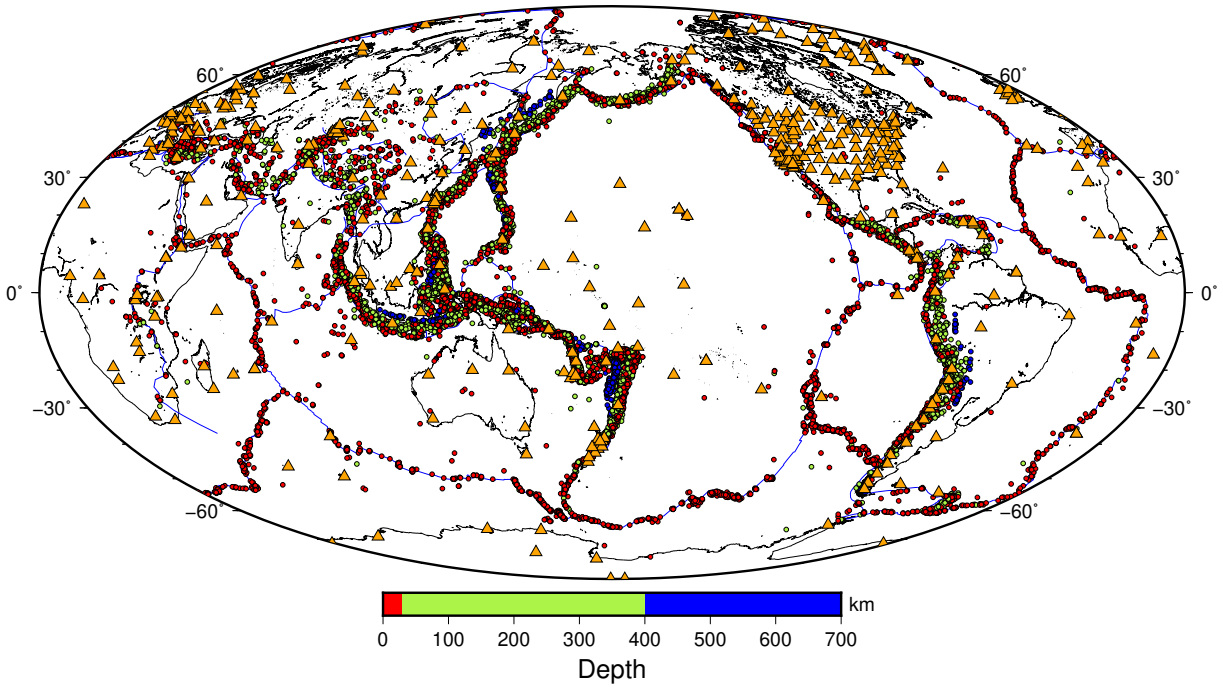

Figure IV.1 – Source-receiver distribution for the shear wave dataset: location of broad-band stations (orange triangles), and selected earthquakes with $5.5 < M_w < 6.5$ from the GCMT catalog (circles filled with depth-dependent colors). Color transitions are at 30km and 400km of depth. Borders of continental plates are indicated by a blue contour.

most of earthquakes are shallow events which implies to carefully take into account depth phase interferences. Therefore we model depth phases since it could substantially improve the fit between synthetic and observed waveforms (e.g., Sigloch and Nolet, 2006).

As an additional remark, finite element methods could also be used to compute synthetic seismograms but the crust must be carefully considered. In SPECFEM3D (e.g., Tromp et al., 2008), sediment layers with a thickness of less than a threshold (e.g., 2 km) are not considered, thus the meshing for some crustal configuration may miss features of crustal models. Besides, a smoothing is applied on the crustal model which could reduce impedance contrasts between layers and thus decrease the crustal phases impact. As a consequence, major crustal FF effects could be missing if the integration of the crust is not carefully handled in finite element methods.

IV.2.2 Observed data

Observed seismograms are retrieved from low noise stations to compare with synthetic seismograms. Stations are selected in order to find a good compromise between low noise levels stations and a good global coverage. We therefore select seismograms from 1976 to March 2017 from 27 networks. Figure IV.1 shows the location of stations and events used in this study. We only consider teleseismic earthquakes with magnitude between 5.5 and 6.5 and half-time duration lower than 6 s. This allows us to limit the complexity of the source and we can approximate the source time function by a Gaussian function for the purpose of

synthetic calculations (Zaroli et al., 2010). Waveforms and metadata are downloaded from IRIS facilities with the help of obspyDMT (Hosseini and Sigloch, 2017).

IV.2.3 Measurement process

We perform finite-frequency measurements on all retrieved seismograms relying on an automated code from Zaroli et al. (2010), which can easily be tuned for measuring specific seismic phases. We measure on five frequency bands: 10 s, 15 s, 22.5 s, 34 s and 51 s for a total number of measurements of 628,733. To face the increasing number of broadband seismometers, it is necessary to handle them in an automatic way. The measurement process can be divided in two main steps. The first one consists in finding the best time window around the target phases in the synthetic and the observed seismograms. The second one involves cross-correlation measurements at different periods using Gaussian filters between the synthetic and the observed seismogram over the previously defined time windows. In order to save memory space, we append to the measurement process the on-the-fly synthetics calculation.

IV.3 Crustal corrections

Crustal corrections can be divided in two parts: a ray-theory (RT) based correction and a finite-frequency (FF) correction. The RT correction is the ray travel-time acquired when traveling through the crust (under the infinite frequency approximation). RT correction takes into account crustal structure under source, receiver and bouncing points, this correction is frequency independent. The FF correction is due to crustal reverberations which disturb the waveform; this effect strongly depends on the filtering period. We only consider FF crustal effects on the receiver side (for technical reasons related to WKBJ synthetics).

We show in this section how much crustal corrections do matter for teleseismic finite-frequency time residual measurements.

IV.3.1 Crustal corrections modeling

IV.3.1.1 Ray-theory based crustal correction

The crustal correction based on ray theory is computed from the raydyntrace code (Tian et al., 2007a). It represents the ray travel-time difference between the crustal model (CRUST2.0 or CRUST1.0) and the crust of the 1D reference model (IASP91); it will be refered as $dt_{\mathsf{synth}}^{\mathsf{crust,\,RT}}$ (see Table IV.1 for a summary of the notations used). This correction is frequency independent. Figure IV.2 compares values of the RT crustal correction for CRUST1.0 and CRUST2.0 at each station. We notice a shift towards negative values for CRUST1.0 compared to CRUST2.0. This indicates that CRUST1.0 under stations is on average faster than CRUST2.0.

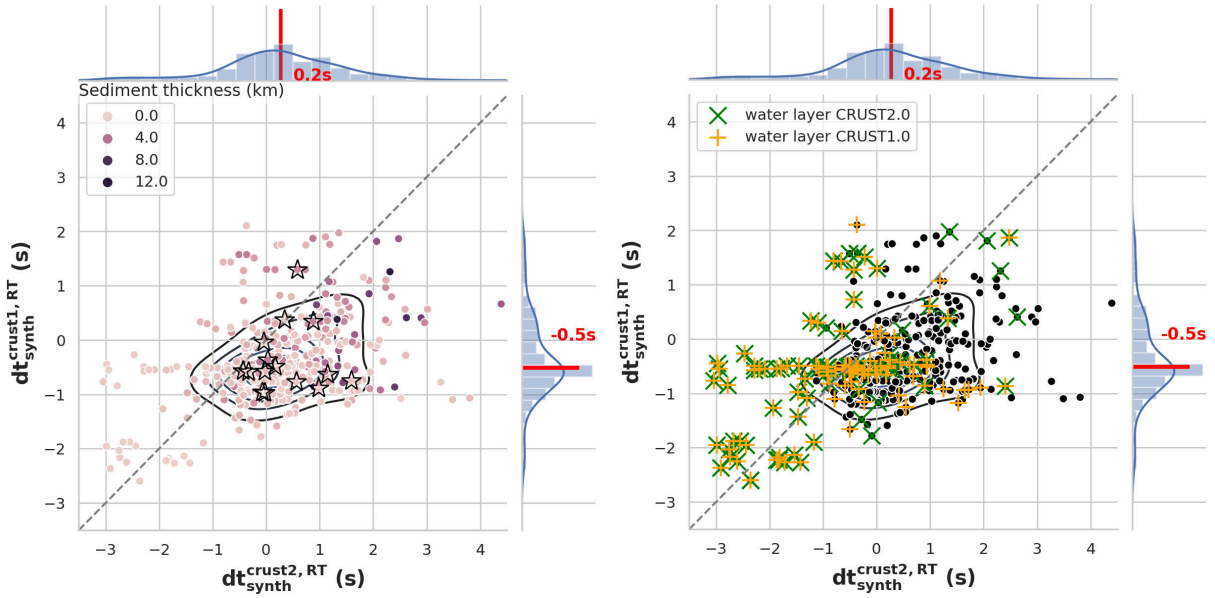

Figure IV.2 – Ray-theory based crustal corrections computed for all stations using CRUST1.0 and CRUST2.0, red bars on histograms indicate the distribution medians. (Left) Color scale represents the sediment thickness under each station in km (mean of CRUST1.0 and CRUST2.0), stations with ice layer are represented by black stars. (Right) Green and orange crosses indicate stations which have a water layer in CRUST2.0 and in CRUST1.0 respectively. We used the raydyntrace software (Tian et al., 2007a) to compute these corrections.

Crustal models have a limited resolution (1° for CRUST1.0 and 2° for CRUST2.0), thus about 22% of our stations have a water layer in their crustal models as we can see in Figure IV.2 (water layers have been removed for synthetic computation). Stations with green crosses indicate that continental stations are considered as oceanic (with a water layer) in CRUST2.0. Most of continental stations considered as oceanic are common for both crustal models. The number of stations with a water layer is larger for CRUST1.0 (107) than CRUST2.0 (87). At the bottom left corner, all stations have a water layer for both crustal models and a very thin sediment layer; these stations are set up on islands. Stations located at the top right corner of Figure IV.2 have high positive RT corrections and a thick sediment layer; they correspond to coastal stations where sediment thickness may be important. RT crustal corrections larger than 3 s for CRUST2.0 correspond to continental stations but with significant changes in elastic parameters or layer thicknesses compared to CRUST1.0. For example, the station GO02 (Chilean network, station with a RT correction for a S wave larger than 4 s for CRUST2.0) has a crustal thickness of 70 km for CRUST2.0 but only 40 km for CRUST1.0. Such crustal variations induce differences in the RT correction up to 4 s between CRUST1.0 and CRUST2.0.

IV.3.1.2 Finite-frequency crustal correction

The FF crustal correction arises from waveform distortions whereas RT crustal correction is a static shift of the main seismic waveform of interest. We define the finite-frequency crustal correction as the time residual measured between a synthetic seismogram with all relevant crustal phases and a synthetic without crustal phases. We can express this correction as:

$$dt^{\text{crust, FF}}_{\text{synth}}(T) = t^{\text{CP}}_{\text{synth}}(T) - t^{\text{NCP}}_{\text{synth}}(T) \tag{IV.1}$$

Table IV.1 – Meaning of main symbols used in this study. All these symbols have seconds as physical unit.

Symbol	Meaning
$dt_{\text{synth}}^{\text{crust, RT}}$	ray-theory crustal correction computed for CRUST1.0/CRUST2.0 with raydyntrace
$dt_{\text{synth}}^{\text{crust, FF}}(T)$	finite-frequency crustal correction for CRUST1.0/CRUST2.0 computed by cross-correlating two synthetics (with and without crustal phases) filtered around the period T
$\Delta dt_{\text{obs}}^{\text{crust, FF}}(T)$	finite-frequency crustal correction for CRUST1.0/CRUST2.0 model estimated on observed data by taking the difference between time-residuals measured with and without crustal phases, filtered around the period T
$dt_{\text{obs}}^{\text{CP}}(T)$	time-residual measured between a synthetic and an observed data by including crustal phases (CP) in synthetics, filtered around period T
$dt_{\text{obs}}^{\text{NCP}}(T)$	time-residual measured between a synthetic and an observed data without including crustal phases (NCP) in synthetics, filtered around the period T

where CP refers to synthetics modeled with crustal phases, and NCP refers to synthetics computed with no crustal phases and T is the central filtering period at which we measure a time residual by cross-correlation. Figure IV.3 shows an example of the importance of taking into account crustal phases in time residual estimations at different periods. We cross-correlate two synthetic seismograms: one composed of the S-wave alone (black waveform) and one composed of the S-wave with all relevant crustal multiples (blue waveform), broadband filtered between 7–81 s. Off course we add supplementary reflections for CRUST1.0 model to handle the additionnal sediment layer. In Figure IV.3a, the dispersion curve shows time residuals measured at different periods with their error bars, as a remark, error bars are not always smaller at long periods than at short periods. There is a clear decreasing trend which is present at almost all stations. For this particular example, there is a difference of 1.8 s between measurements made at 10 s and at 51 s period. If not corrected from the crust, this difference between time residuals measured at two different periods would be considered as mantle-structure related dispersion. One can note that broadband measurement in Figure IV.3b shows a time-shift of -0.4 s between the two waveforms ($dt_{\text{BB}} = -0.4\,\text{s}$). Figure IV.13 shows another synthetic example of the influence of crustal phases on time residual estimation in a different geological context without sediment layers.

For the purpose of better understanding the crustal structure influence over time residuals measurements, cross-correlations of S waves alone and S waves with crustal phases are made over each cell of crustal models. Figure IV.4 presents global time residuals measured at 22.5 s period between an S-wave alone and an S-wave with crustal multiples for CRUST1.0, on a $1^\circ \times 1^\circ$ grid. We use a year of seismicity and model S waves as well as ScS waves

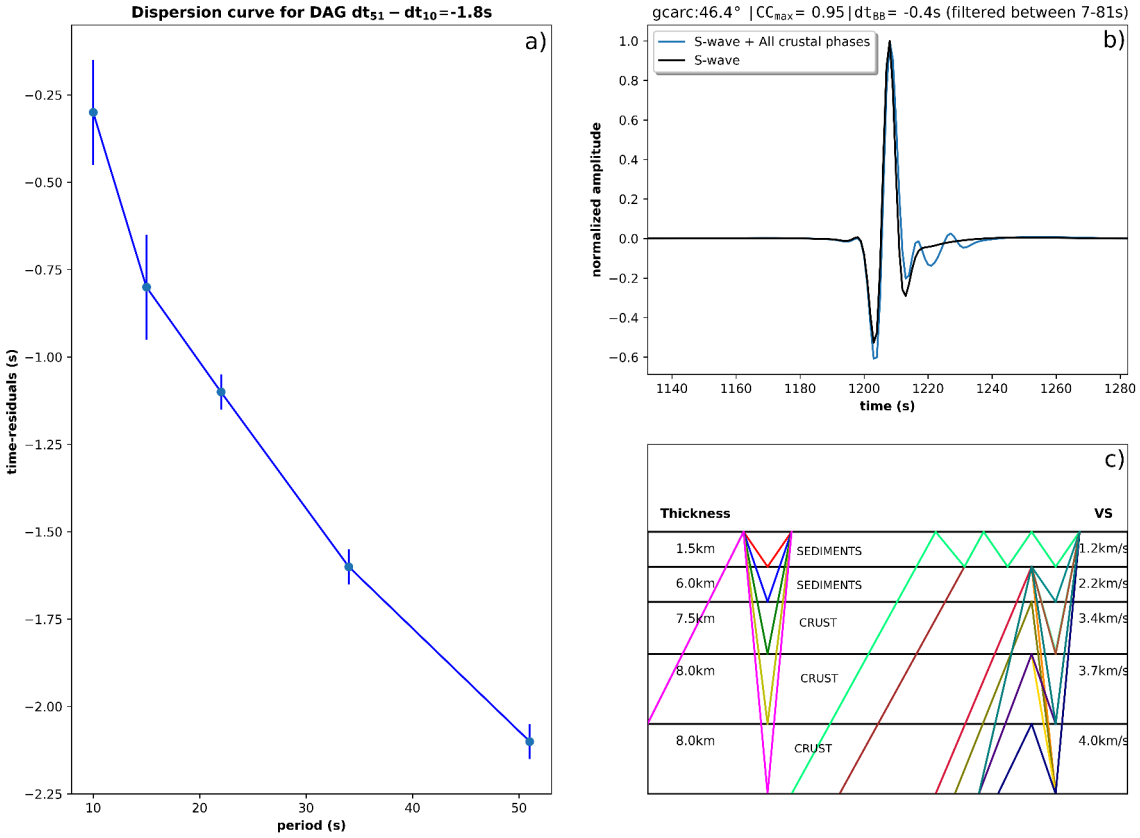

Figure IV.3 – (a) Dispersion curve for time residuals measured at 10 s, 15 s, 22.5 s, 34 s and 51 s. Error bars are estimated by using the method of Chevrot (2002). If the error is smaller than 0.1s we set a minimal error. (b) Waveforms computed for a S-wave alone (black) and a S-wave + crustal phases (blue) recorded at DAG station for the same event, waveforms are filtered between 7–81 s. (c) Crustal model under the DAG station from CRUST2.0 with a schematic representation of modeled crustal phases. Crustal multiples are split into two groups for clarity.

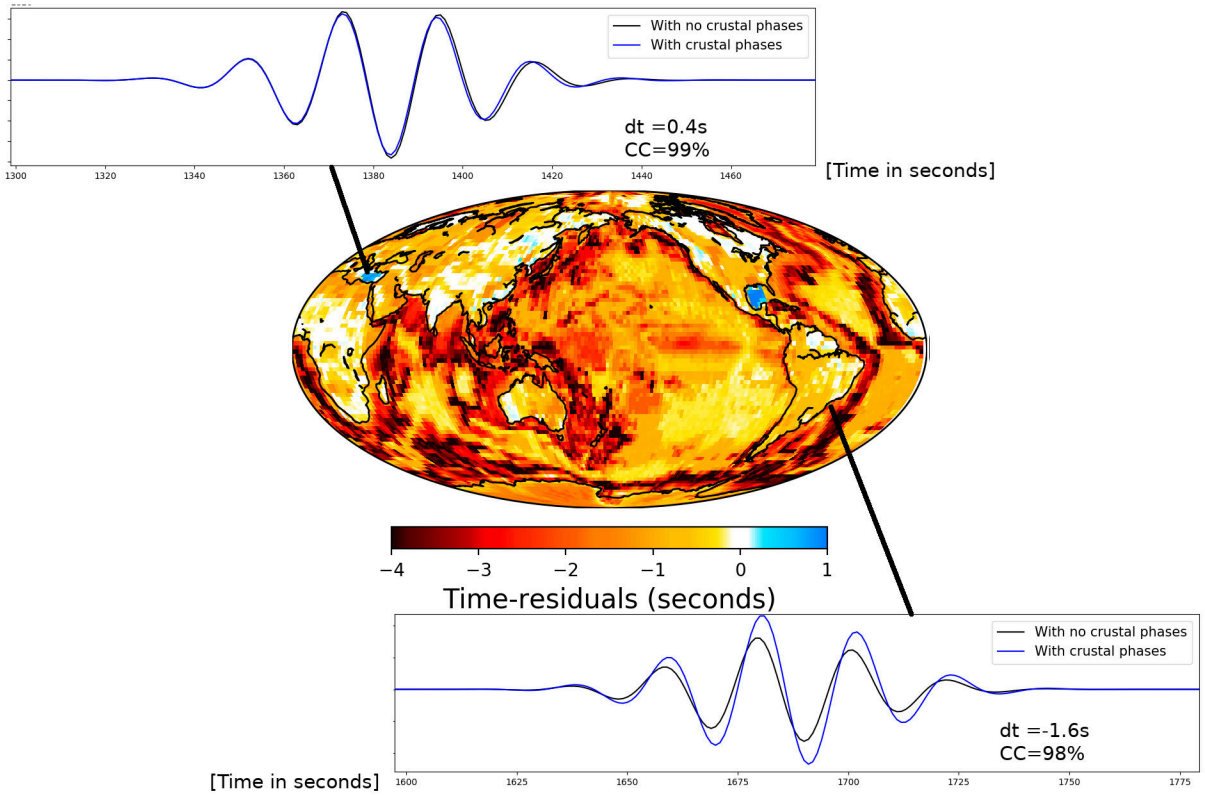

Figure IV.4 – S-wave mean time residuals on a $1° \times 1°$ grid measured by cross-correlating synthetics with and without crustal phases filtered at 22.5 s for CRUST1.0 model ($dt^{\text{crust1, FF}}_{\text{synth}}\,(22.5\,s)$). We modelled S, sS, ScS and sScS for epicentral distances from $30°$ to $95°$, one year of seismicity (with $5.5 < M_w < 6.5$) has been used to generate the whole data set. Seismograms show how the crustal phases can have an advancing or delaying effect on time residuals measured by cross-correlation.

to investigate epicentral distances between $30°$ and $95°$. For these measurements, we apply the same workflow as for observed data. First we can note a clear bias towards negative time residuals and so a clear non-zero mean for FF crustal corrections. We show waveforms filtered at 22.5 s including or not crustal phases (blue and black curves respectively) in two different crustal configurations. According to the location, synthetics with crustal phases may significantly be different from synthetics without crustal phases. Besides, crustal phases can have a delaying or an advancing effect on the time residual measured by cross-correlation, depending on the local crustal structure.

Figure IV.5 compares FF crustal corrections between CRUST1.0 and CRUST2.0 at every station filtered at 22.5 s period. Although median values of FF crustal corrections are similar for CRUST1.0 and CRUST2.0, one sees that FF crustal corrections for CRUST1.0 are much more dispersed (between 0.3 s and -5.2 s) than for CRUST2.0 (between 0 s and -3.3 s). Most stations for CRUST1.0 with large negative FF correction (lower than -1.5s) have a water layer in their crustal model. Variability of FF corrections for CRUST1.0 is mainly noticeable for insular or coastal stations. For coastal stations which have a water layer we could take the closer continental crust from this station, though we cannot ensure the reliability of this crust model neither. Besides the problem is still present for insular stations, where taking the closer continental crust does not mean much especially for volcanic islands. On the left side of Figure

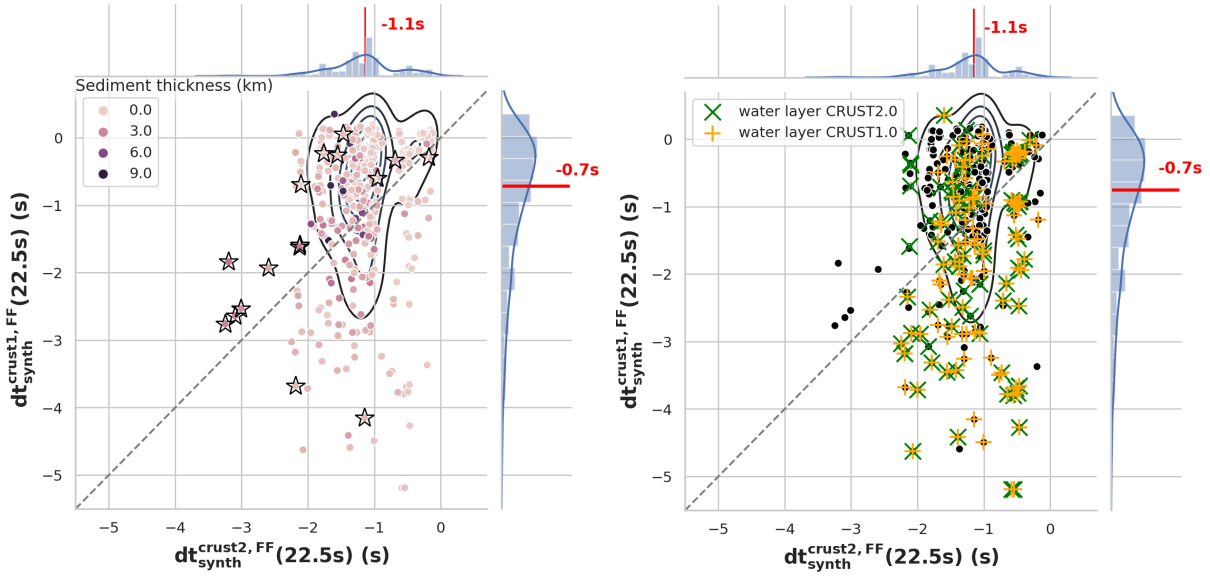

Figure IV.5 – FF crustal corrections computed for each station with CRUST1.0 and CRUST2.0, red bars on histograms indicate the distribution medians. (Left) Color scale represents the sediment thickness under each stations in km (mean of CRUST1.0 and CRUST2.0), stations with ice layer are represented by black stars. (Right) Green and orange crosses indicate stations which have a water layer in CRUST2.0 and in CRUST1.0 respectively.

IV.5, five stations have FF crustal corrections lower than -2.2 s for CRUST2.0; they correspond to inland Greenland stations and the Concordia station (in Antarctica).

Continent-ocean contrast is much more important for CRUST1.0 than CRUST2.0 (see Fig. IV.6). Mean time residuals for CRUST1.0 are more dispersed than those for CRUST2.0, differences are however less striking and more comparable for continental values. For CRUST2.0, deep oceanic regions seem less highlighted than margins and regions where sediment thicknesses are large. This feature is emphasized for CRUST1.0 model where time residuals reach -2 s at margins. Some continental regions in CRUST1.0 almost have a zero mean which implies no FF influence from the crust, only the RT correction needs to be applied. Zero-mean regions seem to be correlated with specific geological settings such as old shields and orogens (India, North-West Canada, Scandinavia) with large crustal thickness and no low-velocity layers. This is in agreement with observations made by Kolstrup and Maupin (2015) in the Scandinavia region.

We show in Figure IV.6 the sediment thickness for CRUST1.0 and CRUST2.0 aside with associated FF crustal corrections. At 22.5 s, larger values of FF crustal corrections in oceanic regions are not directly correlated to large sediment thickness but rather to the borders of thick sediment piles (light blue/green colors). There is no direct correlation because FF crustal effects depend on both crustal structure and the main frequency content of the wave. Indeed at low frequencies high negative values for FF crustal corrections can be seen on regions with various sediment thicknesses (see evolution of worldmap colors as function of period in Fig.IV.18). For a filtering period of 22.5 s, crustal phases generated by very thin layers with high velocities will arrive simultaneously with the main phase and so the shape of waveform will not be disturbed (only its amplitude). Crustal phases from thick layers with low velocities will arrive much later than the main phase and will not influence its waveform. The complex

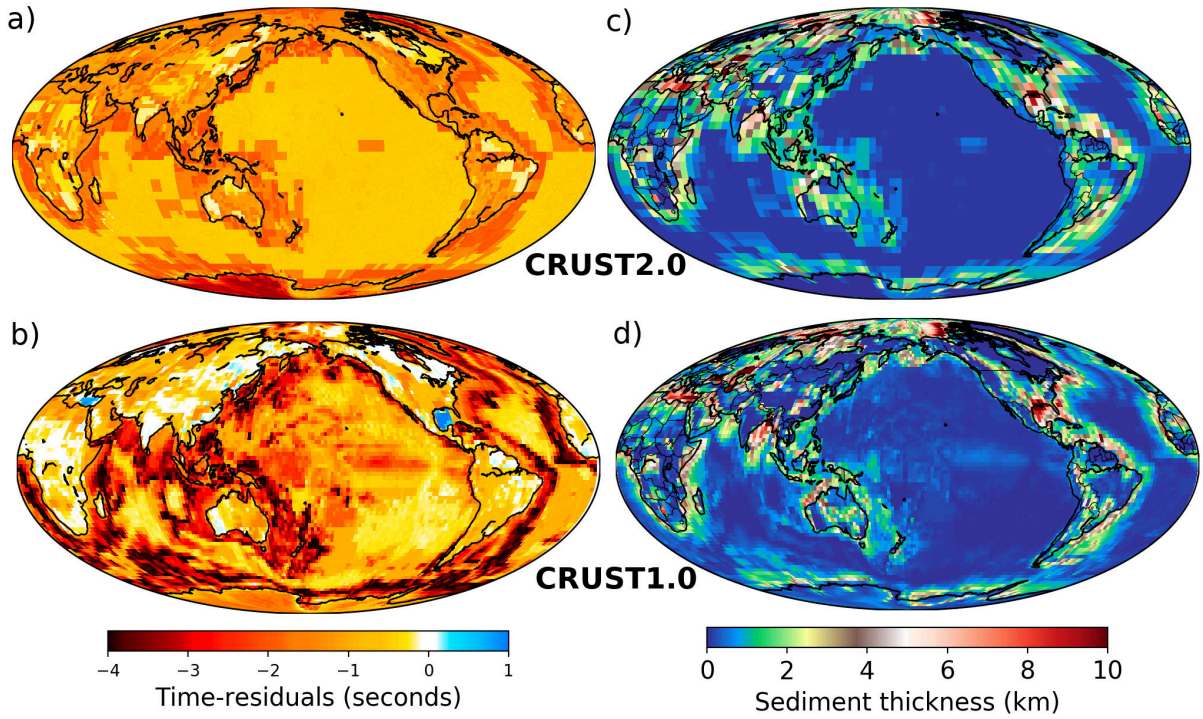

Figure IV.6 – (a,b) S-wave mean time residuals measured by cross-correlating synthetics with and without crustal phases filtered at 22.5s for (a) CRUST2.0 model ($dt_{\text{synth}}^{\text{crust2, FF}}(22.5s)$) on a $2° \times 2°$ grid, (b) CRUST1.0 model ($dt_{\text{synth}}^{\text{crust1, FF}}(22.5s)$) on a $1° \times 1°$ grid. (c, d) Sediment thickness (including ice layer) for CRUST2.0 and CRUST1.0 respectively.

combination of layer thicknesses and elastic impedance contrasts makes it difficult to interpret variations of FF crustal effects over various geological settings. Since low frequency filtering broadens waveforms, crustal phases are more likely to interfere with the target waveform. Measurements made at low frequency are thus more affected by crustal reverberations than at high frequency.

Recent studies underline the fundamental effect of sediments, i.e., low-velocity layers, on FF crustal effects (Kolstrup and Maupin, 2015). For the Scandinavia region they point out large FF effects when low-velocity sediment layers are under stations; but they also show no significant FF effects for crustal thickness variations. Here, we would like to further assess the FF crustal effects as a function of sediment thickness when considering various specific regions. Figure IV.7 aims to show the effect of sediment thickness on finite-frequency crustal corrections at different periods for all stations. Sediment thickness is the sum of the sediment layers and of the ice layer. At first sight, correlation between sediment thickness and FF crustal corrections is not straightforward. Off course, variability in time-residuals reflects the complexity of CRUST1.0. Nevertheless, we can notice that as we increase the filtering period, FF crustal corrections ($dt_{\text{synth}}^{\text{crust1, FF}}(T)$) increase in absolute value (also clearly visible in igures IV.16-IV.18) which supports observations made by Obayashi et al. (2004) on the importance of crustal phases especially at low frequency. Besides, as we move towards lower frequencies the range of sediment thicknesses with large time residuals broadens. This is coherent with geographical information in Figure IV.18 where at low frequency high negative time residuals are correlated with various sediment thicknesses and therefore cover a wider geographical area. Moreover, one can note the presence of a decreasing trend for stations with thin crustal thickness (yellow dots). This quasi-linear trend (see Figure IV.15) appears for stations with

sediment thickness between 0.5 and 1.5 km and very thin crustal thickness (< 12 km). The effect of sediment thickness is maximal for low frequency waves (T=51s) and disappears at high frequency (T=10 s), since all crustal phases do not interfere with high frequency waves. Stations with thin oceanic crust seem to be more influenced by sediment thickness compared to other stations. In Figure IV.15, one clearly sees the strong increase of FF crustal effects when sediment thickness increases. It is however difficult to state that FF crustal correction is clearly correlated to sediment thickness for non-oceanic stations. As we can see, sediment thickness is not the only critical parameter. Thickness and velocity parameters control the time arrival of crustal phases, while elastic impedance contrasts rather control the amplitude of crustal phases. That is why relevant crustal phases arrive in a specific time range, after the main phase, with large amplitude (high energy) to truly disturb the main seismic waveform. These conditions make FF crustal corrections not straightforward to estimate a priori (e.g., Kolstrup and Maupin, 2015) and in any case only dependent on sediment thickness but on the whole crustal structure (see example of Gulf of Mexico in section 3.2.2).

IV.3.1.3 Ray-theory versus finite-frequency crustal corrections

Figure IV.8 shows synthetic FF corrections versus RT corrections for all stations for CRUST2.0 (blue) and CRUST1.0 (red). These corrections are plotted in absolute value for periods 10, 15, 34 and 51 s ($|dt^{\text{crust, FF}}_{\text{synth}}(T)|$). We see that dispersion in FF correction increases with the period, while RT correction remains constant for all periods. Geological setting under stations (thicknesses and shear-wave velocities in layers) are the only cause for the variability in RT corrections as they are independent of the filtering period. Medians of FF crustal corrections for CRUST2.0 are always larger than for CRUST1.0, but variability of FF corrections is larger for CRUST1.0 than CRUST2.0. As we can see, CRUST2.0 has medians for FF crustal effects always very different from RT crustal corrections at all periods compared to CRUST1.0. We can note that some points outline horizontal or vertical lines. Some of these lines can be linked to stations with common features such as without sediment layers: see dots around 0.5 s for FF delay with CRUST2.0 (Figure IV.8a). It is however complex to relate each line to a specific set of stations especially when period increases.

Since the crustal correction is composed of two terms; i.e., ray-theory crustal correction and finite-frequency crustal correction, we can assess the total crustal contribution to time residuals measured at different periods. For a S-wave, the mean and the standard deviation of the crustal correction at 10 s period are 0.7 s $\pm$ 1.1 s for CRUST2.0 and 0.9 s $\pm$ 1.0 s for CRUST1.0. For a period of 51 s, the mean and the standard deviation are 1.4 s $\pm$ 1.1 s for CRUST2.0 and 2.1 s $\pm$ 1.8 s for CRUST1.0. Therefore, crust may induce effects of mostly the same order of magnitude as for measured time residuals.

IV.3.2 Finite-frequency crustal effects estimated from observed data

We show in this section how FF crustal corrections estimated from observed data are coherent with those obtained from synthetic experiments.

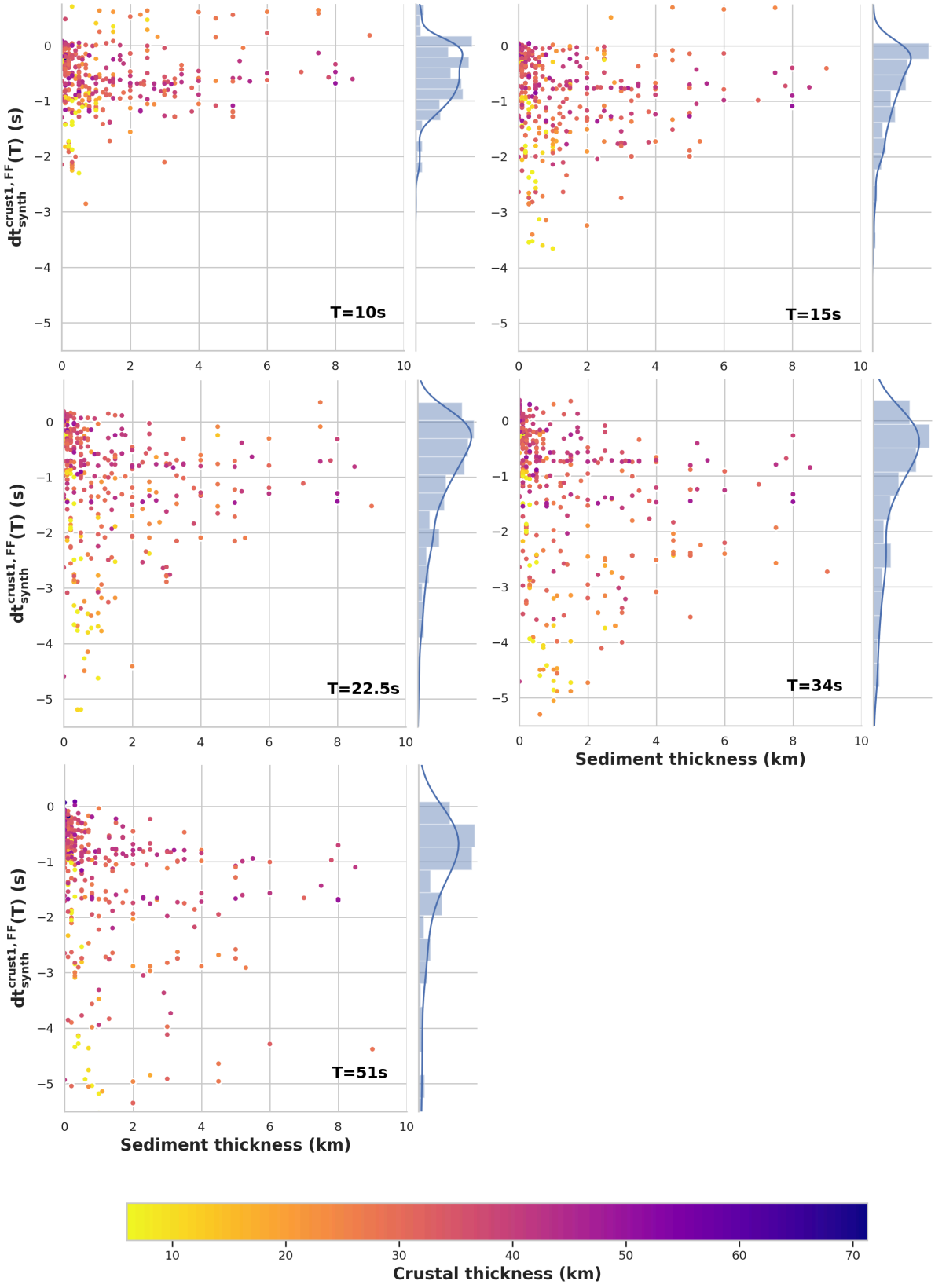

Figure IV.7 – FF crustal corrections as a function of sediment thickness at different periods (10 s, 15 s, 22.5 s, 34 s, 51 s) for CRUST1.0 model. Colour inside circles depends on crustal thickness (in km). Crustal thickness is the sum of sediment thickness with crystalline crustal thickness.

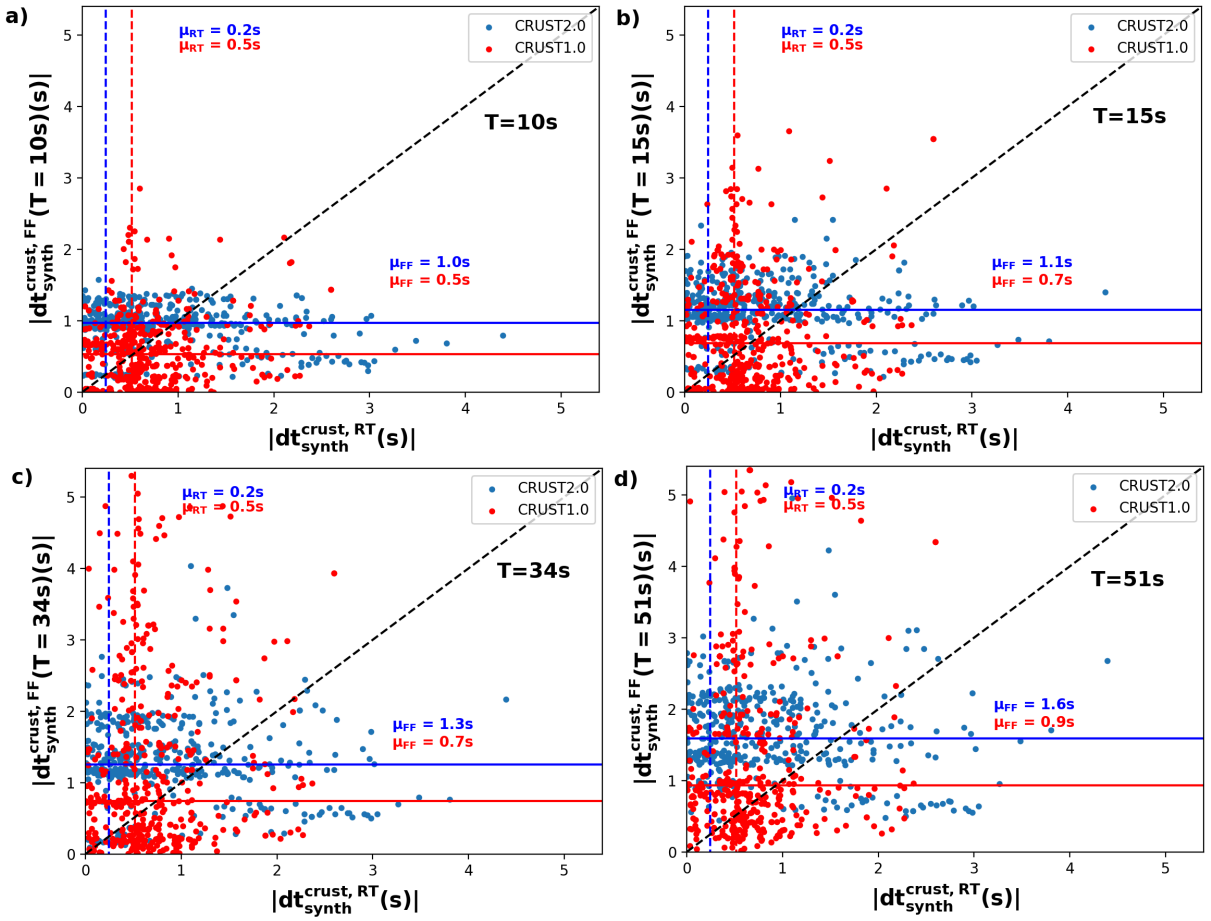

Figure IV.8 – Synthetic FF crustal corrections versus RT crustal corrections for CRUST2.0 (blue) and CRUST1.0 (red) plotted for all the stations. FF correction computed at (a) 10 s, (b) 15 s, (c) 34 s and (d) 51 s. Solid and dashed lines indicate medians of FF and RT crustal corrections respectively.

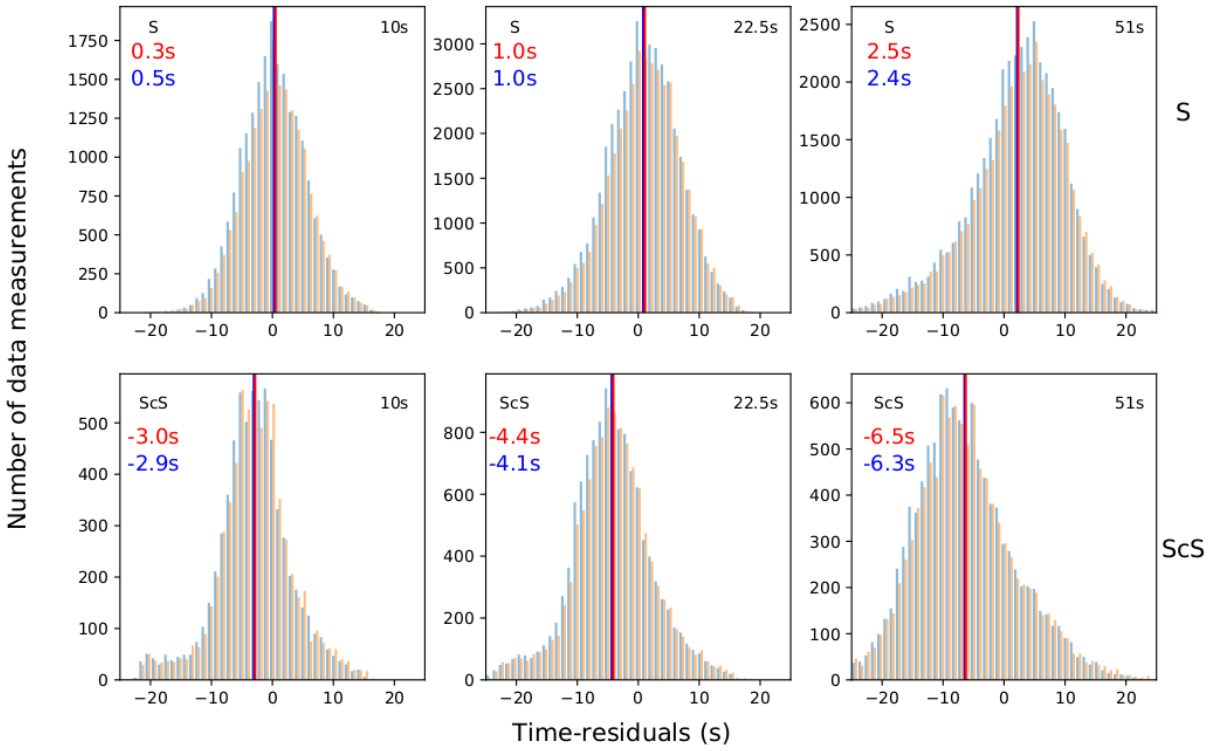

Figure IV.9 – Histograms of time residual measured at 10 s, 22.5 s and 51 s (from left to right) for S-waves (top row) and ScS-waves (bottom row). Blue and orange histograms are measurement distributions for CRUST2.0 and CRUST1.0 respectively. Blue and red vertical lines are the means of the distributions for CRUST2.0 and CRUST1.0 respectively. The total number of successful measurements with CRUST1.0 is of 602,252 and of 628,733 with CRUST2.0, however we keep common window selection parameters for both crustal models, these parameters have been set up from tests with CRUST2.0 only.

IV.3.2.1 Statistics on observed data

Fig. IV.9 shows histograms of measured S and ScS time residuals at 10 s, 22.5 s and 51 s central periods, including interferences with their depth phases (sS and sScS respectively) for both crustal models. S-wave time-residual histograms seems to be nearly gaussian distributed except at 51s where we can notice a strong asymmetry (long tail toward negative time residuals). Distributions for ScS-wave have heavy tails unlike the gaussian shape with noticeably asymmetry for 51s toward positive delays. These asymmetries for S and ScS waves at 51s could be due to their mutual interferences (at large epicentral distance); at short period these waves are less prone to interfere than at long periods.

We notice that time residuals measured for the two different crustal models are not so different on average. At 10 s period, we have a mean time-shift of 0.3 s for CRUST2.0 and of 0.5 s for CRUST1.0, and at 51 s we have 2.5 s and 2.4 s respectively. It is difficult to distinguish those two datasets processed with two different crustal models only based on histograms. However, measurements at specific stations can be significantly different between the two crustal models.

We are working with shear waves generated by earthquakes occuring at different depths. Therefore, for shallow depths it is impossible to measure S-wave alone since the arrival of the

depth phase (sS) is very close to the main phase (S). In these cases we measure S waves with their associated depth phases. We carry out the same statistics by keeping only deep events to get rid of depth phase interference problem. Except the number of measurements, time residual distributions for different periods are significantly the same as for Figure IV.9.

IV.3.2.2 Crustal phases impact on observed data

Figure IV.10 shows histograms of measurements and mean dispersion curves for S-wave and ScS-wave measurements (results for SS and ScS_2-waves are shown in Figure IV.14). On the bottom row of Figure IV.10, histograms represent the number of measurements obtained with and without crustal phases for CRUST2.0. We see for S and ScS waves, and at almost all periods, that we increase of measurements by including crustal phases in synthetic seismograms. This observation can be explained by a better fit between observed and synthetic waveforms when including crustal reverberations in the synthetic.

The top row of Figure IV.10 shows the mean of all our S and ScS dispersion curves for CRUST2.0 and CRUST1.0; dashed lines indicate dispersion curves when crustal phases are not taken into account in synthetics. First, we can notice a clear difference between curves with and without crustal phases which implies an influence of crustal phases on cross-correlation measurements. Inclusion of crustal phases for S and SS induces an important shift (downward) of dispersion curves, though it is weaker for ScS and ScS_2 (in particular with CRUST2.0).

For ScS measurements, crustal models are almost indistinguishable on dispersion curves. This may imply a strong influence coming from the lower mantle which overcomes the crustal influence. Time residuals in Figure IV.10 are corrected for dispersion induced by intrinsic anelastic attenuation assuming a frequency-independent quality factor Q. As a remark, one could also correct for a frequency-dependent quality factor and thus remove remaining dispersive effects observed on mean S-wave time residuals. Zaroli et al. (2010) show that it is possible to have an almost horizontal dispersion curve by tuning a parameter controlling the frequency dependency of the quality factor (at least for S and SS data).

IV.3.2.3 Estimations of finite-frequency crustal effects with observed data

We aim to extract the finite-frequency crustal effects from measurements derived from observed seismograms (Figure IV.11). Worldmap colors represent the synthetic FF crustal correction for CRUST1.0 and CRUST2.0 at 22.5 s period and colored triangles are the observed FF crustal effect extracted from measurements with observed data plotted at station locations. To estimate the FF crustal effect from observed data, we average for each station the time residual differences between measurements made by including or not crustal phases in synthetics, such as:

$$\Delta dt_{\text{obs}}^{\text{crust, FF}}(T) = dt_{\text{obs}}^{\text{CP}}(T) - dt_{\text{obs}}^{\text{NCP}}(T) \tag{IV.2}$$

with T the period at which the time residual has been measured. Thus we are trying to isolate the effect of crustal phases on time residuals on observed data. Figures IV.16 and IV.17 show results at different periods for CRUST1.0 and CRUST2.0, respectively. Most stations (triangle colors) indicate that time residuals measured by including crustal multiples are different from those measured without crustal phases (i.e. $dt_{\text{obs}}^{\text{CP}}(T) \neq dt_{\text{obs}}^{\text{NCP}}(T)$). FF

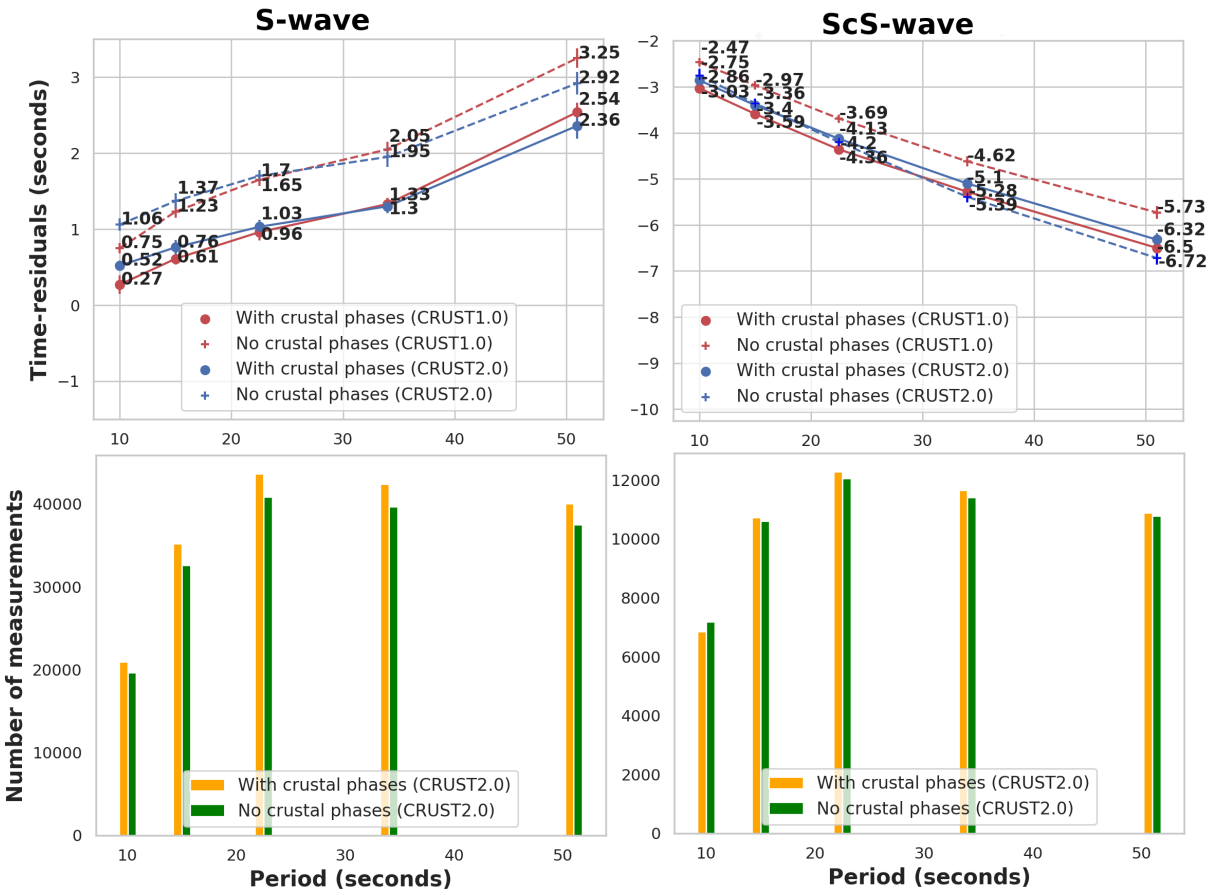

Figure IV.10 – (Top) S-wave and ScS-wave dispersion curves for two crustal models: CRUST1.0 (red), CRUST2.0 (blue). Solid and dashed lines are measurements made with synthetics computed with or without crustal phases respectively. (bottom) S-wave and ScS-wave measurement histograms for CRUST2.0: without crustal phases (green) and with crustal phases (orange). $1-\sigma$ error bars are determined by bootstrap technique and all time residuals have been corrected for intrinsic attenuation.

crustal corrections extracted from observed data are mostly negative which is consistent with FF crustal correction estimated from synthetics (see green dots in Fig. IV.11). We see that FF crustal corrections estimated from observed data are quite coherent with estimations from synthetics (follow the trend y=x). Although there are strong deviations for some stations, the global pattern is coherent. Strong data dispersion (> 3 s) may come from discrepancies between crustal models and the true structure of the crust under some stations. For instance, TBT (Canary island) station has a water layer with a very soft sediment layer in CRUST1.0; however the geological map of this region indicates volcanic rocks (basalt). Similar effects can be noticed on observed data by using CRUST2.0 (Figure IV.11 bottom row). We note that points distribution for CRUST1.0 (Figure IV.11 top row) is more spread than for CRUST2.0 (Figure IV.11 bottom row). However, one may note that crossplots computed with CRUST2.0 are not centered on the y=x line (i.e. black dashed line) but green points are slightly shifted towards the upper left corner, unlike for CRUST1.0 where green points are well centered.

Figure IV.12 is a zoom on the Mediterranean and North American regions, where seismic networks are dense. We see on the top row FF crustal effects for CRUST1.0 at 22.5 s computed from synthetics plotted as worldmap colors and those estimated from data as colored triangles. On the middle and bottom rows, we have the sediment and crystalline crustal thickness respectively associated to these regions. In these two areas, we have a very good agreement between synthetic and observed FF crustal estimations. Clear features of the crust previously highlighted by synthetic experiments are visible on observed data measurements ($dt_{\text{synth}}^{\text{crust1, FF}}(T) \simeq \Delta dt_{\text{obs}}^{\text{crust1, FF}}(T)$ for most stations). Scandinavia region located in the upper part of the Europe map (left column) shows good agreement with Kolstrup and Maupin (2015), that is, weak FF correction for the north-eastern area and negative FF correction for Norway coast and Denmark due to low-velocity sediment layers. Off course, differences in terms of resolution of the two crustal models prohibits a finer analysis. It is noteworthy from Figure IV.12 that sediment layers influence FF crustal effects. In North America, all regions with no sediment have a FF crustal correction equal to zero. But FF crustal variations cannot only be explained by sediment thickness variations, since several FF crustal features are not depicted in sediment maps. For instance, the northern part of the Gulf of Mexico exhibits a large and constant sediment thickness, but with very different FF responses. This thick sediment layer (dark red) overlaps continental and oceanic regions with very different crustal thickness. Consequently, in this specific case, the same sediment thickness for an oceanic crust induces a positive anomaly whereas it induces a negative anomaly for a continental crust. Figure IV.18 is a zoom in North America for CRUST2.0 and CRUST1.0 at all periods. By combining FiguresIV.12 and IV.18, we see that regions with the thickest sediment layers are not those where FF corrections are the largest for all periods, but they are characterized by strong crust-related finite-frequency variations. Time residuals measured at continental stations vary much less than those computed at oceanic stations (Figure IV.18)

Gulf of Mexico shows a positive anomaly for periods from 10 s to 22 s and then a negative anomaly for 34 s and 51 s. Analysis of the crustal structure in CRUST1.0 shows that this region has a very thick sediment pile with three sediment layers in the Gulf, whereas there are only two sediment layers in adjacent regions (Cuba and Mexico). The two first sediment layers have strong shear-wave velocity contrasts. Besides, the sediment sequence is clearly thicker than the crystalline part of crust. We think strong elastic impedance contrasts between crustal layers and large sediment thicknesses (Fig. 12) could induce this change in the sign of the anomaly in the Mexico bassin. In the models used, no other region has such a crust configuration with the exception of the eastern part of the Mediterranean sea.

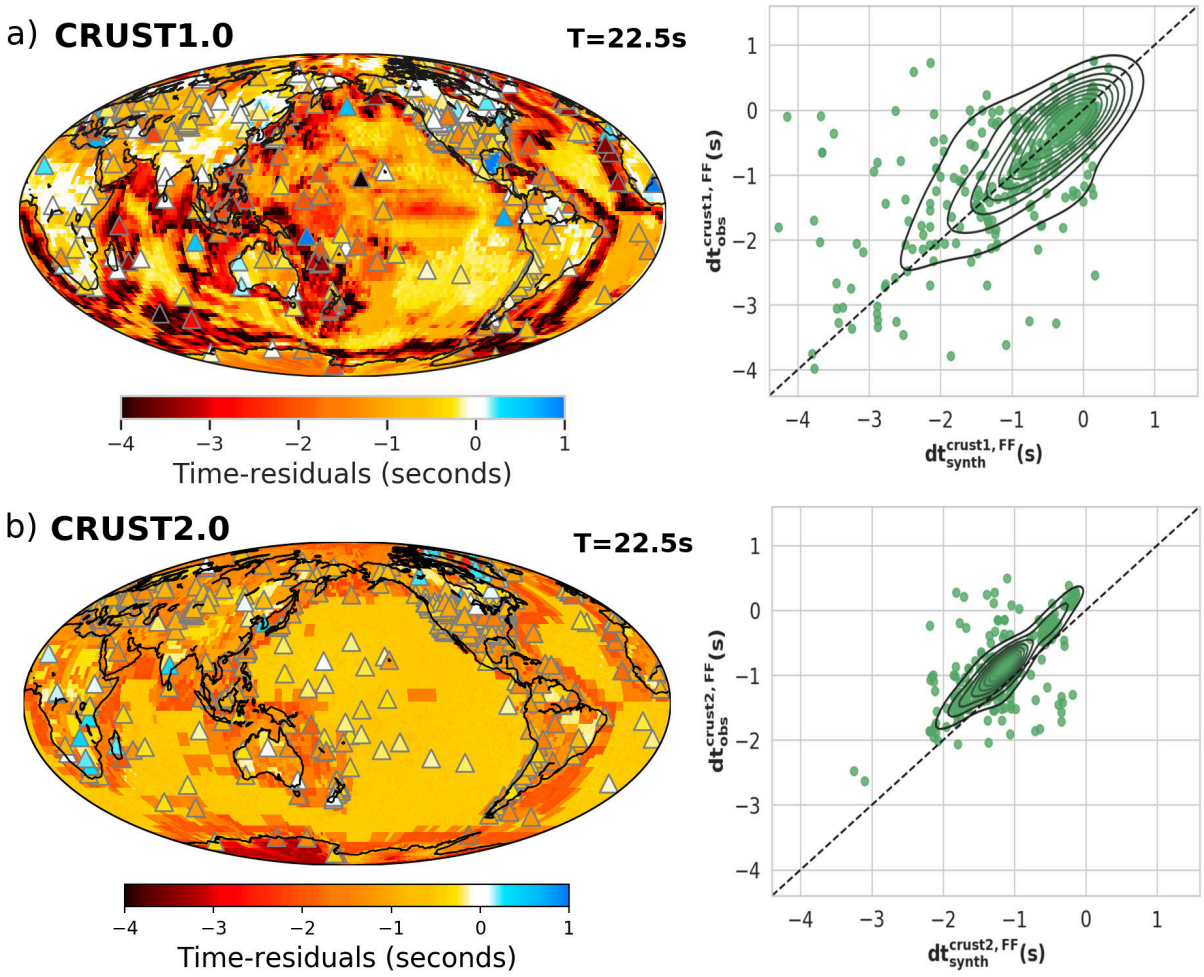

Figure IV.11 – Global mean time residuals measured by cross-correlating synthetics with and without crustal phases filtered at 22.5 s over (a) 1°x 1°grid for CRUST1.0 model, (b) 2°x 2°grid for CRUST2.0 model. Colored triangles indicate the dispersive crustal effect in observed data ($dt^{CP}_{obs}(T)$ - $dt^{NCP}_{obs}(T)$ for T $= 22.5s$). (Right) Comparison of observed and synthetic FF crustal corrections extracted for each station showed by triangles on the left map.

From all these observations we can conclude that CRUST1.0 may be in general a better representation of the crust under stations than CRUST2.0. Indeed, comparisons of FF time residuals between synthetics and data (Figures IV.16 and IV.17, rigth panel) show that dots for CRUST2.0 are not aligned along the y=x line (i.e. black dashed line) but is slightly shifted unlike CRUST1.0. This could be an indication that CRUST1.0 is on average a better representation of the true crust below stations, even if there are more outliers in CRUST1.0 (i.e., dots far from y=x) than in CRUST2.0 (see right-hand plots in Fig.IV.11). This spreading in CRUST1.0 crossplot reflects structural variations which could be in some cases worst than CRUST2.0 which is a coarser crustal model. Therefore, it is difficult to state that one specific crustal model is everywhere better than another (i.e., for all stations); accuracy of crustal models are completely station-dependent; CRUST1.0 is the best representation for some stations, for others, CRUST2.0 is better, and sometimes neither of them is a good representation of the unknown true crust.

IV.4 Conclusion

We have shown that the crust has a major dispersive effect on teleseismic body-wave time residuals and thus needs to be properly accounted for. Integration of crustal phases in synthetic seismograms allows to take into account waveform distortions induced by the crust structure when measuring time residuals by cross-correlation technique. Crustal effects may differ at different frequencies, since they reflect the inherent complexity of three-dimensional (3-D) crust.

We have explored two 3-D crustal models: CRUST1.0 and CRUST2.0. We report that dispersive crustal effects depend on the thickness and velocity of layers as well as elastic impedance contrasts between layers. Although ray crustal corrections remain important, finite-frequency crustal effects may lead to a bias in measurements and on average may reach 0.9–1.6 s for CRUST2.0 and 0.5–1.6 s for CRUST1.0, for filtering central period ranging from 10–51 s, respectively. As a consequence, we report clear differences of crustal corrections between CRUST1.0 and CRUST2.0. For shear waves (S, ScS, SS), the mean and the standard deviation of the total crustal correction (ray-theory and finite-frequency) at 10 s are 0.7 s $\pm$ 1.1 s for CRUST2.0 and 0.9 s $\pm$ 1.0 s for CRUST1.0. At 51 s period, the mean and the standard deviation are 1.4 s $\pm$ 1.1 s for CRUST2.0 and 2.1 s $\pm$ 1.8 s for CRUST1.0. We have shown that if this crust-related correction is not taken into account in cross-correlation measurements, this may lead to a significant dispersive effect in S-wave delay-times that could ultimately bias tomographic models.

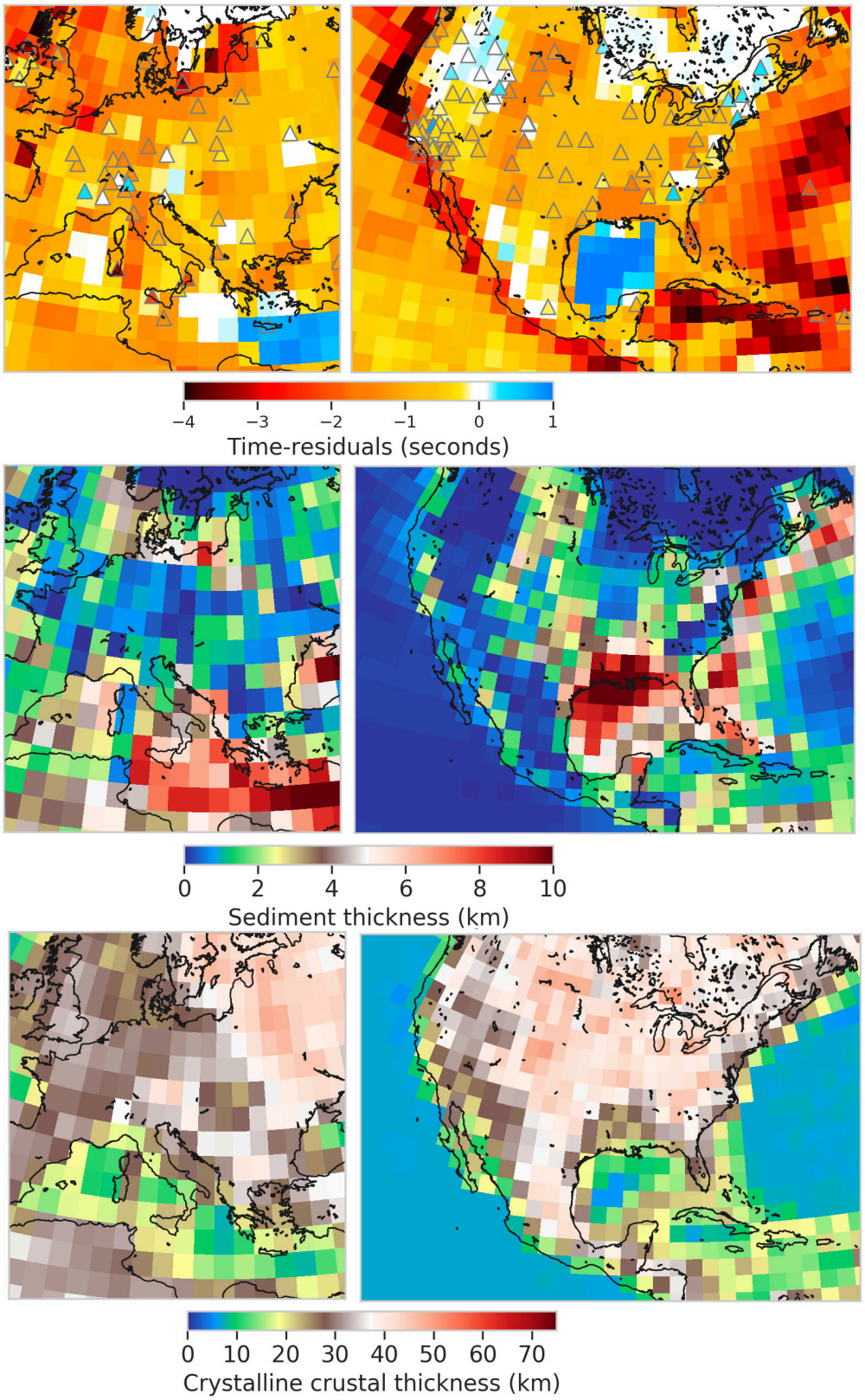

Figure IV.12 – (Top row) Mean time-residuals measured by cross-correlating synthetics with and without crustal phases filtered at 22.5 s for CRUST1.0. Colored triangles indicate the dispersive crustal effect in observed data (dt^{CP}_{obs} - dt^{NCP}_{obs}). (Middle and bottom rows) Sediment and crystalline thickness maps for Europe (left) and North America (right).

In short

- *Cross-correlation measurements of long-period S-wave are impacted by crustal reverberations.*
- *The dispersive properties of the crust depend on the thickness, the velocity as well as the elastic impedance contrast between each layer.*
- *Crustal corrections for cross-correlation measurement can be split in two contributions*
  - *Ray crustal corrections: shifting in time the whole waveform*
  - *Finite-frequency crustal corrections: inducing changes in the waveform*

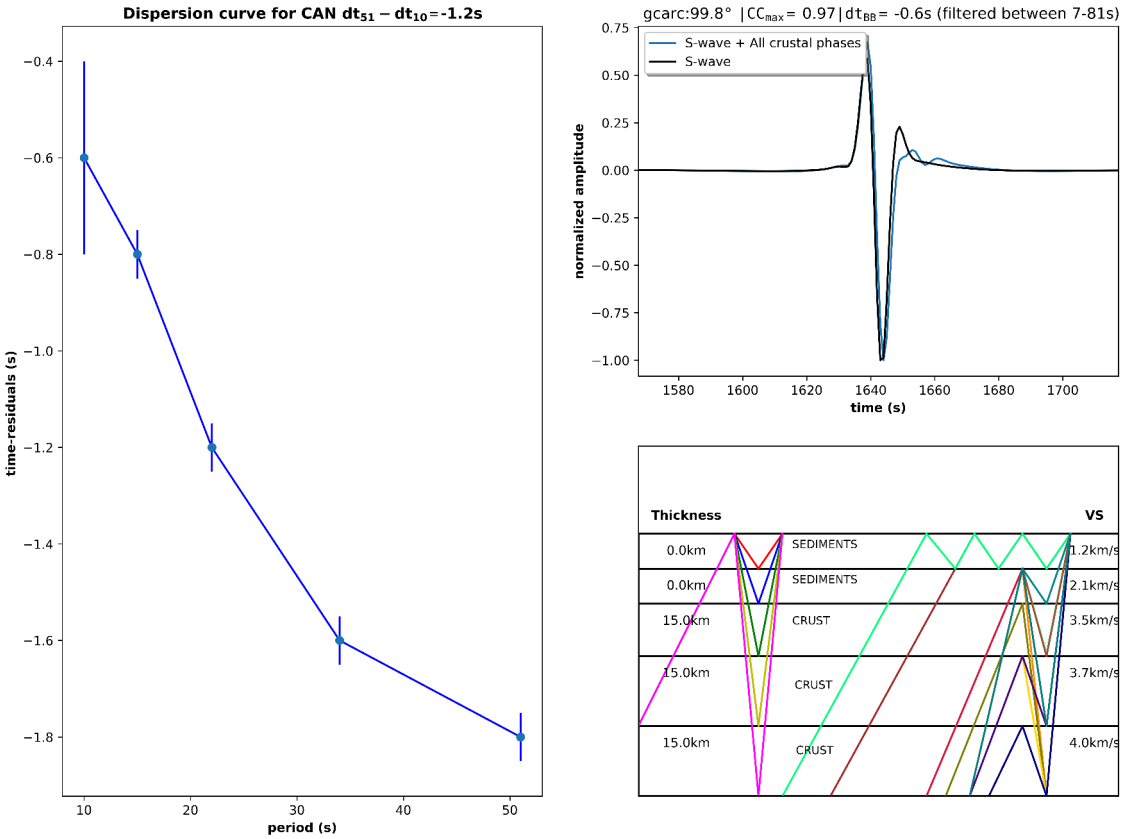

Figure IV.13 – (a) Dispersion curve for time residuals measured at 10 s, 15 s, 22.5 s, 34 s and 51 s. Error bars are estimated by using the method of Chevrot (2002). If the error is smaller than 0.1s we set a minimal error. (b) Waveforms are computed with a S-wave alone (black) and a S-wave + crustal phases (blue) recorded at station CAN. Waveforms are filtered between 7–81 s. (c) Crustal model under the station from CRUST2.0 with a schematic representation of modeled crustal phases. In this case crustal phases drawn in sediment layers are not modelled in our synthetics, only reflections in the last three layers are included.

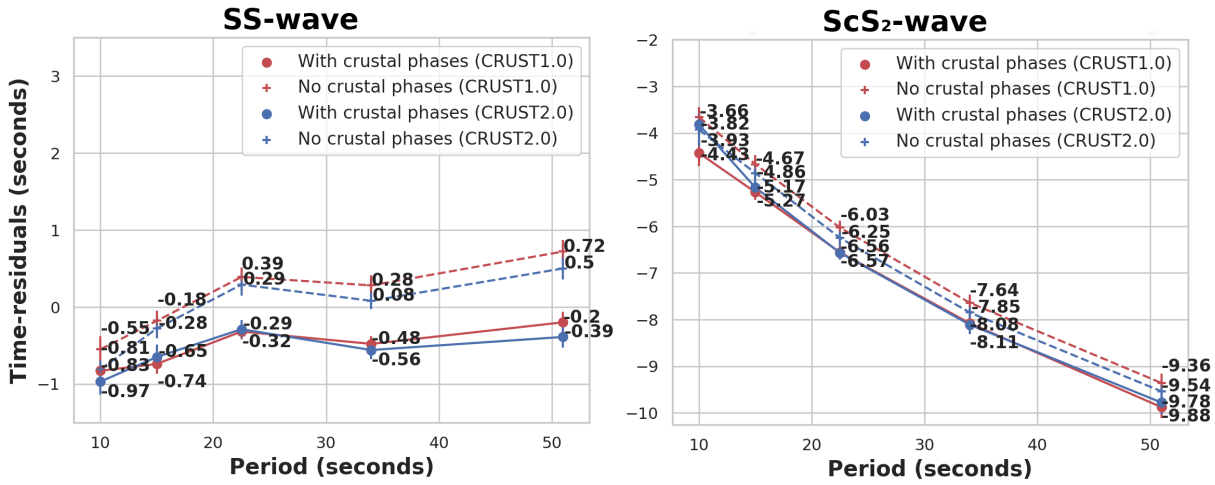

Figure IV.14 – SS and ScS_2-waves dispersion curves for two crustal models: CRUST1.0 (red), CRUST2.0 (blue). Solid and dashed lines are measurements made with synthetics computed with or without crustal phases respectively. SS has same y-axis as for S waves and ScS_2 has same y-axis as for ScS waves in Figure IV.10.

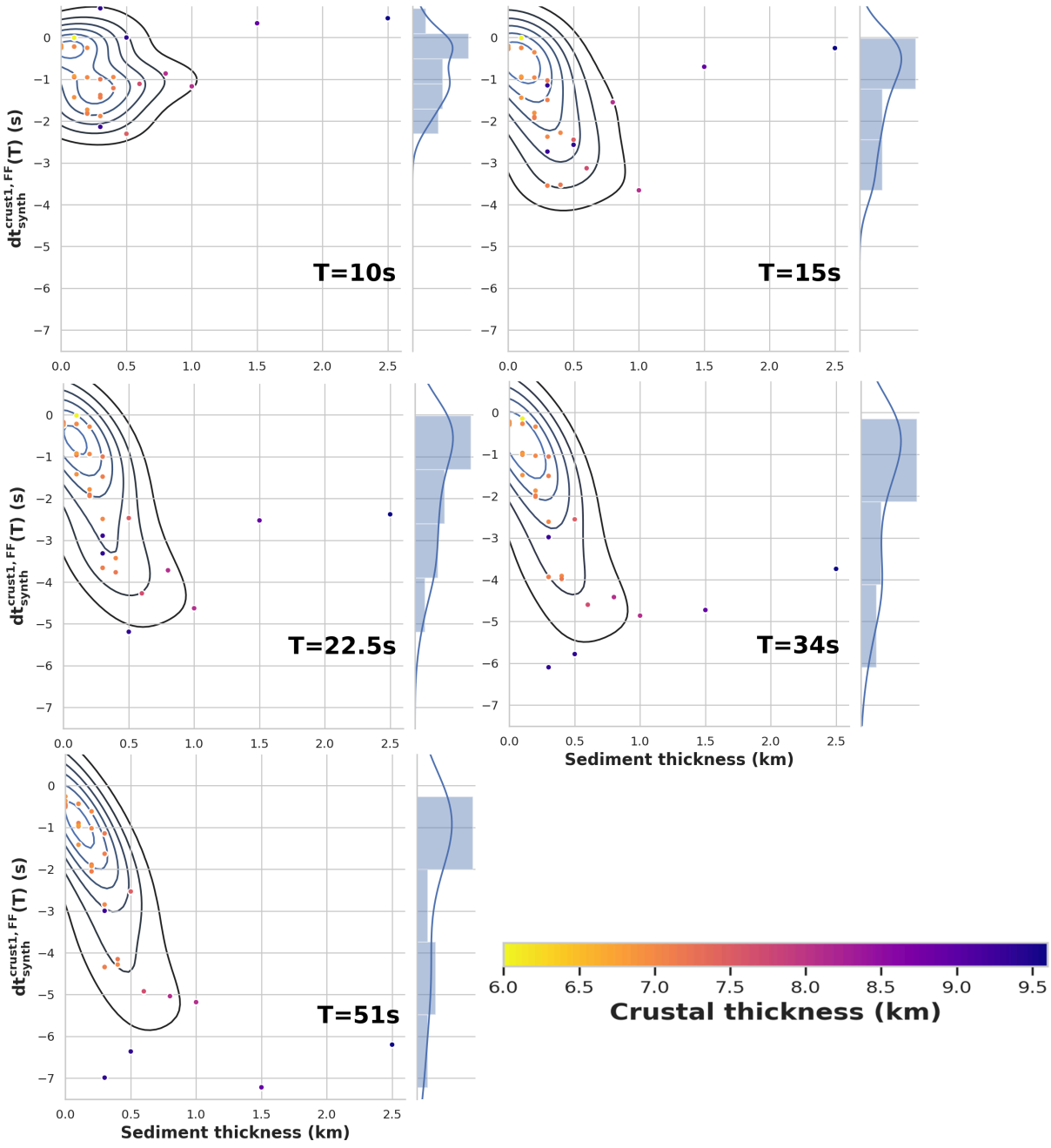

Figure IV.15 – FF crustal corrections as function of sediment thickness at different periods (10 s, 15 s, 22.5 s, 34 s, 51 s) for CRUST1.0. Colour inside circles depends on crustal thickness (in km). Crustal thickness is the sum of sediment and crystalline crustal thicknesses. We plot here only stations with thin crustal thicknesses (<12 km), which are stations for which CRUST1.0 gives an oceanic crust.

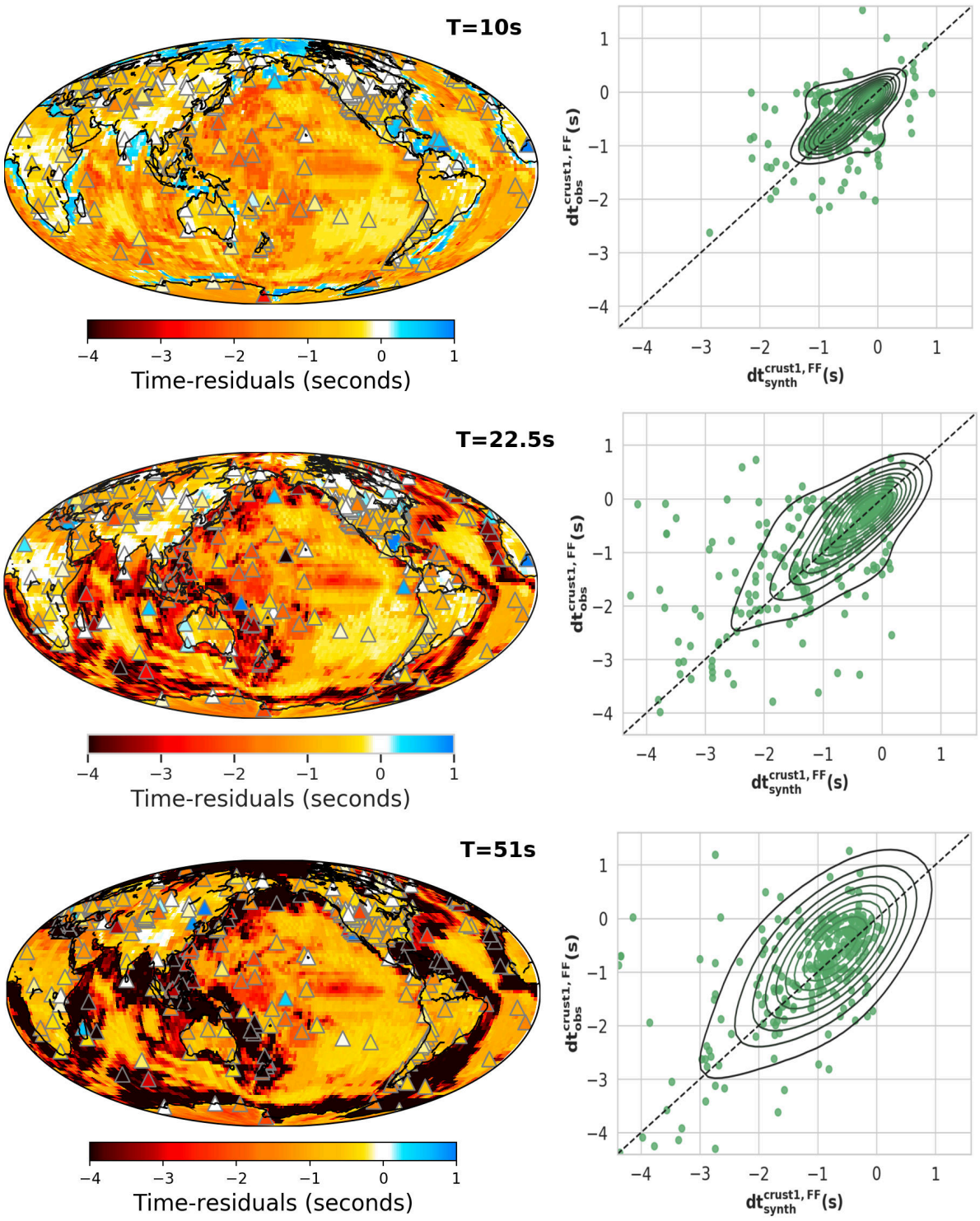

Figure IV.16 – (Left) Global mean time residuals measured by cross-correlating synthetics with and without crustal phases over a 1°x 1°grid filtered at (top row) 10 s, (middle row) 22.5 s and (bottow row) 51 s, for CRUST1.0 model. Colored triangles indicate the dispersive crustal effect in observed data ($dt^{CP}_{obs}(T)$ - $dt^{NCP}_{obs}(T)$). (Right) Comparison of observed and synthetic FF crustal corrections extracted for all the stations shown by triangles on left maps.

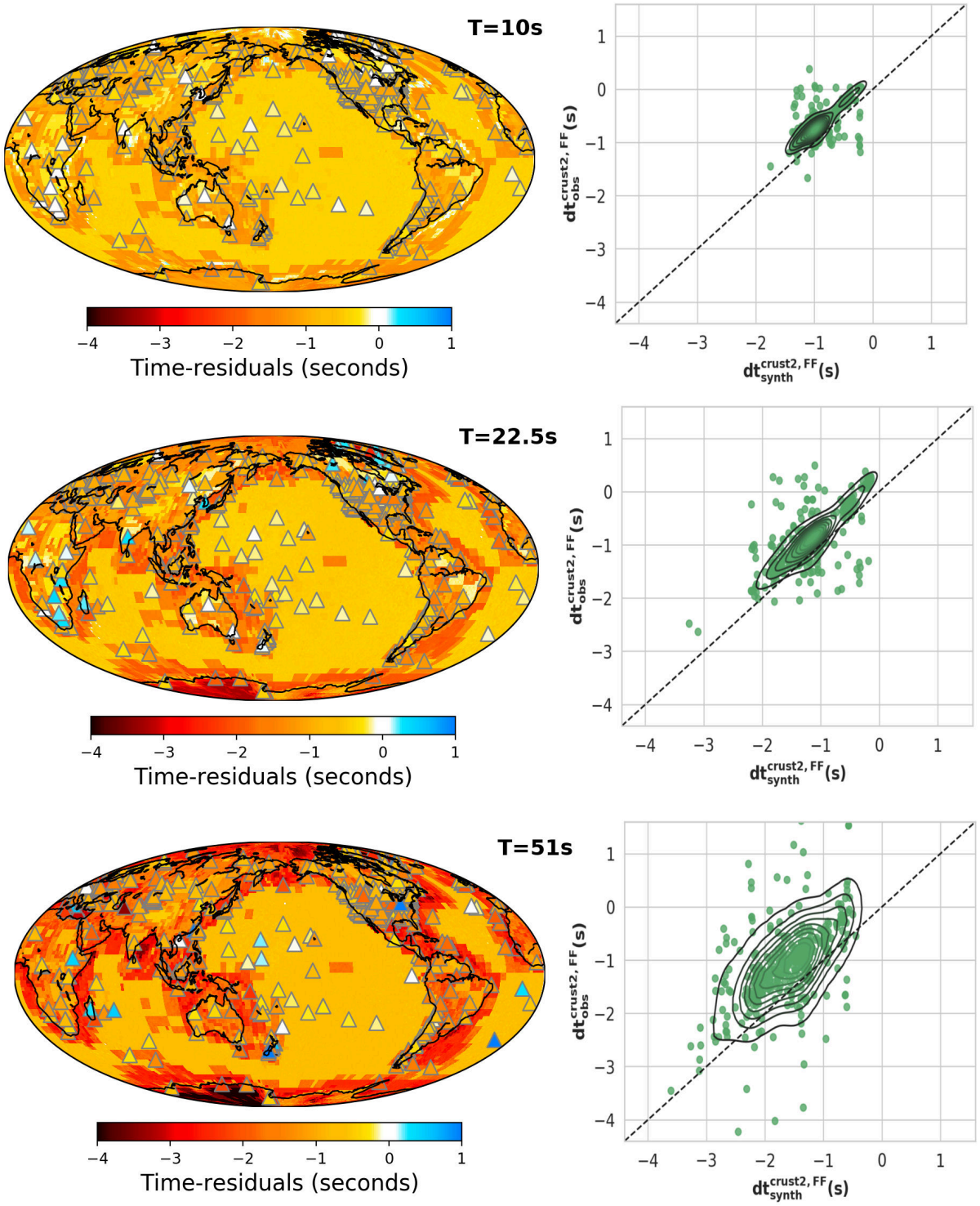

Figure IV.17 – (Left) Global mean time residuals measured by cross-correlating synthetics with and without crustal phases over a 2°x 2°grid filtered at (top row) 10 s, (middle row) 22.5 s and (bottow row) 51 s for CRUST2.0 model. Colored triangles indicate the dispersive crustal effect in observed data ($dt_{\text{obs}}^{\text{CP}}(T)$ - $dt_{\text{obs}}^{\text{NCP}}(T)$). (Right) Comparison of observed and synthetic FF crustal corrections extracted for all the stations shown by triangles on left maps.

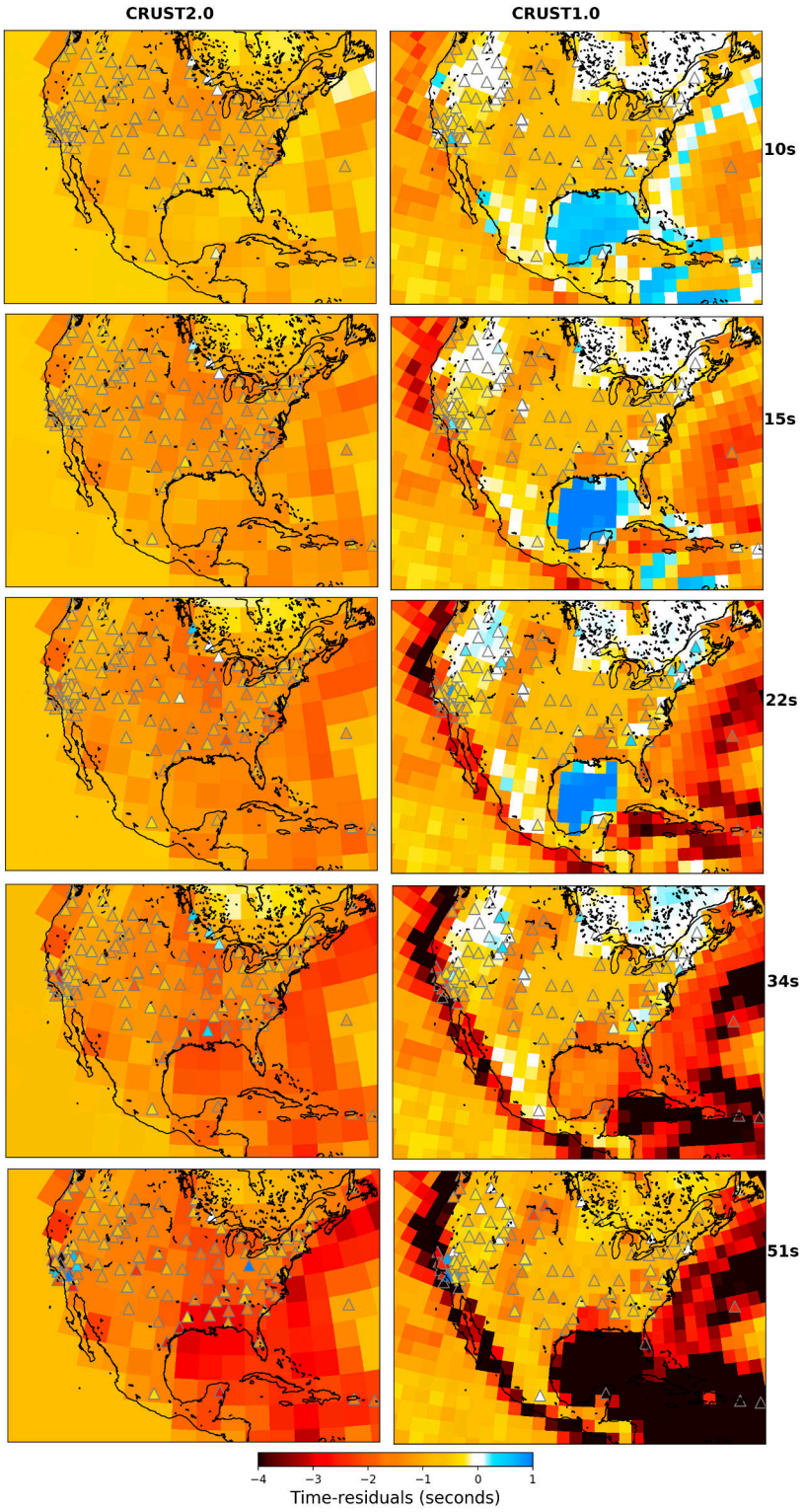

Figure IV.18 – S-wave mean time residuals measured by cross-correlating synthetics with and without crustal phases for (left column) CRUST2.0 model on a $2° \times 2°$ grid (right column) CRUST1.0 model on a $1° \times 1°$ grid filtered at (10 s, 15 s, 22.5 s, 34 s, 51 s). We modelled S, sS, ScS and sScS for epicentral distances from $30°$ to $95°$. One year of seismicity (with $5.5 < M_w < 6.5$) is used to generate the data set (2011). Only stations with at least 5 measurements are plotted, which explains the difference in number of stations between the two crustal models and the different frequencies.

Chapter V

Global mantle tomography using Backus–Gilbert inversion of normal-mode and finite-frequency *S*-wave data

Chapter V

Global mantle tomography using Backus–Gilbert inversion of normal-mode and finite-frequency *S*-wave data

Foreword

In the previous chapter, we have highlighted the potential bias in cross-correlation S-wave time residuals that may be associated to complex, finite-frequency effects of the Earth's crust. This has allowed us to build an extended S-wave data sets that is well suited for finite-frequency mantle tomography — since the crust effects have been carefully corrected for. Although, the previous chapter highlights the urge to use CRUST1.0 for crustal corrections, we used CRUST2.0 as a crustal model. So far too few global tomographic models use CRUST1.0, it seems first important to compare our SOLA tomographic model with common global tomographic model using CRUST2.0. In the future, we will use CRUST1.0 for crustal corrections. The following chapter describes how we have inverted our new body-wave dataset, jointly with additional normal-mode data published in the literature, in order to derive a global scale tomographic model, named SOLA-NOMBOW, which represents 3-D isotropic shear-wave velocity variations in the 410–2890 km depth range. From our finite-frequency body-wave data we only use time-residuals measured at 22.5 s to keep the problem tractable with modest computational facilities. Compared to other models which are all based on variants of the least-squares inversion scheme, SOLA-NOMBOW is built using the (discrete) SOLA—Backus—Gilbert tomographic method recently developed by Zaroli (2016). As we shall see, this new inversion approach allows us to release for the firs time to the community a global tomographic model, SOLA-NOMBOW, which is accompanied with all its resolution/uncertainty informations — enabling everyone to interpret any of its structural features in a more quantitative way compared to other published models. As a remark, the previously mentioned uncertainty informations merely represent the propagation of data errors into the model solution. Hence, the quantification of data errors is crucially important for getting, in the end, reliable appraisals of SOLA-NOMBOW. For example, we have taken into account S-wave data errors related to our imperfect knowledge of the crust, which were estimated in the previous chapter. Finally, the following chapter will be submitted soon (end of December, 2019) in Geophysical Journal International — remaining tasks are : 1) proof-reading the text of this current version, 2) finalizing some figures (including the thousands of model-appraisal figures that we wish to release to to the community via a web link).

Abstract

In this study, we build a global scale tomographic model, named *SOLA-NOMBOW*, which represents isotropic 3-D shear-wave velocity anomalies in the 410-2889 km depth range of the Earth's mantle. This model is derived from a joint linear inversion of spheroidal normal-mode and finite-frequency *S*-wave data. Compared to other models built from body-wave and normal-mode data, which are all based on variants of the least-squares inversion approach, ours is the first one to be derived from a recently developed Backus–Gilbert inversion scheme. First, this allows *SOLA-NOMBOW* to be unbiased, in the sense that its amplitudes do represent true averages over the Earth's properties, while least-squares models can be locally biased toward lower or higher amplitudes in regions of poor data illumination, thus potentially causing physical misinterpretations. Second, our embarrassingly parallel Backus–Gilbert inversion scheme makes computationally efficient to calculate the full generalized inverse required to infer both model resolution and its covariance (uncertainty). We emphasize that these resolution/uncertainty informations are crucially needed for reliable appraisal of model features, that is for quantitatively interpreting their robustness. For example, we show how to assess the reliability of what could (or not) be interpreted as the signature of a lower-mantle plume below Samoa. Third, since the employed Backus–Gilbert approach directly solves for the generalized inverse, it makes it straightforward to identify the contribution to *SOLA-NOMBOW* from every data type, that is, in our case: 1) *S*, *ScS*, *SS*, ScS_2 and *S+ScS* seismic phases, 2) self-coupling (with and without Stoneley) and cross-coupling modes. Indeed, as for any linear inverse problem, the model solution is expressed as a weighted sum of all the data, where the weights represent the generalized inverse. Finally, this study is the first one to release to the community a global tomographic model, *SOLA-NOMBOW*, accompanied with all its resolution/uncertainty informations – enabling everyone to interpret any of its features in a quantitative way.

V.1 Introduction

Global mantle tomographies do not bring large consensus on the fine structures inside the Earth's mantle (e.g., Nolet et al., 2008). Among these, plumes and slabs are particularly debated about their depth extends and lateral geometries. In this context, mantellic plumes are still challenging objects to be tomographically imaged inside the Earth's mantle. Plumes have potential strong implications in the heat dissipation of the Earth by bringing up to the surface hot materials and thus actively participate to the mantle convection. Some of these plumes seem to be characterized in surface by hot spots - i.e., volcanic archipelagos or traps. Lavas emitted from hot spots have different geochemical signature than lavas emitted at mid-ocean ridges. This implies a potential deep origin of the the melted materials produced at hot spot locations which supports a link between the deep mantle and the surface. To better assess the link between surface and the deep mantle, unbiased and quantitative tomographic images need to be produced. Tomographic images, when accompanied by their local resolution/uncertainty informations, can be exploited to decipher the structure and dynamics of the Earth's mantle, on various spatial and time scales (e.g., Schubert et al., 2001). Seismic tomography is then a powerful tool to probe the Earth's interior (e.g., Romanowicz, 2008; Ritsema et al., 2011). Although there seems to be some consensus on large-scale heterogeneities imaged in global

tomography, smaller length scales are more prone to differ in various published models (e.g., Nolet et al., 2008). Amongst these dissensions, the vertical plume extends is debated as well as their lateral thicknesses. To better constrain these structures higher resolution model need to be produced. To that aim joint inversions of different data set can help to cover a largest seismic spectrum. Several kind of seismic data can thus be exploited, such as body-wave, surface-wave and normal-mode measurements.

Over the past decades, global tomographic models have routinely been relying on variants of the damped least-squares (DLS) linear inversion approach (e.g., Aster et al., 2018). However, several authors (e.g., Nolet et al., 2008; Zaroli et al., 2017; Maguire et al., 2018) report that DLS models can be locally 'biased' toward lower or higher amplitudes in regions of poor data illumination – potentially causing physical misinterpretations of tomographic images. For example, these bias effects may be important below receivers located on isolated stations (e.g., on Hawaii), for which seismic rays are all aligned in the vertical direction. Moreover, global tomographic studies usually face massive linear inverse problems to solve, thus often making computationally prohibitive the calculation of the full DLS-related generalized inverse – which is required to infer both the model resolution and its covariance, and thus is needed for robust model interpretations (e.g., Nolet et al., 2008).

Recently, Zaroli (2016) introduced and adapted the SOLA (Subtractive Optimally Localized Averages) inverse method for solving large-scale, linear and discrete seismic tomography problems. The SOLA method was first introduced in helio-seismology by Pijpers and Thompson (1994), and is a – computationally more efficient – variant of the linear, discrete Backus–Gilbert (B–G) inversion scheme (e.g., Backus and Gilbert, 1967, 1968, 1970; Nolet, 1985). Zaroli et al. (2017) summarize the advantages of SOLA tomography over classical DLS tomography: 1) SOLA allows to directly compute (in an embarrassingly parallel way) the 'generalized inverse' operator, while controlling the trade-off between model resolution and uncertainty (e.g., Menke, 2018); 2) There is no need in SOLA to introduce any *ad hoc* regularization of the model solution itself (for removing the non-uniqueness of the solution); 3) The SOLA 'resolution' operator is built such that it leads to true (i.e., unbiased) averages over the true-model parameters. As a remark, Zaroli (2019) recently moved the SOLA tomographic approach from a discrete to a *continuous* model representation named "parameter-free SOLA tomography", whose additional advantage is to fully exploit the data sensitivity kernels in the inversion process – since they do not need anymore to be projected on an often coarse tomographic grid. However, in this study we shall rather opt for the discrete SOLA approach, which is more computationally tractable when dealing with massive data sets as it is the case here.

The main goal of this study is to release to the Earth-Sciences community the first global model, named *SOLA-NOMBOW*, which was derived from a joint discrete SOLA–Backus–Gilbert tomographic inversion of normal-mode and finite-frequency *S*-wave data. This model consists of (unbiased) shear-wave velocity anomalies in the 400–2889 km depth range; its name refers to the employed SOLA inversion scheme, and to the used NOrmal Mode and BOdy Wave data. Although, tests on Backus-Gilbert resolution kernels are computed for S20RTS (Ritsema et al., 1999) and S40RTS (Ritsema et al., 2011) for peculiar locations inside the Earth. No global assessment of the Backus-Gilbert model appraisal have been conducted so far. To the best of our knowledge, this is the first global model to be released with all its resolution/uncertainty informations – enabling everyone to interpret any of its features in a quantitative way. Specifically, we aim to invert for: 1) cross-correlation time residuals

measured for *S*, *ScS*, *SS*, ScS_2 and *S+ScS* body-wave phases, and 2) structure coefficients of spheroidal modes, including self/cross-coupling and Stoneley modes. We make use of Dubois et al. (2019)'s body-wave data set, and of Deuss et al. (2013); Koelemeijer et al. (2013)'s normal-mode data set, and calculate appropriate finite-frequency body-wave data sensitivity kernels (Dahlen et al., 2000) and sensitivity kernels for normal-mode data. This study is among the first to exploit cross-coupling and Stoneley data in global tomography (Koelemeijer et al., 2016; Durand et al., 2017). As a remark, Stoneley modes are specifically sensitive to, hence useful to constrain, velocity anomalies in the lowermost mantle, at depths greater than 2000 km (e.g., Stoneley, 1924; Koelemeijer et al., 2013). Jointly invert normal modes and body-wave data should help us to fill in the data-coverage gaps in the lower mantle, as previously shown by other studies (e.g. Ritsema et al., 1999; Masters et al., 2000; Ritsema et al., 2011; Zaroli et al., 2015; Durand et al., 2017). That is, normal mode data allow to uniformly constrain large-scale seismic heterogeneities in the Earth's interior, whereas small scale heterogeneities can only be constrained in regions with relevant body-wave data coverage.

In a first part, we present the data sets and their estimated errors, the model parameterization used in this study, and also briefly describe the key ingredients of how is employed the SOLA tomographic scheme (Zaroli, 2016) in this joint-inversion study. Then, we present the obtained tomographic model, SOLA-NOMBOW. Though a detailed analysis of model will be the subject of future work, we show how its additional resolution/uncertainty informations can be exploited for appraising the robustness of its apparent features. For example, we show how to assess the reliability of what could (or not) be interpreted as the signature of a lower-mantle plume below Samoa. In addition, we show that the explicit knowledge of the generalized inverse (which is what the SOLA–Backus–Gilbert scheme directly solves for) makes it straightforward to identify and visualize the contribution of each data set to the model *SOLA-NOMBOW*, that is, in the case of this study: 1) *S*, *ScS*, *SS*, ScS_2 and *S+ScS* seismic phases, 2) self-coupling and cross-coupling modes.

V.2 Material and Methods

We use here two types of data: finite-frequency time-residuals (from body waves) and structure coefficients (from normal modes).

V.2.1 Data sets

V.2.1.1 Body waves

Body-wave data are exploiting to better constrain the fine structure of the Earth. These data are finite-frequency time-residuals of shear waves measured at 22.5 s of period (Dubois et al., 2019). Body waves are characterized by a strong heterogeneity in the ray path coverage which is related to the source-station geometry. In order to optimize the ray path coverage we select worldwide earthquakes with magnitude between 5.5 and 6.5 from 1979 to 2017. To ensure a good data quality we only keep data with a SNR ≥ 3, leaving to us 127 000 time-residuals to invert. In addition to usual shear waves such as S, SS, ScS waves used in mantle imaging, improvements to the lower mantle coverage are brought by ScS_2 and

interferences between S and ScS waves. Upper mantle is well constrained by S and SS waves whereas the lower mantle is covered by ScS, ScS_2 and interferences between S and ScS waves. Interferences between S and ScS waves occur at specific epicentral distances between 75°and 95°. Considering the station and earthquake distributions, interference measurements bring valuable information on the lower mantle under the Pacific. Finally, data are corrected for crust, ellipticity, topography and intrinsic attenuation with a frequency independent quality factor. Statistics and further details on finite-frequency crustal corrections can be found in Dubois et al. (2019).

We use a tuned version of the procedure developed by Zaroli et al. (2010) to measure shear-wave data. Time-residuals are time-shifts obtained from the maximums of the cross-correlation function between filtered synthetic and observed seismograms. With synthetic seismograms generate with WKBJ (Chapman, 1978) using the 1-D Earth model IASP91 (Kennett and Engdahl, 1991) and the crustal model, CRUST2.0 (Bassin et al., 2000). To invert time-residuals we rely on the finite-frequency theory presented in Dahlen et al. (2000) making use of the paraxial approximation. Under the paraxial approximation, Tian et al. (2007b) recommend epicentral distances to be less than 140° but significant errors at low frequency can appear below this threshold. To fulfill the paraxial approximation, we only invert time-residuals with epicentral distances at most 130°.

Body-wave data errors have several origins. A first source comes from earthquake mis-location. For this contribution, Bolton and Masters (2001) estimate uncertainties between 1.6 - 2.5 s for an S-wave. We take 2.5 s for all seismic phases as σ_{misloc}. A second source of error originates from the inaccuracy of finite-frequency kernels modeling. Since these kernels have to be projected, degraded kernels will induce inaccuracies (Zaroli, 2019). This error is taken equal to 1 s (σ_{kernel}) since it represents an acceptable compromise between S-wave kernel (0.6 s) and SS-wave kernel (1.4 s) errors. The third source of error is attributed to measurement errors and so represents an individualized error for each data. After analysis of error distribution, we set a minimal error at 0.5 s if error estimation is below this threshold ($\sigma_{\text{xcorr},i}$). Measurement error process for cross-correlation measurements can be found in Zaroli et al. (2010). The last source of error is generated by uncertainties on the crustal model used to correct seismic travel-times (Dubois et al., 2019). From recent error estimations for S waves, a value of 1 s is retained for CRUST2.0 (σ_{crust}). These four factors are then combined to associate an error to each body wave data of the global dataset (see Table V.1):

$$\sigma_i = \sqrt{\sigma^2_{\text{xcorr},i} + \sigma^2_{\text{misloc}} + \sigma^2_{\text{kernel}} + \sigma^2_{\text{crust}}} \tag{V.1}$$

On average, finite-frequency body-wave data have a mean error of 3.3 s. It could be worth to adapt more accurately the error sources to the data type (i.e. $\sigma_{\text{kernel}} = \sigma_{\text{kernel,i}}$, $\sigma_{\text{crust}} = \sigma_{\text{crust,i}}$). However, the dominant error comes for the event mislocation (σ_{misloc}) for which we do not invert. It is thus a waste of time trying to set data dependent errors (kernel, crust and measurement) as long as we do not reduce this dominant source of uncertainties. Different methods exist to reduce event mislocation uncertainties. For instance, by taking differential traveltime measurements such as Pdiff-PKP (e.g., Kárason and van der Hilst, 2001), S-ScS (e.g., Garnero and Lay, 2003), using receiver pairs for a same wave (e.g., Zaroli et al., 2014) or invert for source mislocations (e.g., Ritsema and van Heijst, 2002). This part

Table V.1 – Error components (standard deviation) of our body-wave data

	mislocation	kernel	crust	measurement
value (s)	2.5	1	1	max(0.5, $\sigma_{\text{xcorr},i}$)

is beyond the scope of this article but should definitely be tackled to reduce the dominant uncertainty factor in this inversion.

V.2.1.2 Normal modes

In spite of the good body-wave data coverage, gaps in the lower mantle coverage remain. To address this problem we use spheroidal normal modes sensitive to specific depth ranges, i.e. in the lowermost mantle where the body-wave data are the scarcest. Normal mode data used in seismic tomography are in the form of self and cross-coupling structure coefficients ${}_{\underline{k}}c_s^t$ (with $\underline{k}$ a specific normal mode, s the degree and t the order of spherical decomposition of the structure of the Earth). Self-coupling structure coefficients are only sensitive to even-degree structure of the Earth. To temper the prevailing even degree features of mantle model we complete the normal mode data set with cross-coupling allowing to get access to odd-degrees of the mantle structure. Normal data used in this study are a subset of Deuss et al. (2013) data set and Koelemeijer et al. (2013) for Stoneley normal modes (Table V.2). Stoneley normal modes are characterized by a strong sensitivity to solid/fluid interface, and so help to constrain elastic anomalies in the lowermost mantle (Koelemeijer et al., 2013). We include structure coefficients up to degree 8 which leaves us with 1860 data for normal modes.

To obtain structure coefficients one needs to operate a non-linear inversion, with respect to the source, of seismogram spectra. This non linearity makes the error estimations on structure coefficients poorly constrained, with data uncertainties may be badly estimated. Attempts in reducing the theoritical error are undertaken by, for instance infer directly the elastic parameters from spectra by assuming a full-coupling hypothesis (Akbarashrafi et al., 2018), though this remains a non-linear inversion. We set a minimal error at 0.1 μHz if error estimations coming from the first inversion are below this threshold. Since normal mode data are perturbations from the PREM model (Dziewonski and Anderson, 1981) and body wave time-residuals from IASP91 (Kennett and Engdahl, 1991), we correct the structure coefficients for the difference between these two 1-D models. Structure coefficients are corrected for the crustal structure by using CRUST2.0 (Bassin et al., 2000).

Although normal modes are naturally expressed with spherical harmonics, we choose to parametrize normal modes on an irregular mesh tuned for the body-wave data coverage. To express normal mode sensitivity kernels over the irregular mesh we follow the methodology of Zaroli et al. (2015). Thereby, 3-D normal mode sensitivity kernels can thus be written onto the irregular mesh without loss of generality for normal mode. Once body waves and normal modes are described onto the same parametrization, it is important to ensure that one data type does not take too much importance at the expense of the other.

Table V.2 – Spheroidal normal modes ${}_nS_l$ used in this study. Stars denote Stoneley modes. Last row list all cross-coupling normal modes.

overtone (n)	angular order (l)
n=0	3,4,5,6,14
n=1	2,3,4,5
n=2	1,3,4,8,9,10,15,16*,25*
n=3	6,7,8,9,26*
n=4	3,4,5
n=5	3,11
n=6	3,15
n=7	8,9
n=9	6,10
Cross-coupling:	${}_0S_{14} - {}_2S_9$, ${}_1S_5 - {}_2S_4$, ${}_2S_8 - {}_4S_4$, ${}_2S_{10} - {}_4S_5$, ${}_3S_8 - {}_6S_3$, ${}_7S_8 - {}_5S_{11}$, ${}_6S_{15} - {}_9S_{10}$, ${}_9S_6 - {}_7S_9$.

V.2.1.3 Weighting body-wave and normal-mode data subsets

Data errors are essential in any inversion schemes. In a joint inversion context, bad data error estimations could induce an over expression of a data type and poor model uncertainties. But, errors on body waves data and specifically on normal modes data are not perfectly constrained. So to quickly assess the global coherency of data error for body waves and normal modes, we first proceed to separate DLS inversions of body waves and normal modes. For each inversion, the Euclidean norm of the inverted model ($||m||$) and the data misfit (χ^2_{red}) are computing in order to visualize L-curves.

In our case, the data errors σ_i are increased by 60% such that the χ^2_{red} (Nolet et al., 2008) is equal to one. This brings an average uncertainty of 5.3 s for body wave data which still seems reasonable in terms of uncertainty sources (earthquake mislocation is by far the largest source of error, noisy seismograms and crust model uncertainties). Regarding normal mode data, L-curve indicates that some data are fit with more than 400% error which is too much for global tomography. Therefore, errors associated to some normal mode data used in this study are largely under estimated. It has to be noticed that these preliminary steps to assess and weight data are only needed since the original data error estimates are not perfect.

At the end of the two DLS inversions, two different damping parameters are available: one for the body waves and the second for normal modes. To iteratively solve the linear inverse problem we make use of the LSQR algorithm (Paige and Saunders, 1982). However, LSQR inversion can only accept a single damping parameter which can be problematic when damping parameters are very different for different types of data. We follow the work of (Zaroli et al., 2015) by applying a data weighting over each type of data. This allows to keep the two preferred damping parameters for the normal modes and body waves but only use one for the LSQR process.

V.2.2 Joint tomographic inversion

V.2.2.1 Model parametrization

In this study, the whole Earth's mantle (from 0 to 2889 km depth) is parameterized exactly as in Zaroli et al. (2015) – and the reader is referred to this earlier study for details on this parameterization. To summarize, the mantle is vertically subdivided into 18 spherical layers of 100–200 km width, and each layer is laterally spanned with a data-driven (i.e., driven by body-wave ray density) Delaunay mesh which consists of spherical triangular prisms. This leads to 38,125 model parameters (i.e., nodes). The minimal lateral resolving length corresponds to the local node spacing of the tomographic grid; it ranges from about 200 to 1000 km. In the future, we plan to refine further this tomographic grid in the regions where we now have more data than those used in Zaroli et al. (2015). That is, in this work we have preferred not to do so yet, for keeping limited the number of parameters to be solved for with the SOLA inversion scheme – this allowed us to build the model *SOLA-NOMBOW* without the need for large (e.g., HPC) computational resources.

V.2.2.2 Key ingredients of SOLA inversion

In this study, we face a linear(ized), discrete problem of the form:

$$\mathrm{d} = \mathbf{G}\mathrm{m} + \mathrm{n} \tag{V.2}$$

where $\mathrm{d} = (d_i)_{1 \leq i \leq N}$ denotes the data vector, $\mathrm{n} = (n_i)_{1 \leq i \leq N}$ the noise in the data, $\mathrm{m} = (m_j)_{1 \leq j \leq M}$ the 'true-model' parameters (with the model parametrization as described in Sect. 2.2.1), and $\mathbf{G} = (G_{ij} = \partial d_i / \partial m_j)$ the sensitivity matrix (size $N \times M$). In this study, the model parameters represent (3–D) isotropic shear-wave velocity variations with respect to a reference radial model, IASP91, and we assume that the noise n has zero mean, and the data covariance matrix is $\mathbf{C}_d = \mathrm{diag}(\sigma_{d_i}^2)_{1 \leq i \leq N}$. For linear inverse problems, it is common to seek for the model estimate $\hat{\mathrm{m}}$ as a linear combination of the data:

$$\hat{\mathrm{m}} = \mathbf{G}^{\dagger}\mathrm{d} = \underbrace{\mathbf{R}\mathrm{m}}_{\substack{\text{filtered} \\ \text{true model}}} + \underbrace{\mathbf{G}^{\dagger}\mathrm{n}}_{\substack{\text{propagated} \\ \text{noise}}} \tag{V.3}$$

where $\mathbf{R} = \mathbf{G}^{\dagger}\mathbf{G}$ is the model-resolution matrix (of size $M \times M$). The generalized inverse matrix $\mathbf{G}^{\dagger}$ (of size $M \times N$) directly depends on the employed inversion scheme. The appraisal of the model solution consists in analyzing $\mathbf{R}$ and the covariance matrix, $\mathbf{C}_{\hat{m}} = \mathbf{G}^{\dagger}\mathbf{C}_d(\mathbf{G}^{\dagger})^T$. The heart of Backus-Gilbert inversion is to seek for a *weighted average* over the true-model properties of the form (here expressed in a continuous formalism for simplicity):

$$\hat{m}_k = \int A^{(k)}(\mathrm{r})\, m(\mathrm{r})\, d^3\mathrm{r} \quad (+ \text{ propagated noise}) \tag{V.4}$$

where $A^{(k)}$ denotes an averaging function – often referred to as an averaging kernel (or a resolving kernel) – that we wish to be: 1) spatially localized around a given point of interest $\mathrm{r}^{(k)}$ (for example the k-th node of our tomographic grid), 2) to satisfy to the unimodular condition, i.e., $\int A^{(k)} = 1$, and 3) to be non-negative. As a remark, in our discrete study, the k-th row of the resolution matrix $\mathbf{R}$ represents the resolving kernel $A^{(k)}$ (Zaroli, 2016). The model estimate $\hat{m}_k$ is said to be 'unbiased' if 2) and 3) are verified (see Zaroli et al.

2017 for a discussion on the averaging bias effect that may occur in DLS models, contrary to SOLA–Backus–Gilbert models). The key idea in the SOLA variant of the Backus–Gilbert inversion scheme is to specify an *a priori* 'target' averaging function $T^{(k)}$ for each averaging kernel $A^{(k)}$ (Pijpers and Thompson, 1994). These target functions $T^{(k)}$, hereafter referred to as 'target kernels', need to be specified such that their spatial extent represents some *a priori* estimate of the local spatial resolving-length. In this study, we make use of the same spheroid-shape target kernels as in Zaroli (2016), whose size is driven by the ray-density. Rather than minimizing the spread of each averaging kernel $A^{(k)}$, as in the original Backus–Gilbert formulation, the SOLA method aims at minimizing the integrated squared difference between each averaging kernel and its associated target kernel, while also minimizing the model variance $\sigma^2_{\hat{m}_k}$ (i.e., minimizing the propagation of data noise into the model estimate). As a remark, $\sigma^2_{\hat{m}_k}$ represents the k-th diagonal element of $\mathbf{C}_{\hat{m}}$. More precisely, the SOLA–Backus–Gilbert inversion scheme directly aims at seeking for the k-th row of the generalized inverse $\mathbf{G}^{\dagger}$ by solving the following minimization problem (expressed in a continuous formalism for simplicity):

$$\begin{cases} \underbrace{\int [A^{(k)}(\mathrm{r}) - T^{(k)}(\mathrm{r})]^2 d^3\mathrm{r}}_{\substack{\text{resolution} \\ \text{misfit}}} \quad + \quad \eta^2 \underbrace{\sigma^2_{\hat{m}_k}}_{\substack{\text{model} \\ \text{variance}}} = \text{min} \\ \text{subject to } \underbrace{\int A^{(k)}(\mathrm{r}) d^3\mathrm{r} = 1}_{\substack{\text{unimodular} \\ \text{condition}}}, \end{cases} \tag{V.5}$$

where η denotes a trade-off parameter, that we also choose to be constant valued for every query point (k) as suggested by (Zaroli, 2016; Zaroli et al., 2017; Zaroli, 2019). It is important to realize that the SOLA–Backus–Gilbert approach can solve for all the rows of the generalized inverse $\mathbf{G}^{\dagger}$ in an *embarrassingly parallel* fashion. Moreover, once the generalized inverse $\mathbf{G}^{\dagger}$ is known, then one can infer the model estimate $\hat{\mathrm{m}}$, and also the resolution $\mathbf{R}$ and covariance $\mathbf{C}_{\hat{m}}$ – which are both required for quantitatively appraising the model solution. For more details on the discrete or continuous SOLA tomographic method, the reader is referred to Zaroli (2016) or Zaroli (2019), respectively. Tests on the maximum number of iterations for LSQR as well as the trade-off parameter (η) can be found in appendix A of this thesis.

V.3 Results

V.3.1 Model *SOLA-NOMBOW versus* a classical DLS model

Figure V.1 shows side by side some depths of the DLS and SOLA inversions. At 485 km, body-wave data coverage is reasonable which appears on top row of figure V.1 by few differences between SOLA and DLS inversions. Although, high amplitude anomalies do not show up on SOLA image. For instance, very high slow anomaly located below mount Erebus in DLS has completely faded away on SOLA image. This effect could be due to isolated receivers located in Antarctica and inducing amplitude increase below the station (see figure 2 in Zaroli et al. (2017) for similar effects on synthetic experiment).

At 1810 km (fig.V.1, middle row) body wave bring much less information, and DLS images is highly affected by the raypaths geometry. The slow anomalies shape in Pacific is very affected

by preferential direction of rays, we guess unidirectional raypaths with earthquake positions in south-west Pacific and receivers in Hawaii islands. Zaroli et al. (2017) highlight this effect over a 2-D experiment where anomalies geometry are actually stretched in the direction of raypaths for isolated receivers.

At 2800 km (fig.V.1, last row), normal modes have a larger influence than body waves thanks to Stoneley normal modes. Large features are preserved between DLS and SOLA inversions. Nevertheless, variations in amplitude for slow anomalies under Africa and the Pacific can be observed. Since target kernels are really made for body-wave coverage, changes induced by SOLA inversion with normal mode data are maybe harder to see on these images. But signal coming mainly from normal modes such as the slow anomaly under Africa has an amplitude which varies compared to the DLS inversion. Amplitude is maybe the main change in normal mode SOLA inversion compared to DLS inversion. Solely normal mode SOLA inversion should definitely be carried out in the future to see if geometry of anomalies are also affected by SOLA inversion.

V.3.2 Contributions of every data types to *SOLA-NOMBOW*

Let $(x_i^{(k)})_{1\leq i\leq N}$ be the N elements of the k-th row of the SOLA generalized inverse $\mathbf{G}^\dagger$. One can then write the k-th model-parameter estimate $\hat{m}_k$ as follows:

$$\hat{m}_k = \sum_{i=1}^{N} x_i^{(k)} d_i = \underbrace{\sum_{i\,\equiv\,\text{Type I}} x_i^{(k)} d_i}_{\hat{m}_k^{(\mathrm{I})}} + \underbrace{\sum_{i\,\equiv\,\text{Type II}} x_i^{(k)} d_i}_{\hat{m}_k^{(\mathrm{II})}} + \cdots \tag{V.6}$$

where Types I, II, etc, denote some specific data types, for example: 1) different body-wave seismic phase (*S*, *ScS*, *SS*, *ScS*$_2$, *S*+*ScS*), 2) self-coupling (with/without Stoneley) and cross-coupling modes. Therefore, our explicitit knwoledge of the SOLA generalized inverse makes it straightforward to visualize on 'tomographic map' the contribution of every data type to model *SOLA-NOMBOW*. That is, by plotting the different model vectors $\hat{\mathrm{m}}^{(\mathrm{I})}$, $\hat{\mathrm{m}}^{(\mathrm{II})}$, etc. As a remark, $\hat{\mathrm{m}}^{(\mathrm{I})}$ is not equivalent to a model that would have been obtained from a SOLA inversion restricted to the Type I data only. However, we think that a quick visual inspection of the easy-to-compute pseudo models $\hat{\mathrm{m}}^{(\mathrm{I})}$, $\hat{\mathrm{m}}^{(\mathrm{II})}$, etc, may still help us to better apprehend how the data are 'relatively weighted' in the linear combination, $\mathbf{G}^\dagger \mathrm{d}$, that results into the model *SOLA-NOMBOW*.

Figures V.2 and V.3 show examples of such data contributions to model *SOLA-NOMBOW*, at different depths. At 1410 km (figure V.2), we see that ScS and *ScS*$_2$ weakly contribute to *SOLA-NOMBOW*. This makes sense since their ray paths are nearly vertical in the mid lower-mantle, and thus these data are weakly sensitive to velocity anomalies at that depth. We also see that *S* and *SS* are the biggest contributors to SOLA-NOMBOW at this depth. This also makes sense since their ray paths are almost horizontal in the mid lower-mantle, hence these data are very sensitive to anomalies in this depth range. In our case, removing *ScS* data would have little effect on model *SOLA-NOMBOW* at 1410 km depth, but certainly not at other, deeper depths. At 2800 km depth, ScS wave contributions are much larger than S and SS waves. Besides, modes bring large amount of information by comparing to body waves. Such

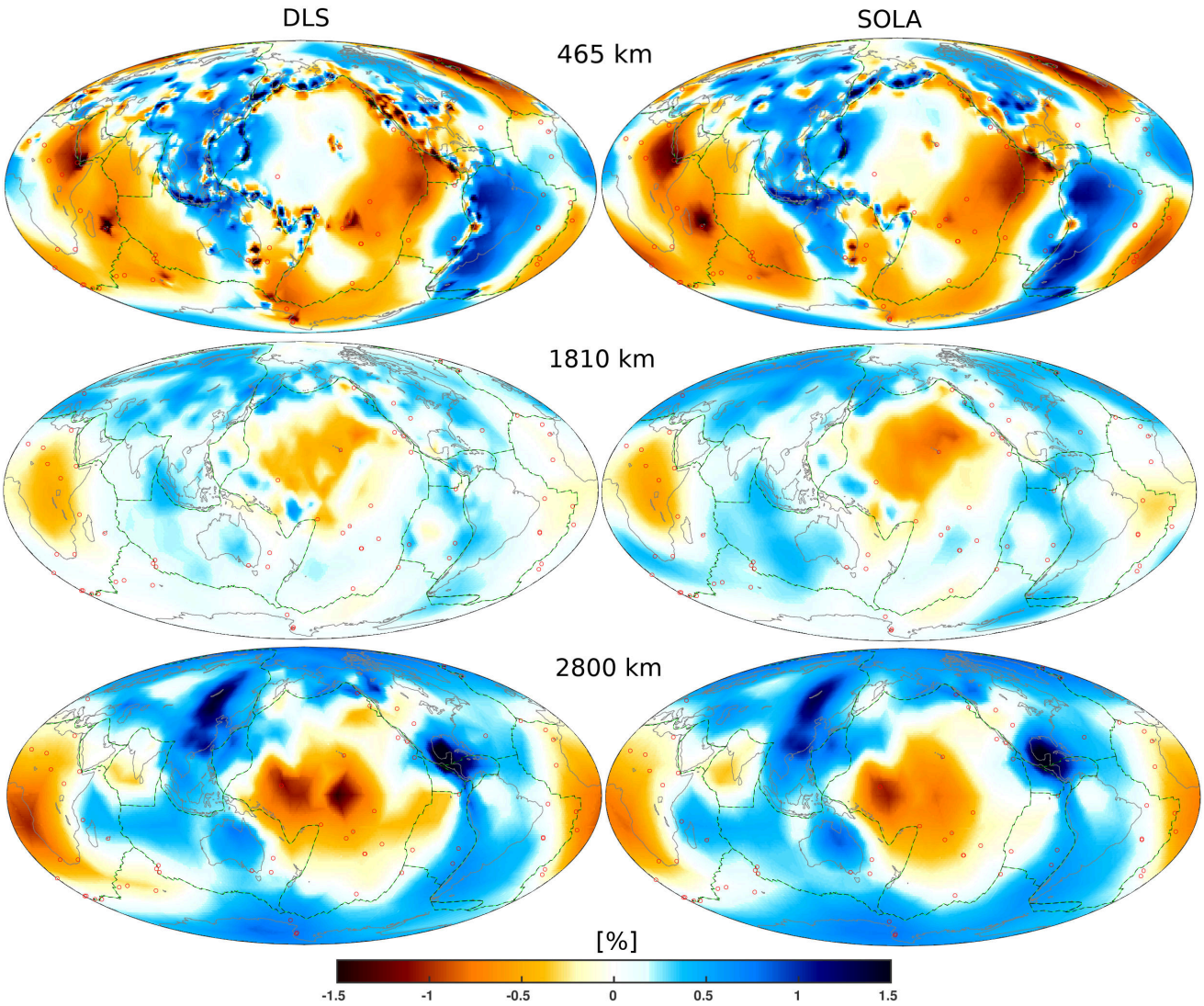

Figure V.1 – Global tomographic images obtained using (left) the damped least-squares inversion and (right) the SOLA inversion. The depth are (top row) 465 km, (middle row) 1810 km and (bottom row) 2800 km. Dashed green-black lines are tectonic plate boundaries and empty red circles depict the hot spots. Perturbations are computed from the 1D-Earth model IASP91 (Kennett and Engdahl, 1991).

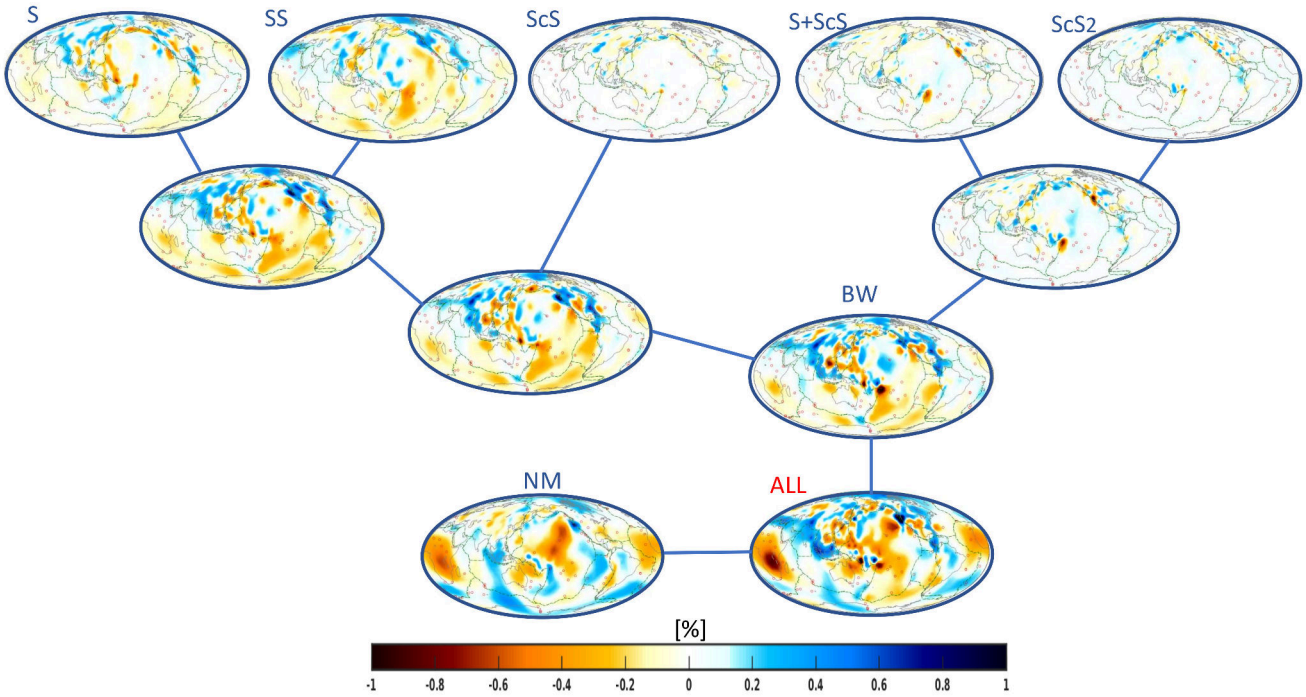

Figure V.2 – SOLA tomographic model at a depth of 1410 km. We split the contribution of all seismic data type into S-wave, SS-wave, ScS-wave, S+ScS-wave, ScS_2-wave and normal modes (NM). Tomographic model labeled with BW for body waves is the sum of all body-wave contributions without normal mode. Lines between every tomographic models indicate contributions used to build the tomographic model. The last tomographic mode (ALL) contain all seismic data types and corresponds to the SOLA model at 1410 km (see Figure V.4). Perturbations are computed from the 1D-Earth model IASP91 (Kennett and Engdahl, 1991). Pay attention to the colorbar +/- 1% aiming to detect small amplitudes contributions for each phase.

a model decomposition can therefore be used to assess the importance of a particular data subset.

V.3.3 Characteristics of model *SOLA-NOMBOW*

Figures V.4 and V.5 display the tomographic images of S-wave velocity variations from 465 km down to 2800 km. Depths shallower than 465 km are not presented here, since we do not include surface waves in this study inducing poor constrains on shallow layers.

In the upper mantle, low seismic anomalies appear beneath mid-ocean ridges in the Pacific and Atlantic. Very slow seismic anomalies are particularly visible beneath the East African rift, La Réunion and Iceland. All these low anomalies seem to fade away below 735 km depth or deflected from their original locations. Fast seismic anomalies are represented by the well delimited Asian subductions from Aleutians until Kermadec-Tonga, South America zone is also clearly visible from 465 km to a least 1035 km. Center Pacific in the upper mantle appear fast in our images, which may seem strange in this region. However since body waves are nearly all vertical and in the same direction, very few constraints are applied to the upper mantle under Hawaii. Due to this lack of constraints, normal modes take the lead in the joint

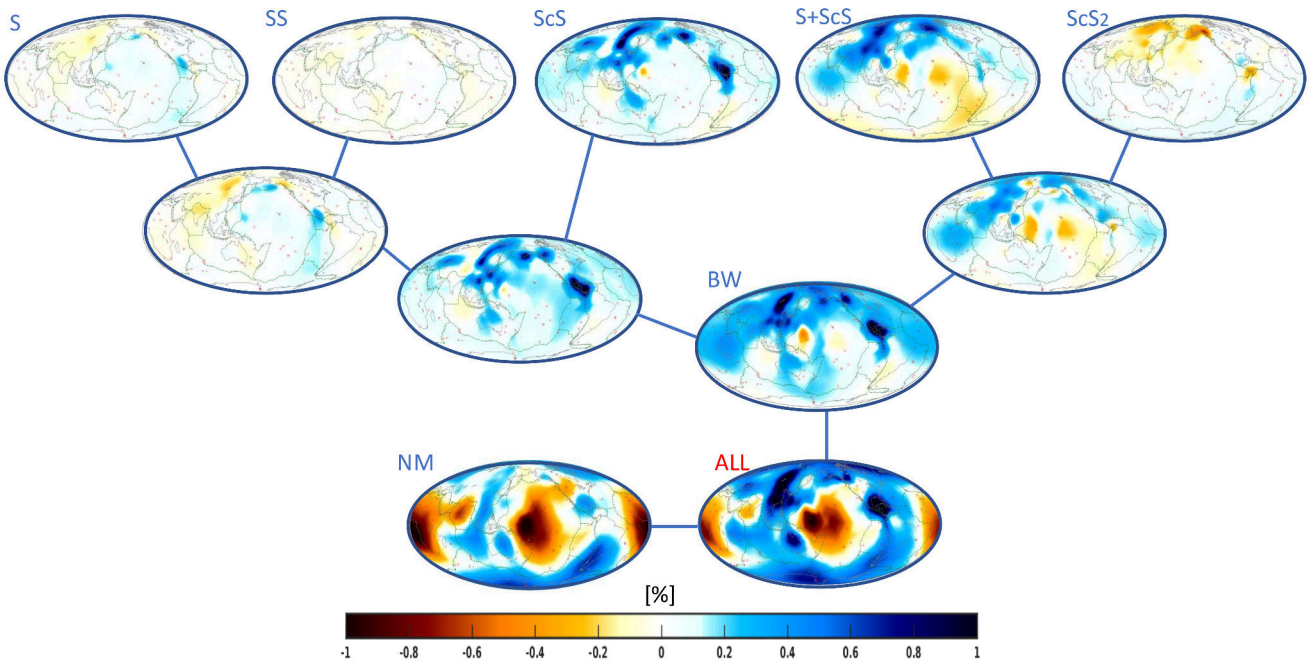

Figure V.3 – SOLA tomographic model at a depth of 2800 km. We split the contribution of all seismic data type into S-wave, SS-wave, ScS-wave, S+ScS-wave, ScS_2-wave and normal modes (NM). Tomographic model labeled with BW for body waves is the sum of all body-wave contributions without normal mode. Lines between every tomographic models indicate contributions used to build the tomographic model. The last tomographic mode (ALL) contain all seismic data types and corresponds to the SOLA model at 2800 km (see Figure V.5). Perturbations are computed from the 1D-Earth model IASP91 (Kennett and Engdahl, 1991). Pay attention to the colorbar +/- 1% aiming to detect small amplitudes contributions for each phase.

inversion and map fast anomalies in this region. We can spot easily the Farallon subduction under North America from 900 km down to 1200 km which is in agreement with other studies (Sigloch et al., 2008; Zaroli, 2016). In the lower mantle, the strong two degree pattern is visible over depths from 1610 to 2800 km. Slow anomalies are located below the Pacific and Africa with a particular high amplitude for the Pacific. These two slow anomalies are generally associated to well-recognized LLSVPs (low large shear velocity provinces). Fast anomalies are located around these two low velocity regions with specifically high amplitudes under Asia and Center-South America. These fast anomalies are generally associated to slabs graveyard where slabs would pond over the CMB.

Figure V.6 shows four computed spectra of four global models SEISGLOB2 (Durand et al., 2017), S40RTS (Ritsema et al., 2011), SP12RTS (Koelemeijer et al., 2016) and SOLA-NOMBOW. SEISGLOB2, S40RTS and SP12RTS are parametrized with spherical harmonics and vertically with splines. All models share strong energy in the first even degrees especially in the transition zone and in the lowermost mantle (vertical lines in the left part of spectra). We see a steady decrease of the energy contained in higher degrees for SOLA-NOMBOW with depth. This decrease is associated to the diminishing body wave ray density in the mantle and a potential increasing size of seismic anomalies. Compared to S40RTS and SEISGLOB2, SOLA-NOMBOW has as much energy in the first degrees as other models but with much less energy in high degrees. This is in agreement with the fact that SOLA model is a smooth model where the inversion cannot resolve small heterogeneities but still keep reasonable energy in very well resolved features.

Above these qualitative assessments of tomographic images (French and Romanowicz, 2015; Durand et al., 2017), we are now going show how we can quantitatively estimate geophysical objects inside the mantle. We will illustrate how the SOLA appraisal is working by assessing the shape and the vertical continuity of the Samoa plume.

V.3.4 Appraisal example of model *SOLA-NOMBOW*

Low velocity structures below Samoa are often considered having the most plume-like behavior amongst all known hot spots (e.g., Romanowicz and Dziewonski, 2010), emerging from the deep mantle and reaching the upper mantle. This region has both high and low velocity anomalies coming first from the Tonga subduction (fast anomalies) and the plume under Samoa (slow anomalies), respectively (Figure V.7). Interaction between the Samoa plume and the Tonga slab makes this region geodynamically complex (e.g., Zhao, 2007; Chang et al., 2016).

In the following, we would like to quantitatively estimate the vertical continuity of the plume below the Samoa islands. To our knowledge, no example of unbiased quantitative assessment of plume continuity from transition zone to the CMB has been carried out so far. Thanks to SOLA inversion it is possible to immediately assess that feature. Contrary to previous studies, where model resolution is sampled by synthetic tests (e.g., French and Romanowicz, 2015), unbiased and quantitative information on plume continuity can be extracted from SOLA appraisals. Since resolution and uncertainties for SOLA inversion are directly available at the end of the inversion, then we avoid the time consuming task of resolution tests as it is usually done for damped least square inversions. For instance, studies with a large number

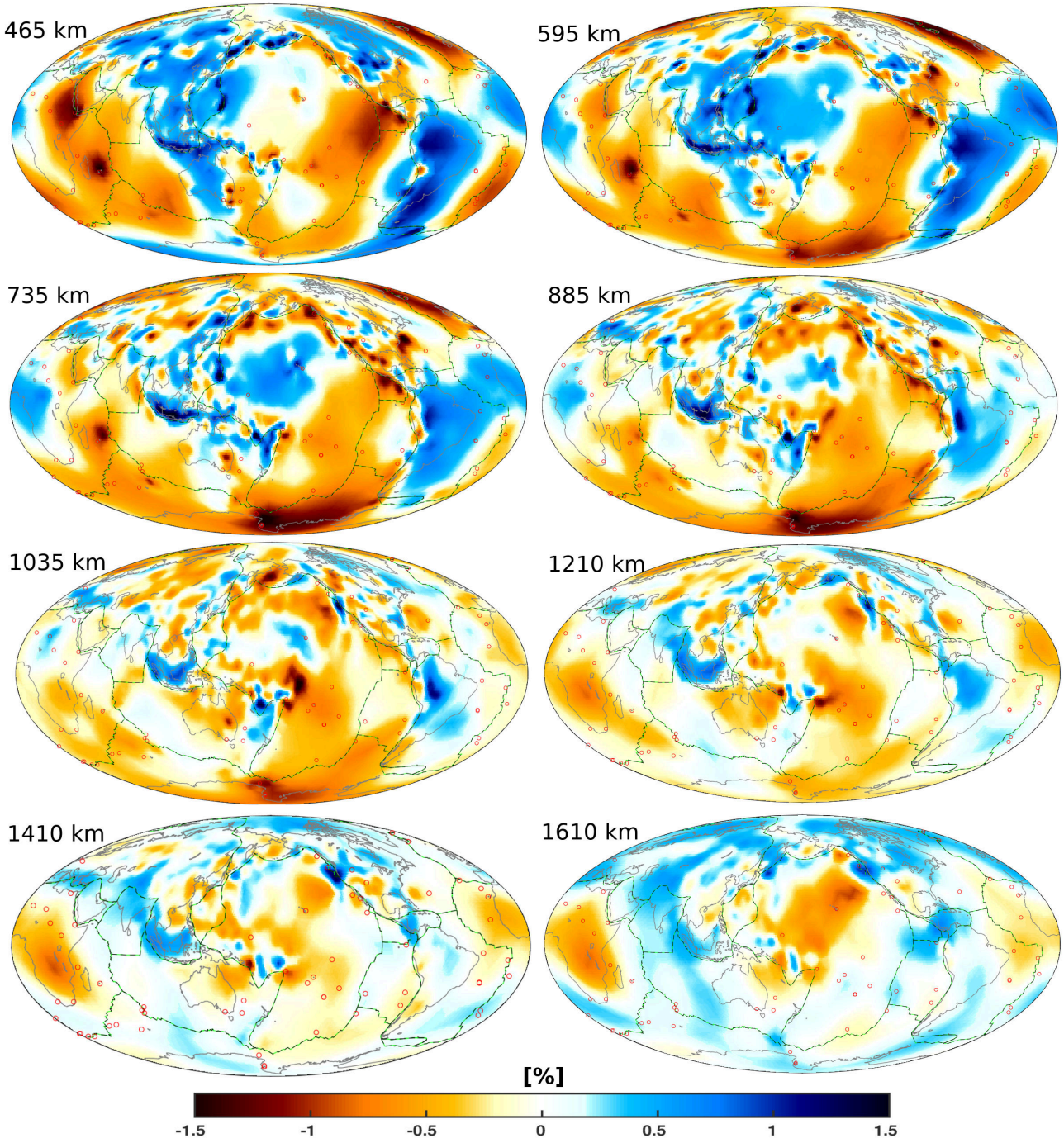

Figure V.4 – Joint global tomographic images obtained using the SOLA inversion. Display depths are (from left to right and top to botom): 465, 595, 735, 885, 1035, 1210, 1410 and 1610 km. Dashed green-black lines are tectonic plate boundaries and empty red circles depict the hot spots. Perturbations are computed from the 1D-Earth model IASP91 (Kennett and Engdahl, 1991).

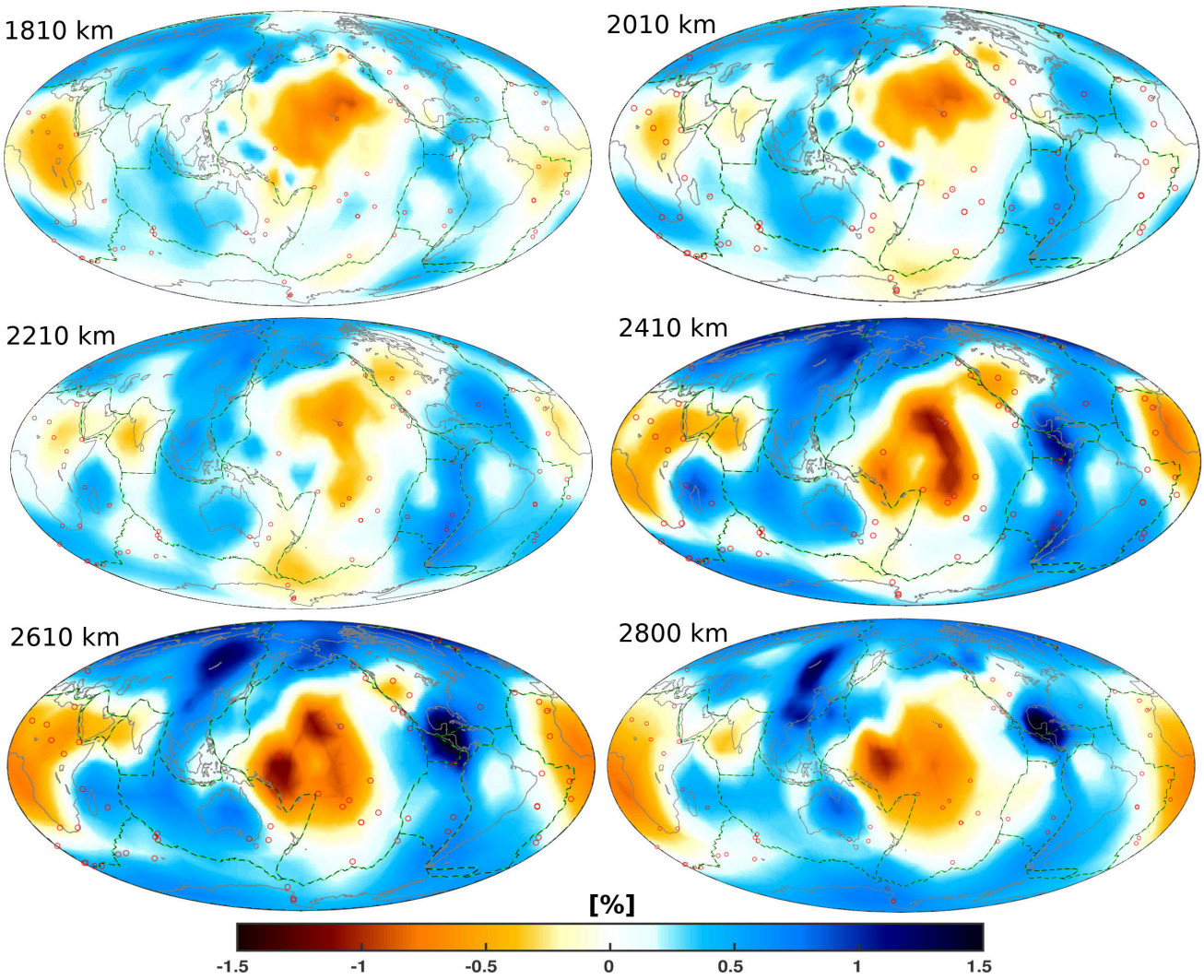

Figure V.5 – Joint global tomographic images obtained using the SOLA inversion. Display depths are (from left to right and top to botom): 1810, 2010, 2210, 2410, 2610 and 2800 km. Dashed green-black lines are tectonic plate boundaries and empty red circles depict the hot spots. Perturbations are computed from the 1D-Earth model IASP91 (Kennett and Engdahl, 1991).

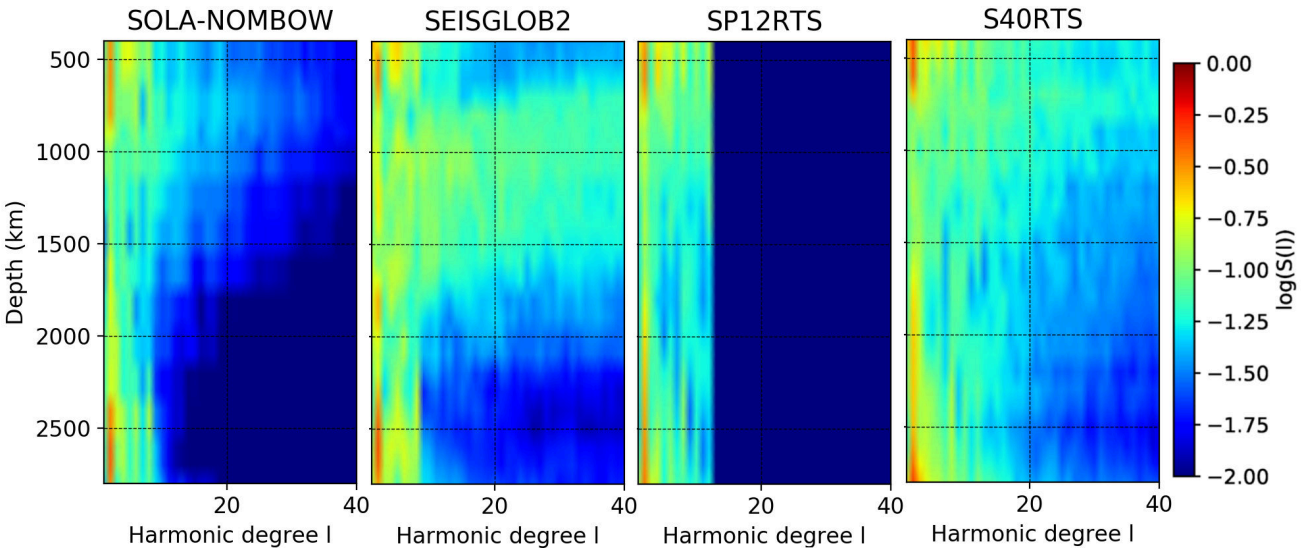

Figure V.6 – Logarithm of the amplitude spectra for (from left to right) SOLA-NOMBOW, SEISGLOB2, SP12RTS, S40RTS. SOLA-NOMBOW model has horizontal lines across the spectrum representing the different layers of the model. S40RTS, SP12RTS and SEISGLOB2 are vertically parametrized by splines. This figure is made with the help of Seistomopy (Durand et al., 2018).

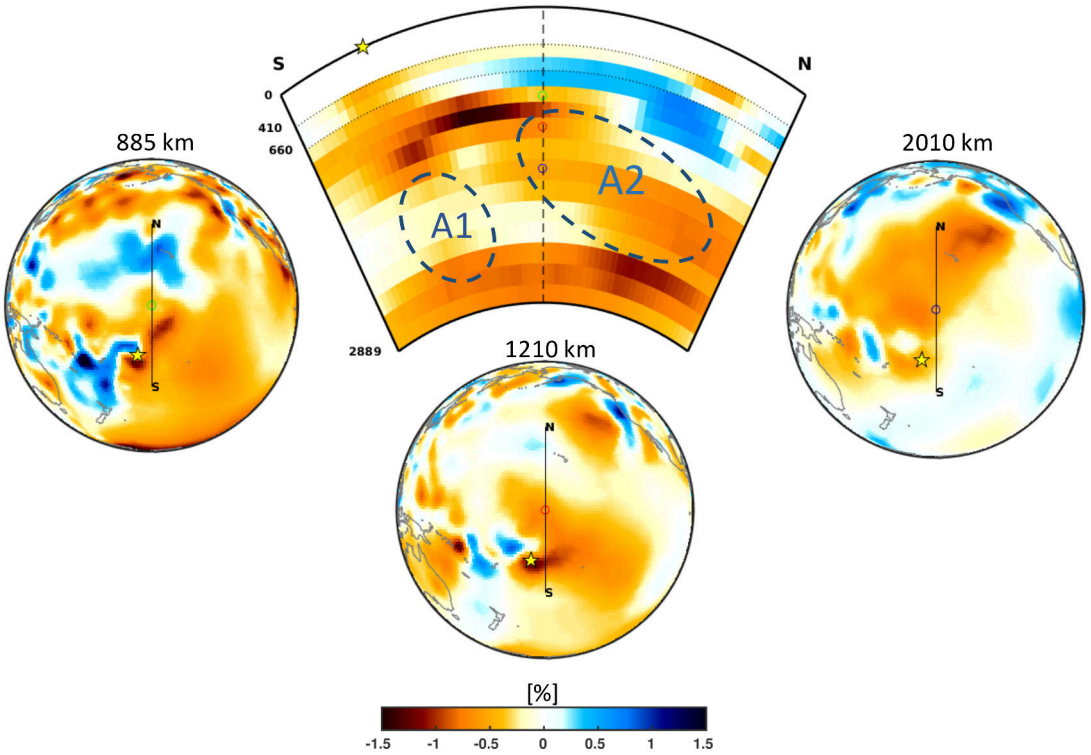

Figure V.7 – North-South cross-section over Pacific through the Samoa plume. Blue dashed ellipses indicate the areas to assess. Yellow star indicates the Samoa hot spot location at the Earth's surface. Perturbations are computed from the 1-D-Earth model IASP91 (Kennett and Engdahl, 1991).

of parameters ($> 10^6$ parameters) carry out resolution tests to ascertain the limit of plume detectability considering various array geometry (Maguire et al., 2018). Although useful, these studies could be prohibitive without access to large computational resources (HPC).

A first intuition about the geometry of the anomaly below the Samoa hot spot would be a vertical plume. Figure V.7 introduces the plume continuity problem below Samoa. We may think that there is a vertical connection between the surface (hot spot) and the CMB (A1 ellipse on figure V.7). However, we see a nearly zero seismic anomaly between 1900 km and 2400 km of depth. To better assess this hypothesis we present the appraisal figures at 2110 and 2310 km (Figures V.8 and V.9) right below the Samoa hotspot. Appraisal figures are composed of four elements: a model $\hat{m}_k$, the uncertainties $\sigma_{\hat{m}_k}$, the averaging kernels $A^{(k)}$ and the target kernels $T^{(k)}$ (see section V.2.2.2). For each of these elements we have 3 different views: an horizontal slice, a north-south and east-west cross-section. All horizontal slices are centered over the point of interest. The model $\hat{m}_k$ shows the seismic anomalies with the same colorbar as previously with a range of [-1.5:1.5]%. $A^{(k)}$ indicates the actual volume on which the average is carried out and $\sigma_{\hat{m}_k}$ the uncertainties on this average. $T^{(k)}$ represents the target volume over which we would like to average. The target kernel is defined to be the more spiky as possible considering the ray density in the vicinity of the model parameter.

We are only be interested in the deep layers of the model (deeper than 660 km) since resolution in the upper mantle is not good enough. Model parameters in the upper mantle exhibit a distorted averaging kernel toward the surface indicating a stretching potentially induced by seismic rays traveling in the same direction (see the appraisal figure in the Samoa tar file: node 11009). Figures V.8 and V.9 show the model appraisals where the velocity anomalies are close to zero at 2110 nd 2310 km depth. The third column, $A^{(k)}$ shows different slices of the averaging kernel. This kernel is well localized and widely spread compared to the target kernel $T^{(k)}$ (fourth column). Meaning that a large volume is averaged to produce the value at the targeted model parameter. Then we compare the size of the averaging kernel with the size seismic anomalies displayed on the first column. One can note the incoming slab from west and seemingly ponding at 2110-2310 km. This last remark may be quite important since we could, at this depth, average very low (plume) with very high (the slab) seismic anomalies. Such regions with large averaging kernels would exhibit seismic anomalies close to zero. As a consequence, we could miss the vertical plume continuation due to a combined effect of: 1) complex intricated structures (slab-plume interaction) and 2) a poor resolution at this depth compared to the heterogeneity sizes. It is therefore not possible to state that the Samoa plume can be followed vertically from the transition zone down to the CMB.

A second hypothesis could appear by analyzing the figure V.7. Slow seismic structure below Samoa could come from a deflected plume originating farther north (see A2 ellipse on figure V.7). Since we do not want to show hundreds of parameter appraisals, we only are going to assess the more decisive depths for the vertical continuity of the plume. Though we only show the most relevant points to evaluate the plume continuity, appraisal figures of any model parameters could be obtained.

Let see if the potential deflecting point occurring around 1110 km depth can be resolved or not (red circle on figure V.7). Figure V.10 shows the appraisal of a model parameter at 1110 km depth in this region. The averaging kernel ($A^{(k)}$) is well localized but is stretched in the north-east direction. This is potentially due to a preferential ray direction owing to the distribution of stations and earthquakes. Cross-sections for the averaging kernel $A^{(k)}$ indicate

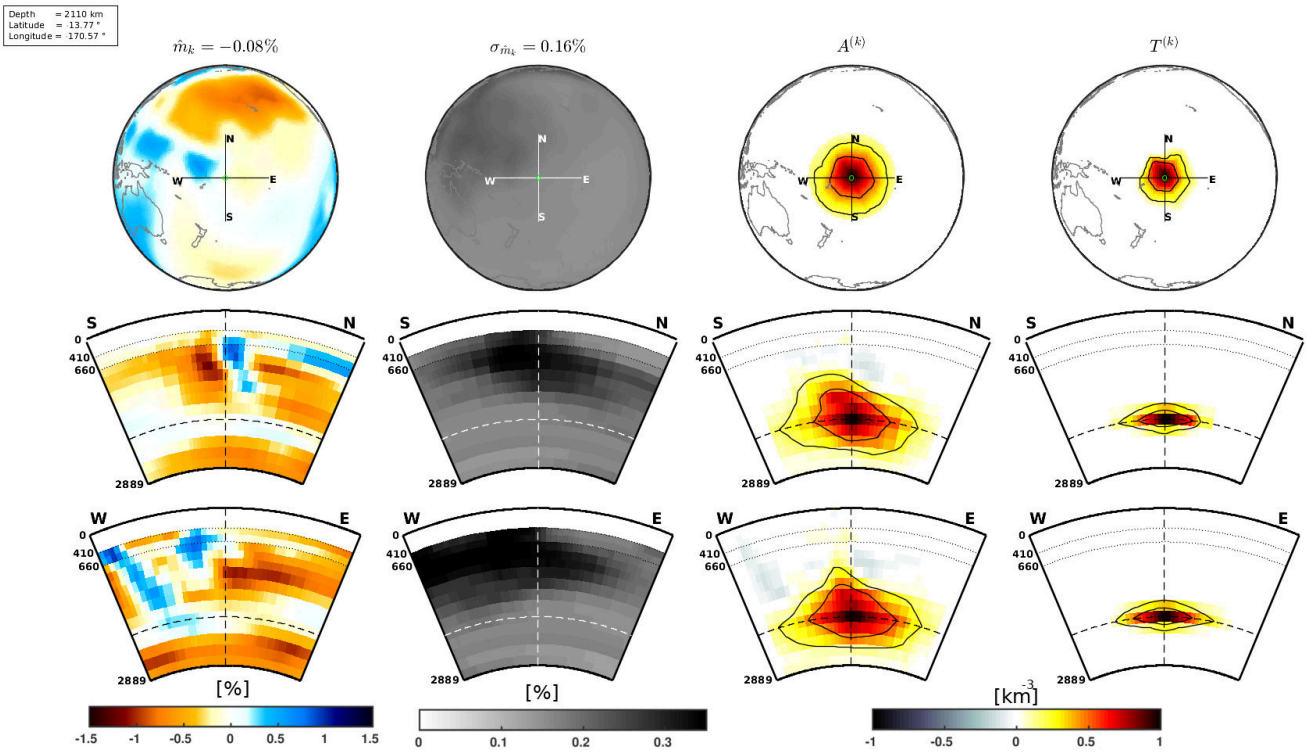

Figure V.8 – Appraisal for a model parameter at a depth of 2110 km under Samoa hot spot. Uncertainties colorbar indicates large uncertainties for black regions with range of [0:0.35]% and light colored regions for low uncertainties. Colorbars for $T^{(k)}$ and $A^{(k)}$ are the same and normalized with a range of [0:1], with black colors for high amplitudes and white for null amplitude. Contours for averaging and target kernels are drawn for values at 0.2 and 0.5.

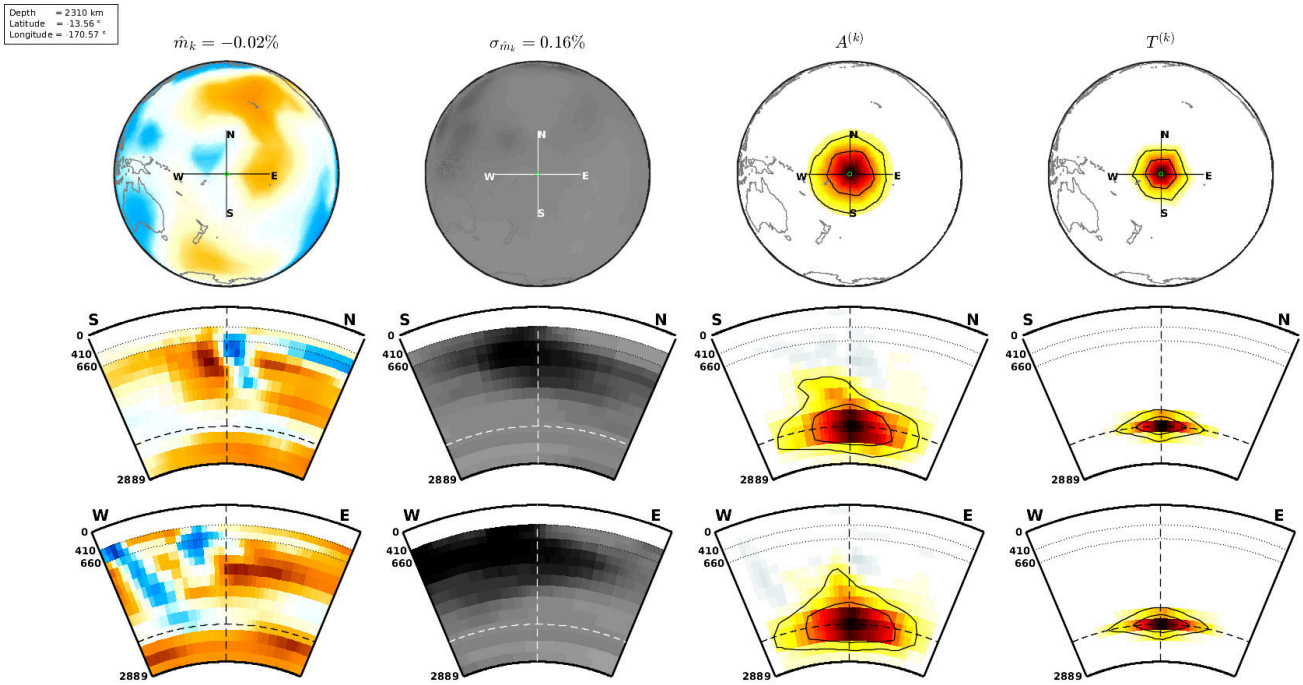

Figure V.9 – Appraisal for a model parameter at a depth of 2310 km under Samoa hot spot. Uncertainties colorbar indicates large uncertainties for black regions with range of [0:0.35]% and light colored regions for low uncertainties. Colorbars for $T^{(k)}$ and $A^{(k)}$ are the same and normalized with a range of [0:1], with black colors for high amplitudes and white for null amplitude. Contours for averaging and target kernels are drawn for values at 0.2 and 0.5.

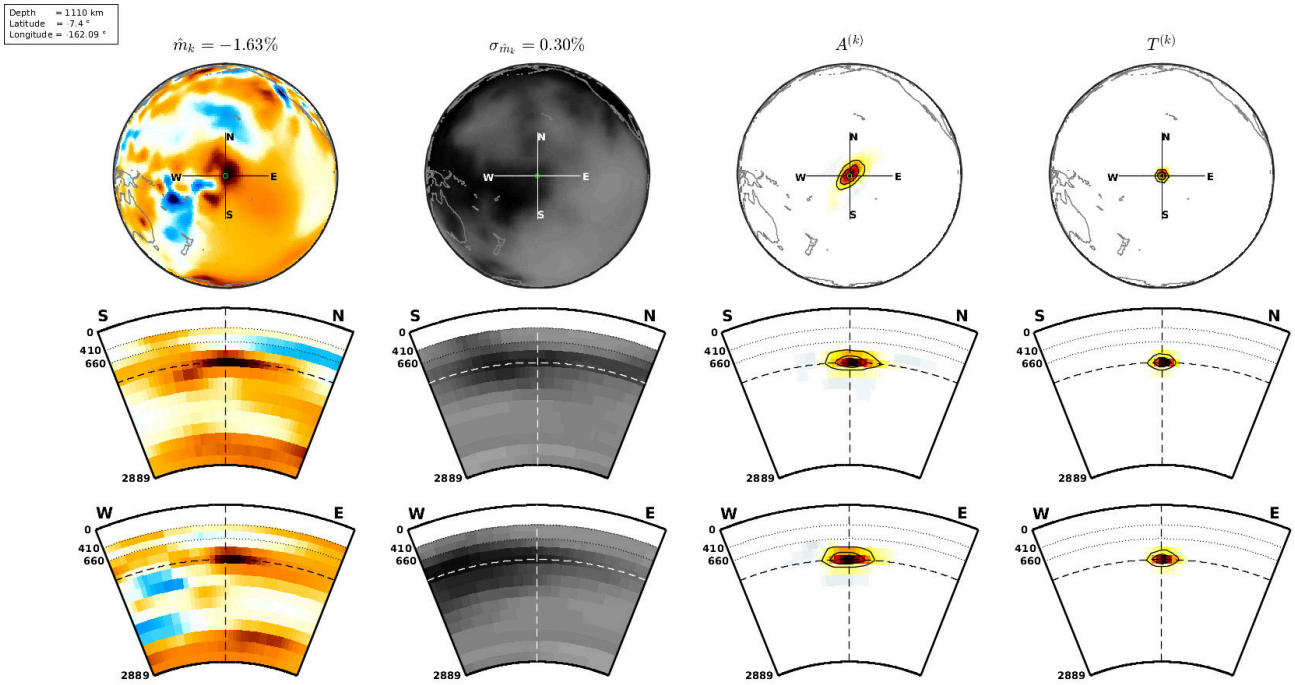

Figure V.10 – Appraisal for a model parameter at a depth of 1110 km under Samoa hot spot. Uncertainties colorbar indicates large uncertainties for black regions with range of [0:0.35]% and light colored regions for low uncertainties. Colorbars for $T^{(k)}$ and $A^{(k)}$ are the same and normalized with a range of [0:1], with black colors for high amplitudes and white for null amplitude. Contours for averaging and target kernels are drawn for values at 0.2 and 0.5. Same color bars thant figure V.8.

a very well localized and centered over the point of interest. Their extended shapes in the horizontal directions are due to S and SS-waves travelling horizontally at this depth (turning points at this depth). Although slightly stretched horizontally, averaging kernels are sufficiently thin compared to seismic anomalies $\hat{m}_k$. From model and uncertainty maps, we have a slow seismic anomaly (-1.63%) with an uncertainty of 0.3% computed from the averaging volume $A^{(k)}$. This point is thus clearly resolved both laterally and vertically with seismic anomaly well above the uncertainty. This model parameter at 1110 km is thus resolved horizontally and vertically owing to our data and their associated errors.

Figure V.11 shows the appraisal for a model parameter at 1710 km. At this depth, the averaging kernel is much larger than the target kernel in both lateral and vertical directions. However, kernels are mainly distorted horizontally and keep good vertical shape. Although, the actual averaging volume is larger than the targeted one, it is good enough to make seismic features resolvable. As a remark, since the averaging volume is large it is associated to small uncertainties. The uncertainty associated to the averaging volume is $0,21\%$ which is small compared to the seismic anomaly of the model -0.78%. We can conclude the targeted parameter is resolved according to the resolution and uncertainty.

Appraisal figures for deeper model parameters are available and their interpretations are similar to those presented here. To conclude on the vertical continuity of the plume under Samoa. The plume is tomographically resolved from 660 km down to 2800 km considering our data and their associated uncertainties. However the main difficulty remains in the plume

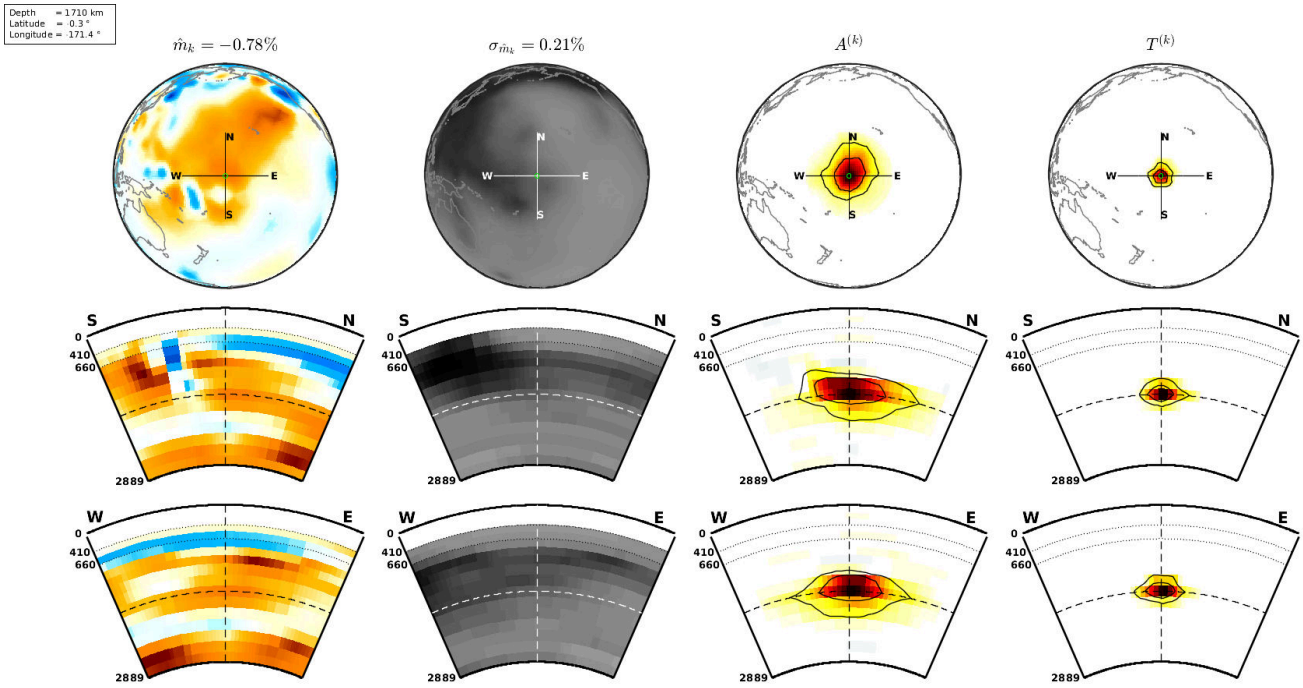

Figure V.11 – Appraisal for a model parameter at a depth of 1710 km. Uncertainties colorbar indicates large uncertainties for black regions with range of [0:0.35]% and light colored regions for low uncertainties. Colorbars for $T^{(k)}$ and $A^{(k)}$ are the same and normalized with a range of [0:1], with black colors for high amplitudes and white for null amplitude. Contours for averaging and target kernels are drawn for values at 0.2 and 0.5. Same color bars that figure V.8.

geometry. If we consider a plume perfectly vertical, this last can only be followed deep to 1900 km, below that depth, a mixing between high and low seismic velocities make the averages close to zero. Although we cannot prove the vertical continuity of the plume right below Samoa, an alternative may exist. Samoa hot spot may be fueled by a deflected plume coming from the farther north below Hawaii. Though the path from the LLSVP below Hawaii up to Samoa is tomographically resolved, it does not mean that Samoa hot spot arose from that plume. A finer parametrization could help to better resolved depths directly below the Samoa hot spot. This would allow to assess if the plume is actually present between 1900 to 2400 km depth where we cannot currently see with SOLA-NOMBOW.

V.4 Perspectives and conclusions

To conclude, we have presented a global scale tomographic model, named *SOLA-NOMBOW*, which represents isotropic shear-wave velocity variations in the 410–2889 km depth range. This model is characterized by the fact that it results, for the very first time, from a joint SOLA–Backus–Gilbert inversion (Zaroli, 2016) of finite-frequency S-wave time residuals and normal-mode structure coefficients. Furthermore, since the SOLA–Backus–Gilbert inversion scheme solves at the same time for the model estimation *and* the model appraisal – i.e. the model resolution and covariance (uncertainty) – we are able to provide to the community our model *SOLA-NOMBOW* accompanied with all its local resolution/uncertainty informations. Therefore, this will enable everyone to interpret its structural features in a more quantitative way than for other published global tomographic models.

Finally, to illustrate how these resolution/uncertainty informations may be used for appraising a given feature in *SOLA-NOMBOW*, we have shown that the mantle plume located under Samoa, which seems to be interacting with the Tonga slab, can 'reasonably' be tracked in the from 660 to 2800 km depth – in the sense that this slow-velocity conduit appears to be resolved in this entire depth range, given our data and their errors.

In short

- *The first B–G joint tomographic image of the mantle from 410 to 2889 km.*
- *We can analyze the contribution of each data type with the access of the generalized inverse.*
- *Apparaisals at interesting parameters enable quantitative interpretations of the seismic model.*

General conclusions, discussions and perspectives

Conclusions and perspectives

General summary

The general goal of this study is to produce an unbiased tomographic image of the Earth's mantle with its related appraisal (SOLA-NOMBOW). In this aim, we jointly invert normal mode data and finite-frequency S-wave time-residuals in an recently up-to-date Backus–Gilbert (B–G) inversion scheme. Compared to other global tomographic models, all based on least-squares inversion, ours is the first one to be derived using a recently developed discrete SOLA-Backus–Gilbert inversion scheme (Zaroli, 2016), which leads to several advantages. First, this allows the model SOLA-NOMBOW to be unbiased (in the sense that its values represent true averages over the Earth's properties). Second, this makes computationally feasible (with modest computational facilities) to calculate all the resolving kernels and model uncertainties (i.e., the level of data noise that propagates into the model solution) – these resolution/uncertainties information are crucially needed for reliable model appraisal, hence for quantitative interpretations. As an example, we assess the reliability of the vertical continuity of the slow velocities that could be related to the Samoa mantle plume from 660 km to 2889 km.

A first step in this tomographic work is to constitute a new S-wave time-residuals database. We use an automatic process to measure shear wave time-residuals by cross-correlation at different periods. To better constrain the lower mantle we measure interferences between S and ScS waves occurring at large epicentral distance (between 75°and 95°). However, interfering seismic phases are more complicated to measure than an simple body wave. To succeed in measuring various seismic phases, a strict measurement process has to be set. An adaptive cross-correlation window is defined for each specific phase which allows to take into account the different characteristics of every seismic phases. The improvement of body wave data coverage comes firstly from new seismic phases measured (S+ScS, ScS_2) as well as new stations located in remote locations. However, gaps remain in this coverage particularly at some depths. To overcome this problem we include normal mode data with a global sensitivity to the Earth but sensitive to large features only.

The third chapter is an article published in the *Geophysical Journal International* dedicated to the finite-frequency crustal corrections for long-period body-waves. In order to fully exploit the information contained in finite-frequency body-wave data, proper body-wave data corrections need to be set. We study, in a more systematically way, the crustal influence over S-wave time-residuals measured for different periods and over various geological settings. This study brings forth interesting questions about crustal corrections for long-period body-wave. First, it recognizes the importance to apply the correct crustal correction for every seismic phases (com-

puted from ray theory) and specifically when one measures interfering phases. Although, the scale of crustal heterogeneities is well below our resolving length, crustal heterogeneities have large influences on body-wave measurements. Second, crustal influence over time-residuals is varying as a function of the measurement period. This is problematic since we aim to exploit time-residuals differences measured at different periods to infer mantle properties. Besides, this study enables a reassessment of data uncertainties related to used crustal models. These error estimates are essentials for the inversion procedure since bad error uncertainties would induced poor model uncertainties. Crustal model uncertainty is thus added to the global error and then contributes to more robust data error estimates.

Although, the primary version of the B–G inversion is parameter-free, we make use of the discrete version of B–G recently adapted to seismic tomographic problems (Zaroli, 2016). This allows to reduce the computational cost needed to get the tomographic model as well as its associated appraisal. Joint tomographic images obtained with this method seem appealing and coherent compared to the most well-known global tomographic models (S40RTS, SEIS-GLOB2, PRI-S05). We present an example of the appraisal for SOLA inversion by assessing the vertical continuity of the plume below Samoa. SOLA-NOMBOW is made available to the whole geoscience community with its associated appraisal. This is the first model of its kind where geoscientists can study their regions of interest and by their own. We encourage tomographers to associate to their published models all tools allowing to anyone to interpret imaged structures. Quantitative interpretations can then be used as data support for other studies in geoscience.

Perspectives

Data improvements

- Body-wave: data error

  Improve data error estimations is paramount for the future of tomographic inversion. Although, we are now identifying more precisely the different contribution of all errors. An individualized data error according to the measurement process or the earthquake mislocation to go further seem necessary. Besides, a reduction of this error could be of substantial use in the tomographic interpretation. As a matter of fact, a significant reduction of earthquake mislocation, the main source of uncertainty, would allow to improve the model uncertainties. And ultimately to refine the interpretation of the tomographic model.

- Body-wave: new measurements

  Diffracted S-wave should be definitely tackled for future studies. They have strong sensitivities to the lowermost mantle and could considerably improve the body-wave data coverage in this zone. However, analytical expressions for sensitivity kernels require high computational cost for high frequency seismograms (normal mode summation,

Kárason and van der Hilst (2001)). To do so, our robust measurement process should be tuned to measure S_{diff} which is not complicated so far. But, accurate sensitivity kernels associated to these diffracted phases have to be generated to extract the best as possible the strong dispersive finite-frequency signals of diffracted waves. Nevertheless, if one keeps an discrete parametrization for the inverse problem, a numerical S_{diff} sensitivity kernel can be enough (see projecting kernels on grid at the end of chapter 2). But for parameter-free inversion, a very accurate description of this kernel is mandatory.

Another phase can be consider in the future: SKS wave. This S-wave is traveling inside the outer core under the form of a P-wave and then is transmitted as a S-wave to the mantle. Though, this wave must be be handful, hypothesis taken in this work impeded the use of SKS waves. First, in this study we only consider SH wave in order to get rid of any P-to-S conversion problem. However, to measure SKS waves, S-waves with a vertical polarization have to be considered since we suppose an isotropic mantle. This hypothesis can be quite far from truth. Thus, the risk of interpreting SKS time-residuals anomalies for anisotropy should be assessed before starting a new SKS-wave database.

- Body wave: crustal phases

  Shear waves do contain energy over a broad range of frequencies. In order to extract a maximum of information from shear-wave data, measurements at different frequency have been carried out. Although low-frequency measurements are much more impacted by crustal phases than high-frequency measurements, shear waves measured at 22s (maximum of energy for long-period shear waves in our data set) are strongly impacted by crustal phases. Filtering out the lowest periods (51s) could decrease the number of crustal phases takes into account and thus the computationnal time of the synthetic generation. However, this time is small compared to the whole computationnal time for synthetic generation. Besides, measurements at 51s with those at 10s and 22s could substantially support the multifrequency tomography in a parameter-free inversion compared to the ray-based inversion. Off course, meaningful uncertainties should be attributed to each measurements before inversion, with higher uncertainties for measurements made at low frequency. As part of reducing the number of crustal phases injected in the synthetic, another option can emerge. We could shrink the cross-correlation window in order to not taking into account late and powerful crustal phases. However, this means we need to shrink the sensitivity volume associated to this measurement. The question is: to what extend we want to reduce this finite-frequency kernel knowing that at some point we will reach the (projected) infinite-frequency kernel (ray theory). There is a trade-off between simplicity of the synthetic generation and the complexity of the wave propagation that we consider for the inversion.

- Normal modes: better estimations of uncertainties on structure coefficients

  As seen in the previous chapter, uncertainties on normal mode data are largely under estimated. However, it is essential to have good uncertainties on data in B–G inversion. Better estimation of uncertainties on structure coefficients is fundamental for one eagers to obtain realistic model uncertainties from SOLA inversion. Possible improvements could come from derivative-free parameter search as neighborhood algorithm based on the autoregressive method (Pachhai et al., 2015). Or full-coupling hypothesis in the seismic spectra computation (Akbarashrafi et al., 2018).

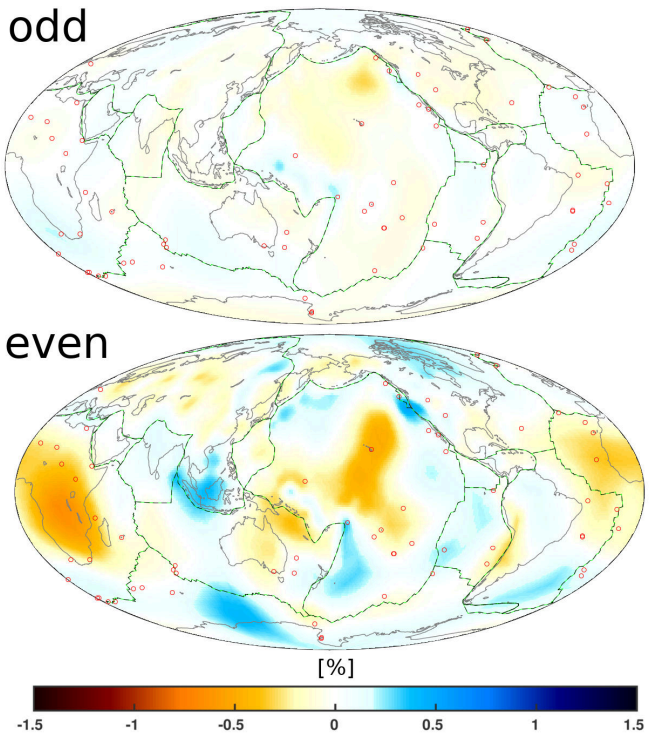

Figure 1 – Tompographic image at 1450 km of the joint SOLA inversion. Plate boundaries are indicated with green and blacks dashes. Red circles represent the hot spot locations. Perturbations are computed from the 1D-Earth model IASP91 (Kennett and Engdahl, 1991).

One possibility to assess the quality of normal mode data uncertainties would be to compute the splitting functions predicted by the SOLA joint model. Then, it would be possible to compare with splitting function coming from observed seismograms.

- Normal modes: even and odd decomposition

  We use in this study self and cross-coupling between structure coefficients while inverting normal modes. Since self-coupling only constrains the even degree structure of the Earth, we have a partial image of the true Earth structure. For that reason we add in this study cross-coupling between structure coefficients allowing to get information over the even and odd degree structures. As shown on figure 1, information bring by even degrees is dominant compared to odd degrees. This is especially due to the large number of self-coupling measurements compared to cross-coupling measurements inducing disparity between even and odd degrees (only 19% of our normal mode dataset is sensitive to odd-degree structures).

- Surface waves

  Surface wave data should definitely be integrated into the joint B-G inversion. As previously, our choice over body-wave and normal-mode data was driven by the lower mantle coverage. Although, surface waves can greatly improve the imaging of this region by better constraining the inversion, they still have a secondary role in terms of coverage compared to normal modes and body waves. Then, we did not use surface waves for computational reasons, we did not want to inject too many data and thus have too large computational time. Besides, inversion of surface waves is a compound inversion

much like normal modes data. A first non linear inversion is applied and then a second linear inversion is carried out, though B-G scheme cannot handle strongly non-linear inversion. As a perspective, we try to invert directly surface wave data with a linear inversion by making use of 3D finite-frequency kernels. This step is paramount if we want meaningful data uncertainties and not poor estimations coming from a non-linear process. As an additionnal remark, surface wave data obviously help to better constrain the lower mantle for joint inversion by helping the fit of the data. But for B-G inversion, the averaging volume is defined as the data density over a specific volume. Though we add surface data this will not change the target averaging volumes in the lower mantle (since it won't change data density in this region). As a consequence, changes induce by adding surface wave data could be minimal compared to their impact for data-fitting inversion schemes.

Parametrization

The parametrization used in this work is optimized for the Zaroli et al. (2010) data set (see appendix B to have an insight of the parameter coverage for every layers showed in this work). Since we considerably improve the data coverage especially in the lower mantle, we could have updated the node density to the new data base. But, for this first joint global SOLA inversion, we wanted to minimize the computational cost at most. The aim was first to show the possibility to create a global SOLA model of the Earth mantle with modest computational facilities (see Appendix A: computational facilities) before to extend to a larger parameter number. Now that is possible we would like to increase the number of parameters and of data.

The perspective of increasing the number of parameters in our inversion is twofold. First, we can better exploit information contained in the new data set and thus have potentially an increase in our model resolution for none significant increase of uncertainties. Second, we want to decrease the size of cells for discrete inversions. As shown in chapter 2, sensitivity kernels are projected on a coarse mesh to be inverted which significantly degrade the sensitivity kernels. Besides, we would like to avoid abrupt changes in cell sizes which increase the effect of kernel degrading.

A additional step toward a global parameter-free Backus–Gilbert inversion would be to build an hybrid approach between continuous and discrete SOLA inversion. Before, the continuous version of the Backus-Gilbert inversion, we could increase, in the discrete SOLA version, the number of parameter by following the data density. This will improve both data resolution exploitation as well as quality of projected kernels. Once the number of parameter is close of the data number, the transition toward free-parameter SOLA inversion will not be a problem any more.

The B-G inversion scheme should not be mixed with parametrization, after all, the original form was parameter-free (Backus and Gilbert, 1967, 1968, 1970). It is not a matter of how we consider the parameters in our mesh but more over which volume we can compute localized averages of the true model. This averaging volume is characterized in our inversion scheme

(SOLA) by the data density over a specific area. Some regular parametrization can be used with very heterogeneous data coverage. Global tomography is absolutely a strong mixed-determined problem and the non-uniqueness of this problem cannot allow to have a single estimate for every parameters. But the advantage of estimating averages of parameters rather than parameters themselves is that, most of the time, we can find unique averages even if model parameters themselves are not. In that sense, you can remove the non-uniqueness of the inverse problem without introducing prior information coming from other sources.

Interpretation of tomographic images

Samoa

Quantitatively images of the Samoa plume geometry and vertical continuity could help to understand it origin and dynamic (e.g., Chang et al., 2016). Samoa plume is considered from most studies (Rose and Koppers, 2019; Courtillot et al., 2003) as a “primary hot spot" meaning that its origin lies in the deep mantle (LLSVP) as well as Hawaii, Louisville or Ascension. The other group of hot spots called “secondary hot spot" are supposed to root in the upper mantle.

Montelli et al. (2006) and French and Romanowicz (2015) produce global tomographic images of plumes and give estimations of the vertical extend of Samoa plume. Montelli et al. (2006) indicates that Samoa plume is well resolved until 1450 km depth at least, and then collapse with another plume into the lower mantle (Cook island).

What should we do with our tomographic images ?

Future works to fully exploit the tomographic appraisal toolkit could be to answer important geodynamical questions. For instance, debates on the heat flux conveyed by plumes are still hot, it would be interesting to infer new heat flux from new S-wave velocity images with their associated uncertainties. Previous studies with P-wave tomography tried to estimate that heat flux from Stoke's flow models (Nolet et al., 2006). However, unbiased seismic velocities uncertainties are not propagated through heat flux maps. Besides, S-wave velocities are significantly more affected by thermal anomalies than P waves. These new S-wave tomographic images may be used to produce more precise and quantitative estimation of the heat flux transport through plumes with associated uncertainties.

Geochemistry sorely lacks of precise mantle flow models. Recent studies relate the helium and lead isotopic ratios of island ocean basalt to LLSVP (e.g. Jackson et al., 2017). However, for now only vertical projection of hot-spot locations on the CMB is done which is not taking into account the potential deflection induced by mantle flow. One desires to properly model the path of some geochemical elements from CMB to surface needs precise and quantitative image of mantle plumes. Implications for these combined seismological-geochemical studies can be huge in terms of LLSVP composition (old portions of oceanic crust) and of time stability.

Bibliography

Agrusta, R., Goes, S., and van Hunen, J. (2017). Subducting-slab transition-zone interaction: Stagnation, penetration and mode switches. *Earth and Planetary Science Letters*, 464:10–23.

Akbarashrafi, F., Al-Attar, D., Deuss, A., Trampert, J., and Valentine, A. (2018). Exact free oscillation spectra, splitting functions and the resolvability of Earth's density structure. *Geophysical Journal International*, 213(1):58–76.

Anderson, O. (2002). The power balance at the core–mantle boundary. *Physics of the Earth and Planetary Interiors*, 131(1):1–17.

Anderson, O. L., Schreiber, E., Liebermann, R. C., and Soga, N. (1968). Some elastic constant data on minerals relevant to geophysics. *Reviews of Geophysics*, 6(4):491–524.

Aster, R., Borchers, B., and Thurber, C. (2012). Parameter estimation and inverse problems, revised edn.

Aster, R. C., Borchers, B., and Thurber, C. H. (2018). *Parameter estimation and inverse problems*. Elsevier.

Backus, G. and Gilbert, F. (1968). The resolving power of gross earth data. *Geophysical Journal International*, 16(2):169–205.

Backus, G. and Gilbert, F. (1970). Uniqueness in the inversion of inaccurate gross earth data. *Philosophical Transactions of the Royal Society of London. Series A, Mathematical and Physical Sciences*, 266(1173):123–192.

Backus, G. E. and Gilbert, J. (1967). Numerical applications of a formalism for geophysical inverse problems. *Geophysical Journal International*, 13(1-3):247–276.

Bassin, C., Laske, G., and Masters, G. (2000). The current limits of resolution for surface wave tomography in North America. *Eos*, 81.

Bolton, H. and Masters, G. (2001). Travel times of P and S from the global digital seismic networks: Implications for the relative variation of P and S velocity in the mantle. *Journal of Geophysical Research: Solid Earth*, 106(B7):13527–13540.

Burke, K., Steinberger, B., Torsvik, T. H., and Smethurst, M. A. (2008). Plume generation zones at the margins of large low shear velocity provinces on the core–mantle boundary. *Earth and Planetary Science Letters*, 265(1-2):49–60.

Camp, V. E. (2019). Plume-modified mantle flow in the northern basin and range and southern cascadia back-arc region since ca. 12 ma. *Geology*.

Capitanio, F., Morra, G., and Goes, S. (2007). Dynamic models of downgoing plate-buoyancy driven subduction: Subduction motions and energy dissipation. *Earth and Planetary Science Letters*, 262(1-2):284–297.

Carrier, A. and Got, J.-L. (2014). A maximum a posteriori probability time-delay estimation for seismic signals. *Geophysical Journal International*, 198(3):1543–1553.

Chang, S.-J., Ferreira, A. M., and Faccenda, M. (2016). Upper-and mid-mantle interaction between the Samoan plume and the Tonga–Kermadec slabs. *Nature communications*, 7:10799.

Chapman, C. H. (1978). A new method for computing synthetic seismograms. *Geophysical Journal of the Royal Astronomical Society*, 54(3):481–518.

Chevrot, S. (2002). Optimal measurement of relative and absolute delay times by simulated annealing. *Geophysical Journal International*, 151(1):164–171.

Courtillot, V., Davaille, A., Besse, J., and Stock, J. (2003). Three distinct types of hotspots in the Earth's mantle. *Earth and Planetary Science Letters*, 205(3-4):295–308.

Dahlen, F. and Baig, A. M. (2002). Fréchet kernels for body-wave amplitudes. *Geophysical Journal International*, 150(2):440–466.

Dahlen, F., Hung, S.-H., and Nolet, G. (2000). Fréchet kernels for finite-frequency traveltime - I. Theory. *Geophysical Journal International*, 141(1):157–174.

Deuss, A., Ritsema, J., and van Heijst, H. (2013). A new catalogue of normal-mode splitting function measurements up to 10 mhz. *Geophysical Journal International*, 193(2):920–937.

Dubois, F., Lambotte, S., Zaroli, C., and Rivera, L. (2019). Global finite-frequency S-wave delay-times: how much crust matters. *Geophysical Journal International*, 218(3):1665–1684.

Durand, S., Abreu, R., and Thomas, C. (2018). Seistomopy: Fast visualization, comparison, and calculations in global tomographic models. *Seismological Research Letters*, 89(2A):658–667.

Durand, S., Debayle, E., Ricard, Y., Zaroli, C., and Lambotte, S. (2017). Confirmation of a change in the global shear velocity pattern at around 1000 km depth. *Geophysical Journal International*, 211(3):1628–1639.

Dziewonski, A., Chou, T.-A., and Woodhouse, J. (1981). Determination of earthquake source parameters from waveform data for studies of global and regional seismicity. *Journal of Geophysical Research: Solid Earth*, 86(B4):2825–2852.

Dziewonski, A. M. and Anderson, D. L. (1981). Preliminary reference Earth model. *Physics of the Earth and planetary interiors*, 25(4):297–356.

Dziewonski, A. M., Lekic, V., and Romanowicz, B. A. (2010). Mantle anchor structure: an argument for bottom up tectonics. *Earth and Planetary Science Letters*, 299(1-2):69–79.

Edmonds, A. (1960). *Angular momentum in quantum physics*. Princeton University Press.

Ekström, G., Nettles, M., and Dziewoński, A. (2012). The global CMT project 2004–2010: Centroid-moment tensors for 13,017 earthquakes. *Physics of the Earth and Planetary Interiors*, 200:1–9.

Encyclopedia, P. S. G. (2016). The Structure of the Earth. `http://geography.parkfieldprimary.com/rocks-and-soils/the-earth`. [Online; accessed 18-June-2019].

Ferroir, T. and Dequincey, O. (2008). La post-perovskite, un minéral de très haute pression. `https://planet-terre.ens-lyon.fr/article/post-perovskite.xml#D-post-perovskite`. [Online; accessed 23-July-2019].

French, S. W. and Romanowicz, B. (2015). Broad plumes rooted at the base of the Earth's mantle beneath major hotspots. *Nature*, 525(7567):95.

Fukao, Y. and Obayashi, M. (2013). Subducted slabs stagnant above, penetrating through, and trapped below the 660 km discontinuity. *Journal of Geophysical Research: Solid Earth*, 118(11):5920–5938.

Fukao, Y., To, A., and Obayashi, M. (2003). Whole mantle P wave tomography using P and PP-P data. *Journal of Geophysical Research: Solid Earth*, 108(B1):ESE–8.

Garnero, E. J. and Lay, T. (2003). D" shear velocity heterogeneity, anisotropy and discontinuity structure beneath the caribbean and central america. *Physics of the Earth and Planetary Interiors*, 140(1-3):219–242.

Garnero, E. J. and McNamara, A. K. (2008). Structure and dynamics of earth's lower mantle. *science*, 320(5876):626–628.

Garnero, E. J., McNamara, A. K., and Shim, S.-H. (2016). Continent-sized anomalous zones with low seismic velocity at the base of earth's mantle. *Nature Geoscience*, 9(7):481.

Gilbert, F. and Dziewonski, A. M. (1975). An application of normal mode theory to the retrieval of structural parameters and source mechanisms from seismic spectra. *Philosophical Transactions of the Royal Society of London. Series A, Mathematical and Physical Sciences*, 278(1280):187–269.

Goarant, F., Guyot, F., Peyronneau, J., and Poirier, J.-P. (1992). High-pressure and high-temperature reactions between silicates and liquid iron alloys, in the diamond anvil cell, studied by analytical electron microscopy. *Journal of Geophysical Research: Solid Earth*, 97(B4):4477–4487.

Goes, S., Agrusta, R., Van Hunen, J., and Garel, F. (2017). Subduction-transition zone interaction: A review. *Geosphere*, 13(3):644–664.

Graham, D. W., Michael, P. J., and Shea, T. (2016). Extreme incompatibility of helium during mantle melting: Evidence from undegassed mid-ocean ridge basalts. *Earth and Planetary Science Letters*, 454:192–202.

Gurrola, H., Minster, J., and Owens, T. (1994). The use of velocity spectrum for stacking receiver functions and imaging upper mantle discontinuities. *Geophysical Journal International*, 117(2):427–440.

Hafkenscheid, E., Wortel, M., and Spakman, W. (2006). Subduction history of the Tethyan region derived from seismic tomography and tectonic reconstructions. *Journal of Geophysical Research: Solid Earth*, 111(B8).

Helffrich, G., Asencio, E., Knapp, J., and Owens, T. (2003). Transition zone structure in a tectonically inactive area: 410 and 660 km discontinuity properties under the northern north sea. *Geophysical Journal International*, 155(1):193–199.

Hernlund, J. W., Thomas, C., and Tackley, P. J. (2005). A doubling of the post-perovskite phase boundary and structure of the earth's lowermost mantle. *Nature*, 434(7035):882.

Heyn, B. H., Conrad, C. P., and Trønnes, R. G. (2018). Stabilizing effect of compositional viscosity contrasts on thermochemical piles. *Geophysical Research Letters*, 45(15):7523–7532.

Hosseini, K., Matthews, K., Sigloch, K., Shephard, G., Domeier, M., and Tsekhmistrenko, M. (2018). Submachine: Web-based tools for exploring seismic tomography and other models of earth's deep interior. *Geochemistry, Geophysics, Geosystems*, 19.

Hosseini, K. and Sigloch, K. (2015). Multifrequency measurements of core-diffracted P waves (Pdiff) for global waveform tomography. *Geophysical Journal International*, 203(1):506–521.

Hosseini, K. and Sigloch, K. (2017). obspyDMT: A Python toolbox for retrieving and processing of large seismological datasets. *Solid Earth*, 8.

Hung, S.-H., Dahlen, F., and Nolet, G. (2000). Fréchet kernels for finite-frequency traveltimeséii. examples. *Geophysical Journal International*, 141(1):175–203.

Hung, S.-H., Dahlen, F., and Nolet, G. (2001). Wavefront healing: a banana–doughnut perspective. *Geophysical Journal International*, 146(2):289–312.

Hung, S.-H., Shen, Y., and Chiao, L.-Y. (2004). Imaging seismic velocity structure beneath the Iceland hot spot: A finite frequency approach. *Journal of Geophysical Research: Solid Earth*, 109(B8).

Ishii, M. and Tromp, J. (1999). Normal-mode and free-air gravity constraints on lateral variations in velocity and density of earth's mantle. *Science*, 285(5431):1231–1236.

Jackson, M., Konter, J., and Becker, T. (2017). Primordial helium entrained by the hottest mantle plumes. *Nature*, 542(7641):340.

Jameson, I. (2006). Time delay estimation. Technical report, DEFENCE SCIENCE AND TECHNOLOGY ORGANISATION EDINBURGH (AUSTRALIA) ELECTRONIC ....

Kárason, H. and van der Hilst, R. D. (2001). Tomographic imaging of the lowermost mantle with differential times of refracted and diffracted core phases (PKP, Pdiff). *Journal of Geophysical Research: Solid Earth*, 106(B4):6569–6587.

Keith, C. M. and Crampin, S. (1977). Seismic body waves in anisotropic media: reflection and refraction at a plane interface. *Geophysical Journal International*, 49(1):181–208.

Kennett, B. and Engdahl, E. (1991). Traveltimes for global earthquake location and phase identification. *Geophysical Journal International*, 105(2):429–465.

Kennett, B. L., Engdahl, E., and Buland, R. (1995). Constraints on seismic velocities in the earth from traveltimes. *Geophysical Journal International*, 122(1):108–124.

Kincaid, C. and Olson, P. (1987). An experimental study of subduction and slab migration. *Journal of Geophysical Research: Solid Earth*, 92(B13):13832–13840.

Koelemeijer, P., Deuss, A., and Ritsema, J. (2013). Observations of core-mantle boundary Stoneley modes. *Geophysical Research Letters*, 40(11):2557–2561.

Koelemeijer, P., Deuss, A., and Ritsema, J. (2017). Density structure of Earth's lowermost mantle from Stoneley mode splitting observations. *Nature communications*, 8:15241.

Koelemeijer, P., Ritsema, J., Deuss, A., and Van Heijst, H.-J. (2016). SP12RTS: a degree-12 model of shear-and compressional-wave velocity for Earth's mantle. *Geophysical Journal International*, 204(2):1024–1039.

Kolstrup, M. and Maupin, V. (2015). Measuring and crust-correcting finite-frequency travel time residuals–application to southwestern Scandinavia. *Solid Earth*, 6(4):1117–1130.

Lallemand, S., Heuret, A., and Boutelier, D. (2005). On the relationships between slab dip, back-arc stress, upper plate absolute motion, and crustal nature in subduction zones. *Geochemistry, Geophysics, Geosystems*, 6(9).

Laske, G., Masters, G., Ma, Z., and Pasyanos, M. (2013). Update on CRUST1. 0-A 1-degree global model of Earth's crust. In *Geophys. Res. Abstr*, volume 15, page 2658. EGU General Assembly Vienna, Austria.

Laske, G., Widmer-Schnidrig, R., Herring, T., Romanowicz, B., and Schubert, G. (2007). Normal mode and surface wave observations. *Treatise on Geophysics*, 1:67–125.

Lay, T. and Garnero, E. J. (2004). Core-mantle boundary structures and processes. *The State of the Planet: Frontiers and Challenges in Geophysics*, 19:25–41.

Lay, T., Hernlund, J., and Buffett, B. A. (2008). Core–mantle boundary heat flow. *Nature geoscience*, 1(1):25.

Lee, C. and King, S. D. (2011). Dynamic buckling of subducting slabs reconciles geological and geophysical observations. *Earth and Planetary Science Letters*, 312(3-4):360–370.

Maguire, R., Ritsema, J., Bonnin, M., van Keken, P. E., and Goes, S. (2018). Evaluating the resolution of deep mantle plumes in teleseismic traveltime tomography. *Journal of Geophysical Research: Solid Earth*, 123(1):384–400.

Marquering, H., Dahlen, F., and Nolet, G. (1999). Three-dimensional sensitivity kernels for finite-frequency traveltimes: the banana-doughnut paradox. *Geophysical Journal International*, 137(3):805–815.

Masters, G., Laske, G., Bolton, H., and Dziewonski, A. (2000). The relative behavior of shear velocity, bulk sound speed, and compressional velocity in the mantle: Implications for chemical and thermal structure. *Earth's deep interior: mineral physics and tomography from the atomic to the global scale*, 117:63–87.

Masters, T. G., Johnson, S., Laske, G., and Bolton, H. (1996). A shear-velocity model of the mantle. *Phil. Trans. R. Soc. Lond. A*, 354(1711):1385–1411.

McGowan, N. M., Griffin, W. L., González-Jiménez, J. M., Belousova, E., Afonso, J. C., Shi, R., McCammon, C. A., Pearson, N. J., and O'Reilly, S. Y. (2015). Tibetan chromitites: Excavating the slab graveyard. *Geology*, 43(2):179–182.

Menke, W. (2018). *Geophysical data analysis: Discrete inverse theory*. Academic press.

Mercerat, E. D., Nolet, G., and Zaroli, C. (2013). Cross-borehole tomography with correlation delay times. *Geophysics*, 79(1):R1–R12.

Merkel, S. (2001). Structures minérales et composition de la Terre profonde. `http://planet-terre.ens-lyon.fr/objets/java/mineraux-profonds`. [Online; accessed 23-July-2019].

Montelli, R., Nolet, G., Dahlen, F., and Masters, G. (2006). A catalogue of deep mantle plumes: New results from finite-frequency tomography. *Geochemistry, Geophysics, Geosystems*, 7(11).

Montelli, R., Nolet, G., Dahlen, F., Masters, G., Engdahl, E. R., and Hung, S.-H. (2004). Finite-frequency tomography reveals a variety of plumes in the mantle. *Science*, 303(5656):338–343.

Morgan, W. J. (1968). Rises, trenches, great faults, and crustal blocks. *Journal of Geophysical Research*, 73(6):1959–1982.

Moulik, P. and Ekström, G. (2016). The relationships between large-scale variations in shear velocity, density, and compressional velocity in the earth's mantle. *Journal of Geophysical Research: Solid Earth*, 121(4):2737–2771.

Murakami, M., Hirose, K., Kawamura, K., Sata, N., and Ohishi, Y. (2004). Post-perovskite phase transition in mgsio3. *Science*, 304(5672):855–858.

Nolet, G. (1985). Solving or resolving inadequate and noisy tomographic systems. *Journal of computational physics*, 61(3):463–482.

Nolet, G. et al. (2008). A breviary of seismic tomography. *Imaging the Interior*.

Nolet, G., Karato, S.-I., and Montelli, R. (2006). Plume fluxes from seismic tomography. *Earth and Planetary Science Letters*, 248(3-4):685–699.

Obayashi, M., Ishihara, Y., and Suetsugu, D. (2017). Effects of shallow-layer reverberation on measurement of teleseismic P-wave travel times for ocean bottom seismograph data. *Earth, Planets and Space*, 69(1):44.

Obayashi, M., Suetsugu, D., and Fukao, Y. (2004). PP-P differential traveltime measurement with crustal correction. *Geophysical Journal International*, 157(3):1152–1162.

Oganov, A. R. and Ono, S. (2004). Theoretical and experimental evidence for a post-perovskite phase of mgsio 3 in earth's d "layer. *Nature*, 430(6998):445.

Olivieri, M. and Pino, N. (1998). The ScS precursors for the study of the lowermost mantle. *Il nuovo cimento C*, 21(5):503–514.

O'nions, R. and Oxburgh, E. (1983). Heat and helium in the earth. *Nature*, 306(5942):429.

Ouattara, Y. (2019). *Structure sismique de l'Afrique de l'Ouest par tomographie d'ondes de surface*. PhD thesis.

Pachhai, S., Tkalčić, H., and Masters, G. (2015). Estimation of splitting functions from Earth's normal mode spectra using the neighbourhood algorithm. *Geophysical Journal International*, 204(1):111–126.

Paige, C. C. and Saunders, M. A. (1982). Lsqr: An algorithm for sparse linear equations and sparse least squares. *ACM Transactions on Mathematical Software (TOMS)*, 8(1):43–71.

Pavlis, N. K., Holmes, S. A., Kenyon, S. C., and Factor, J. K. (2012). The development and evaluation of the Earth Gravitational Model 2008 (EGM2008). *Journal of geophysical research: solid earth*, 117(B4).

Peltier, W. (2007). Mantle dynamics and the d" layer: Impacts of the post perovskite phase. *GEOPHYSICAL MONOGRAPH-AMERICAN GEOPHYSICAL UNION*, 174:217.

Pijpers, F. and Thompson, M. (1992). Faster formulations of the optimally localized averages method for helioseismic inversions. *Astronomy and Astrophysics*, 262:L33–L36.

Pijpers, F. and Thompson, M. (1994). The SOLA method for helioseismic inversion. *Astronomy and Astrophysics*, 281:231–240.

Ritsema, J., Deuss, a. A., Van Heijst, H., and Woodhouse, J. (2011). S40RTS: a degree-40 shear-velocity model for the mantle from new rayleigh wave dispersion, teleseismic traveltime and normal-mode splitting function measurements. *Geophysical Journal International*, 184(3):1223–1236.

Ritsema, J., Van Heijst, H., Woodhouse, J., and Deuss, A. (2009). Long-period body wave traveltimes through the crust: implication for crustal corrections and seismic tomography. *Geophysical Journal International*, 179(2):1255–1261.

Ritsema, J. and van Heijst, H.-J. (2002). Constraints on the correlation of P-and S-wave velocity heterogeneity in the mantle from P, PP, PPP and PKPab traveltimes. *Geophysical Journal International*, 149(2):482–489.

Ritsema, J., van Heijst, H. J., and Woodhouse, J. H. (1999). Complex shear wave velocity structure imaged beneath Africa and Iceland. *Science*, 286(5446):1925–1928.

Ritzwoller, M., Masters, G., and Gilbert, F. (1986). Observations of anomalous splitting and their interpretation in terms of aspherical structure. *Journal of Geophysical Research: Solid Earth*, 91(B10):10203–10228.

Ritzwoller, M., Masters, G., and Gilbert, F. (1988). Constraining aspherical structure with low-degree interaction coefficients: Application to uncoupled multiplets. *Journal of Geophysical Research: Solid Earth*, 93(B6):6369–6396.

Romanowicz, B. (2008). Using seismic waves to image earth's internal structure. *Nature*, 451(7176):266.

Romanowicz, B. and Dziewonski, A. (2010). *Seismology and Structure of the Earth: Treatise on Geophysics*, volume 1. Elsevier.

Rose, J. and Koppers, A. A. (2019). Simplifying Age Progressions within the Cook-Austral Islands using ARGUS-VI High-Resolution 40Ar/39Ar Incremental Heating Ages. *Geochemistry, Geophysics, Geosystems*.

Rudolph, M. L., Lekić, V., and Lithgow-Bertelloni, C. (2015). Viscosity jump in Earth's mid-mantle. *Science*, 350(6266):1349–1352.

Schaff, D., Waldhauser, F., Kim, W., and Richards, P. (2001). Cross-correlation measurements and the double-difference earthquake location technique. In *AGU Fall Meeting Abstracts*.

Schaff, D. P. and Waldhauser, F. (2005). Waveform cross-correlation-based differential travel-time measurements at the northern california seismic network. *Bulletin of the Seismological Society of America*, 95(6):2446–2461.

Schubert, G., Turcotte, D. L., and Olson, P. (2001). *Mantle convection in the Earth and planets*. Cambridge University Press.

Shearer, P. M. (1997). Improving local earthquake locations using the l1 norm and waveform cross correlation: Application to the whittier narrows, california, aftershock sequence. *Journal of Geophysical Research: Solid Earth*, 102(B4):8269–8283.

Sigloch, K., McQuarrie, N., and Nolet, G. (2008). Two-stage subduction history under North America inferred from multiple-frequency tomography. *Nature Geoscience*, 1(7):458.

Sigloch, K. and Nolet, G. (2006). Measuring finite-frequency body-wave amplitudes and traveltimes. *Geophysical Journal International*, 167(1):271–287.

Spasojevic, S., Gurnis, M., and Sutherland, R. (2010). Mantle upwellings above slab graveyards linked to the global geoid lows. *Nature Geoscience*, 3(6):435.

Stanford, E. E. L. (2019). Earth's D" Layer . `https://eel.stanford.edu/earth-s-d-layer0`. [Online; accessed 30-Septembre-2019].

Stein, S. and Wysession, M. (2009). *An introduction to seismology, earthquakes, and earth structure*. John Wiley & Sons.

Stoneley, R. (1924). Elastic waves at the surface of separation of two solids. *Proceedings of the Royal Society of London. Series A, Containing Papers of a Mathematical and Physical Character*, 106(738):416–428.

Tackley, P. J. (2000). Mantle convection and plate tectonics: Toward an integrated physical and chemical theory. *Science*, 288(5473):2002–2007.

Tackley, P. J. (2011). Living dead slabs in 3-D: The dynamics of compositionally-stratified slabs entering a "slab graveyard" above the core-mantle boundary. *Physics of the Earth and Planetary Interiors*, 188(3-4):150–162.

Tamim, N. S. M. and Ghani, F. (2010). Techniques for optimization in time delay estimation from cross correlation function. *Int J Eng Technol*, 10(2):69–75.

Tian, Y., Hung, S.-H., Nolet, G., Montelli, R., and Dahlen, F. A. (2007a). Dynamic ray tracing and traveltime corrections for global seismic tomography. *Journal of computational physics*, 226(1):672–687.

Tian, Y., Montelli, R., Nolet, G., and Dahlen, F. A. (2007b). Computing traveltime and amplitude sensitivity kernels in finite-frequency tomography. *Journal of Computational Physics*, 226(2):2271–2288.

Torsvik, T. H., Smethurst, M. A., Burke, K., and Steinberger, B. (2006). Large igneous provinces generated from the margins of the large low-velocity provinces in the deep mantle. *Geophysical Journal International*, 167(3):1447–1460.

Trampert, J. (1998). Global seismic tomography: the inverse problem and beyond. *Inverse Problems*, 14(3):371.

Trampert, J., Vacher, P., and Vlaar, N. (2001). Sensitivities of seismic velocities to temperature, pressure and composition in the lower mantle. *Physics of the Earth and Planetary Interiors*, 124(3-4):255–267.

Tromp, J., Komattisch, D., and Liu, Q. (2008). Spectral-element and adjoint methods in seismology. *Communications in Computational Physics*, 3(1):1–32.

Van Camp, M. (2006). Sumatra-Andaman Islands Earthquake. `http://www.iris.iris.edu/sumatra/free_oscillations_second.htm`. [Online; accessed 19-September-2019].

Wielandt, E. (1987). On the validity of the ray approximation for interpreting delay times. In *Seismic tomography*, pages 85–98. Springer.

Williams, C., Mukhopadhyay, S., Rudolph, M., and Romanowicz, B. (2019). Primitive helium is sourced from seismically slow regions in the lowermost mantle. *Geochemistry, Geophysics, Geosystems*.

Woodhouse, J. H. and Dahlen, F. A. (1978). The effect of a general aspherical perturbation on the free oscillations of the earth. *Geophysical Journal International*, 53(2):335–354.

Woodward, R. L. and Masters, G. (1991a). Global upper mantle structure from long-period differential travel times. *Journal of Geophysical Research: Solid Earth*, 96(B4):6351–6377.

Woodward, R. L. and Masters, G. (1991b). Lower-mantle structure from ScS–S differential travel times. *Nature*, 352(6332):231–233.

Worzewski, T., Jegen, M., Kopp, H., Brasse, H., and Castillo, W. T. (2011). Magnetotelluric image of the fluid cycle in the Costa Rican subduction zone. *Nature Geoscience*, 4(2):108.

Yang, T. and Shen, Y. (2006). Frequency-dependent crustal correction for finite-frequency seismic tomography. *Bulletin of the Seismological Society of America*, 96(6):2441–2448.

Yang, T., Shen, Y., van der Lee, S., Solomon, S. C., and Hung, S.-H. (2006). Upper mantle structure beneath the Azores hotspot from finite-frequency seismic tomography. *Earth and Planetary Science Letters*, 250(1-2):11–26.

Zaroli, C. (2010). *Global multiple-frequency S-wave tomography of the Earth's mantle*. PhD thesis, Strasbourg.

Zaroli, C. (2016). Global seismic tomography using Backus-Gilbert inversion. *Geophysical Journal International*, 207:876–888.

Zaroli, C. (2019). Seismic tomography using parameter-free Backus–Gilbert inversion. *Geophysical Journal International*, 218(1):619–630.

Zaroli, C., Debayle, E., and Sambridge, M. (2010). Frequency-dependent effects on global S-wave traveltimes: wavefront-healing, scattering and attenuation. *Geophysical Journal International*, 182(2):1025–1042.

Zaroli, C., Koelemeijer, P., and Lambotte, S. (2017). Toward seeing the Earth's interior through unbiased tomographic lenses. *Geophysical Research Letters*, 44(22).

Zaroli, C., Lambotte, S., and Lévêque, J.-J. (2015). Joint inversion of normal-mode and finite-frequency S-wave data using an irregular tomographic grid. *Geophysical Journal International*, 203(3):1665–1681.

Zaroli, C., Lévêque, J.-J., Schuberth, B. S., Duputel, Z., and Nolet, G. (2014). Global S-wave tomography using receiver pairs: an alternative to get rid of earthquake mislocation. *Geophysical Journal International*, 199(2):1043–1057.

Zhao, D. (2007). Seismic images under 60 hotspots: search for mantle plumes. *Gondwana Research*, 12(4):335–355.

Zhao, L., Jordan, T. H., and Chapman, C. H. (2000). Three-dimensional fréchet differential kernels for seismicdelay times. *Geophysical Journal International*, 141(3):558–576.

Zhong, S. (2006). Constraints on thermochemical convection of the mantle from plume heat flux, plume excess temperature, and upper mantle temperature. *Journal of Geophysical Research: Solid Earth*, 111(B4).

Appendix A: SOLA inversion

Philosophy and theory

Backus–Gilbert inversion belongs to an inversion scheme category called OLA (optimally localized averages). It was introduced by the pioneering works of Backus and Gilbert (Backus and Gilbert, 1967, 1968, 1970).

The main idea of Backus–Gilbert inversion is to produce models that are results of localized averages of the true properties of the studied object (seismic velocities, density, resistivity). The term "localized" has a profound impact on the expecting result. As a matter of fact, the model will be a composite of different averages localized at different geographical locations. This means that nothing ensures a globally coherent model at the end of the inversion process. Besides, in terms of variance, one may appreciate that meaningful variances for model values can not be obtained for a point estimate (Nolet et al., 2008). Meaningful values for model are always averages over volumes which depends on the data density around the targeted location.

Linear problem can be set under the following form:

$$\mathrm{d} = \mathbf{G}\mathrm{m} \tag{7}$$

with d referring to observed data, m the model and $\mathbf{G}$ the matrix containing the physics of the problem. Data can thus be predicted from a model representing specific properties of the Earth. In a same way, we can predict the values of the model from the observed data such as

$$\hat{\mathrm{m}} = \mathbf{G}^{\dagger}\mathrm{d} \tag{8}$$

we generally call $\mathbf{G}^{\dagger}$ a generalized inverse since it is not the true inverse of $\mathbf{G}$. Combining equations (7) and (8), we get

$$\hat{\mathrm{m}} = \underbrace{\mathbf{G}^{\dagger}\mathbf{G}}_{\substack{\text{model resolution}\\ \text{matrix R}}} \quad \mathrm{m} \tag{9}$$

If the matrix $\mathrm{R}(= \mathbf{G}^{\dagger}\mathbf{G}) = Id_M$ then the values of the model are uniquely determined (with M the number of parameter). However, in most cases $\mathrm{R} \neq Id_M$ which implies that the estimates of the model values are weighted averages of the true model values (Menke, 2018). Since we compute weighted averages of the true model values, we would like to produce unbiased averages of model values such as the following condition is respected:

$$\sum_{j=1}^{M} \mathrm{R}_{ij} = 1 \tag{10}$$

However, it has be shown that $\sum_{j=1}^{M} \mathrm{R}_{ij}$ can be either < 1 (e.g., Nolet et al., 2008) or > 1 (Zaroli, 2016). In these cases, the model estimates are biased towards lower $(\mathrm{R} < 1)$ or higher $(\mathrm{R} > 1)$ values than those given by the true model. These estimates are thus no more unbiased averages of the true model values. This effect can be attributed to the way that we solve the inverse problem.

Seismic tomographic imagery is intrinsically a mixed-determined problem. This means that we have globally more data than parameters but some parameters might be completely not constrained by data. And the non-unicity of the problem remains strong. To solve this problem, we usually make use of data-fitting procedures and remove the non-unicity by regularizing the problem. Dampings are used to temper noise affecting the data, for instance by favoring models with minimum norms.

Although data-fitting method are easy to understand and to apply, some drawbacks appear to be noxious for quantitative assessment of tomographic images. Data-fitting methods aim at finding a trade-off between goodness of the data dit and the norm of the resulting model. This implies to set direct constrains on the value of the model but does not put particular constrains on model resolution matrix and thus may produce biased images of the true Earth properties. To overcome this problem, we can apply a other kind of inversion called Backus-Gilbert inversions where the trade-off is expressed between the spread of the model resolution matrix and the covariance on the model. In that case, any constrain is put on the model. However, this method was stated as too computationnaly intensive to be applied on data contaminated by error in a context of large-scale tomographic problems (e.g., Trampert, 1998). To go around that problem, Zaroli (2016) took advantage of a Backus-Gilbert-variant developped in helioseismology (Pijpers and Thompson, 1992, 1994) for an application to large-scale tomographic problems. This derived Backus-Gilbert inversion is called SOLA for "substractive optimally localized averages". The idea was to introduce a prior averaging volume called "target kernel" (T) to guide the minimization of the resolution matrix spread R. Unlike the data-fitting procedure, Backus–Gilbert inversion schemes aim at finding a trade-off between resolution spread (or resolution misfit for SOLA) and variances on averages computed at each locations. This resolution spread can thus be compared to an averaging volume inside which we are computing the estimate of the model value. Whether or not the value of the average is localized will depend on the spread of the resolution matrix.

As a simple example, we consider a seismic experiment with sources and receivers in a 2D geometry (Figure 2). For clarity, we consider a unique ray between couple of source-receiver. We are interested in the true model value at the green point location. In a SOLA inversion context, we define a target averaging surface delimited by the red circle. All data (seismic rays) crossing or touching the circle will be considered in the linear combinaison of the data to produce the model estimate. In that case, we will have a poor resolution (only constrains on large features) but a very low uncertainty on the model estimate at the green point location. On the contrary in figure 3, we will have a small averaging volume indicating a very good resolution but a large uncertainty on the model estimate.

Influence of the trade-off parameter on SOLA images

The misfit function of the Backus–Gilbert inversion introduced in chapter 4 can be written as:

$$\min_{x^{(k)}} \int (A^{(k)} - T^{(k)})^2 + \eta_k^2 \, \sigma^2_{\hat{m}_k} \tag{11}$$

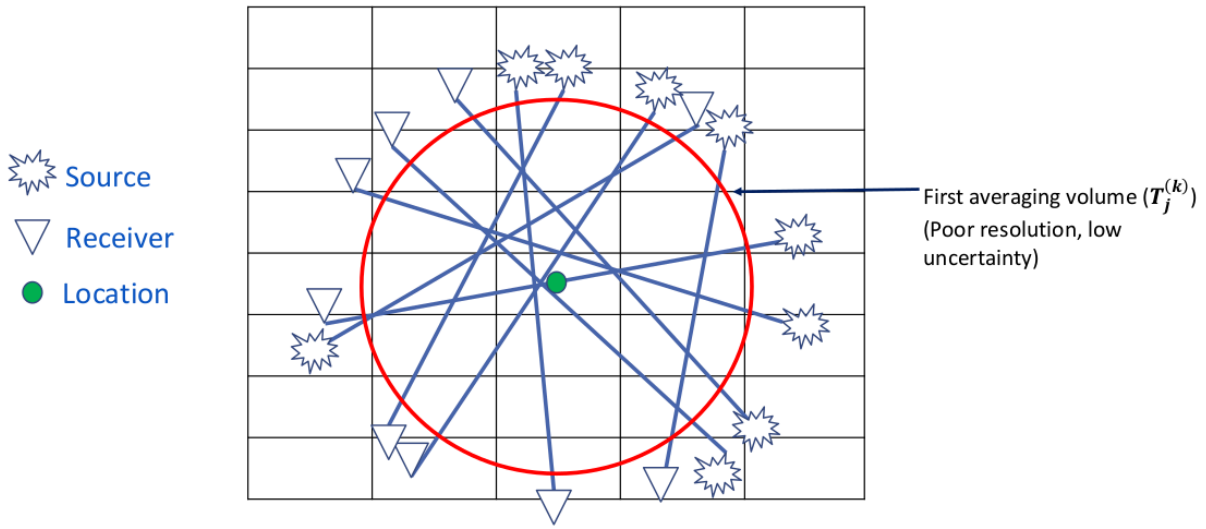

Figure 2 – Target kernel illustration for SOLA inversion scheme. Large averaging volume indicating a poor resolution but a low uncertainty on the model value.

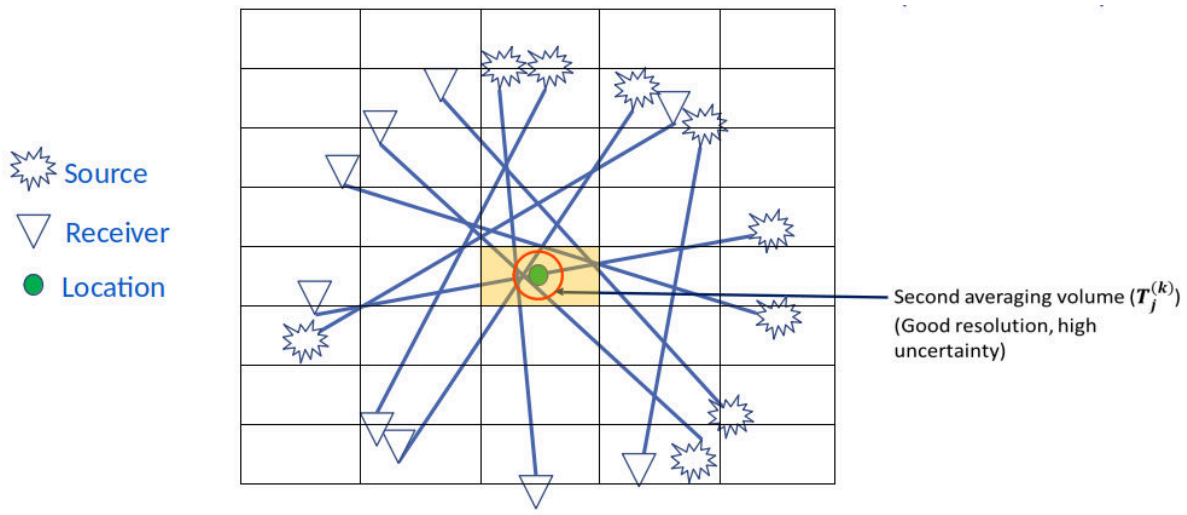

Figure 3 – Target kernel illustration for SOLA inversion scheme. Small averaging volume indicating a good resolution but a highuncertainty on the model value.

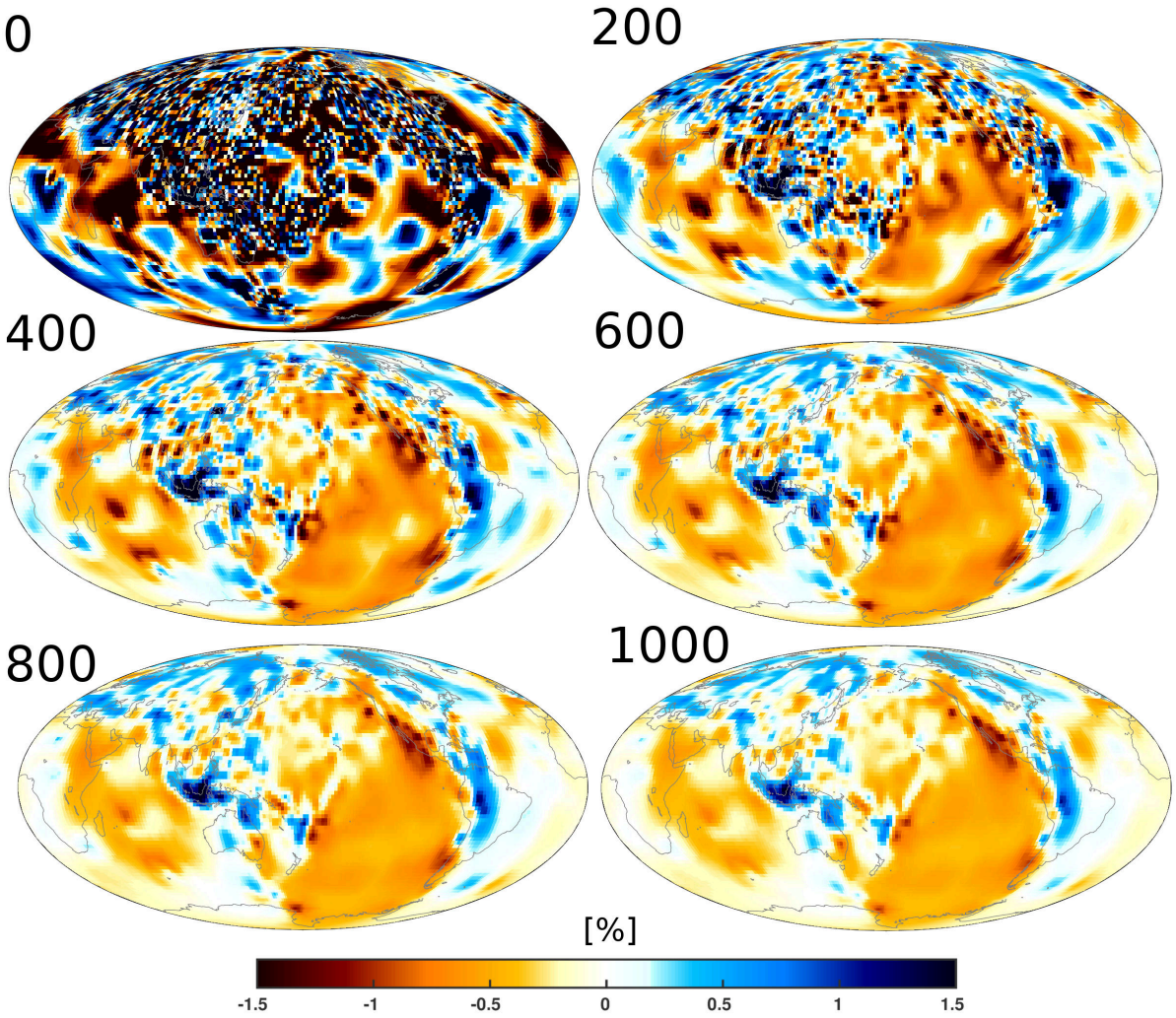

Figure 4 – SOLA tomography at 875 km depth using S and SS waves only. Number indicated beside each image is the value of the tade-off parameter η between the resolution misfit and uncertainties. Perturbations are computed from the 1D-Earth model IASP91 (Kennett and Engdahl, 1991).

The trade-off parameter $\eta_k (= \eta)$ is considered independent of the target parameter k. Therefore, we invert the whole model with only one value of the trade-off parameter. In the previous chapter we only show images with a trade-off parameter of 600 for the joint inversion. To illustrate the variability of the tomographic images with η, we show the SOLA image at 875 km for S and SS waves with trade-off parameters of 0, 200, 400, 600, 800, 1000.

As expected, for a low trade-off parameter, inversion try to reach to best resolution as possible making the image very high frequency. In return, uncertainties on each average is huge (balance of eaqution 11). For a trade-off parameter of 1000, averaging kernels are wide and thus averages are carried out over large volumes. The resulting image are showing only large feature of the tomographic model with low uncertainties.

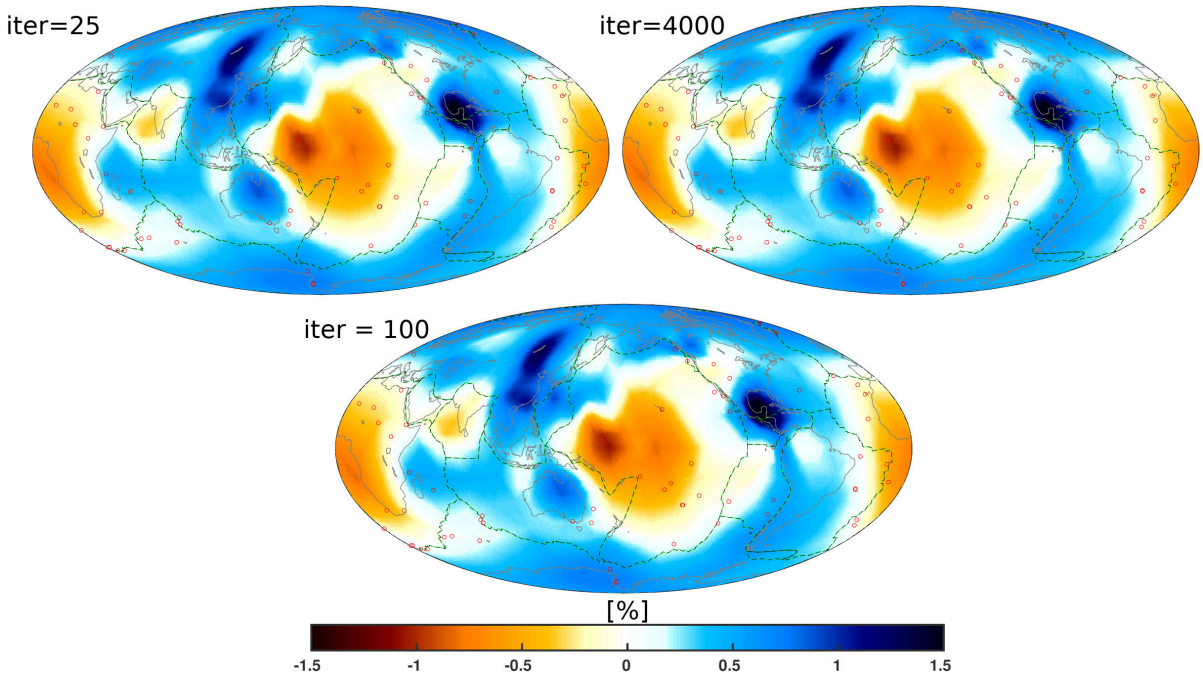

Figure 5 – SOLA joint tomography model at 2800 km depth. Number indicated beside each image is the maximum number of iteration imposed to the LSQR process for each node of the model. Perturbations are computed from the 1D-Earth model IASP91 (Kennett and Engdahl, 1991).

Computational facilities

All SOLA inversions are performed on a single computer with 8 physical processors Intel(R) Xeon(R) E5-2643 v3 at 3.4 GHz. We fully use the RAM memory (125G) to store twice a modified version of the G matrix ($\mathbf{Q}^{(\eta)}$ matrix, see appendix A1 in (Zaroli, 2016)). The 8 processors are using in parallel the LSQR (Paige and Saunders, 1982) code for a subset of model parameters. For each parameter, the LSQR code takes about 3 min to run 100 iterations for a single node k. For instance, the layer located at 1610 km and containing 2,177 parameters needs 20 hrs of LSQR running. This computational time is for a G matrix of 4.4 G stored twice on each of the 8 processors.

Number of LSQR iterations

Figure 5 shows the depth slice at 2800 km for our joint model for different values of maximum number of iteration imposed to LSQR process. No clear differences appear between thee different values as well as for the averaging kernels. Slight amplitude differences for the model with 25 iterations can appear with another color bar.

Appendix B: Parametrization (Zaroli et al., 2010)

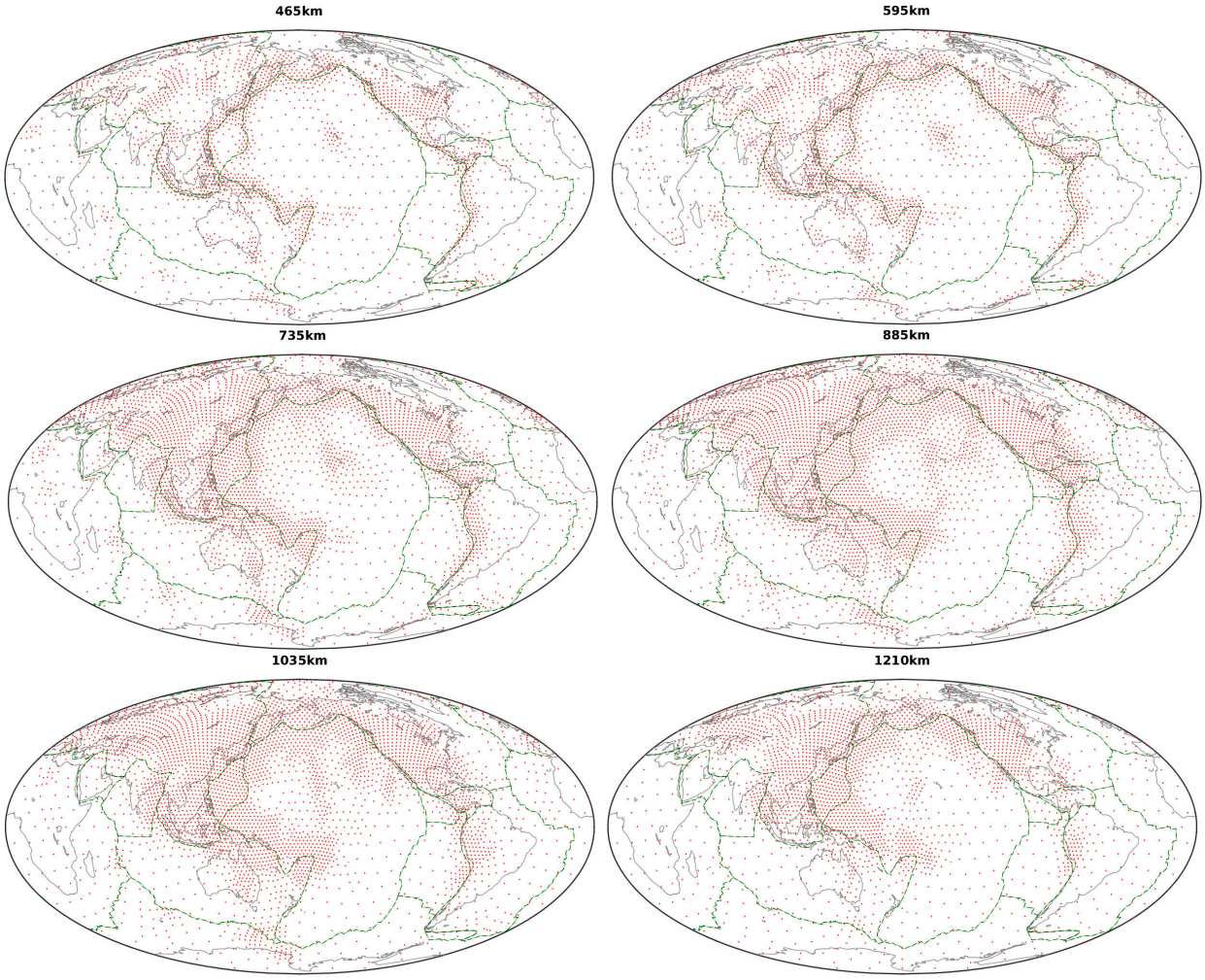

Figure 6 – Irregular lateral parametrization. Nodes agency is carried out according to the ray density from the Zaroli (2010) dataset. The minimal distance between nodes is 200 km and the maximum is 1000 km. Depths presented here are 465, 595, 735, 885, 1035, 1210 km.

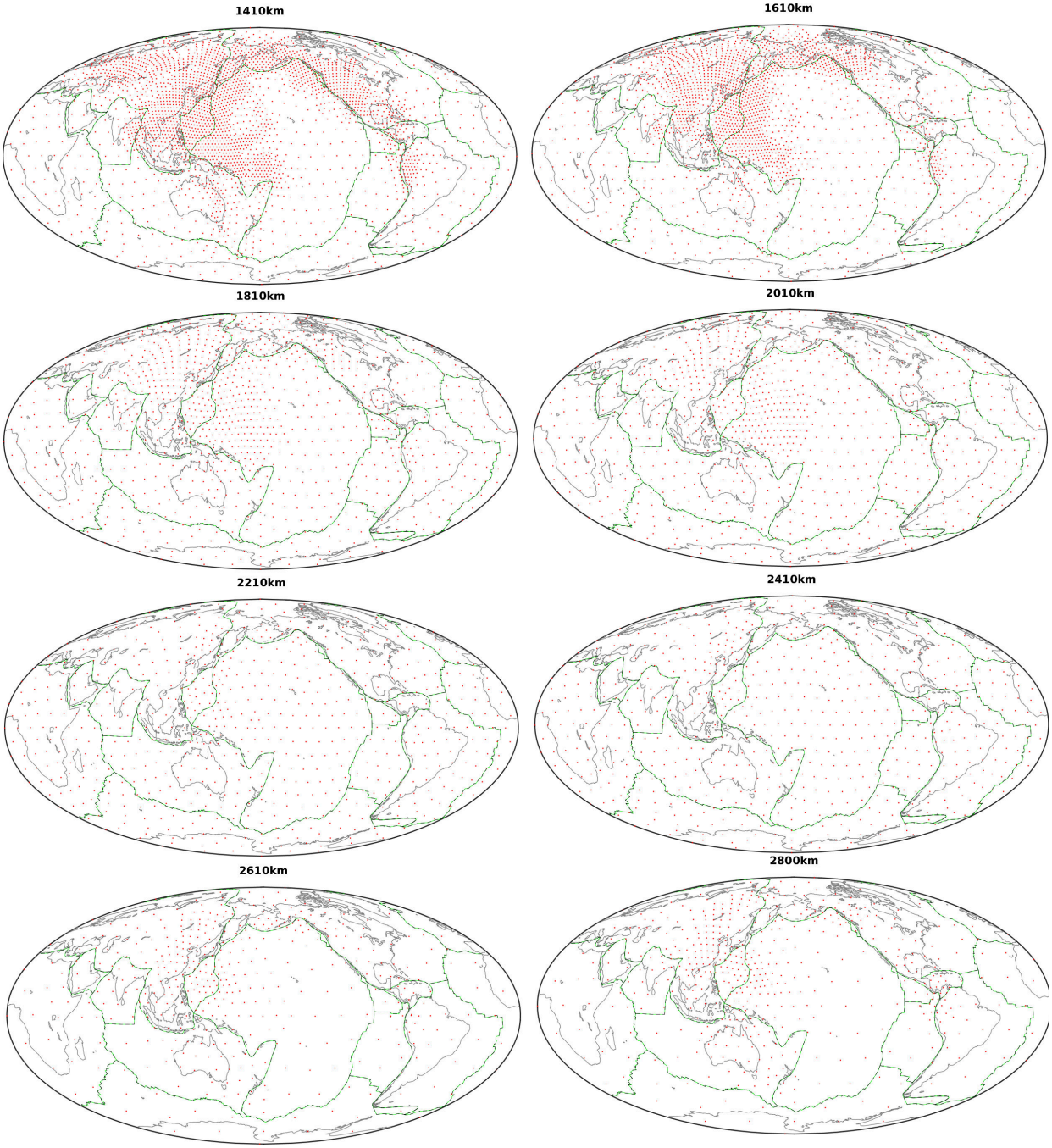

Figure 7 – Irregular lateral parametrization. Nodes agency is carried out according to the ray density from the Zaroli (2010) dataset. The minimal distance between nodes is 200 km and the maximum is 1000 km. Depths presented here are 1410, 1610, 1810, 2010, 2210, 2410, 2610, 2800 km.

Appendix C: Cross-correlation measurement

At the end of the window selection step, it may leave several pairs of time windows around the target phase. For each pair, we compute the cross-correlation function between the synthetic and the observed seismogram. An extensive explanation of cross-correlation measurements to measure observed seismogram in the Born approximation can be found in Nolet et al. (2008) (p.100 and p.121). Time residual is obtained from the maximum of the cross-correlation function, as defined by:

$$\gamma(\tau) = \int_{t_1}^{t_2} s(t)d(t-\tau)\,\mathrm{d}t \tag{12}$$

with d the observed signal, s the corresponding synthetic seismogram, τ the time-shift between the two waveforms, t_1 and t_2 the beginning and the end of the selected time window, respectively. Figure 8 shows an example of cross-correlation measurement of a S-wave recorded at Wushi in China (WUS) generated by an earthquake in Sumatra. The measurement is made between a synthetic and an observed seismogram filtered between 11 s and 81 s. If the maximum of the normalized cross-correlation is less than 0.8, windows pairs are rejected. In this example the maximum of cross-correlation is equal to 0.87 with an associated delay time of -3.0 s.

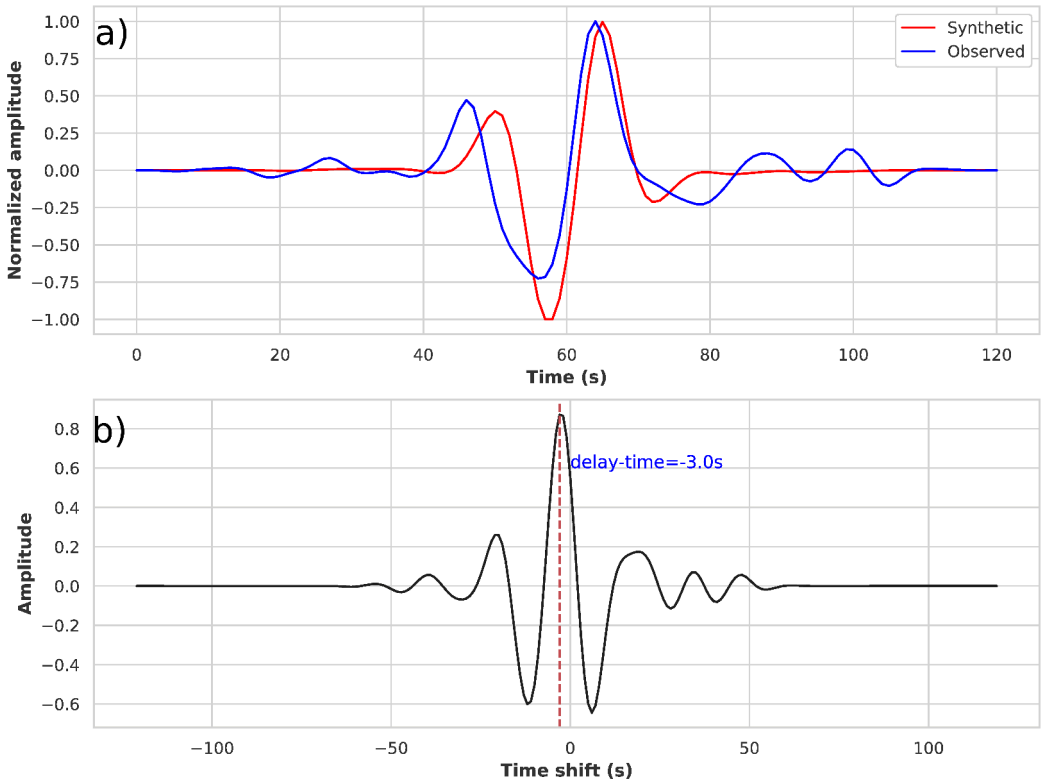

Figure 8 – (a) Two broadband waveforms tapered and filtered between 11 s and 81 s recorded at WUS station for a S-wave (and sS-wave) generated by the Sumatra earthquake ($\mathrm{depth} = 15\,\mathrm{km}$, $\mathrm{m_b} = 5.5$) the 9 october 1990. (b) Cross-correlation function between these two waveforms is displayed on (a).

Cross-correlation method have a serious drawback when two filtered seismograms are strongly dominated by one frequency and thus lead to large error on delay-time estimation (e.g., Zaroli et al., 2010; Kolstrup and Maupin, 2015). To prevent this problem called cycle-skipping, we followed Zaroli et al. (2010).

Appendix D: Body-wave database statistics

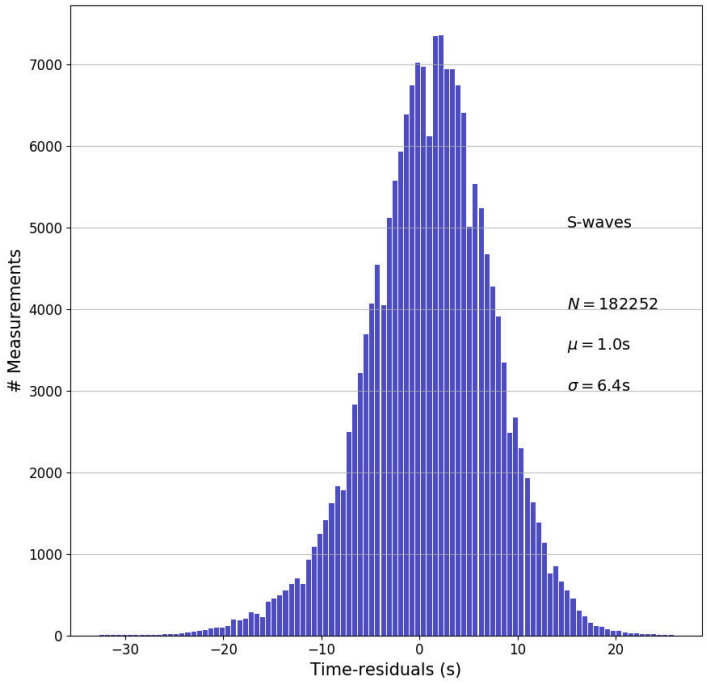

Figure 9 – Histogram for S-wave measurements at all periods (10 s, 15 s, 22.5 s, 34 s, 51 s. Number of measurements (N), the mean of the distribution (μ) as well as the standard deviation (σ) are indicated on the graph.

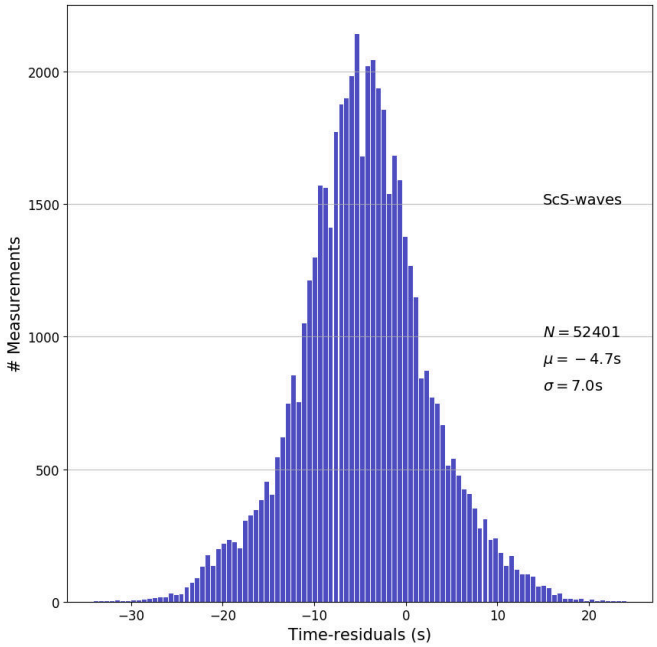

Figure 10 – Histogram for ScS-wave measurements at all periods (10 s, 15 s, 22.5 s, 34 s, 51 s. Number of measurements (N), the mean of the distribution (μ) as well as the standard deviation (σ) are indicated on the graph.

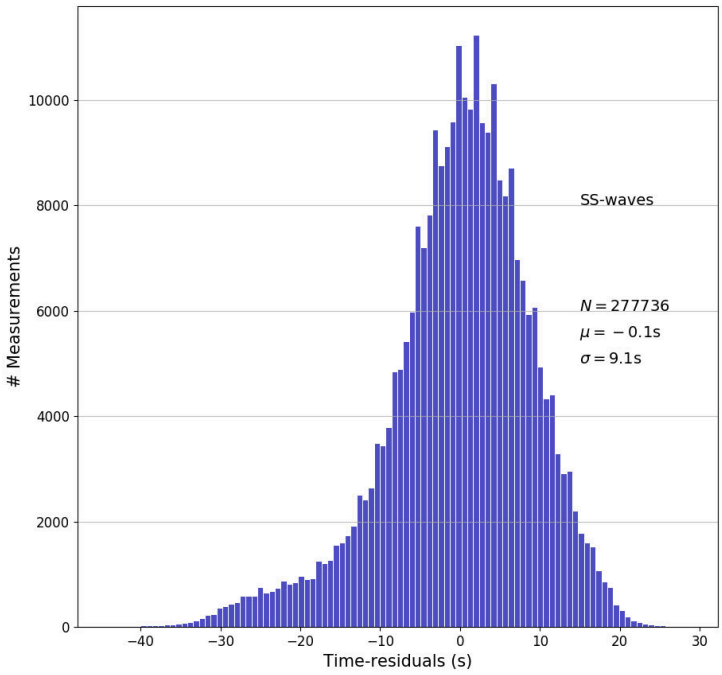

Figure 11 – Histogram for SS-wave measurements at all periods (10 s, 15 s, 22.5 s, 34 s, 51 s. Number of measurements (N), the mean of the distribution (μ) as well as the standard deviation (σ) are indicated on the graph.

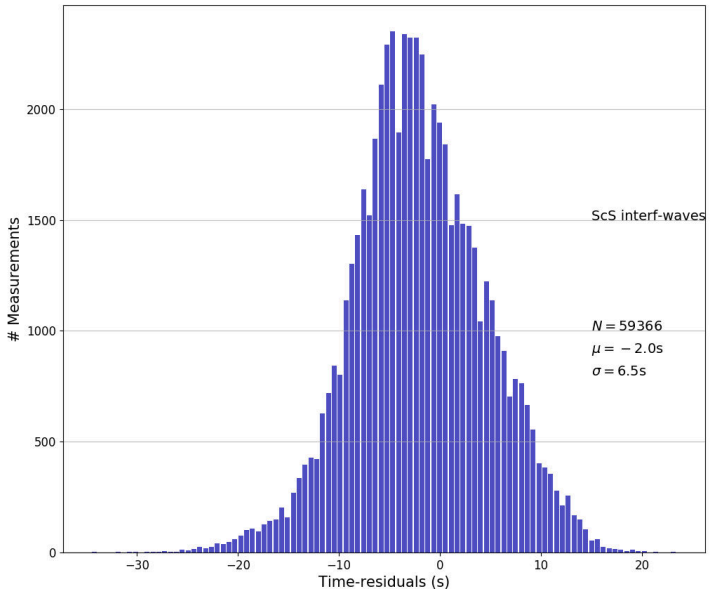

Figure 12 – Histogram for interferences S+ScS measurements at all periods (10 s, 15 s, 22.5 s, 34 s, 51 s. Number of measurements (N), the mean of the distribution (μ) as well as the standard deviation (σ) are indicated on the graph.

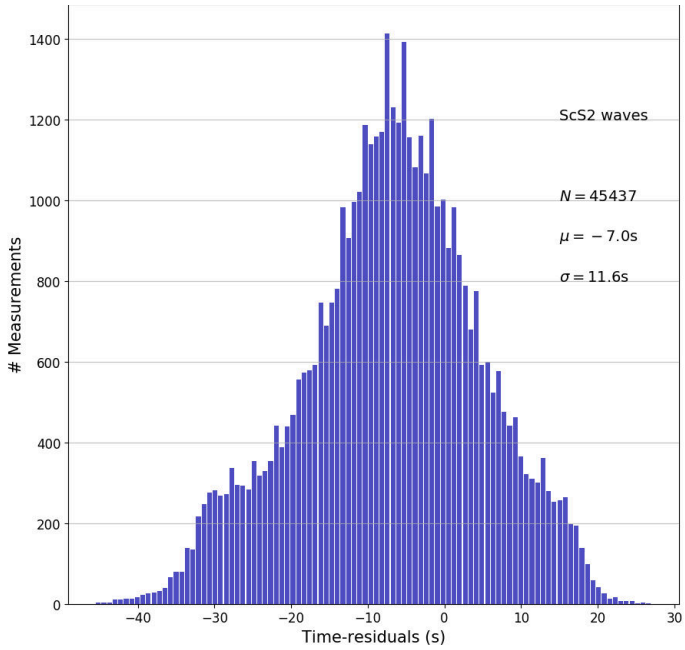

Figure 13 – Histogram for interferences $\mathrm{ScS_2}$ measurements at all periods (10 s, 15 s, 22.5 s, 34 s, 51 s. Number of measurements (N), the mean of the distribution (μ) as well as the standard deviation (σ) are indicated on the graph.

149